

University of Nebraska - Lincoln

DigitalCommons@University of Nebraska - Lincoln

Mechanical (and Materials) Engineering --
Dissertations, Theses, and Student Research

Mechanical & Materials Engineering,
Department of

Winter 11-30-2021

Novel Peridynamic Models for Material Degradation and Mass Transport

Jiangming Zhao

University of Nebraska-Lincoln, jmzhao@huskers.unl.edu

Follow this and additional works at: <https://digitalcommons.unl.edu/mechendis>



Part of the [Applied Mechanics Commons](#)

Zhao, Jiangming, "Novel Peridynamic Models for Material Degradation and Mass Transport" (2021).
Mechanical (and Materials) Engineering -- Dissertations, Theses, and Student Research. 179.
<https://digitalcommons.unl.edu/mechendis/179>

This Article is brought to you for free and open access by the Mechanical & Materials Engineering, Department of at DigitalCommons@University of Nebraska - Lincoln. It has been accepted for inclusion in Mechanical (and Materials) Engineering -- Dissertations, Theses, and Student Research by an authorized administrator of DigitalCommons@University of Nebraska - Lincoln.

NOVEL PERIDYNAMIC MODELS FOR MATERIAL DEGRADATION AND MASS
TRANSPORT

by

Jiangming Zhao

A DISSERTATION

Presented to the Faculty of

The Graduate College at the University of Nebraska

In Partial Fulfillment of Requirements

For the Degree of Doctor of Philosophy

Major: Mechanical Engineering and Applied Mechanics

Under the Supervision of Professor Florin Bobaru

Lincoln, Nebraska

December, 2021

NOVEL PERIDYNAMIC MODELS FOR MATERIAL DEGRADATION AND MASS TRANSPORT

Jiangming Zhao, Ph.D.

University of Nebraska, 2021

Advisor: Florin Bobaru

Fracture and corrosion are two major causes of structure failure. They can interact with each other, leading to faster material degradation. They are also under the influence of environmental conditions. The corrosion rate highly depends on the transportation rate of involving substances, while the fracture can be accelerated significantly due to fluid flow. These complex mechanisms involved in structure failure have troubled classical models for decades. The peridynamic (PD) theory introduced in 2000 has shown great potential in modeling such problems. In this work, we develop novel PD models for fracture, corrosion, mass transport, and viscous flow, which are building blocks to make comprehensive predictions on structure failure.

We first introduce a partially-homogenized PD model for concrete fracture. The model links microscale information to macroscale fracture behavior, while costing the same as a fully homogenized model. This model successfully predicts corrosion-induced fracture in concretes with a single or multiple rebars. We then develop a new PD corrosion model which can update the distribution of corrosion rates along arbitrary metal surface, particularly useful for simulating galvanic corrosion. We couple the new PD corrosion model with the PD fracture model and solve a problem under combined electro-chemical attack and mechanical forces to demonstrate the capability of PD

models. We also construct PD models for transient advection-diffusion and viscous flow from fundamental conservation principles. The constructive approach in deriving these models allows for future modeling of complex fluid-structure interaction problems in which solid degradation takes place, such as erosion-corrosion and hydraulic fracture.

In PD models, boundary conditions (BCs) are naturally nonlocal, but usually only local BCs are available from measurements. The existing mirror-type fictitious nodes method (FNM) can convert local BCs to nonlocal ones, but its application is limited to domains with simple geometries. We introduce a new algorithm to make the mirror-type FNM work autonomously for domains with arbitrary geometries. The algorithm developed is general and should also work for any type of peridynamic model, including corrosion, fracture, and fluid-structure interactions.

Copyright © 2021, Jiangming Zhao.

All rights reserved.

To my family for their support and encouragement

Acknowledgements

First and foremost, I would like to thank my advisor, Professor Florin Bobaru, for all the support, encouragement, and guidance he has offered me over the years. Without him, I would not be able to finish my PhD program. His passion and enthusiasm in research influenced me greatly and I feel more than fortunate to have him as my advisor.

I would like to thank Dr. Stewart Silling, father of peridynamics. I feel honored to have him as the special member of my committee. I am also grateful to Professor Ruqiang Feng and Professor Adam Larios for being the readers of my dissertation, Professor Yuris Dzenis for being my committee member and Professor Hongfeng Yu for being the outside representative of my committee. Their insightful comments helped improve this work significantly.

I have to thank Professor Ziguang Chen and Dr. Siavash Jafarzadeh for their invaluable contributions to this work, and my other labmates, Longzhen Wang, Farzaneh Mousavi, Javad Mehrmashhadi, Sina Niazi, Guanfeng Zhang and Zhanping Xu for their support and encouragement.

I would also like to thank my dear parents, Wenjun and Xianying, my elder sisters Qiaoyun and Juan, and my beloved girlfriend Liyun for their unconditional love, encouragement, and support.

Finally, I would like to say thank you to all my friends that had accompanied me on this tough journey. Those joys and sorrows shared with you are precious gifts to me. They are with me and will follow me forever.

Preface

Chapter 2 has been published in *Engineering Fracture Mechanics*. (J. Zhao, Z. Chen, J. Mehrmashhadi, and F. Bobaru, ‘A Stochastic Multiscale Peridynamic Model for Corrosion Induced Fracture in Reinforced Concrete’, *Engineering Fracture Mechanics* 229 (2020): 106969. DOI: 10.1016/j.engfracmech.2020.106969)

Chapter 3 has been published in *Electrochimica Acta*. (J. Zhao, S. Jafarzadeh, M. Rahmani, Z. Chen, Y. Kim, and F. Bobaru, ‘A Peridynamic Model for Galvanic Corrosion and Fracture’, *Electrochimica Acta* 391 (2021): 138968. DOI: 10.1016/j.electacta.2021.138968)

Chapter 4 has been published in *International Journal of Heat and Mass Transfer*. (J. Zhao, Z. Chen, J. Mehrmashhadi and F. Bobaru, ‘Construction of a Peridynamic Model for Transient Advection-diffusion Problems’, *International Journal of Heat and Mass Transfer* 126 (2018): 1253-1266. DOI: 10.1016/j.ijheatmasstransfer.2018.06.075)

Chapter 5 is a manuscript under review for publication in a refereed journal. (J. Zhao and F. Bobaru, ‘Construction of a Peridynamic Model for Viscous Flow’, under review)

Chapter 6 is a manuscript to be submitted for publication in a refereed journal. (J. Zhao, S. Jafarzadeh, and F. Bobaru, ‘Generalized strategies to impose local boundary conditions in bond-based peridynamic model of diffusion’, to be submitted.)

Table of Contents

Chapter 1	Introduction.....	1
1.1	Motivation and objectives.....	1
1.2	Dissertation organization	7
1.3	Dissertation organization	8
	Reference	9
Chapter 2	A Stochastic Multiscale Peridynamic Model for Corrosion Induced Fracture in Reinforced Concrete.....	14
2.1	Introduction.....	14
2.2	Brief review of bond-based peridynamic theory	19
2.3	Numerical discretization	23
2.4	The IH-PD model for concrete	26
2.5	Radial displacement model for effective expansion of corrosion product	31
2.6	Fracture in concrete due to corrosion of single/multiple rebars	35
2.6.1	Concrete structure with a top-sided middle rebar	35
2.6.2	Concrete structure with a corner rebar	48
2.6.3	Corrosion induced fracture from multiple rebars.....	53
2.7	Conclusions.....	55
	Acknowledgments	56

Appendix A.	Rebar corrosion patterns from diffusion of chlorides	57
Appendix B.	Applying radial displacement at the rebar hole surface	60
Appendix C.	Parametric study on corrosion-induced pressure profiles	62
Appendix D.	Influence of different realizations of the IH-PD material model	63
References.....		65
Chapter 3	A Peridynamic Model for Galvanic Corrosion and Fracture.....	71
3.1	Introduction.....	71
3.2	Kinetics of galvanic corrosion	75
3.3	A coupled PD model for electric potential-driven corrosion and fracture.....	78
3.3.1	Bond-based PD mechanical model	80
3.3.2	PD corrosion model	82
3.3.3	PD corrosion-fracture model.....	97
3.4	Verification and validation of the PD corrosion model	101
3.4.1	Verification of the new PD formulation for galvanic corrosion.....	101
3.4.2	Validation against experimental results from the literature	106
3.5	Application of the PD-CF model to galvanic corrosion-induced fracture	113
3.6	Conclusions.....	119
Acknowledgments		120
Appendix A.	Boundary conditions in PD elastic and electrostatic solvers	121

Appendix A.	Computing effective corrosion depth.....	124
Appendix B.	COMSOL modeling of galvanic corrosion.....	125
Appendix C.	Galvanic corrosion of a AE44-AA6063 couple.....	129
References.....		130
Chapter 4	Construction of a Peridynamic Model for Transient Advection-	
diffusion Problems	135
4.1	Introduction and motivation.....	135
4.2	The peridynamic formulation for advection-diffusion problems.....	137
4.2.1	Peridynamic equation for diffusion problems.....	137
4.2.2	Derivation of peridynamic transient advection equation	139
4.2.3	Peridynamic advection-diffusion models	144
4.2.4	Calibration of micro-velocity parameters	145
4.3	Numerical methods	147
4.4	Numerical tests and convergence to classical solutions	151
4.4.1	Test example in 1D.....	152
4.4.2	Test example in 2D.....	157
4.4.3	Convergence study.....	161
4.5	Mass flow over a 2-D heterogeneous medium	164
4.6	Conclusions.....	167

Acknowledgements.....	168
Appendix A. Derivation of the micro-velocity parameters for steady flow	168
Appendix B. Convergence study for the 1D example	172
References.....	173
Chapter 5 Construction of a Peridynamic Model for Viscous Flow	178
5.1 Introduction.....	178
5.2 Peridynamic constructive model for viscous flow	181
5.2.1 The peridynamic continuity equation	183
5.2.2 Convergence of the peridynamic continuity equation to its classical counterpart	186
5.2.3 The peridynamic formulation for viscous flow	188
5.2.4 Boundary conditions	192
5.3 Numerical implementation.....	193
5.4 Computational validation.....	195
5.4.1 Couette flow	195
5.4.2 Poiseuille flow	197
5.4.3 Flow through a Periodic Lattice of Cylinders.....	198
5.5 Conclusions.....	200
Acknowledgments	200

Appendix A.	Convergence of the PD gradient operator to the classical one	200
Appendix B.	Computing PD stress component from bond force densities	202
References.....		204
Chapter 6	An algorithm for imposing local boundary conditions in peridynamic models of diffusion on arbitrary domains	210
6.1	Introduction.....	210
6.2	The peridynamic model for diffusion	213
6.3	Fictitious nodes methods.....	216
6.3.1	Naïve FNM	218
6.3.2	Taylor-based FNM.....	219
6.3.3	Mirror-based FNM.....	221
6.3.4	An algorithm to find mirror nodes for the mirror-based FNM	224
6.4	Results and discussion	229
6.4.1	The performance of the three FNM versions in enforcing local BCs in peridynamics for problems without singularities	229
6.4.2	The performance of the three FNMs for Motz’s problem	232
6.4.3	Steady-state diffusion in disks with single and multiple pre-cracks.....	235
6.5	Conclusions.....	240
Acknowledgments		241

Appendix A. Numerical implementation of peridynamic diffusion model with the fictitious nodes method.....	241
Appendix B. FEM modeling of the steady-state thermal problem.....	244
References.....	244
Chapter 7 Conclusions and future work.....	247

List of Figures

Figure 2.1. Nonlocal interaction between point \mathbf{x} and an arbitrary point located in the horizon of \mathbf{x}	21
Figure 2.2. Possible discretization types for a peridynamic model.	24
Figure 2.3. Flowchart for the simulation process of PD quasi-static fracture modeling. .	26
Figure 2.4. Determining the properties of a PD bond in the IH-PD model	29
Figure 2.5. A possible distribution of bond properties at a node in the IH-PD model.	29
Figure 2.6. The pre-processing step for instantiating bond properties in the IH-PD model	30
Figure 2.7. The von Mises radial displacement model.	34
Figure 2.8. Imposing displacement boundary conditions at the rebar hole surface using a fictitious node layer.....	35
Figure 2.9. Geometry of the concrete structure with a top-sided middle rebar (mm).	36
Figure 2.10. FEM mesh and displacements computed using ANSYS	37
Figure 2.11. Displacements obtained with the PD models	38
Figure 2.12. Experimental results for different samples of reinforced concrete under accelerated corrosion test	39
Figure 2.13. Convergence study for the FH-PD model	41
Figure 2.14. Convergence study for the IH-PD model	42

Figure 2.15. Typical fracture evolution using the IH-PD model.	44
Figure 2.16. Fracture patterns produced by different choices for the aggregates' fracture energy.....	46
Figure 2.17. Comparison of surface deformation at two different corrosion stages between IH-PD results, experimental observations (see the sample in Figure 2.12 (a)) as well as the RBSM solutions in [81].	48
Figure 2.18. Concrete structure with a corner rebar: geometry and mechanical boundary conditions.....	49
Figure 2.19. Experimental results for cracking in reinforced concrete due to corrosion of a corner rebar	51
Figure 2.20. Corrosion profile for the corner rebar.	52
Figure 2.21. Damage maps from the IH-PD models for corner rebar (with the same bond-structure realization) with different γ and k values	52
Figure 2.22. Geometry for the concrete structure with three rebars.	53
Figure 2.23. Corrosion pattern for three-rebar cases.	54
Figure 2.24. Experiment result of corrosion with three rebars	54
Figure 2.25. Fracture patterns for different tilt angles of the pressure profile on the side bars (angle γ) and different levels of non-uniformity.....	55
Figure 2.26. A zoom-in sketch of the concrete structure with a top-sided middle rebar under diffusion of chloride.....	58

Figure 2.27. Computed diffusion/”corrosion” for rebars in two different concrete structures.	59
Figure 2.28. Points in the rebars with a concentration larger than a threshold value (shown in red) obtained from chloride diffusion (from the top surface only) for the concrete structure with three rebars.	60
Figure 2.29. Rebar cross-section (half) is split into n equal sectors.	61
Figure 2.30. Applying radial displacements increments for different sectors around the rebar considering the evolution of the corrosion process.	61
Figure 2.31. Fracture patterns with the IH-PD model for the concrete sample with a top-sided middle.	63
Figure 2.32. Fracture patterns obtained from different realizations of the bond-structure in the IH-PD model for the top-sided middle rebar geometry.	64
Figure 2.33. Fracture patterns for different realizations of IH-PD model for the three rebars example, with $\gamma = \pi/18$ and $k = 20$	64
Figure 3.1. Schematic polarization curves of anode and cathode in a galvanic couple	76
Figure 3.2. Nonlocal interaction between point \boldsymbol{x} and an arbitrary point located in the horizon of \boldsymbol{x}	79
Figure 3.3. A schematic of different regions and bonds defined in the PD corrosion model at the corrosion front.....	86
Figure 3.4. Examples of dissolving points.....	88
Figure 3.5. Computation of the PD flux at a point \boldsymbol{p} at a flat anode surface.	90

Figure 3.6. A schematic of corrosion front after spatial discretization.....	93
Figure 3.7. Workflow of the PD corrosion-fracture (PD-CF) model.	100
Figure 3.8. Sketch of the example used to verify the PD galvanic corrosion model.....	102
Figure 3.9. Schematic of the implementation of periodic BCs in PD simulations.	103
Figure 3.10. Comparison of the corrosion depth vs. time between PD solution and classical solution	106
Figure 3.11. (a) Geometry and BCs for the galvanic corrosion problem	108
Figure 3.12. Electric potential distribution for mild steel-AE44 galvanic couple	109
Figure 3.13. Initial current density along the electrode surface for mild steel-AE44 couple	110
Figure 3.14. Corrosion profiles for the mild steel-AE44 galvanic couple.....	110
Figure 3.15. Corrosion depths obtained from the PD corrosion model ($\delta = 0.4$ mm), COMSOL with and without the artificial step (our work), and experiments from [3] for mild steel-AE44 galvanic couple.	112
Figure 3.16. Geometry and BCs for the galvanic couple under combined mechanical loading and galvanic corrosion attack.....	115
Figure 3.17. Damage index for the mild steel-AE44 galvanic couple under stress corrosion cracking.....	118
Figure 3.18. Schematic of a PD domain (Ω), its boundary ($\partial\Omega$), and its fictitious region	122

Figure 3.19. An illustration of the electrolyte domain (Ω), boundaries ($\partial\Omega$) and fictitious region in the PD electrostatic model for a general corrosion problem.	122
Figure 3.20. A schematic of orthogonal projection of \mathbf{x} onto $\partial\Omega$ and the reflection of \mathbf{x} through/across $\partial\Omega$ in mirror-based FNM.....	123
Figure 3.21. Illustration of enforcing a local Dirichlet BC in the mirror FNM.....	124
Figure 3.22. A schematic of $\psi(x_0)$ over which the PD effective corrosion depth is computed in this work.....	125
Figure 3.23. A schematic of the artificial geometric step at the interface between the anode and the cathode.....	127
Figure 3.24. Finite element mesh in COMSOL for the galvanic cell.....	128
Figure 3.25. Quantitative comparison of the final corrosion depth for AE44-AA6063 galvanic couple between experimental measurement [3], PD simulation and COMSOL simulation.....	130
Figure 4.1. Mass transfer under a uniform fluid flow in a cylinder bounded by two planes which are at different concentrations.....	140
Figure 4.2. The PD description of a body (a, b, c) and the concentration bond (d).....	141
Figure 4.3. Illustration of the central kernel.	144
Figure 4.4. Illustration of the upwind kernel.....	144
Figure 4.5. Two possible types of the weighting function and their variations over the PD horizon.	145

Figure 4.6. A constant concentration flux for one dimensional steady flow in the absence of diffusion.....	146
Figure 4.7. Numerical discretization around a node \mathbf{x}_i	148
Figure 4.8. Boundary and initial conditions for 1D advection-diffusion in a semi-infinite tube.....	152
Figure 4.9. The comparison between classical solution and PD solutions for the 1D example case 1.	153
Figure 4.10. Concentration over the tube obtained with PD for the constant-type and linear-type micro-velocity functions for the 1D example case 2	154
Figure 4.11. The PD results with different ω using the <i>constant-type</i> micro-velocity function compared to classical results	155
Figure 4.12. The PD results with different ω using the <i>linear-type</i> micro-velocity function compared to classical results	156
Figure 4.13. Boundary and initial conditions for 2D advection-diffusion in a semi-infinite plate.....	158
Figure 4.14. Classical and PD solutions for $D = 1 \text{ cm}^2/\text{s}$ and $V = 1 \text{ cm}/\text{s}$	159
Figure 4.15. Classical and PD solutions for advection-dominant case.....	160
Figure 4.16. Comparison between classical and PD solutions along the center line for advection-dominant case.....	160
Figure 4.17. The convergence study of the 1D example, case 1.	162

Figure 4.18. Relative difference for the whole domain with different horizon sizes and m values	164
Figure 4.19. Concentration at $x = 0.5$ cm, $y = 0.5$ cm with different horizon sizes and m values	164
Figure 4.20. Example 3: flow in a heterogeneous medium.	166
Figure 4.21. Concentration distribution for permeable circular inclusions	167
Figure 4.22. Concentration distribution for impermeable random elliptical inclusions .	167
Figure 4.23. The decomposition of vector e_{xx} '	171
Figure 5.1. A peridynamic body with a generic point \mathbf{x} and its horizon.	183
Figure 5.2. A cylinder in the fluid domain with two points located at the top and bottom.	184
Figure 5.3. Velocity decomposition	189
Figure 5.4. Schematic of a peridynamic domain (Ω), its boundary ($\partial\Omega$), and its fictitious region	192
Figure 5.5. Uniform discretization for the 2D PD model.	193
Figure 5.6. Comparison of PD solutions (for $\delta = 40$ μm and $m = 4$) and series solutions of the corresponding classical model (using the first 50 terms in the series) for Couette flow.	196
Figure 5.7. Comparison of PD (for $\delta = 40$ μm and $m = 4$) and classical series solutions (using the first 50 terms in the series) for Poiseuille flow.	198

Figure 5.8. Schematic of fluid flow driven by a body force around a disk.	199
Figure 5.9. Contour plots of velocity magnitude	199
Figure 5.10. Computation of force per unit area, at a generic point \mathbf{p} , from bond force densities.....	203
Figure 6.1. A peridynamic body with a generic point \mathbf{x} and its horizon \mathcal{H}_x	214
Figure 6.2. Schematic of a peridynamic domain	217
Figure 6.3. Illustration of using the naïve FNM to enforce the local (a) Dirichlet and (b) homogeneous Neumann BCs.....	219
Figure 6.4. Illustration of enforcing the local Dirichlet BC by using the Taylor FNM..	220
Figure 6.5. A schematic of mirror points in mirror-based FNM	222
Figure 6.6. Illustration of enforcing a local Dirichlet BC in the mirror FNM	223
Figure 6.7. Schematic of $\Omega_1 \subset \Omega$ near an acute corner	224
Figure 6.8. Schematic of $\Omega_2 \subset \Omega$ near an acute corner	226
Figure 6.9. Schematic diagram of determining \mathbf{x}^P and \mathbf{x}^R for a generic \mathbf{x}	227
Figure 6.10. Real examples of some \mathbf{x} and their corresponding $\mathbf{x}^R \in \Omega$	229
Figure 6.11. The geometry and boundary conditions for diffusion in a square domain.	230
Figure 6.12. The classical analytical solution and PD solutions with different FNMs for the steady-state diffusion problem	231
Figure 6.13. Domain and boundary conditions for an example of Motz’s problem.....	232
Figure 6.14. (a) Contours for the classical solution for Motz’s problem;.....	233

Figure 6.15. The classical and PD solutions with different FNMs for Motz’s problem.	234
Figure 6.16. δ -convergence of PD solution (using the different FNMs) to the classical solution.....	235
Figure 6.17. Local boundary conditions imposed for diffusion in a disk with a pre-crack at the center.	236
Figure 6.18. Contours for the solution to problem shown in Figure 6.17.....	237
Figure 6.19. Part of the crack segment, shown by the red segment, and the PD grid after counterclockwise rotation by (a) 30° and (b) 45°.	238
Figure 6.20. Contours of PD solutions obtained with the mirror FNM for counterclockwise-rotated grids by (a) 30° and (b) 45°.	238
Figure 6.21. Diffusion in a disk with two intersecting cracks and associated local boundary conditions.....	239
Figure 6.22. Contour-plot for the PD solution obtained with the mirror FNM	239
Figure 6.23. Uniform discretization for a peridynamic model.	242
Figure 6.24. Workflow for the peridynamic simulation with Taylor/mirror FNM.	243
Figure 6.25. FEM mesh	244

List of Tables

Table 2.1. The meaning for parameters used in Eq. (2.10).....	33
Table 2.2. Material properties for all concrete structures to be analyzed (from [19, 81, 87, 88]).....	36
Table 2.3. Geometry data for two samples of the reinforced concrete structure shown in Figure 2.18 [92].	49
Table 3.1. Parameter values for the example shown in Figure 3.8.	103
Table 3.2. Numerical errors (for different values of m) for the resulting current density when the discrete version of Eq. (3.20) is used to update the concentration in the corrosion dissolution model.	105
Table 3.3. Data used in the piecewise linear interpolation of the polarization curves from [2].....	108
Table 3.4. Material properties for the galvanic problem	108
Table 3.5. Mechanical properties for materials in the galvanic couple	116
Table 3.6. Convergence study on the maximum corrosion depth as the height of the initial step decreases, for the AE44-AA6063 galvanic couple.....	128
Table 3.7. Data used in the Tafel's equation for AA6063	129
Table 4.1. The micro-velocity parameters for different types of weighting functions (constant and linear) under the flow field defined by velocity \mathbf{V} (V in 1D)	147

Table 4.2. Relative differences in concentration along the tube between the classical model and PD solutions	156
Table 4.3. δ -convergence results on relative differences and convergence rates between classical model and peridynamic using central model.....	172
Table 4.4. Numerical results on relative differences between classical model and peridynamics using the hybrid model.....	173
Table 5.1. δ -convergence study for the PD solution of Couette flow.	197
Table 5.2. Parameters for flow through periodic lattice of disks.....	199
Table 6.1. Computational time of the simulation using the three different FNMs.....	231

Chapter 1 Introduction

1.1 Motivation and objectives

The recent tragedy in Surfside, Florida [1] clearly demonstrated the consequences of unexpected structural failure and the importance of being able to make predictions at low cost. Corrosion of the rebar and the subsequent concrete spalling due to the expansion of corrosion product, coupled with the structural loading, played a critical role in the collapse of the condo building. Fracture and corrosion often coexist and interact with each other (i.e., stress corrosion cracking [2]), leading to faster and more complex degradation of materials. The proximity of the building to the Atlantic Ocean, with its corrosive seawater, significantly accelerated the corrosion process and thus the degradation of the structure [3].

Reinforced concrete is one of the most used construction materials. The load carrying capacity of reinforced concrete structures exposed to a corrosive environment can be greatly affected by rebar corrosion [4]. The expansion of corrosion products can lead to cracks propagating through the concrete cover. These cracks act as additional channels for aggressive agents (e.g. chlorides) that can now reach faster and over larger areas the rebars, accelerating the corrosion process [5]. Corrosion decreases the rebar's effective cross-sectional area, breaks the bond between the rebar and concrete, causing performance degradation of the structure [6]. Moreover, changes in the layer affected by corrosion trigger significant reductions in ductility [7], in addition to hydrogen embrittlement (see pp. 334-336 in [8]). Degraded rebars can fail, resulting in the collapse of the structure. During this entire process, concrete fracture due to rebar corrosion

expansion plays a key role, thus, it is necessary to have an efficient and reliable computational model to make predictions.

Classical models employ spatial (partial) derivatives to formulate their governing equations. These partial differential equations (PDEs), however, are not defined at spatial discontinuities such as crack/corrosion surfaces. The crack path requires to be tracked explicitly. Besides, in classical models, a crack is only a mathematical thin line/surface, while in some problems, the crack comes along with a damage process zone that influences its evolution. Thus, classical models do not allow sufficiently general type of description of damage growth. Moreover, descriptions of crack initiation and propagation (speed and direction) requires additional criteria which add complexity in classical models. Finite element method (FEM), commonly used to numerically solve classical models for fracture, requires remeshing the domain every step the crack grows.

Traditional FEMs use techniques such as element-deletion and cohesive zone to model crack propagation. These approaches only allow cracks to pass along element edges, leading to inaccurate crack paths. XFEM [9] allow cracks to pass through elements, providing better approximations of the crack path. However, subdivision of the cut elements for numerical integration purposes also introduces complexities. These additional treatments work for simple fracture problems (e.g., single crack propagation). However, for problems with coupled fracture and corrosion (e.g., stress corrosion cracking [8,10,11]), or the interaction of multiple cracks (e.g., crack branching [12,13] and fragmentation [14]), their efficacy and efficiency become doubtful.

In 2000, a nonlocal alternative of the classical theory named “peridynamics”, originally aimed for solving fracture problems, was developed by Silling [15]. Peridynamic (PD)

models offer important advantages over classical ones in modeling fracture. PD formulations use spatial integration rather than differentiation, leading to a mathematically consistent formulation that works naturally for problems in which discontinuities in the domain (such as cracks) appear. Moreover, by using simple meshfree discretization, PD models can autonomously capture the initiation and propagation of cracks/damage [16].

Peridynamics has received considerable attention since its introduction [17–19]. It has been successfully applied to model fracture of brittle materials such as glass [14], damage in composite [20] and ductile [21] materials, fatigue failure [22], etc.

For heterogeneous materials such as concrete, the microstructure plays a significant role in how cracks initiate and grow, thus, meso-scale models have often been used for concrete fracture [23]. However, issues such as the selection of the geometric shape of the aggregates can significantly affect the fracture behavior [24]. Thus, the general application of these models is rather limited. A more desirable approach would be to develop a partially-homogenized model which implicitly involves some of concrete's microscale features, including their randomness. Such models, spanning multiple scales, would allow for efficient simulation of fracture and failure at the macro-scale while accounting for the correct crack initiation at the micro-scale.

In the first part of this dissertation, we introduce a multiscale stochastic peridynamic model for concrete to simulate concrete fracture induced by the expansion of rebar corrosion-products. This model implicitly uses information about the concrete meso-scale structure, leading to a partially-homogenized model, and uses the simplest possible linear

elastic with brittle failure constitutive relation. A mathematical distribution function is used to mimic the expansion process of the corrosion product, which is the loading that induces fracture in this setting. We validate the model for concrete structures with a single and multiple rebars, for which experimental data is available in the literature.

While the PD method has been primarily used to deal with mechanical fracture, it has also been employed in diffusion-type problems involving cracks and damage, including thermal diffusion [25] and mass transport (e.g. corrosion) [26]. In 2015, Chen and Bobaru [27] introduced a PD model for corrosion damage. PD corrosion models allow for autonomous propagation of corrosion damage in the solid subdomain as an intrinsic solution to a nonlocal damage-dependent mass transfer equation. The PD corrosion formulation offers some major advantages [28] when compared with other approaches such as phase field (PF) and Cellular Automata (CA). For example, the concentration-dependent damage index in the PD model monitors the phase changes continuously from solid to electrolyte across the “Diffuse Corrosion Layer” (DCL). This helps us capture the subsurface damage and degradation of mechanical properties (strength, ductility, etc.) observed in corroded samples [7]. Moreover, the PD corrosion model can be easily coupled with the powerful peridynamic fracture models for investigating the potential stress-corrosion cracking and structural failure when mechanical loads are present in addition to the environmental attack [11,29]. However, there are also two limitations in the existing PD corrosion model. One is that the initial distribution of corrosion rate along the corrosion surface must be given as an input. This does not work for problems such as galvanic corrosion [2] in which the corrosion rate distribution can change significantly as the corrosion front evolves and thus should be updated on the fly. The

other is that numerical calibration (which requires a trial solution in a pre-processing step) of certain coefficients in the formulation is required for each simulation. The PD corrosion model needs to be extended in order to be applied to a larger class of corrosion problems.

In the second part of this dissertation, we reformulate and extend the existing PD corrosion model such that it becomes applicable to a larger class of corrosion problems such as galvanic corrosion. We introduce a PD electric potential model, and couple it with the existing PD corrosion model [30]. In addition, we reformulate the PD corrosion dissolution model in [27,30] based on electrochemistry, and replace the previous numerical calibration stage (which required a trial solution in the pre-processing step) with an analytical one. With above changes, the new model is autonomous and significantly more efficient in problems with highly non-uniform current densities along an arbitrary-shape corroding surface, such as galvanic corrosion. Moreover, the new model eliminates the required artificial changes to a given geometry of a galvanic couple which we found is necessary in models based on PDEs (e.g., COMSOL, phase-field) in order to match the experimental observations. The new PD model is validated against experimental galvanic corrosion results available in the literature. A coupled corrosion-fracture problem is solved to show the potential of the new PD model in resolving failure caused by the combination of sharp corrosion damage (induced by galvanic corrosion) and mechanical loading.

Participation of fluid flow can significantly accelerate corrosion and fracture process, either by transporting corrosive substances, or by directly exerting additional mechanical

forces on the structure. Thus, it is important to consider these factors into our corrosion and fracture models for problems under such circumstances. PD formulations and applications to fluid mechanics are rather few. State-based PD models for fluid flow in porous media are presented in [31–33]. More general models for fluid flow based on Navier-Stokes equations (NSEs) have been developed in the PD framework to simulate viscous flow. Some of them use the PD correspondence model [34–37] and thus suffer from zero-energy modes [38,39]. Others use “PD differential operators” [40–42] to translate classical NSEs to integro-differential equations. The “nonlocality” introduced in these translations is merely a computational parameter, instead of a length-scale in true nonlocal formulation which can capture the nonlocal effect in complicated fluid motions (e.g., turbulent flow).

In the third part of this dissertation, we construct PD models for diffusion-advection and viscous flow from fundamental conservation principles, such that the influence of fluid flow and mass transport on corrosion and fracture will be possible to be modeled under the same PD framework. We test the PD diffusion-advection model using examples with classical solutions and use the new model to simulate advection-diffusion in complex heterogeneous media. For the PD model of viscous flow, we investigate the convergence of the PD continuity equation to its classical counterpart as the nonlocal size in PD equations approaches zero. We also verify the PD model numerically using examples for which (classical) analytical or numerical solutions are available in the literature.

For PD formulations, associated BCs are of nonlocal type, and they are sometimes referred to as “nonlocal volume constraints” [43,44]. In reality, however, only surface conditions

are measurable, not through a finite thickness layer at the surface. Therefore, imposing local BCs accurately in nonlocal/peridynamic models is often desired/needed. Another issue caused by nonlocality is the surface effect [45] which appears because, unlike in the bulk, points near the free surface/boundary do not have a full horizon region. A popular strategy to handle above issues is to extend the solution domain by a fictitious layer (such that each point in the solution domain has a full horizon region) and then convert local BCs into nonlocal volume constraints on this fictitious region. This strategy is called fictitious nodes method (FNM). However, while this works fine for regular geometries, it is still a challenge to apply it to problems with irregular geometries, curved boundaries, etc.

In the last part of this dissertation, we introduce a new algorithm which enables us to use the mirror-type FNM for arbitrary geometries, including for domains with cracks. We select the PD diffusion model to test our algorithm. With small modifications, the algorithm presented here is also applicable to PD models solving other types of problems, such as fracture and corrosion damage. We verify this new algorithm using two problems: one is a simple problem without singularity and the other is the Motz's problem with a singularity (in fluxes) along a boundary where Dirichlet and Neumann boundary conditions meet [46,47]. We further demonstrate the capability of the new algorithm by solving examples with crack surfaces and curved boundaries.

1.2 Dissertation organization

This dissertation is written in a paper-based format, meaning that the main chapters are either published articles, under-review manuscripts submitted for publication, or manuscripts ready for submission for publication at the time that this document is being

written. Each chapter stands alone and does not refer the reader back and forth to other chapters. The content of this dissertation is as follows:

In Chapter 2, a multiscale stochastic peridynamic model for concrete is introduced to simulate concrete fracture. This model is validated against experimentally observed patterns of corrosion-induced concrete fracture. In Chapter 3, a new PD corrosion model is introduced to handle corrosion problems with arbitrary distribution of corrosion rate along arbitrary corrosion surface. This model is used to simulate galvanic corrosion and the results are validated by experimental results in the literature. A coupled corrosion-fracture problem is solved to show the potential of the new model in resolving failure caused by the combination of sharp corrosion damage (induced by galvanic corrosion) and mechanical loading. In Chapter 4 and Chapter 5, we construct PD models for diffusion-advection and viscous flow, respectively, from fundamental conservation principles. Both models are verified by examples with (classical) analytical or numerical solutions from the literature. In Chapter 6, a new algorithm is developed for the mirror-type fictitious nodes method to allow local boundary conditions to be imposed in PD models with arbitrary boundary geometries. We select the PD diffusion model to test the new algorithm. Finally, in Chapter 7, conclusions of this dissertation are summarized, and future works are discussed.

1.3 Dissertation organization

This dissertation is written in a paper-based format, meaning that the main chapters are either published articles, under-review manuscripts submitted for publication, or manuscripts ready for submission for publication at the time that this document is being

written. Each chapter stands alone and does not refer the reader back and forth to other chapters. The content of this dissertation is as follows:

In Chapter 2, a multiscale stochastic peridynamic model for concrete is introduced to simulate concrete fracture. This model is validated against experimentally observed patterns of corrosion-induced concrete fracture. In Chapter 3, a new PD corrosion model is introduced to handle corrosion problems with arbitrary distribution of corrosion rate along arbitrary corrosion surface. This model is used to simulate galvanic corrosion and the results are validated by experimental results in the literature. A coupled corrosion-fracture problem is solved to show the potential of the new model in resolving failure caused by the combination of sharp corrosion damage (induced by galvanic corrosion) and mechanical loading. In Chapter 4 and Chapter 5, we construct PD models for diffusion-advection and viscous flow, respectively, from fundamental conservation principles. Both models are verified by examples with (classical) analytical or numerical solutions from the literature. In Chapter 6, a new algorithm is developed for the mirror-type fictitious nodes method to allow local boundary conditions to be imposed in PD models with arbitrary boundary geometries. We select the PD diffusion model to test the new algorithm. Finally, in Chapter 7, conclusions of this dissertation are summarized, and future work is discussed.

Reference

- [1] J. Lawson, What we know about the Surfside condo collapse - ABC News, ABC News. (2021). <https://abcnews.go.com/US/surfside-condo-collapse/story?id=80068218> (accessed October 3, 2021).
- [2] E. McCafferty, Introduction to Corrosion Science, Springer New York, New York, NY, 2010. <https://doi.org/10.1007/978-1-4419-0455-3>.
- [3] C. Devine, As engineers hunt for answers in the Surfside building collapse, signs

point to the building's lower reaches, CNN. (2021).

<https://www.cbs58.com/news/as-engineers-hunt-for-answers-in-the-surfside-building-collapse-signs-point-to-the-buildings-lower-reaches> (accessed October 3, 2021).

- [4] L. Bertolini, B. Elsener, E. Redaelli, R. Polder, *Corrosion of Steel in Concrete: Prevention, Diagnosis, Repair: Second Edition*, Wiley-VCH Verlag GmbH & Co. KGaA, Weinheim, Germany, 2013. <https://doi.org/10.1002/9783527651696>.
- [5] E. Kato, Y. Kato, T. Uomoto, Development of simulation model of chloride ion transportation in cracked concrete, *J. Adv. Concr. Technol.* 3 (2005) 85–94. <https://doi.org/10.3151/jact.3.85>.
- [6] A. Djerbi, S. Bonnet, A. Khelidj, V. Baroghel-bouny, Influence of traversing crack on chloride diffusion into concrete, *Cem. Concr. Res.* 38 (2008) 877–883. <https://doi.org/10.1016/j.cemconres.2007.10.007>.
- [7] S. Li, Z. Chen, L. Tan, F. Bobaru, Corrosion-induced embrittlement in ZK60A Mg alloy, *Mater. Sci. Eng. A.* 713 (2018) 7–17. <https://doi.org/10.1016/j.msea.2017.12.053>.
- [8] D.A. Jones, *Principles and prevention of corrosion*, Macmillan, 1992.
- [9] N. Moës, J. Dolbow, T. Belytschko, A finite element method for crack growth without remeshing, *Int. J. Numer. Methods Eng.* 46 (1999) 131–150. [https://doi.org/10.1002/\(SICI\)1097-0207\(19990910\)46:1<131::AID-NME726>3.0.CO;2-J](https://doi.org/10.1002/(SICI)1097-0207(19990910)46:1<131::AID-NME726>3.0.CO;2-J).
- [10] T.L. Anderson, *Fracture Mechanics*, CRC Press, 2017. <https://doi.org/10.1201/9781315370293>.
- [11] Z. Chen, S. Jafarzadeh, J. Zhao, F. Bobaru, A coupled mechano-chemical peridynamic model for pit-to-crack transition in stress-corrosion cracking, *J. Mech. Phys. Solids.* 146 (2021) 104203. <https://doi.org/10.1016/j.jmps.2020.104203>.
- [12] F. Bobaru, G. Zhang, Why do cracks branch? A peridynamic investigation of dynamic brittle fracture, *Int. J. Fract.* 196 (2015) 59–98. <https://doi.org/10.1007/s10704-015-0056-8>.
- [13] Z. Xu, G. Zhang, Z. Chen, F. Bobaru, Elastic vortices and thermally-driven cracks in brittle materials with peridynamics, *Int. J. Fract.* 209 (2018) 203–222. <https://doi.org/10.1007/s10704-017-0256-5>.
- [14] W. Hu, Y. Wang, J. Yu, C.-F. Yen, F. Bobaru, Impact damage on a thin glass plate with a thin polycarbonate backing, *Int. J. Impact Eng.* 62 (2013) 152–165. <https://doi.org/10.1016/j.ijimpeng.2013.07.001>.
- [15] S.A. Silling, Reformulation of elasticity theory for discontinuities and long-range forces, *J. Mech. Phys. Solids.* 48 (2000) 175–209. [https://doi.org/10.1016/S0022-5096\(99\)00029-0](https://doi.org/10.1016/S0022-5096(99)00029-0).
- [16] S.A. Silling, E. Askari, A meshfree method based on the peridynamic model of solid mechanics, *Comput. Struct.* 83 (2005) 1526–1535.

- <https://doi.org/10.1016/j.compstruc.2004.11.026>.
- [17] E. Madenci, E. Oterkus, *Peridynamic Theory and Its Applications*, Springer New York, New York, NY, 2014. <https://doi.org/10.1007/978-1-4614-8465-3>.
- [18] F. Bobaru, J.T. Foster, P.H. Geubelle, S.A. Silling, *Handbook of Peridynamic Modeling*, CRC press, 2016. <https://doi.org/10.1201/9781315373331>.
- [19] A. Javili, R. Morasata, E. Oterkus, S. Oterkus, Peridynamics review, *Math. Mech. Solids*. 24 (2019) 3714–3739. <https://doi.org/10.1177/1081286518803411>.
- [20] Y.L. Hu, N. V. De Carvalho, E. Madenci, Peridynamic modeling of delamination growth in composite laminates, *Compos. Struct.* 132 (2015) 610–620. <https://doi.org/10.1016/j.compstruct.2015.05.079>.
- [21] J.T. Foster, S.A. Silling, W.W. Chen, Viscoplasticity using peridynamics, *Int. J. Numer. Methods Eng.* 81 (2010) 1242–1258. <https://doi.org/10.1002/nme.2725>.
- [22] G. Zhang, Q. Le, A. Loghin, A. Subramaniyan, F. Bobaru, Validation of a peridynamic model for fatigue cracking, *Eng. Fract. Mech.* 162 (2016) 76–94. <https://doi.org/10.1016/j.engfracmech.2016.05.008>.
- [23] X.F. Wang, Z.J. Yang, J.R. Yates, A.P. Jivkov, C. Zhang, Monte Carlo simulations of mesoscale fracture modelling of concrete with random aggregates and pores, *Constr. Build. Mater.* 75 (2015) 35–45. <https://doi.org/10.1016/j.conbuildmat.2014.09.069>.
- [24] X. Xi, S. Yang, C.Q. Li, A non-uniform corrosion model and meso-scale fracture modelling of concrete, *Cem. Concr. Res.* 108 (2018) 87–102. <https://doi.org/10.1016/j.cemconres.2018.03.009>.
- [25] F. Bobaru, M. Duangpanya, The peridynamic formulation for transient heat conduction, *Int. J. Heat Mass Transf.* 53 (2010) 4047–4059. <https://doi.org/10.1016/j.ijheatmasstransfer.2010.05.024>.
- [26] J. Zhao, Z. Chen, J. Mehrmashadi, F. Bobaru, Construction of a peridynamic model for transient advection-diffusion problems, *Int. J. Heat Mass Transf.* 126 (2018) 1253–1266. <https://doi.org/10.1016/j.ijheatmasstransfer.2018.06.075>.
- [27] Z. Chen, F. Bobaru, Peridynamic modeling of pitting corrosion damage, *J. Mech. Phys. Solids*. 78 (2015) 352–381. <https://doi.org/10.1016/j.jmps.2015.02.015>.
- [28] S. Jafarzadeh, Z. Chen, F. Bobaru, Computational modeling of pitting corrosion, *Corros. Rev.* 37 (2019) 419–439. <https://doi.org/10.1515/correv-2019-0049>.
- [29] S. Jafarzadeh, Z. Chen, S. Li, F. Bobaru, A peridynamic mechano-chemical damage model for stress-assisted corrosion, *Electrochim. Acta.* 323 (2019) 134795. <https://doi.org/10.1016/j.electacta.2019.134795>.
- [30] S. Jafarzadeh, Z. Chen, J. Zhao, F. Bobaru, Pitting, lacy covers, and pit merger in stainless steel: 3D peridynamic models, *Corros. Sci.* 150 (2019) 17–31. <https://doi.org/10.1016/j.corsci.2019.01.006>.

- [31] A. Katiyar, J.T. Foster, H. Ouchi, M.M. Sharma, A peridynamic formulation of pressure driven convective fluid transport in porous media, *J. Comput. Phys.* 261 (2014) 209–229. <https://doi.org/10.1016/j.jcp.2013.12.039>.
- [32] H. Ouchi, A. Katiyar, J. York, J.T. Foster, M.M. Sharma, A fully coupled porous flow and geomechanics model for fluid driven cracks: a peridynamics approach, *Comput. Mech.* 55 (2015) 561–576. <https://doi.org/10.1007/s00466-015-1123-8>.
- [33] S. Oterkus, E. Madenci, E. Oterkus, Fully coupled poroelastic peridynamic formulation for fluid-filled fractures, *Eng. Geol.* 225 (2017) 19–28. <https://doi.org/10.1016/j.enggeo.2017.02.001>.
- [34] S.A. Silling, Stability of peridynamic correspondence material models and their particle discretizations, *Comput. Methods Appl. Mech. Eng.* 322 (2017) 42–57. <https://doi.org/10.1016/j.cma.2017.03.043>.
- [35] Q. Tu, S. Li, An updated Lagrangian particle hydrodynamics (ULPH) for Newtonian fluids, *J. Comput. Phys.* 348 (2017) 493–513. <https://doi.org/10.1016/j.jcp.2017.07.031>.
- [36] J. Yan, S. Li, A.M. Zhang, X. Kan, P.N. Sun, Updated Lagrangian Particle Hydrodynamics (ULPH) modeling and simulation of multiphase flows, *J. Comput. Phys.* 393 (2019) 406–437. <https://doi.org/10.1016/j.jcp.2019.05.017>.
- [37] J. Wang, X. Zhang, Improved Moving Particle Semi-implicit method for multiphase flow with discontinuity, *Comput. Methods Appl. Mech. Eng.* 346 (2019) 312–331. <https://doi.org/10.1016/j.cma.2018.12.009>.
- [38] M.A. Bessa, J.T. Foster, T. Belytschko, W.K. Liu, A meshfree unification: reproducing kernel peridynamics, *Comput. Mech.* 53 (2014) 1251–1264. <https://doi.org/10.1007/s00466-013-0969-x>.
- [39] G.C. Ganzenmüller, S. Hiermaier, M. May, On the similarity of meshless discretizations of Peridynamics and Smooth-Particle Hydrodynamics, *Comput. Struct.* 150 (2015) 71–78. <https://doi.org/10.1016/j.compstruc.2014.12.011>.
- [40] Y. Gao, S. Oterkus, Nonlocal numerical simulation of low Reynolds number laminar fluid motion by using peridynamic differential operator, *Ocean Eng.* 179 (2019) 135–158. <https://doi.org/10.1016/j.oceaneng.2019.03.035>.
- [41] Y. Gao, S. Oterkus, Multi-phase fluid flow simulation by using peridynamic differential operator, *Ocean Eng.* 216 (2020) 108081. <https://doi.org/10.1016/j.oceaneng.2020.108081>.
- [42] Y. Mikata, Peridynamics for fluid mechanics and acoustics, *Acta Mech.* 232 (2021) 3011–3032. <https://doi.org/10.1007/s00707-021-02947-0>.
- [43] Q. Du, M. Gunzburger, R.B. Lehoucq, K. Zhou, Analysis and Approximation of Nonlocal Diffusion Problems with Volume Constraints, *SIAM Rev.* 54 (2012) 667–696. <https://doi.org/10.1137/110833294>.
- [44] Q. Du, M. Gunzburger, R.B. Lehoucq, K. Zhou, A nonlocal vector calculus, nonlocal volume-constrained problems, and nonlocal balance laws, *Math. Model.*

- Methods Appl. Sci. 23 (2013) 493–540.
<https://doi.org/10.1142/S0218202512500546>.
- [45] F. Bobaru, Y.D. Ha, Adaptive refinement and multiscale modeling in 2D peridynamics, *Int. J. Multiscale Comput. Eng.* 9 (2011) 635–659.
<https://doi.org/10.1615/IntJMultCompEng.2011002793>.
- [46] H. Motz, The treatment of singularities of partial differential equations by relaxation methods, *Q. Appl. Math.* 4 (1947) 371–377.
<https://doi.org/10.1090/qam/18442>.
- [47] Z.C. Li, T.T. Lu, Singularities and treatments of elliptic boundary value problems, *Math. Comput. Model.* 31 (2000) 97–145. [https://doi.org/10.1016/S0895-7177\(00\)00062-5](https://doi.org/10.1016/S0895-7177(00)00062-5).

Chapter 2 A Stochastic Multiscale Peridynamic Model for Corrosion Induced Fracture in Reinforced Concrete

2.1 Introduction

Reinforced concrete is one of the most commonly used construction materials.

Reinforced concrete structures exposed to a corrosive environment can be greatly affected as penetration of aggressive substances (water, oxygen, chloride, carbon dioxide, etc.) can lead to degradation of the steel rebars [1, 2]. If the concrete cover is thick and free of defects, this process usually is slow, extending over decades. However, concrete may contain or develop small cracks, caused during the manufacturing or early loading stages [3, 4]. Small amounts of aggressive elements then reach the rebars and can initiate their corrosion. When the corrosion reaches a certain stage (less than 1% of cross-section area of the initial rebar), the expansion of corrosion products (volume of corrosion products can be 3-4 times the volume of consumed iron [2]) can lead to major cracks propagating through the concrete cover. These major cracks can then act as additional channels for penetration of aggressive agents, accelerating the corrosion process [5]. The corrosion of the steel rebar decreases its effective cross-sectional area and breaks the bond between the rebar and concrete, causing performance degradation of the structure [6]. Moreover, changes in the layer affected by corrosion trigger significant reductions in ductility [7], in addition to hydrogen embrittlement (see pp. 334-336 in [8]). Corrosion of the rebar is usually non-uniform (e.g. pitting corrosion [8]). Non-uniformities in corrosion damage of the rebars can reduce the concrete cracking pressure by more than 50% compared with uniform corrosion [9]. Degraded rebars can fail, resulting in the

collapse of the structure. During this entire process, concrete's fracture plays a key role. Corrosion-induced concrete fracture is the focus of our paper.

Analytical methods based on the thick-walled cylinder theory are available to estimate conditions that would lead to cracking of the concrete cover due to rebar corrosion, but these cannot model the actual failure process, and, in general, are limited to a single rebar [10-12]. Experimental investigations of corrosion-induced fracture in concrete can offer some insights into the process but they are expensive and time-consuming. Usually, these are performed using external currents to accelerate the corrosion process, making corrosion patterns more uniform than those resulting from natural environmental conditions. Departures from uniformity in the corrosion process, and the complex evolution of concrete fracture induced by rebar corrosion require the use of computational modeling to obtain a more complete understanding of this phenomenon [13, 14].

An important contribution to computational modeling in this field has appeared in [13, 14], where a 3D chemo-hygro-thermo-mechanical model for concrete (with a specialized constitutive model for concrete) is used to simulate corrosion-induced damage and transport of corrosion products into cracks. These works assumed that the reinforcement bar was already depassivated. Several choices for corrosion sites along the longitudinal direction and around the cross-section of rebars were tried. For some of these choices, the obtained fracture patterns agree with experimental observations very well. However, although the crack band theory used in these publications can alleviate mesh size dependence for smeared crack approach, it cannot solve the mesh orientation dependence [15]. For each example, only one mesh was employed, and convergence studies were not

presented for comparing variability of crack patterns with those from experiments. A 2D mechano-chemical model ([16]) coupled the ingress of chloride ions, carbonation, electrochemical reaction and mechanical damage for the prediction of rebar corrosion and concrete damage. In this model, the active zone on the rebar evolves automatically. However, for the fracture model, using the crack band theory, no details (material properties, boundary conditions, etc.) were provided. Recently, a 2D diffusion-mechanical model [17] studied depassivation of the steel surface due to chloride ingress in concrete and the subsequent corrosion of steel and crack propagation in concrete. The distribution of rust thickness obtained is close to what is measured experimentally, but fracture patterns obtained for the 3-rebar case do not capture the experimental observation very well.

One of the limitations of the above-mentioned works is that they all use a homogenized model for the concrete structure. This may not work well in cases where the concrete microstructure does play a role in how cracks initiate and grow. Around corroding rebars that create pressures against the concrete, microcracks develop leading to major concrete cracks reaching the concrete cover. The evolution of such cracks can depend on certain microstructure characteristics. Meso-scale models have shown their potentials for such problems [18]. However, issues such as the selection of the geometric shape of the aggregates can significantly affect the fracture behavior [19-21]. It is possible to use a meso-scale structure acquired from X-ray tomography images [22], but it is computationally costly to extend meso-scale models to meter-scale samples. Thus, the general application of these models is rather limited. A more desirable approach would be to develop a partially-homogenized model which implicitly involves some of concrete's

microscale features, including their randomness. Such models, spanning multiple scales, would allow for efficient simulation of fracture and failure at the macro-scale while accounting for the correct crack initiation at the micro-scale.

While most of the above-mentioned models are based on the classical (local) continuum mechanics, nonlocal models offer some important advantages over local ones in modeling fracture behavior of heterogeneous materials like concrete ([23]). Classical (local) continuum-based models lead to spurious mesh sensitivity in fracture problems, while nonlocal ones can prevent it. Another reason for using nonlocality is the complex interactions between microcracks: these appear at scales too small to efficiently model with a local formulation, and their formation and growth are interlinked, resulting in an effectively nonlocal damage behavior. Nonlocality is also necessary in a macroscale framework to describe microstructural phenomena in concrete such as cohesion, friction and aggregate interlock [24].

Peridynamics (PD) is a nonlocal theory which has received considerable attention since its introduction almost two decades ago [25, 26]. PD reformulates the classical continuum mechanics by eliminating spatial derivatives to model mechanical [27-37], diffusion/corrosion [38-43], or mechano-chemical [44-46] etc., behaviors in materials involving damage. Using spatial integration rather than differentiation leads to a mathematically consistent formulation that works naturally for problems in which discontinuities in the domain (such as cracks) appear. In a PD model, cracks/damage can initiate and propagate autonomously [47].

One of the first applications of the PD theory to concrete structures was [48]. A micropolar PD model to better simulate damage in concrete was introduced in [49]. Later, this model was employed in [50] for simulating fracture in short fiber-reinforced concrete. The authors of [50] introduced a semi-discrete method to represent the fiber-concrete interaction and considered the random nature of concrete by reducing the particle strength of some PD nodes. A formulation of pressure-dependent PD plasticity model was shown to work well for compression, impact, and spallation of concrete structures [51]. The trilinear peridynamic model introduced in [52] has shown good results in terms of the load-CMOD curves for three-point-bending tests. This model, however, being a homogenized one, cannot capture the rough and tortuous crack trajectories. Tortuous crack paths are an indication of considerable local mode-mixity, and this is lost in some models [53]. Homogenized models may also fail to capture the observed fracture modes in porous/composite materials [54, 55]. A mesoscopic PD model for concrete (using explicit geometrical representation of aggregates) was shown in [56], but when comparing to experiments, different normalization schemes are used for the simulation results and the experimental data, which raises questions about the validity of the comparison.

In this paper, we introduce a multiscale stochastic peridynamic model that implicitly uses some information about the concrete meso-scale structure, to simulate fracture induced in reinforced concrete induced by the expansion of rebar corrosion-products. The model does not require the explicit geometrical representation of aggregates, for example, and in that sense is a partially- or Intermediately-Homogenized peridynamic (IH-PD) model.

Notably, the model uses the simplest possible linear elastic with brittle failure constitutive relation.

A mathematical distribution function is used to mimic the expansion process of the corrosion product, which is the loading that induces fracture in this setting. The results from this multiscale peridynamic model are compared with experiments and with results from a “fully-homogenized” PD (FH-PD) model, to highlight deficiencies of complete homogenization in modeling failure in concrete and the need for preserving some information about material heterogeneity. We test the model for concrete structures with a single and multiple rebars, for which experimental data is available in the literature. We also perform parametric studies to show how the aggregates’ fracture energy and various possible rebar corrosion patterns can affect the evolution of fracture in reinforced concrete.

This paper is organized as follows: in Section 2.2 we give a brief review of the bond-based peridynamic theory; in Section 2.3 we present the numerical discretization of the peridynamic formulation; in Section 2.4 we show the IH-PD model for concrete and its implementation; Section 2.5 discusses the radial displacement model for imposing the effective expansion of corrosion product as a boundary condition on the concrete in the hole where the rebar is; numerical results are gathered in Section 2.6, where we test the IH-PD model in corrosion-induced fracture in concrete structures with a single (several configurations) and multiple rebars; conclusions are drawn in Section 2.7.

2.2 Brief review of bond-based peridynamic theory

Bond-based PD (BBPD) is the original version of peridynamics, later generalized as state-based PD (SBPD) [25, 47]. BBPD leads to material models with a fixed Poisson’s

ratio (1/3 in 2D plane stress problems, and 1/4 in 2D plane strain and 3D problems). The focus of our paper is on concrete's fracture behavior and Poisson's ratio has little effect on such problems (see theoretical analyses in [57, 58]). It is then reasonable to use the BBPD model, and the results and conclusions should not be affected by this choice. Given the geometry of the experimental samples used to compare our simulation results with, we employ the BBPD for plane strain conditions (Poisson's ratio equals 1/4) everywhere in the paper.

The equations of motion for the BBPD can be written as [25];

$$\rho(\mathbf{x})\ddot{\mathbf{u}}(\mathbf{x}, t) = \int_{H_{\mathbf{x}}} \mathbf{f}(\mathbf{u}(\hat{\mathbf{x}}, t) - \mathbf{u}(\mathbf{x}, t), \hat{\mathbf{x}} - \mathbf{x}) dV_{\hat{\mathbf{x}}} + \mathbf{b}(\mathbf{x}, t) \quad (2.1)$$

where ρ is the density field, \mathbf{u} is the displacement vector field, \mathbf{f} is the pairwise force in the peridynamic bond $\mathbf{x} - \hat{\mathbf{x}}$, and \mathbf{b} is the body force field. $H_{\mathbf{x}}$ is called the "horizon" of \mathbf{x} , and is the region in which pairwise forces exist between \mathbf{x} and $\hat{\mathbf{x}}$, an arbitrary point located inside $H_{\mathbf{x}}$ (see Figure 2.1). $V_{\hat{\mathbf{x}}}$ is the volume (area in 2D, length in 1D) occupied by the material point $\hat{\mathbf{x}}$, and t is the time (or a parameter tracking the loading step in quasi-static problems, in which case the acceleration in the equation above is zero). The horizon is usually taken to be a ball (sphere in 3D, disk in 2D, line segment in 1D) of radius δ .

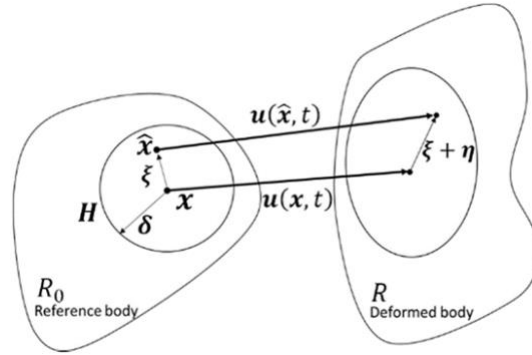


Figure 2.1. Nonlocal interaction between point \mathbf{x} and an arbitrary point located in the horizon of \mathbf{x} .

The pairwise force for a prototype microelastic brittle material [47] is defined as:

$$\mathbf{f}(\boldsymbol{\xi}, t) = g(s(\boldsymbol{\xi}, t))h(\boldsymbol{\xi}, t) \frac{\boldsymbol{\xi} + \boldsymbol{\eta}}{\|\boldsymbol{\xi} + \boldsymbol{\eta}\|} \quad (2.2)$$

where $\boldsymbol{\xi} = \hat{\mathbf{x}} - \mathbf{x}$ is the relative position of $\hat{\mathbf{x}}$ and \mathbf{x} in the reference configuration, $\boldsymbol{\eta} = \mathbf{u}(\hat{\mathbf{x}}, t) - \mathbf{u}(\mathbf{x}, t)$ is the relative displacement with respect to the reference configuration,

$s = \frac{\|\boldsymbol{\xi} + \boldsymbol{\eta}\| - \|\boldsymbol{\xi}\|}{\|\boldsymbol{\xi}\|} = \frac{\zeta - \xi}{\xi}$ is the relative deformation or bond strain ($\xi = \|\boldsymbol{\xi}\|$ and $\zeta =$

$\|\boldsymbol{\xi} + \boldsymbol{\eta}\|$). g and h are respectively given by:

$$g(s) = \begin{cases} c(\xi)s & \xi \leq \delta \\ 0 & \xi > \delta \end{cases} \quad (2.3)$$

$$h(\boldsymbol{\xi}, t) = \begin{cases} 1 & \text{if } s(\boldsymbol{\xi}, t') < s_0 \text{ for all } 0 \leq t' \leq t \\ 0 & \text{otherwise} \end{cases} \quad (2.4)$$

where $c(\xi)$ is the micro-modulus function or the elastic stiffness of the bond. The micro-modulus function can take different forms, depending on the required horizon-scale behavior [59]. Here we only consider plane strain conditions and the ‘‘conical’’ micromodulus function [60]:

$$c(\xi) = c_1 \left(1 - \frac{\xi}{\delta}\right) = \frac{192E}{5\pi\delta^3} \left(1 - \frac{\xi}{\delta}\right) \quad (2.5)$$

For heterogeneous materials, micro-modulus depends on the location. This is discussed in the next section.

To simulate fracture and failure, peridynamics uses the notion of bond damage [25, 47]. Peridynamic bonds break irreversibly when they reach the critical relative deformation s_0 , which can be related to material's fracture energy G_0 . Note that other types of failure can be considered in PD models, including reforming bond connections [61]. For the case of the conical micro-modulus function, s_0 is given by [60]:

$$s_0 = \sqrt{\frac{25\pi G_0}{48E\delta}} \quad (2.6)$$

Note that in heterogeneous materials s_0 also depends on location. With the breakage of bonds, failure starts to accumulate, and cracks begin to initiate and propagate. The damage index d is used to measure the damage level:

$$d(\mathbf{x}, t) = 1 - \frac{\int_{H_{\mathbf{x}}} h(\xi, \eta) dV_{\hat{\mathbf{x}}}}{\int_{H_{\mathbf{x}}} dV_{\hat{\mathbf{x}}}} \quad (2.7)$$

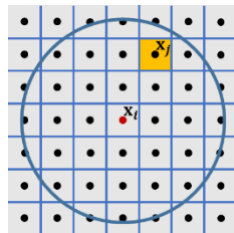
which, in the discrete version (see below) is the ratio of the number of broken bonds to that of total bonds connected to point \mathbf{x} at time (or load step) t . When all bonds connected to point \mathbf{x} are broken, $d(\mathbf{x}, t) = 1$ and point \mathbf{x} becomes a free point.

2.3 Numerical discretization

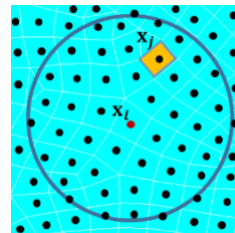
Eq. (2.1) can be solved by any method that can solve integro-differential equations, including mesh-free direct discretization [47], the finite element method (FEM) [62, 63], or a combination of both in which the FEM is used far from cracks, and the meshfree discretization is used where damage happens [63-65]. Spectral methods can be alternative approaches to achieve efficient peridynamic computations [66]. Here we use the meshfree discretization, which makes it easiest to handle damage and fracture [31, 67].

We discretize the domain into cells with nodes in the center of those cells, effectively using the mid-point integration scheme to approximate the integral in Eq. (2.1). Both uniform [47] and non-uniform [68-70] grids are possible. Figure 2.2 (a) shows a 2D uniform discretization with grid spacing Δx around a node \mathbf{x}_i . Non-uniform grids conform better for shapes with rounded boundaries. Such grids can be easily obtained based on finite element meshes generated, for example, with ANSYS and a simple APDL code (see the appendix in [55]). As shown in Figure 2.2 (b), the PD nodes are centroids of elements, and the PD nodal area of each node is the element area. To keep the quadrature error low, it is important to have meshes with relatively uniform element sizes.

Comparisons between uniform and non-uniform grids for corrosion-induced fracture are shown in Section 2.6.1.2.1.



(a) Uniform grid.



(b) Non-uniform grid.

Figure 2.2. Possible discretization types for a peridynamic model. The circular region is the horizon region of node \mathbf{x}_i .

At time t , the spatially discretized form of Eq. (2.1) is written as:

$$\rho \ddot{\mathbf{u}}_i^t = \sum_{j, j \in H_i} c_{ij} s_{ij}^t V_{ij} \mathbf{n} + \mathbf{b}_i^t \quad (2.8)$$

where \mathbf{u}_i^t is the displacement of node i , H_i is the horizon region of node i , $j \in H_i$ includes all the nodes covered by H_i (fully or partially), c_{ij} is the micro-modulus of the bond $i - j$, s_{ij}^t is the relative stretch of bond $i - j$, V_{ij} is the area of node j covered by H_i , \mathbf{n} is the unit vector pointing from node i to node j in the current configuration and \mathbf{b}_i^t is the body force at node i .

Since node j may be only partially covered by the horizon of node i , the ‘‘partial volume’’ integration scheme is used to improve the quadrature accuracy [31, 71]. Note that the partial volume integration scheme was developed for regular grids. We used the same scheme on irregular grids because the irregular grids used here do not depart much from uniform grids (most element sizes are about the same). Moreover, the use of the ‘‘conical’’ micromodulus (see Eq. (2.5)) helps with reducing the quadrature error since the influence of nodes near the edges of the horizon is smaller than that of nodes near the center of the horizon.

For the type of fracture we simulate, inertial effects are likely minor, thus all of the simulations performed in this work are quasi-static. The displacement-controlled loads are applied step-by-step, and at each step we solve the nonlinear (in displacements) system in Eq. (2.8) and use the criteria in Eq. (2.6) to determine which bonds need to

break at this step. The values for the micro-moduli c_{ij} and the critical relative deformation s_0 for each bond are determined by the bond type (see Section 2.4 below). We solve the equilibrium nonlinear system in Eq. (2.8) via the energy minimization method, using the nonlinear conjugate gradient (NCG) method with secant line search. The detail of the algorithm can be found in [32, 35]. Instead of the Polak-Ribiere formula [72], we use the hybrid Hu-Storey (HuS) formula [73], for a faster convergence. Note that other methods, such as the adaptive dynamic relaxation (ADR) method [74] and the direct sparse matrix solver [75], can also be used for quasi-static fracture problems in PD. Compared with a direct matrix solver, the NCG solver is faster and uses less memory. The ADR uses a variable artificial viscosity coefficient that sometimes can lead to some unphysical effects in the solution [76]. The NCG does face convergence difficulties in problems in which the relation between bond force and bond stretch has a softening part, due to loss of positive definiteness. Here we are using the linear elastic (with brittle failure) force-bond strain model, and the NCG is a good option.

The overall simulation process is shown in Figure 2.3. At a given load step, the NCG solver is called to find the equilibrium displacement field. On these displacements, the bond-breaking subroutine is called to check if any bonds exceeded their critical strain. If there are any such bond breaks, the NCG solver is called again (at the same load step) until no more bonds break and the physical system reaches equilibrium. If too many bonds break after one NCG solution, numerical instabilities may result [32]. To prevent this, once the number of broken bonds at a step reaches a user-provided parameter N_{\max} , we need to go back half a step (re-compute the equilibrium for half of the load increment used in the previous iteration) and repeat the static solution. In the examples shown in

this paper, the crack growth is stable, and as long as a reasonable number of load steps are used, numerical instabilities are avoided. We have conducted tests with 100 and 1,000 load steps and found no significant difference between these splits. All the results shown here are therefore using 100 load steps.

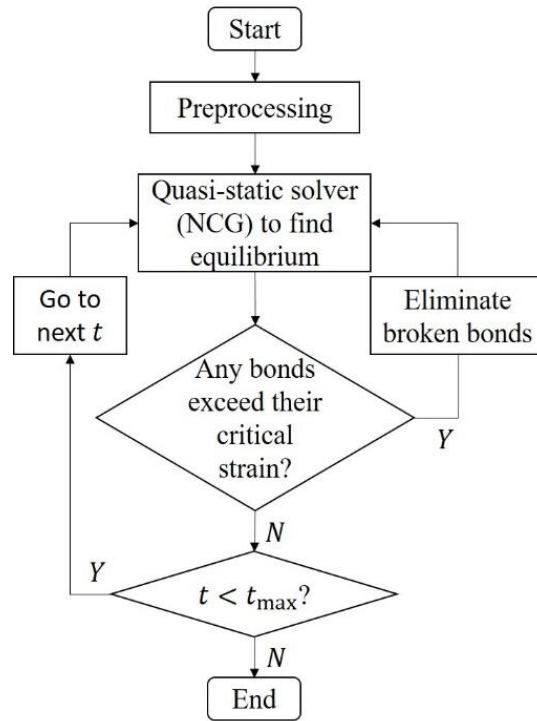


Figure 2.3. Flowchart for the simulation process of PD quasi-static fracture modeling. Here t is the load step.

2.4 The IH-PD model for concrete

In this paper, the regular homogenization approach is called the “fully-homogenized” peridynamic (FH-PD) model to distinguish it from the “intermediately-homogenized” peridynamic (IH-PD) model discussed below [58]. In the FH-PD model, concrete is seen as a *locally homogeneous* material in terms of its mechanical properties (elasticity, density, and fracture energy). The properties used in the FH-PD model are the macro-scale properties obtained from direct experimental measurements. The multiscale IH-PD

model has been originally introduced for functionally graded materials (FGMs) and porous materials, like rock, in [54, 58]. Here we adapt it for a two-phase composite, in which we define three types of intermingled sets of bonds: one bond-type for each of the phases (aggregates and matrix), and one for interfacial (aggregate-matrix) bonds. The model uses some meso-scale information (volume fraction of the phases) but does not preserve the topology of the microstructure phases. A discussion on conditions under which this approach is still sufficient to capture the fracture behavior accurately and efficiently can be found in [55].

Consider the two-phase (phases A and B) composite material shown on the left side of Figure 2.4. At the microscale, an arbitrary PD bond connects points \mathbf{x} and $\hat{\mathbf{x}}$, whose geometrical positions fall in one of the two phases, A and B. We assume that the horizon, and therefore the size of the nodal volumes, are at a scale larger than that of the inclusions so that the composite volume fractions in a nodal volume are statistically representative of the macro-scale value. The probability for a bond to have the properties of phase A, B, or interfacial properties, depends on the volume fraction of the phases over the nodal volumes/areas of the two nodes.

A bond with properties of the A or B phases will be called an A-bond or a B-bond, respectively, while a bond with interfacial properties will be called an AB-bond. Figure 2.5 shows an example of bond-type distribution in the IH-PD model around a particular node.

In the IH-PD model, we assume a linear relationship between the chance of the bond type and the local phase volume fractions at the two end nodes, but other choices could also be

made. If the volume fractions of phase A are R and R' at \mathbf{x} and $\hat{\mathbf{x}}$, respectively, the chance for this bond to be an A-bond, B-bond, or an AB-bond is RR' , $(1 - R)(1 - R')$, or $1 - (1 - R)(1 - R') - RR'$, respectively. While we will not use the specific distribution of the continuous or discontinuous phases (in order to end up with a computationally efficient model), the volume fraction information is included, and the model is, at the small scale, heterogeneous. For a discussion on when the topology of the phases is important, see [55]. Since the explicit microstructure is not used here, and only the volume fraction information is input data, we generate the bond properties as a preprocessing step shown in Figure 2.6. Notice that we only select bond types, not node types. The algorithm visits each node in the discretization, then considers each bond in that node's family (if it had not previously been assigned its properties) and assigns its properties based on a random number generated from a uniform distribution (see Figure 2.6).

For concrete, phase A is aggregate and phase B is cement. We assume that the concrete is homogeneous at the larger scale so that the phase volume-fractions are constants throughout the domain, i.e., $R = R'$. For example, if $R = R' = 40\%$, then 16% of all PD bonds end up as aggregate-bonds, 36% as cement-bonds and the remaining 48% as interfacial (aggregate-cement) bonds.

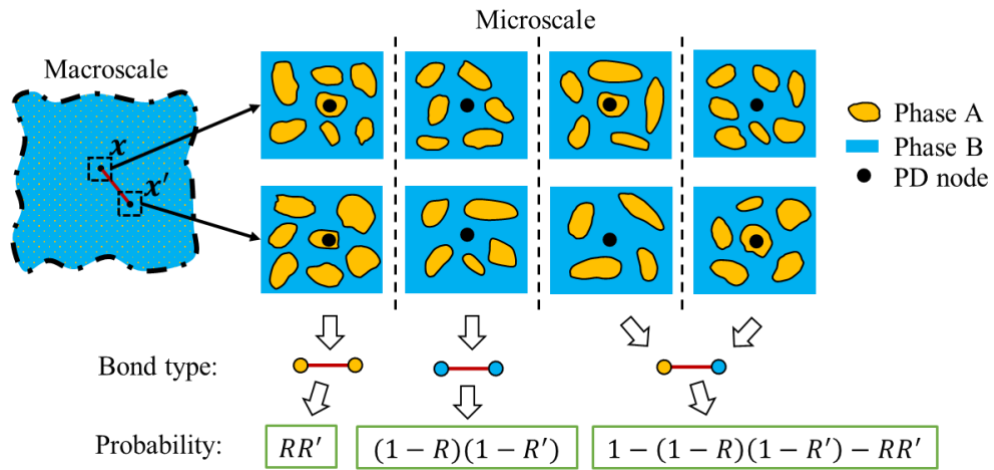


Figure 2.4. Determining the properties of a PD bond in the IH-PD model, based on the local volume fractions of phase A at points x (R), and x' (R'). Note: here we only use the overall volume fraction of the phases in concrete, not the local ones. The microscale geometry is not used.

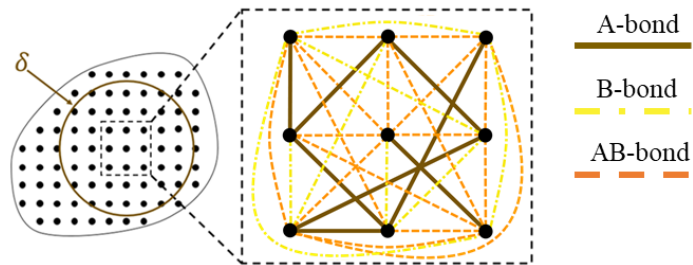


Figure 2.5. A possible distribution of bond properties at a node in the IH-PD model. Only bonds connecting the nearest eight neighbors of the central node are shown.

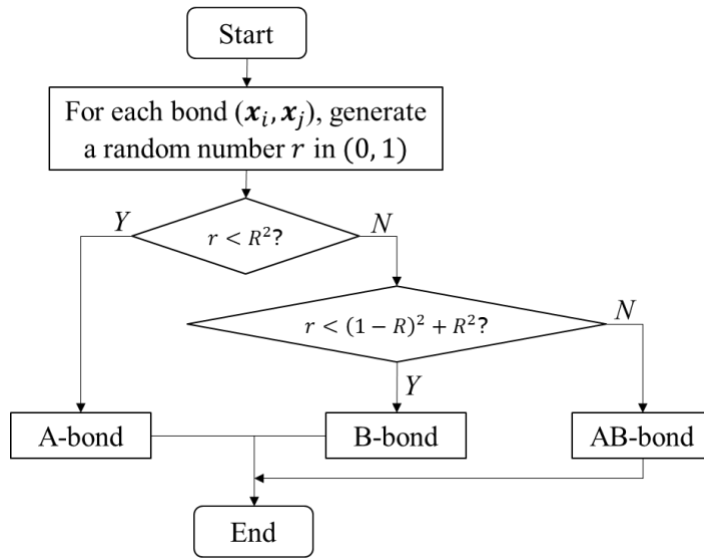


Figure 2.6. The pre-processing step for instantiating bond properties in the IH-PD model, at a node x_i for each x_j node in its family.

The mechanical properties for the interface can be chosen as the arithmetic or the harmonic averages [58] of the two phases A and B. In a recent paper on failure in solder joints [77], an area-weighted harmonic average method was introduced for computing elastic properties of PD interfacial bonds in order to reduce/eliminate oscillations in strains observed at an interface when other options are used. For concrete, the harmonic average is a good option for the elasticity of the interface, according to the test results given in [78]:

$$M_{AB} = \frac{2M_A M_B}{M_A + M_B} \quad (2.9)$$

where M_A , M_B , and M_{AB} are the mechanical properties corresponding to aggregate, matrix, and interface, respectively. The micromoduli of the three bond-types will be computed to match (see Eq. (2.5)) the M_A , M_B , and M_{AB} moduli, respectively.

The fracture properties (s_0 values in Eq. (2.6)) for A- and B-bonds are computed based on the fracture energies of the two material phases: aggregate and mortar. In terms of the interfacial fracture property, we take into account that in concrete, the interface between aggregates and matrix is generally weaker than both of them. The fracture energy of the interface in concrete materials is found in experiments to be 4% - 34% that of the mortar, with a value estimated to be between 2.5 – 25.3 N/m [79]. Surface roughness also affects the fracture energy, increasing fracture energy with increasing roughness [79]. We choose the fracture energy of the interface to be 25% of mortar [19], and the corresponding property (s_0) of AB-bonds will be computed to match this value. (see Eq. (2.6)).

Note that the stochastic pre-processing step illustrated in Figure 2.6 can generate different realizations of bond structure in different simulations if a different “seed” is used in the random number generator. Different simulations with the same IH-PD realization and same input data give, obviously, the same result. Different results are found using different microstructure realizations of the IH-PD model, even when the rest of the input data is the same. However, for a fixed horizon size, differences between such solutions become smaller the finer the grid (the larger the ratio of horizon to grid spacing, or the “ m -value” [80]) is.

2.5 Radial displacement model for effective expansion of corrosion product

Carbon dioxide and chloride ions from the environment can both depassivate the rebar surface [1, 2]. Carbon dioxide can neutralize the alkalinity of concrete and make the passive film unstable. Corrosion induced by carbonation usually happens uniformly. Chlorides, however, usually destroy the passive film locally, which results in non-

uniform pitting corrosion on the rebar surface. Corrosion can be more non-uniform when one considers the heterogeneities (defects and pores) at the concrete-rebar interface. Non-uniform corrosion leads to the non-uniformly distributed expansion of corrosion products. Various methods have been developed to *mimic* this expansion, rather than solve for it: radial displacement [81], internal pressure [82], or thermal expansion [83]. The purpose for these models is to use the distribution of displacements/pressures created by the expansion of corrosion products onto the concrete as a boundary condition, thus eliminating the need for explicitly modeling the rebar itself.

Here, we choose the radial displacement method and select the von Mises distribution model to approximate the corrosion pattern. We implement this distribution as displacement boundary condition on the inner surface of the rebar hole [19], without actually modeling the rebar. The von Mises model for corrosion pattern is simple to implement and has shown good accuracy compared to available experimental data. The parameters in the formula have physical meanings and are easy to manipulate.

Using the von Mises model, the expansion of corrosion product can be written in the form of a radial displacement as (see Figure 2.7):

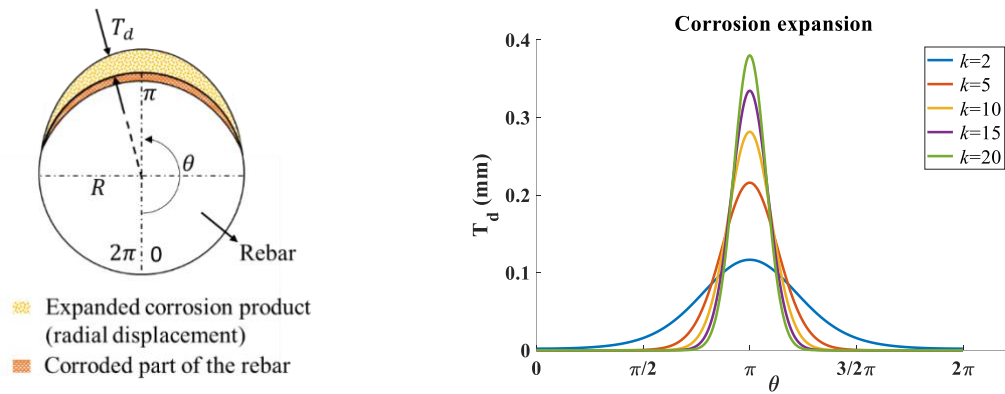
$$T_a(\theta) = (a - 1)\pi R\eta \frac{e^{k \cos(\theta - \mu)}}{2\pi I_0(k)} \quad (2.10)$$

where $I_0(k)$ is the modified Bessel function of order 0 written as $I_0(k) = \sum_{i=0}^{\infty} \frac{(\frac{1}{4}k^2)^i}{(i!)^2}$. The meaning of all parameters can be found in Table 2.1. The values of a and η are fixed to be 4 and 0.0003, respectively, for all the following numerical problems, while the values for other parameters depend on each problem.

A sketch of the von Mises radial displacement model and displacement plots for different k values (level of non-uniformity, $k = 0$ means uniform corrosion) are given in Figure 2.7. The thickness of the expanded corrosion product around the rebar surface (see Eq. (2.10)) will be used in our model as displacement boundary condition on the concrete inner hole surface, where the rebar expansion pushes against. To apply these conditions, considering the surface effect in peridynamic models [84], we use a fictitious layer of nodes outside of the domain (in the hole region) and enforce these displacements to all of the nodes in the fictitious region instead of only to the domain nodes located nearest to the surface of the hole. This is done to reduce the peridynamic surface effect. This layer is shown in Figure 2.8, and its thickness equals the horizon size δ . With the horizon size approaching zero, the PD boundary condition converges to the classical boundary condition [85].

Table 2.1. The meaning for parameters used in Eq. (2.10).

Parameter	Meaning
T_d	Thickness of the expanded layer
a	Ratio of rust expansion to corroded rebar
R	Radius of the rebar
η	Corrosion degree
μ	Location of maximum thickness
k	Non-uniform coefficient



(a) Schematic distribution of radial displacements caused by corrosion product expansion (redrawn from [19]).

(b) Thickness of the expanded layer around the rebar, for different parameter k values.

Figure 2.7. The von Mises radial displacement model.

There are different ways to implement the displacement boundary conditions defined by Eq. (2.10). For the elastic problem (no damage is allowed), the radial displacement boundary condition at the rebar hole surface is assigned in one step. For cases involving fracture, we incrementally increase the imposed displacements. One way to reach the values provided by the formula in Eq. (2.10) is to split the total/final radial displacement distribution, at each point around the (initially) circular rebar hole surface, in multiple equal steps (e.g. 100 steps). This is a simple option. However, in reality, certain part of the rebar corrodes earlier than other parts of the rebar, as shown in Figure 2.27 in Appendix A. Notice that the modeling of chloride diffusion given in Appendix A is important because it helps us in applying the von Mises boundary conditions on the rebar hole surface in Figure 2.8. Therefore, another option is to control the sequence of radial displacement at different locations around the rebar hole surface, as described in Appendix B.

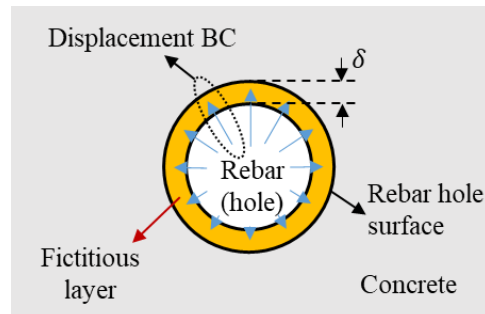


Figure 2.8. Imposing displacement boundary conditions at the rebar hole surface using a fictitious node layer. Notice that the rebar is not included in the model.

Other factors such as the porous zone at the concrete-rebar interface [19] and the movement of corrosion products into cracks [13, 86] also play a role in the cracking process, affecting the crack initiation time and the speed of crack growth. In the present work, we focus on the fracture patterns and its evolution in a quasi-static setting.

2.6 Fracture in concrete due to corrosion of single/multiple rebars

2.6.1 Concrete structure with a top-sided middle rebar

In this section, we study a particular reinforced concrete structure with one rebar located as shown in Figure 2.9. For this case, only the region inside the red dashed contour will be shown in the numerical results. The bottom of the concrete structure is under roller support. The displacement boundary condition at the rebar hole surface was presented in Section 2.5. The material properties, used in all of the following simulations are gathered from several references and given in Table 2.2. Concrete properties listed in Table 2.2 are measured directly, not derived from those of concrete components. The volume fraction of aggregates is 40%, which is a common value used in literature [19, 56]. We first verify the elastic solution by comparing with FEM results. Then we conduct a PD convergence study of the fracture patterns using different horizon sizes. We perform a parametric study to show the influence of aggregate fracture energy on the formation of cracks. We

also show the evolution of fracture. After that, we compare the numerical simulation results for deformation of concrete surface with experiments.

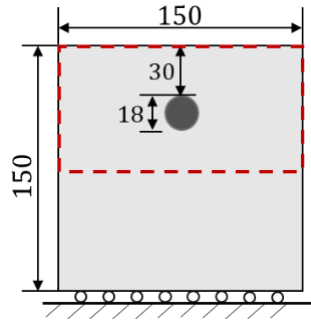


Figure 2.9. Geometry of the concrete structure with a top-sided middle rebar (mm).

Table 2.2. Material properties for all concrete structures to be analyzed (from [19, 81, 87, 88]).

Material	Young's modulus (GPa)	Fracture energy (N/m)
Concrete	31.5	52.5
Matrix	25.0	60.0
Aggregate	70.0	500*
Interface	36.8 (see Eq. (2.9))	15.0

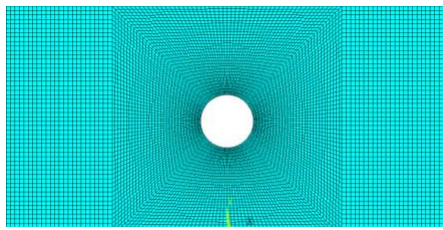
* See section 2.6.1.2.3 for a parametric study.

2.6.1.1 Verification for the elastic response

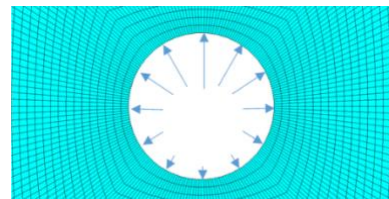
We first verify the PD model for the elastic response (damage is not active) using the concrete structure with a top-sided middle rebar shown in Figure 2.9. We compare the FH-PD and IH-PD results with those from a FEM solution, when the displacements induced from the rebar corrosion are given by taking $k = 5$ in Eq. (2.10). It should be noticed that the FEM solves the local model while the PD-solutions are for corresponding nonlocal models. The local and nonlocal solutions, in general, are different, but the

nonlocal model, in the limit of the horizon going to zero, should converge to the local elasticity solution [25, 80].

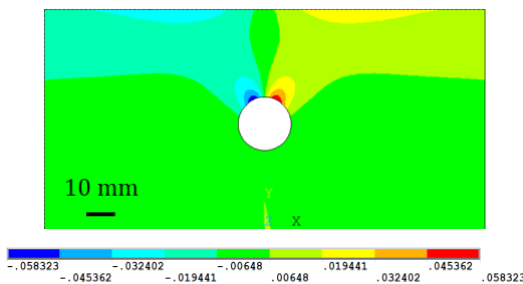
For the FEM simulation, we generate a conforming map-mesh around the circular rebar with the total node number of 14,048 (see Figure 2.10 (a) and (b)). The rebar is not included in the model, but the displacement boundary condition at the concrete inner hole surface is the same as that used in the PD simulation (but only applied at the interface nodes, not over a layer of nodes). Figure 2.10 (c) and (d) show the displacements obtained with ANSYS using four-node plane strain elements (plane 182).



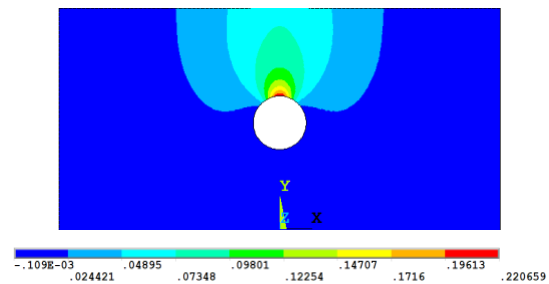
(a) Map-mesh for the concrete with one rebar.



(b) Zoom-in of the map-mesh for the concrete around the rebar (arrows schematically represent the imposed displacement boundary condition on the rebar hole surface in Figure 2.8).

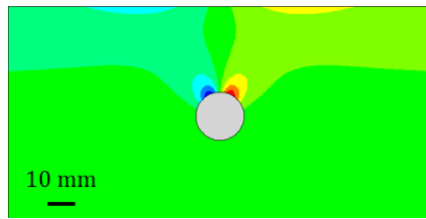


(c) Horizontal displacement.

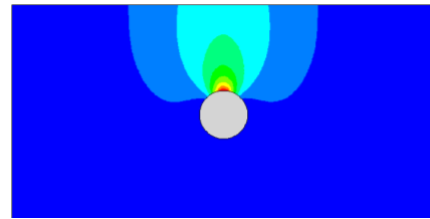


(d) Vertical displacement.

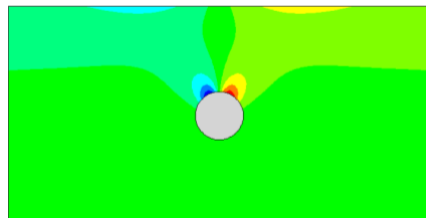
Figure 2.10. FEM mesh and displacements computed using ANSYS (only the highlighted region from Figure 2.9 is shown).



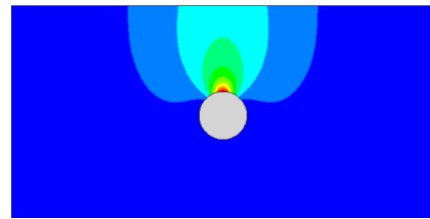
(a) Horizontal displacement, FH-PD model.



(b) Vertical displacement, FH-PD model.



(c) Horizontal displacement, IH-PD model.



(d) Vertical displacement, IH-PD model.



Figure 2.11. Displacements obtained with the PD models (only the highlighted region from Figure 2.9 is shown).

For the PD simulations with a uniform grid (for horizon size 2 mm and node spacing 0.5 mm; total number of nodes 90,000), the displacements with both FH-PD and IH-PD models are shown in Figure 2.11. The contour plots for both PD models (plotted with Tecplot) and the FEM ANSYS solution are close to identical. The same color legend was used in all PD results, and we tried to match with the ones produced by ANSYS (some colors may have slightly different nuances between Tecplot and ANSYS). Note that the horizon size must be smaller than the smallest relevant geometrical feature of the model [29], the rebar size in our case. Otherwise, stress concentrations and cracks initiating from the rebar may not be captured accurately. The horizon size may need also to be correlated to the damage process zone if damage is involved [29]. The agreement between the PD and FEM solutions is very good, except for some small differences near

the boundary, caused by the peridynamic surface effect [84]. Note that a map-mesh cannot be used directly in the PD model due to the large size differences between elements near the rebar and those far from it. With an adaptive approach [68] or with the dual-horizon PD model [89], one could use such a mesh to generate the discretization nodes for the PD model. In the following PD simulations, we either use a uniform grid ($dx = \delta/m$ with $m = 4$) or free-mesh conforming grid generated in ANSYS (linear quad elements with edge-length equal to $\delta/4$). See Section 2.3 for how non-uniform grids generated with ANSYS are transformed into PD grids.

2.6.1.2 Fracture of concrete with a top-sided middle rebar

Figure 2.12 shows the experimental results from [81], for fracture patterns in the case with a top-sided middle rebar. In our simulations we use the same geometry as used in the experiments. However, material properties for the aggregate, mortar and interface used in our simulation are from other sources (see Table 2.2) because they are not provided in [81]. External current was used to speed up the corrosion process in this experiment, which may result in different corrosion profile compared to natural conditions. Also, experimental results for only two samples were given in [81], with significant variability between their fracture patterns. As a result, we can only use these experimental observations for *qualitative comparisons* with our simulation results.



Figure 2.12. Experimental results for different samples of reinforced concrete under accelerated corrosion test [81].

2.6.1.2.1. The δ -convergence study

First, for the concrete structure with a top-sided middle rebar (see Section 2.6.1), we compare the fracture pattern obtained by FH-PD and IH-PD models, using uniform and non-uniform grids, respectively. The fracture energy of aggregates is taken as 500 N/m and $k = 5$ (level of non-uniformity, see Eq. (2.10)). It should be noticed that fracture of aggregates is not considered in previous works [19, 21], this being equivalent to selecting an infinite fracture energy for aggregates. In our model, however, we select a large but finite value to also allow failure of aggregate PD bonds because aggregates do, sometimes, fracture when concrete fractures. As seen in Figure 2.13, with the FH-PD model we do not get convergence in terms of fracture patterns as we take the horizon size δ to zero while keeping the ratio of δ and dx fixed (the δ -convergence, see [80]). With either uniform or non-uniform grids, the fracture patterns change rather significantly when different horizon sizes are used. Although one of the fracture patterns (obtained using the larger horizon and the corresponding coarser grid) appears similar to one of the experimental observations, (see Figure 2.12), the vertical crack found by the FH-PD model for this case initiates at the rebar hole surface and then propagates to the concrete surface. This is opposite to what is reported in the experiments [81, 86] as well as previous numerical studies [17, 19]. In this fully homogenized model, with linear-elastic and brittle fracture, once the cracks start from the rebar hole surface, stress is redistributed uniformly through the material, and the tensile bending deformation at the concrete surface is relieved. Lower tensile stress at the surface means a crack cannot initiate there. The initial cracks continue to grow towards the concrete surface. Meanwhile, one or more cracks may initiate at the interface and propagate.

The reasons for the failure of the FH-PD model to converge come from changes in stress distribution caused by different grids around the rebar hole surface. Small changes in the location of highest tensile stress (strain) induced by use of different discretization grid sizes (especially with uniform grids), leads to variations in the location of crack initiation. These relative differences increase as the cracks grow. The differences in crack patterns are smaller when non-uniform (and not symmetric) conforming grids are used (see Figure 2.13 (b)) because the stress state is less dependent on the grid. Nevertheless, any small difference is still amplified in terms of crack paths because the material is homogeneous and brittle, and therefore, sensitive to any small numerical perturbations.

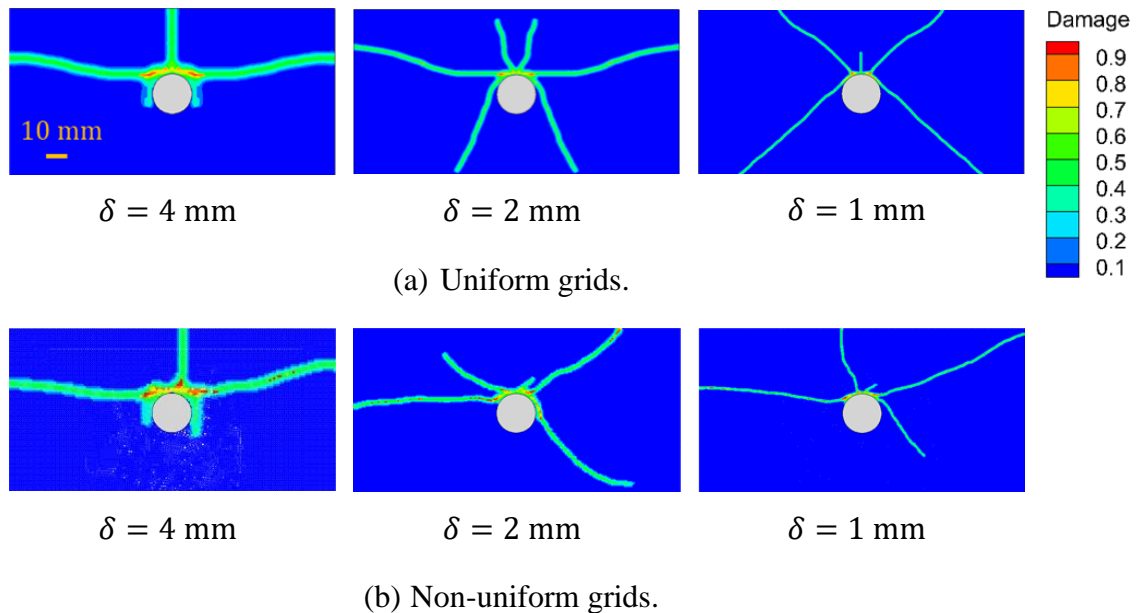
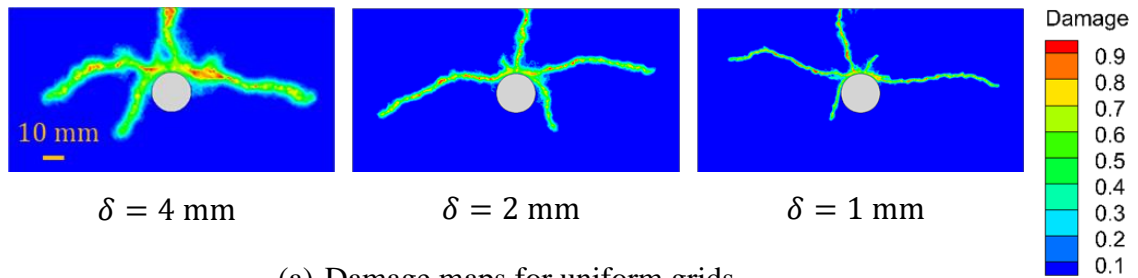


Figure 2.13. Convergence study for the FH-PD model ($m = 4$) for parameter $k = 5$ in Eq. (2.10).

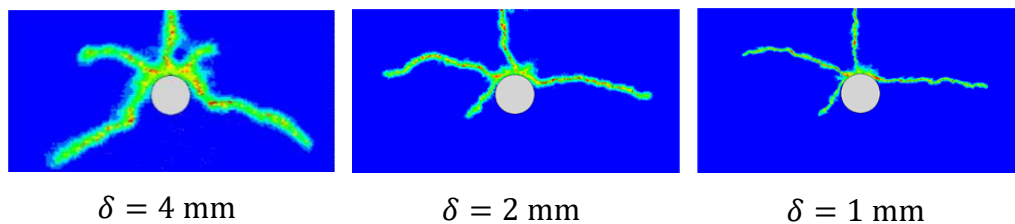
In the IH-PD models, the bond structures are different between the tests because different grid densities are used. When we use the same horizon size but create a new realization of the PD bond structure, the fracture patterns obtained are remarkably similar to one another (see Appendix D). As can be seen from Figure 2.14, the fracture patterns show

similar features for different horizon sizes too, matching well those from experiments (see Figure 2.12). Note that the fracture pattern obtained by the IH-PD model is not symmetric because the bond structure generated by the stochastic process (see Figure 2.6) is not symmetric. Moreover, with the IH-PD models, the vertical crack happens before the horizontal ones fully split the sample, which is consistent with the experimental observations. To further explore the reasons for the apparent success of the IH-PD model in contrast with the FH-PD model, in the next section, we discuss in detail the evolution of the fracture process in the IH-PD simulations.

Since the fracture patterns obtained with $\delta = 2$ mm are not much different from those with $\delta = 1$ mm, for the remaining simulations we use the IH-PD model with $\delta = 2$ mm, unless otherwise stated. Also, for simplicity, we only use uniform grids for the rest of the simulations.



(a) Damage maps for uniform grids.



(b) Damage maps for non-uniform grids.

Figure 2.14. Convergence study for the IH-PD model ($m = 4$) for parameter $k = 5$ in Eq. (2.10).

2.6.1.2.2. Fracture evolution with the multiscale PD model

To explain why δ -convergence for crack patterns happens in IH-PD but not in FH-PD, it helps to recall that bond properties are randomly distributed (to match the volume fraction of the phases in terms of the elastic response) in the IH-PD case. This small-scale variability leads to a relative insensitivity to variability in the computational grid. The results in Figure 2.14 (a) and (b) show that crack patterns are about the same for the uniform grid and the non-uniform grid (conforming to the round rebar).

A typical evolution of fracture obtained with the IH-PD model is shown in Figure 2.15. Micro-damage first accumulates around the rebar hole surface due to failure of weaker bonds (most of them should be AB-bonds) around the interface where the displacement loading conditions are applied. Damage starts to localize into horizontal cracks. However, since the material ahead of the crack tip is composed of PD bonds with different failure resistance, the horizontal cracks propagate but may arrest in regions with higher crack growth resistance. When that happens, due to the continued loading, a vertical crack can initiate on the top surface and propagate across the concrete cover towards the rebar. The horizontal cracks may continue to grow and approach the sides of the concrete specimen. As the expansion of corrosion products continues, additional cracks may start from the rebar hole surface and propagate.

The stage when micro-damage around the rebar forms is difficult to detect experimentally. Nevertheless, the initiation and propagation of the vertical crack are both consistent with the post-mortem experimental observations [81, 86, 90] and other numerical simulations which utilized the meso-scale structure of concrete [19-21, 81]. It can be shown by both theoretical and FE analysis that, before fracture occurs, the

maximum circumferential stress is located symmetrically about the vertical axis of the rebar [17]. From these locations, horizontal cracks initiate and propagate first, but the propagation is constrained by “chains” of aggregate bonds. Once horizontal cracks have grown sufficiently, the loading is similar to bending of a beam: vertical cracks start from the concrete surface because the top concrete surface is under highest tensile horizontal loading, while the rebar top region is under bi-axial compression [91]. Because of this, tensile horizontal stresses at the concrete surface build up and eventually lead to breakage of bonds. Only when the vertical crack reaches the rebar, can the horizontal cracks continue their propagation.

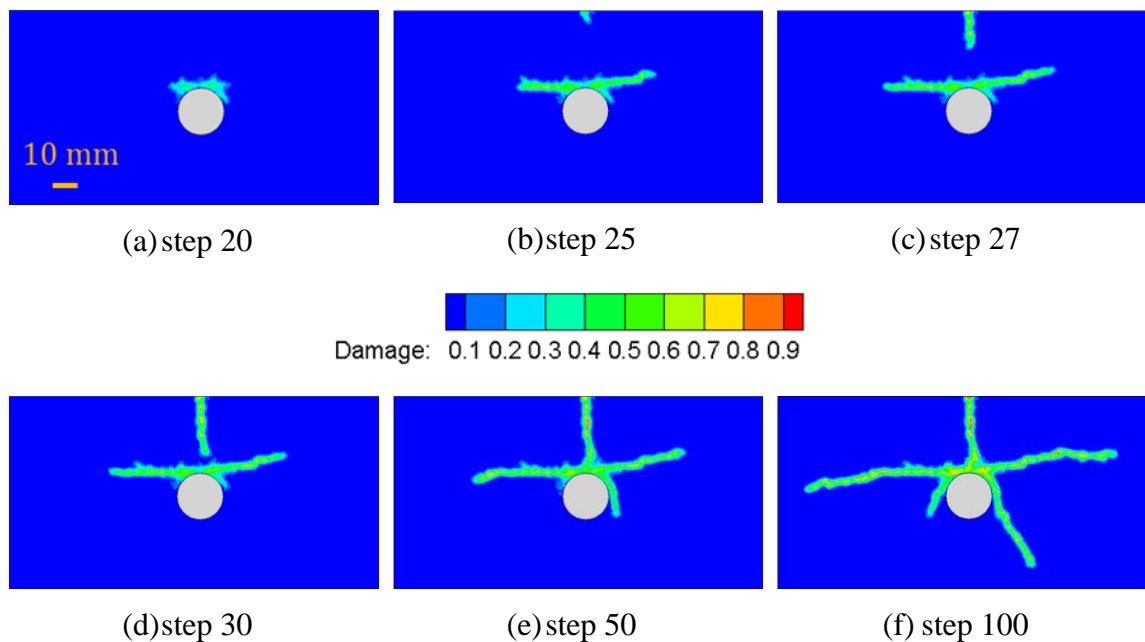


Figure 2.15. Typical fracture evolution using the IH-PD model.

In real problems, the microstructure randomness of concrete can lead to significantly different corrosion profiles around the rebar. We use our model to test how different “shapes” of corrosion distribution can affect the fracture patterns in the reinforced

concrete. The results presented in Figure 2.31 (Appendix C) show that the shape of the corrosion product pressure function (see the parameter k in Eq. (2.10)) and the sequence of the imposed displacements (gradual or simultaneous corrosion around the rebar) affect the final fracture pattern but not in a significant way. Therefore, for the remaining simulations for the sample with a top-sided middle rebar (see Figure 2.9), we only use the $k = 5$ value. The corrosion process is assumed to happen simultaneously around the rebar in all remaining simulations.

It should also be noticed that, due to the embedded randomness, slightly different fracture patterns are obtained when using different bond-scale realizations of the IH-PD model. A brief study on this is included in Appendix D.

2.6.1.2.3. Parametric study in terms of the aggregates' fracture energy

As mentioned before, aggregate fracture is ignored in the available meso-scale models which use explicit representations of the aggregates. However, in physical tests, cracks do sometimes cut through aggregates. In order to understand the effect of aggregate-type bonds in the IH-PD model has on the overall failure behavior of the concrete-rebar structure, we perform a parametric study. Fracture patterns obtained by using different fracture energy for computing the critical strain for aggregate bonds in the IH-PD model are shown in Figure 2.16. We vary the fracture energy for such bonds from the small value equal to that of the mortar (not entirely realistic) to some arbitrary value (eight times larger than that of the mortar). When the fracture energy for aggregate bonds is too small, the vertical crack does not match the behavior seen in reality (Figure 2.16 (a)). When it is too large, significant damage spreads sideways from the major crack paths (Figure 2.16 (d)), also not observed experimentally. The latter result is caused by the

presence of the network of aggregate-type bonds in the IH-PD model, which is in contrast with the actual concrete microstructure (aggregates are inclusions, not long chains spanning the sample). The different topology at the micro-scale in the IH-PD model compared with the actual microstructure does not affect the material behavior in the elastic regime, but it can affect it once damage is considered [55]. With an intermediate value of $G = 500 \text{ N/m}$, the crack patterns match well the trends seen in experiments. This value will be used for the remaining simulations.

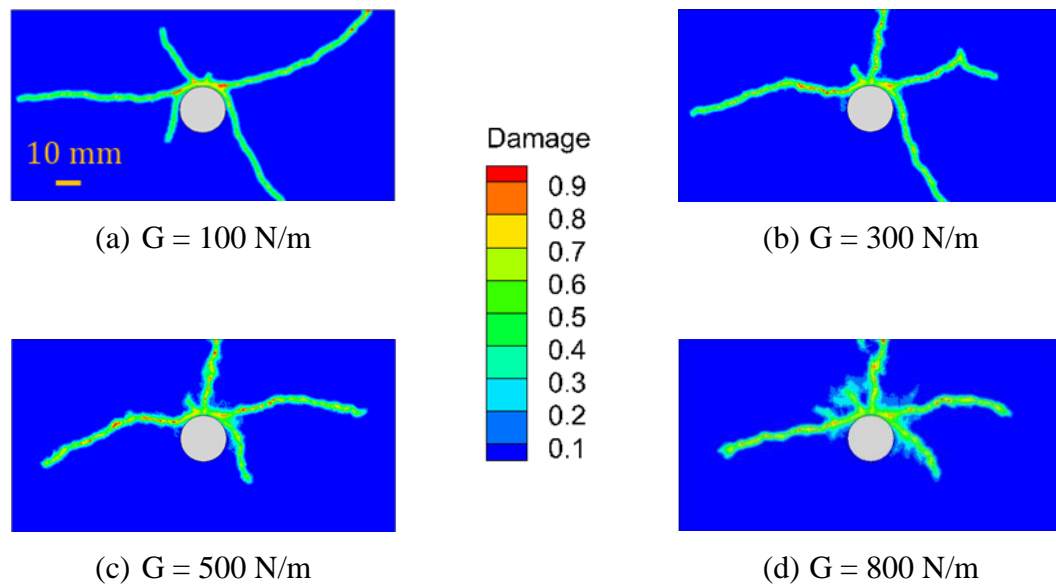


Figure 2.16. Fracture patterns produced by different choices for the aggregates' fracture energy (case with $k = 5$ in Eq. (2.10)) with $\delta = 2 \text{ mm}$ and $m = 4$.

2.6.1.2.4. Surface deformation

As the rebar corrodes and the expansion of the corrosion product leads to internal pressure build-up, the concrete surface is experiencing horizontal tensile stresses, similar to the case of beam bending. The surface crack initiates once these tensile stresses/strains reach a critical value. A comparison with experimental results can be made for the vertical deformation of the concrete surface [81]. We also compare the width of the

surface crack. For these simulations, we choose a horizon size equal to 1 mm because the smallest width of the surface crack measured in experiment is around 2 mm.

To estimate the surface crack width, we assume it to equal the smallest relative displacement between any two top-surface nodes on opposite sides of the crack with damage index bigger than 0.4. In Figure 2.17 we plot the deformation of the concrete surface (vertical displacement) and give the values of the crack opening width in the legend. The experimental curves were measured from the sample given in Figure 2.12 (a) at two different times. While the crack opening width is only qualitatively matched, the surface deformation curves are very similar to those measured in experiments. Some difference between experimental data and our numerical results is expected because our input data (the pressure profile) is only a rough approximation of the actual conditions. It should be noticed that in Figure 2.17 (b) the maximum deformation in experimental curve is not located at the surface crack of the experimental fracture pattern (see Figure 2.12 (a)), which is unexpected. No reason was given for this inconsistency, but it is possible that the deformation was not measured exactly at the location of the cross-section shown in Figure 2.12 (a), but at a different location.

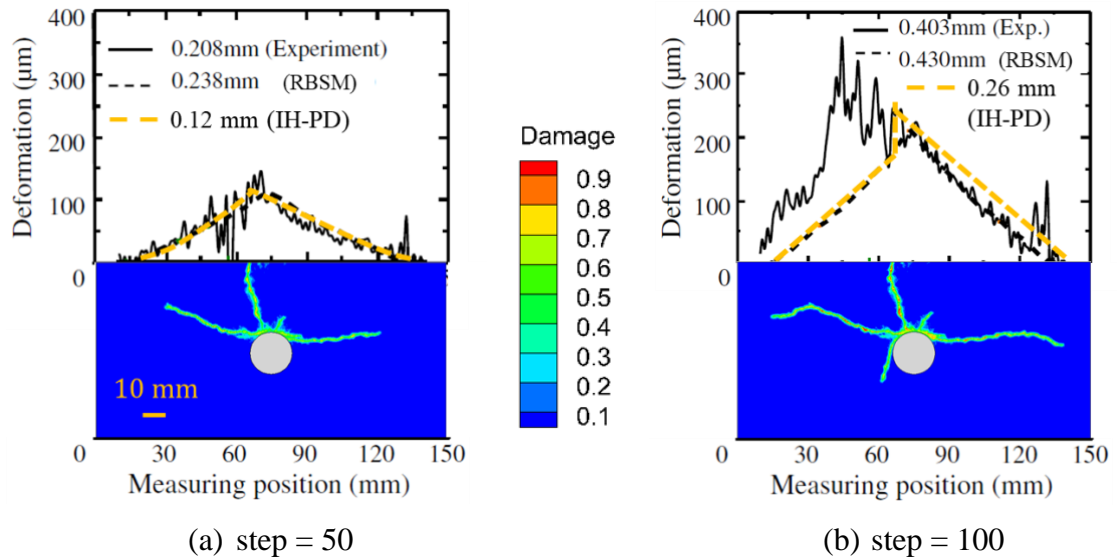


Figure 2.17. Comparison of surface deformation at two different corrosion stages between IH-PD results, experimental observations (see the sample in Figure 2.12 (a)) as well as the RBSM solutions in [81]. Data in the legends refers to the crack opening width at the top of the sample.

2.6.2 Concrete structure with a corner rebar

In this section, we study two cases in which the rebar is located at the corner of the concrete structure as shown in Figure 2.18. The material properties are the same as those in the case with a top-sided middle rebar. The geometry data is given in Table 2.3. The horizon size is 1 mm, and node spacing is 0.25 mm. A smaller horizon size is used because the rebar size here is smaller than the concrete structure in the previous example (see Section 2.6.1.1 for a discussion on selecting the horizon size).

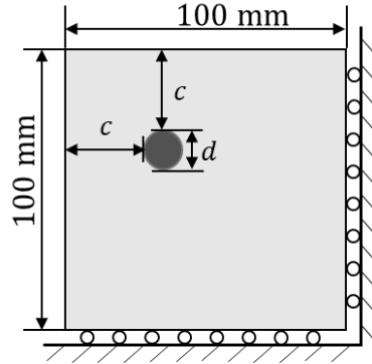


Figure 2.18. Concrete structure with a corner rebar: geometry and mechanical boundary conditions. The bottom and right sides are symmetry lines.

Table 2.3. Geometry data for two samples of the reinforced concrete structure shown in Figure 2.18 [92].

Geometry data	Sample 1 (mm)	Sample 2 (mm)
c	35	20
d	16	12

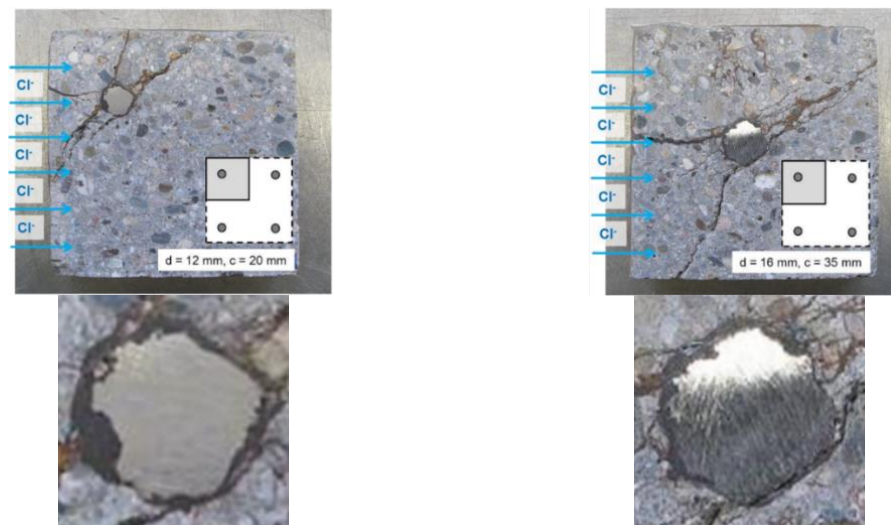
The experimental results (and zoom-in images) for two different samples (see Table 2.3) are shown in Figure 2.19. We note that the experimental setup used external current to accelerate corrosion [92]. The chloride appears to penetrate through the left side of the concrete cover according to Figure 2.19 (a) and (b). The zoom -in images show that the corrosion profiles vary significantly between the two samples, which could be, besides the slightly different geometrical setups, the main reason why the observed fracture patterns are also significantly different.

For our PD model, we assume the corrosion profile for the top-sided middle rebar is rotated by an angle γ , as shown in Figure 2.20, to account for the chloride penetration from the left side. For sample 1 with $\gamma = \pi/2$, $\gamma = 3\pi/8$ and $\gamma = \pi/4$, we obtain fracture patterns in Figure 2.21 (a), (b) and (c), respectively, with two different k values.

The crack patterns for sample 1 in the experiment, shown in Figure 2.19 (a), have a corner-type symmetry, while the computed results less so. For sample 2, Figure 2.21 (d) shows fracture patterns obtained with $\gamma = \pi/4$. The fracture pattern for $k = 10$ shows diagonal symmetry, while the experimental fracture pattern, shown in Figure 2.19 (b) does not. Because only one sample was provided in the experimental work [92] for each geometry, it is difficult to draw a definitive conclusion in these cases. Some differences between our simulation results shown in Figure 2.21 and the experimental observations shown in Figure 2.19 may be attributed to several factors, such as: the partially-homogenized PD bond structure is not an exact representation of the actual concrete microstructure; the boundary condition used to mimic the expansion of the corrosion products is an assumed approximate distribution instead of real values; some features could be reflections of 3D effects (possibly more significant for the corner rebar case than the previous symmetric rebar case), that our 2D model cannot be expected to replicate.

We noticed that references [13, 14] (using a specialized constitutive model for concrete) obtained fracture patterns very similar to experimental observations using a 3D model. They obtained the radial expansion of corrosion product from the corrosion of rebar and applied it to the contact element between the rebar and the concrete. This coupling may produce more realistic boundary conditions for the corrosion expansion. However, the anodic regions around the rebar were determined beforehand in all simulations, by selecting just one pair of anode and cathode in each activated cross-section of the rebar. This may not be realistic since microcell corrosion in reality usually consists of many pairs of mixed anodic and cathodic areas [2], which would result in a relatively uniformly accumulated corrosion product along the depassivated rebar surface. The actual corrosion

process is a combination of micro- and macro-cell corrosion [2]. Macrocell corrosion involves pitting corrosion, leading to non-uniform corrosion patterns. Our way of applying radial displacement boundary condition (see Section 2.5) is a grossly simplified, but perhaps more reasonable approximation of real conditions because it can be seen as a weighted combination of pitting corrosion and uniform corrosion. Also, according to the pressure profile in [13, 14], the corrosion product accumulates in zones that do not seem to agree with the experimental observations from [92] (shown in Figure 2.19). Only one mesh was used for each example shown in [13, 14]. Since the crack band theory used to simulate the fracture process in [13, 14] has mesh orientation dependence ([15]), it would be interesting to see if any changes take place in the reported results if one uses a differently oriented mesh and whether possible changes in fracture patterns would match the fracture patterns variability seen experimentally.



(a) Sample 1 and the zoom-in at the rebar (b) Sample 2 and the zoom-in at the rebar

Figure 2.19. Experimental results for cracking in reinforced concrete due to corrosion of a corner rebar (from [92]).

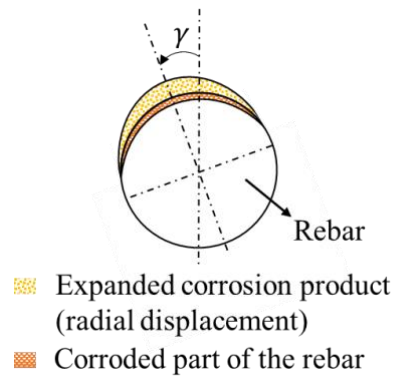


Figure 2.20. Corrosion profile for the corner rebar.

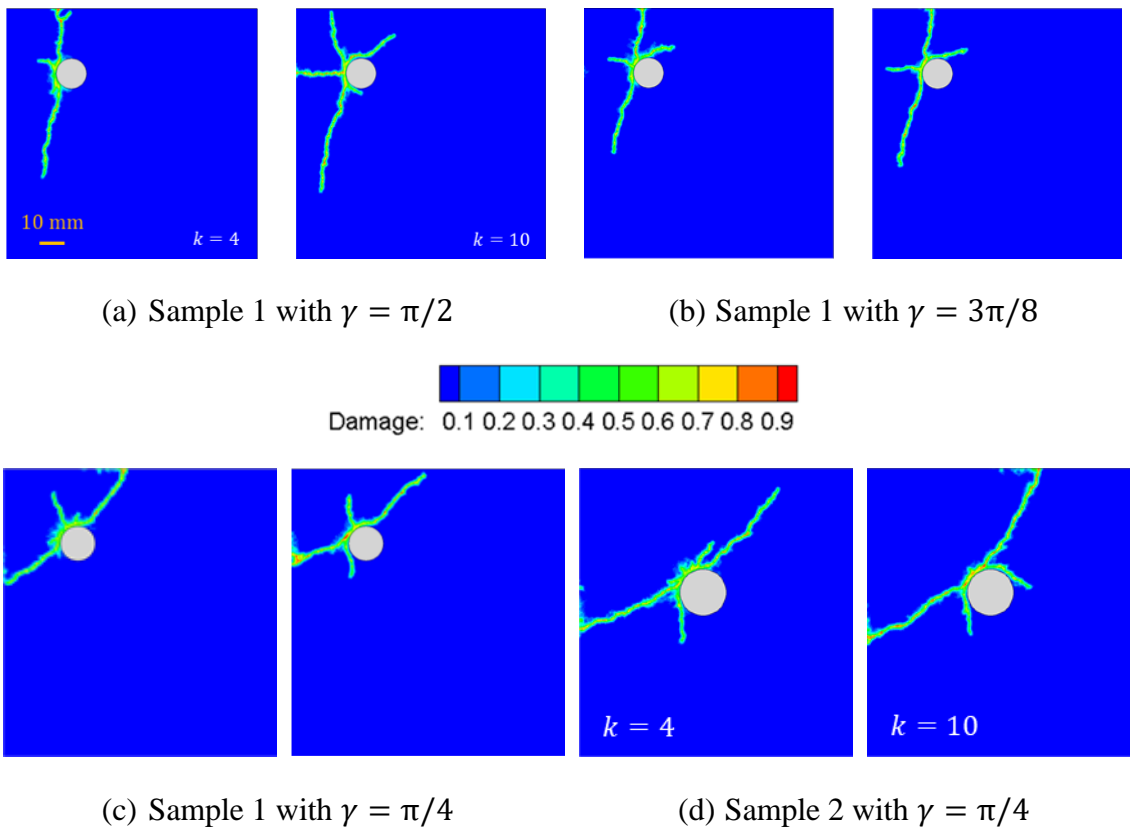


Figure 2.21. Damage maps from the IH-PD models for corner rebar (with the same bond-structure realization) with different γ and k values in Eq. (2.10).

2.6.3 Corrosion induced fracture from multiple rebars

A reinforced concrete structure with three rebars, shown in Figure 2.22, is analyzed next.

Only the region inside the red dash contour is shown in the following numerical results.

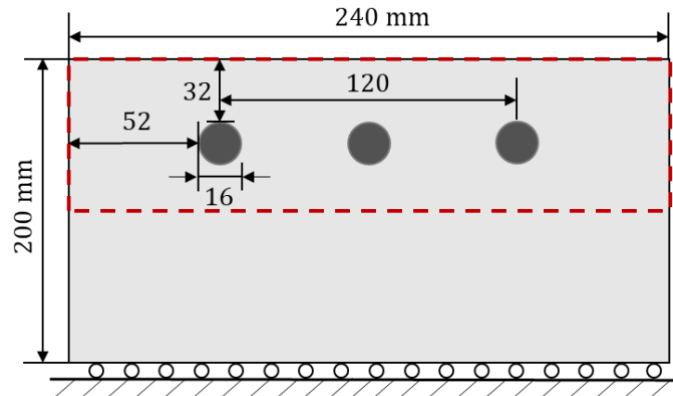


Figure 2.22. Geometry for the concrete structure with three rebars.

In order to determine the departures from vertical symmetry for the pressure profiles for the left and right bars (due to the corner effect), we use the diffusion-based model in [38, 93] to find the approximate corrosion patterns shown in Figure 2.28 (a). From the results shown in Figure 2.28 (b), the “tilt” in the corrosion pattern induced by the edge/corner effect is small but clear. Considering this, we choose the parameter μ in Eq. (2.10) to be $\pi + \gamma$ and $\pi - \gamma$ respectively for the two side rebars so that their corrosion patterns are tilted by γ and $-\gamma$ respectively towards the two sides of the structure (see Figure 2.23). The corrosion pattern shown in Figure 2.28 (b) is obtained by a simplified diffusion-corrosion model and thus may not be used directly to determine γ with high accuracy. Instead, we try several values for γ and observe the effects on fracture patterns.

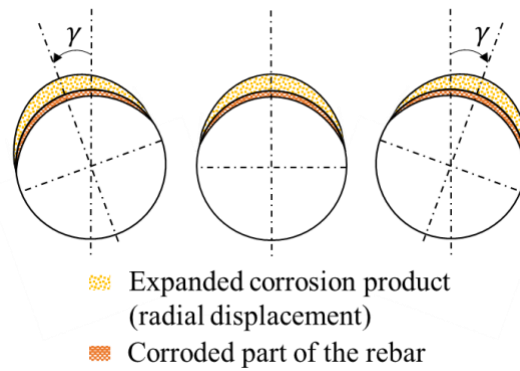


Figure 2.23. Corrosion pattern for three-rebar cases.



Figure 2.24. Experiment result of corrosion with three rebars (from [94]).

The fracture patterns from the experiments in [94] (corrosion process was accelerated with applied current) are shown in Figure 2.24. With tilt angles $\gamma = 0, \pi/18, \text{ and } \pi/8$, we obtain the results shown in Figure 2.25 (a), (b) and (c), respectively, with different k values. The PD results capture the merger of horizontal cracks observed in the experiment. Moreover, for $\gamma = \pi/18$ and $k = 20$, for example, two vertical cracks fully form, just like what was observed in the experiment. Unlike the case with one top-sided middle rebar, the fracture caused by the corrosion of multiple rebars is more complicated and is more sensitive to the microstructure of the concrete. Fracture patterns obtained with different realizations of IH-PD bond-structure are shown in Appendix D (Figure 2.33).

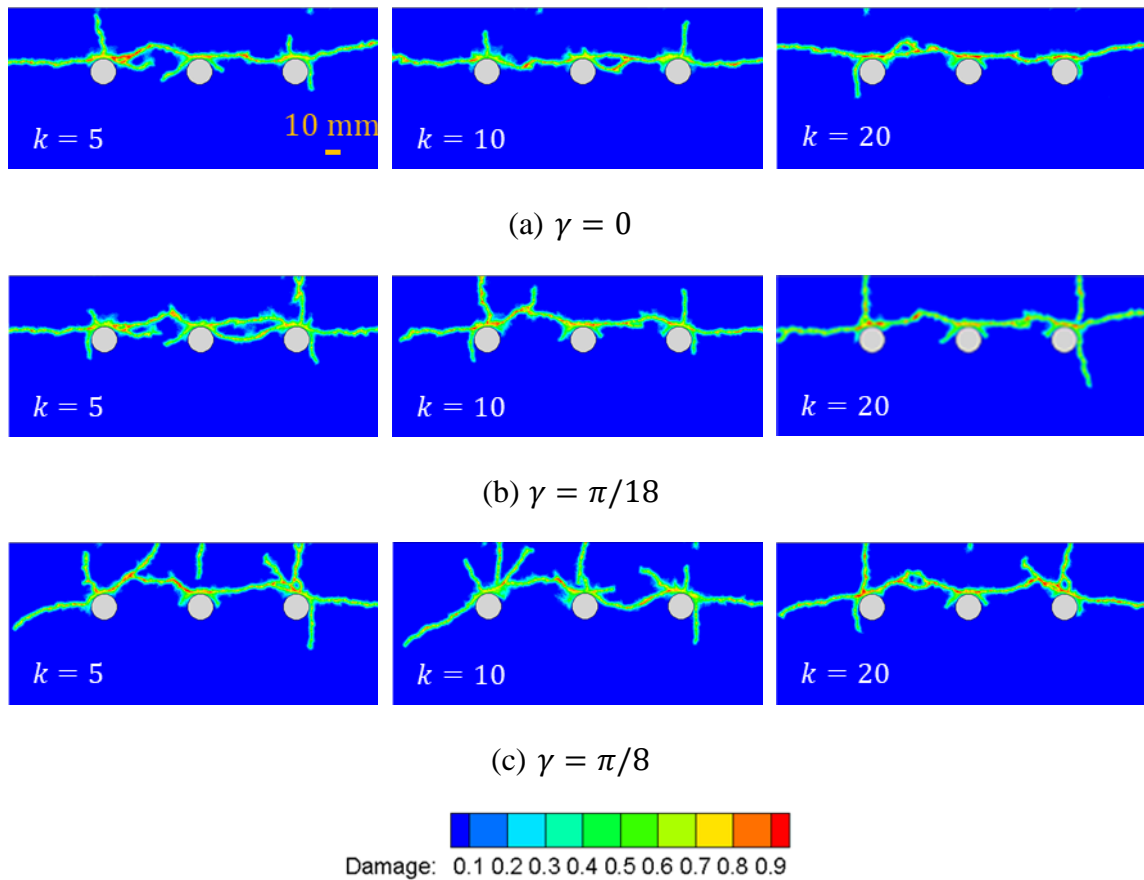


Figure 2.25. Fracture patterns for different tilt angles of the pressure profile on the side bars (angle γ) and different levels of non-uniformity in Eq. (2.10).

2.7 Conclusions

We introduced a 3-phase stochastic multiscale intermediately-homogenized peridynamic (IH-PD) model to study fracture in reinforced concrete due to non-uniform rebar corrosion. Different from traditional meso-scale heterogeneous models, our model only uses the volume fraction of different phases in the heterogeneous material. A simple constitutive model, linear-elastic with brittle failure, is used. We show and explain the reasons for which a fully homogenized peridynamic model leads to fracture patterns and failure evolution different from what is observed experimentally, while the new IH-PD model results match experimental observations very well. The model does not consider

details such as aggregate sizes and shapes, making the analysis much simpler/cheaper than that of models with explicit representation of the microstructure geometry, matching the computational cost of a fully homogenous model.

The corrosion product expansion around the rebar was approximated here by the “von Mises model” from the literature. This simplified the analysis. For a more accurate representation of pressures induced by corrosion product formation around the rebar, the current model could be coupled with an explicit corrosion model.

We tested the IH-PD model on concrete structures with a single or multiple rebars. The numerical results match well experimentally observed crack patterns as well as the sequence/evolution of their growth. We performed computations using several different stochastic realizations of the peridynamic bond structures and found that fracture patterns remain within the variability of features observed experimentally.

The IH-PD model succeeds in balancing the accuracy of fracture prediction in concrete from (expensive) models that use an explicit representation of aggregates, with the efficiency of homogeneous models. It can be used for larger scale modeling without losing the influence the microscale has on the failure behavior of the material.

Acknowledgments

This work was supported, in part, by the ONR project “Stress-Corrosion Cracking: the Importance of Damage Evolution in the Layer Affected by Corrosion” (program manager William Nickerson), the AFOSR MURI Center for Materials Failure Prediction through Peridynamics (program managers: Jaimie Tiley, Ali Sayir, David Stargel, and Fariba Fahroo), and by a Nebraska System Science award. This work was completed utilizing

the Holland Computing Center of the University of Nebraska, which receives support from the Nebraska Research Initiative.

Appendix A. Rebar corrosion patterns from diffusion of chlorides

To better understand how to apply the equivalent boundary conditions that would mimic the expansion of the corrosion products in the concrete rebar hole, we use the PD diffusion model [38, 93] to compute the diffusion of chloride into the concrete cover, estimate the regions in the rebar where the chloride concentration reaches a certain threshold and approximate the potential corrosion regions around of the rebar. Notice that the result obtained here is only used to help with the selection of radial displacement boundary conditions at the rebar hole surface. Once chloride concentration around the rebar reaches the threshold value [1, 2], the passive film covering the rebar is destroyed and the rebar corrodes. We can assume that the breaking of the passive film and corrosion of the rebar happen immediately since the time needed for this process is much shorter than that for the chloride to diffuse to the rebar. Here we only “mimic” the evolution of corrosion (with a simpler diffusion-only model). Of course, a full PD corrosion-damage simulation [39] could be used for a more precise analysis, but here we only need a rough approximation, given the uncertainties and variations in these types of problems. Note that we do not take into account the likely defects/pores at the rebar-concrete interface that affects this process in reality.

Because the PD diffusion model is nonlocal, we have three different options to judge when the chloride concentration at a point x reaches the threshold value:

1. if point x reaches the threshold;

2. if any of its family points reaches the threshold;
3. if half of its family points reach the threshold.

Here we use the third option (Figure 2.26), which takes a slightly longer time for the corrosion to happen, to compensate for the assumption that the passive film breaks immediately when the chloride content reaches the threshold value. When the horizon size is small enough compared to the rebar size (its diameter), there is little difference between the three options above. The boundary conditions for the concrete structure with a top-sided middle rebar are shown in Figure 2.26. The chloride penetrates the concrete from all edges of the concrete. The same boundary and initial conditions (zero concentration over the RC structure) are used for all other cases except for the last one with three rebars.

Diffusion/”corrosion” patterns obtained for different concrete structures are shown in Figure 2.27 and Figure 2.28. Modeling of corrosion processes as a diffusion-only process is a major simplification. However, the patterns obtained with this simplified model are sufficient to inform us about the possible spread of corrosion products.

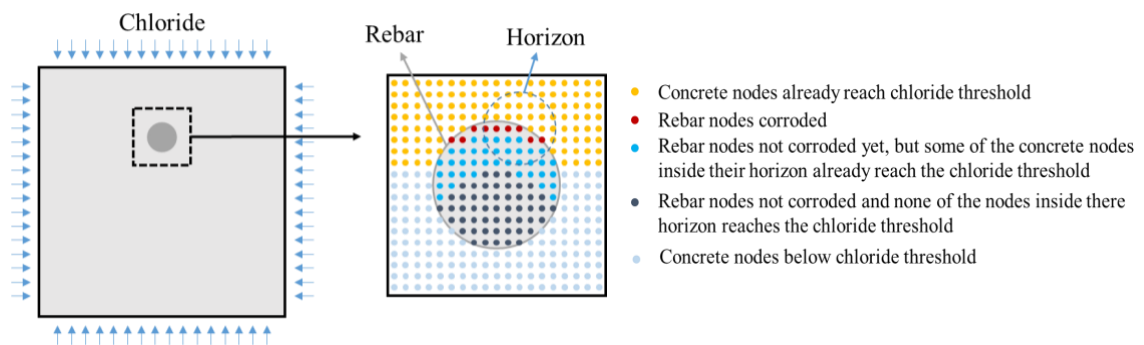


Figure 2.26. A zoom-in sketch of the concrete structure with a top-sided middle rebar under diffusion of chloride. A rebar node is “corroded” once half of its family nodes reach the critical chloride concentration.

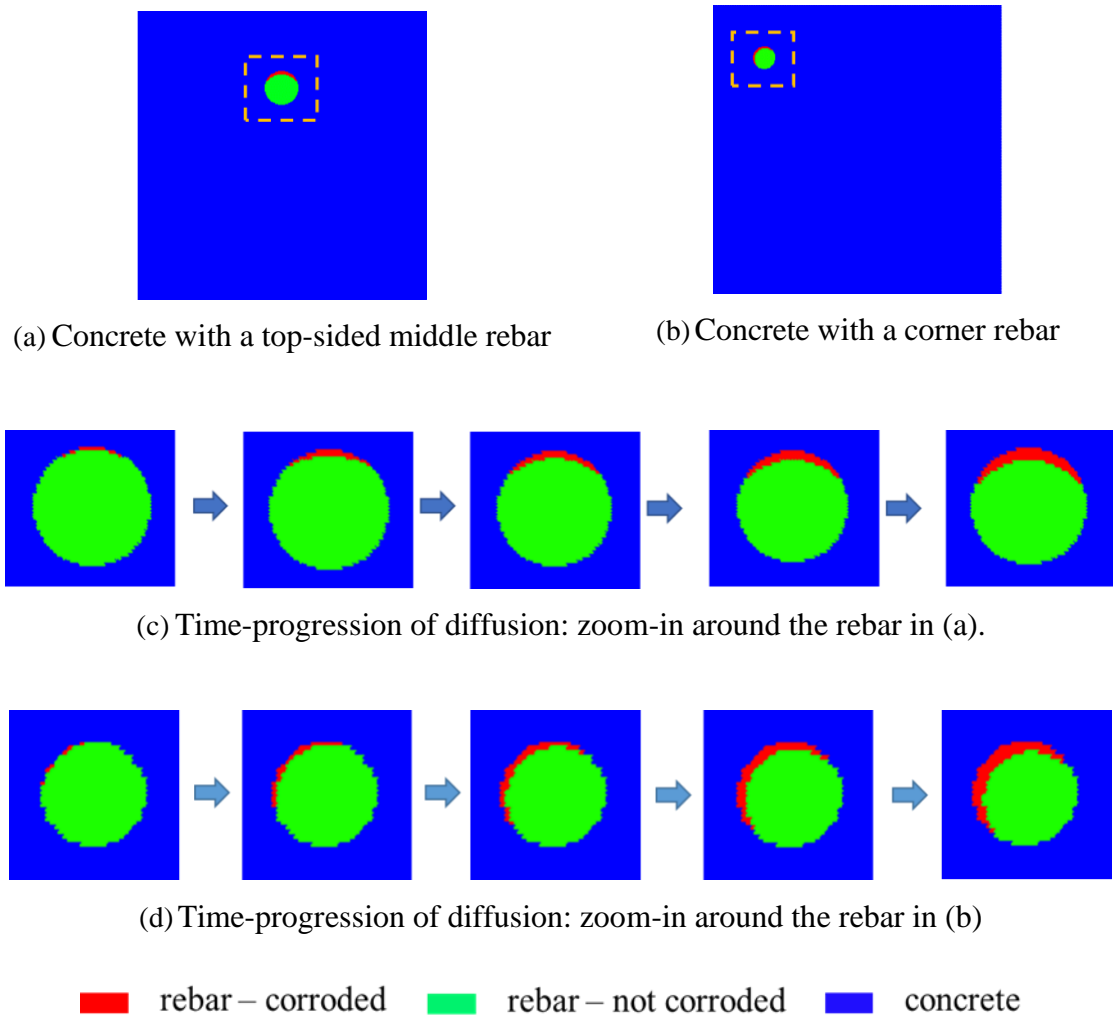


Figure 2.27. Computed diffusion/”corrosion” for rebars in two different concrete structures. Points in the rebars with a concentration larger than a threshold value are shown in red.

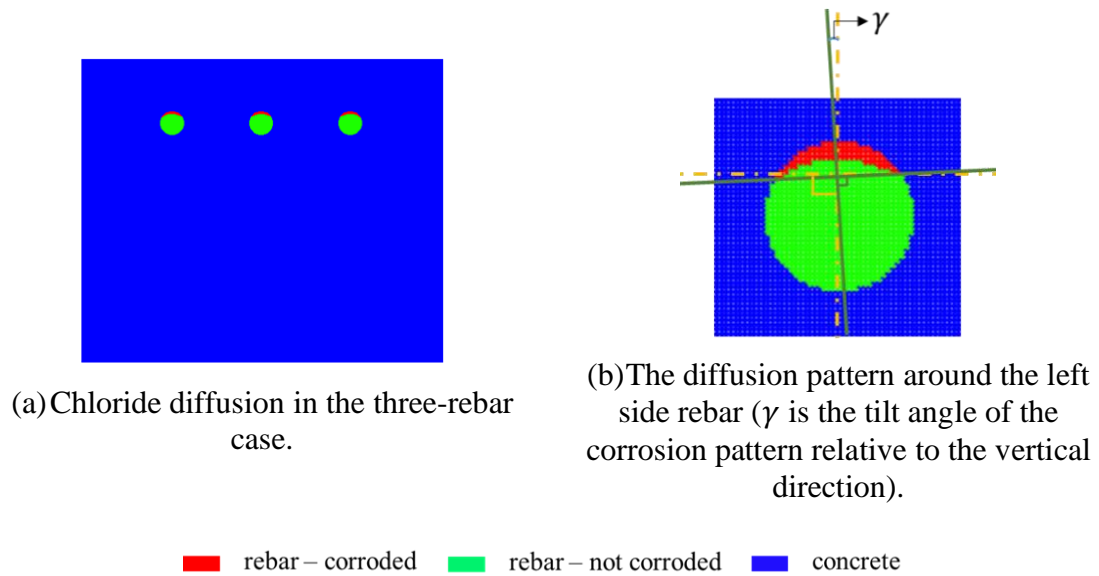


Figure 2.28. Points in the rebars with a concentration larger than a threshold value (shown in red) obtained from chloride diffusion (from the top surface only) for the concrete structure with three rebars.

Appendix B. Applying radial displacement at the rebar hole surface

As mentioned in Section 2.5, the simplest way to apply the radial displacement boundary condition is to incrementally increase the imposed displacements at each point around the rebar hole surface in multiple equal steps, assuming that the corrosion around the interface happens simultaneously. However, considering the fact that certain part of the rebar corrodes earlier than other parts, as shown in Figure 2.27, another option is to control the sequence of radial displacement at different locations around the rebar hole surface to mimic the evolution of the corrosion front (or corrosion products) around the rebar. To explain the idea, we only consider the right half of the rebar hole surface because of symmetry. As shown in Figure 2.29, the right half of the interface is evenly divided into n sectors. The incremental steps (total number of 100) at which these sectors are applied the radial displacements are shown in Figure 2.30. For boundary nodes in sector k , the radial displacement is applied evenly from t_{k-1} to t_n . We consider both

these options in Appendix D. Because the total radial displacement is very small (the concrete is very stiff), we can assume that the shape of the rebar hole surface is close to circular at all times, and therefore the direction of the radial displacement is always normal to the rebar hole surface.

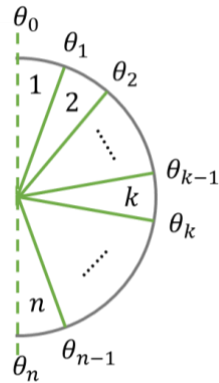


Figure 2.29. Rebar cross-section (half) is split into n equal sectors.

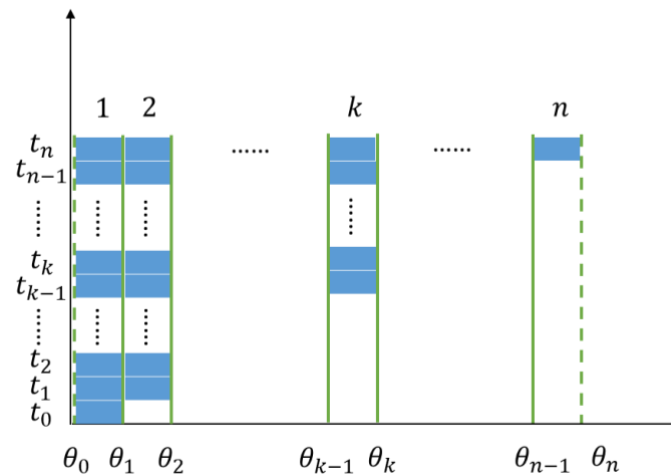


Figure 2.30. Applying radial displacements increments for different sectors around the rebar considering the evolution of the corrosion process. Radial displacement for each sector is applied incrementally during different time periods.

Appendix C. Parametric study on corrosion-induced pressure profiles

In real problems, due to the randomness of the microstructure of concrete, the corrosion-induced pressure profile around the rebar can take different shapes, which may lead to different fracture patterns in the concrete. Thus, it is necessary to try different shapes of corrosion distribution in our simulations. The parameter k in Eq. (2.10), expressing the level of non-uniformity in the pressure profile, is the main factor which affects the shape of the pressure distribution (imposed as applied displacements here) around the rebar. Here we test the influence different k values have on the fracture patterns obtained. We also study the influence the way incremental displacements are applied (as discussed in Section 2.5 and Appendix B) have on fracture patterns.

Fracture patterns for different k values are given in Figure 2.31, using the constant or sectorial implementation of imposed displacements around the rebar. We notice that the effects of the particular imposition of internal pressures are negligible. When k is small, four major cracks develop. As k increases, the pressure from corrosion products is more pronounced near the top of the rebar, and, as a result, there is less cracking around the rebar and the crack growing vertically down does not form when $k = 20$. All of these different fracture patterns, nevertheless, match well with the experimental results shown in Figure 2.12, which also exhibit three or four major cracks. Because of microstructure randomness in concrete and since the IH-PD model does not consider it explicitly, our goal was not to exactly match the experimental results, but to obtain the trends seen experimentally.

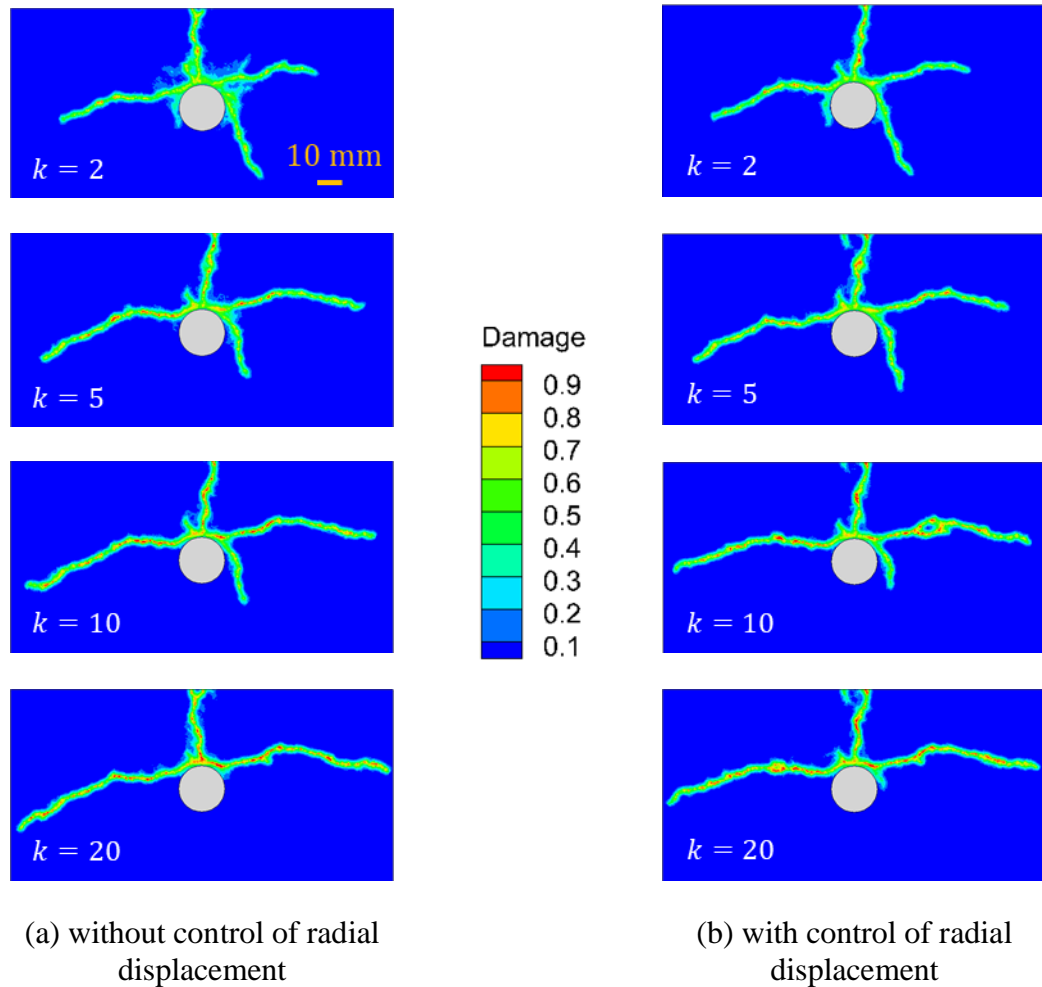


Figure 2.31. Fracture patterns with the IH-PD model for the concrete sample with a top-sided middle shown in Figure 2.9.

Appendix D. Influence of different realizations of the IH-PD material model

Different bond-scale realizations/bond-structures of the IH-PD model, due to the embedded randomness, lead to slightly different fracture patterns. Figure 2.32 gives four such results for the concrete structure with one top-sided middle rebar. The main fracture pattern features are reproduced in all cases, with some differences in the finer details. This is not unlike what is observed in experiments between different samples (see Figure 2.12).

Different realizations of bond-structure in the IH-PD models for the concrete structure with three rebars also give similar fracture patterns (see Figure 2.33). These results show that the randomness in the IH-PD model leads to results that are in the range of variability seen in experimental results.

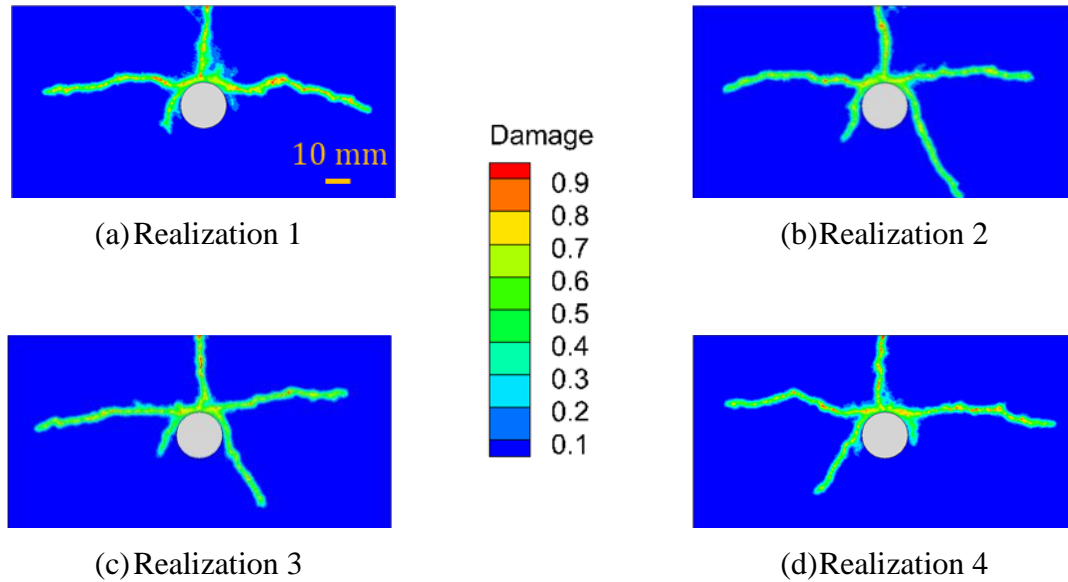


Figure 2.32. Fracture patterns obtained from different realizations of the bond-structure in the IH-PD model for the top-sided middle rebar geometry.

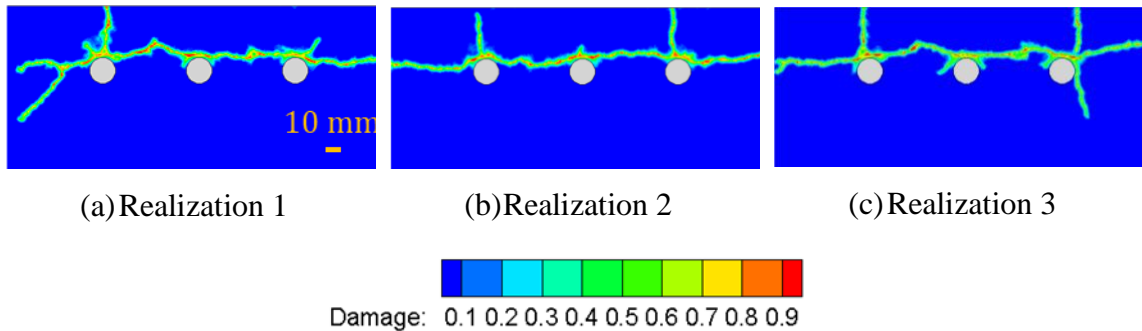


Figure 2.33. Fracture patterns for different realizations of IH-PD model for the three rebars example, with $\gamma = \pi/18$ and $k = 20$.

References

- [1] Tuutti K. Corrosion of steel in concrete. CBI forskning: Cement- och betonginst; 1982.
- [2] Bertolini L, Elsener B, Pedferri P, Redaelli E, Polder R. Corrosion of steel in concrete: prevention, diagnosis, repair. John Wiley & Sons; 2013.
- [3] Win PP, Watanabe M, Machida A. Penetration profile of chloride ion in cracked reinforced concrete. *Cement Concrete Res.* 2004;34:1073-9.
- [4] Poursae A, Hansson CM. The influence of longitudinal cracks on the corrosion protection afforded reinforcing steel in high performance concrete. *Cement Concrete Res.* 2008;38:1098-105.
- [5] Kato E, Kato Y, Uomoto T. Development of simulation model of chloride ion transportation in cracked concrete. *J Adv Concr Technol.* 2005;3:85-94.
- [6] Djerbi A, Bonnet S, Khelidj A, Baroghel-Bouny V. Influence of traversing crack on chloride diffusion into concrete. *Cement Concrete Res.* 2008;38:877-83.
- [7] Li SM, Chen ZG, Tan L, Bobaru F. Corrosion-induced embrittlement in ZK60A Mg alloy. *Mat Sci Eng a-Struct.* 2018;713:7-17.
- [8] Jones DA. Principles and prevention of corrosion: Macmillan; 1992.
- [9] Jang BS, Oh BH. Effects of non-uniform corrosion on the cracking and service life of reinforced concrete structures. *Cement Concrete Res.* 2010;40:1441-50.
- [10] Šavija B, Luković M, Pacheco J, Schlangen E. Cracking of the concrete cover due to reinforcement corrosion: A two-dimensional lattice model study. *Constr Build Mater.* 2013;44:626-38.
- [11] Bazant ZP. Physical model for steel corrosion in concrete sea structures-theory. *ASCE J Struct Div.* 1979;105:1137-53.
- [12] Balafas I, Burgoyne CJ. Modeling the structural effects of rust in concrete cover. *J ENG MECH.* 2010;137:175-85.
- [13] Ozbolt J, Orsanic F, Balabanic G. Modeling pull-out resistance of corroded reinforcement in concrete: Coupled three-dimensional finite element model. *Cement Concrete Comp.* 2014;46:41-55.
- [14] Ozbolt J, Orsanic F, Balabanic G, Kuster M. Modeling damage in concrete caused by corrosion of reinforcement: coupled 3D FE model. *Int J Fracture.* 2012;178:233-44.
- [15] Burnett DJ, Schreyer HL. A mesh objective method for modeling crack propagation using the smeared crack approach. *Int J Numer Meth Eng.* 2019;117:574-603.
- [16] Zhu X, Zi G. A 2D mechano-chemical model for the simulation of reinforcement corrosion and concrete damage. *Constr Build Mater.* 2017;137:330-44.
- [17] Cheng X, Su Q, Ma F, Liu X, Liang X. Investigation on crack propagation of concrete cover induced by non-uniform corrosion of multiple rebars. *Eng Fract Mech.* 2018;201:366-84.

- [18] Wang XF, Yang ZJ, Jivkov AP. Monte Carlo simulations of mesoscale fracture of concrete with random aggregates and pores: a size effect study. *Constr Build Mater.* 2015;80:262-72.
- [19] Xi X, Yang S, Li C-Q. A non-uniform corrosion model and meso-scale fracture modelling of concrete. *Cement Concrete Res.* 2018;108:87-102.
- [20] Xi X, Yang S, Li C-Q, Cai M, Hu X, Shipton ZK. Meso-scale mixed-mode fracture modelling of reinforced concrete structures subjected to non-uniform corrosion. *Eng Fract Mech.* 2018;199:114-30.
- [21] Du XL, Jin L, Zhang RB. Modeling the cracking of cover concrete due to non-uniform corrosion of reinforcement. *Corros Sci.* 2014;89:189-202.
- [22] Skarzynski L, Nitka M, Tejchman J. Modelling of concrete fracture at aggregate level using FEM and DEM based on X-ray mu CT images of internal structure. *Eng Fract Mech.* 2015;147:13-35.
- [23] Bazant ZP, Planas J. *Fracture and size effect in concrete and other quasibrittle materials*: CRC press; 1997.
- [24] Ozbolt J, Li YJ, Kozar I. Microplane model for concrete with relaxed kinematic constraint. *Int J Solids Struct.* 2001;38:2683-711.
- [25] Silling SA. Reformulation of elasticity theory for discontinuities and long-range forces. *J Mech Phys Solids.* 2000;48:175-209.
- [26] Bobaru F, Foster JT, Geubelle PH, Silling SA. *Handbook of peridynamic modeling*: CRC Press; 2016.
- [27] Warren TL, Silling SA, Askari A, Weckner O, Epton MA, Xu J. A non-ordinary state-based peridynamic method to model solid material deformation and fracture. *Int J Solids Struct.* 2009;46:1186-95.
- [28] Foster JT, Silling SA, Chen WW. Viscoplasticity using peridynamics. *Int J Numer Meth Eng.* 2010;81:1242-58.
- [29] Bobaru F, Hu W. The Meaning, Selection, and Use of the Peridynamic Horizon and its Relation to Crack Branching in Brittle Materials. *Int J Fracture.* 2012;176:215-22.
- [30] Silling SA, Askari A. *Peridynamic model for fatigue cracking*. SAND2014-18590 Albuquerque: Sandia National Laboratories. 2014.
- [31] Bobaru F, Zhang G. Why do cracks branch? A peridynamic investigation of dynamic brittle fracture. *Int J Fracture.* 2015;196:59-98.
- [32] Zhang G, Le Q, Loghin A, Subramaniyan A, Bobaru F. Validation of a peridynamic model for fatigue cracking. *Eng Fract Mech.* 2016;162:76-94.
- [33] Madenci E, Oterkus S. Ordinary state-based peridynamics for plastic deformation according to von Mises yield criteria with isotropic hardening. *J Mech Phys Solids.* 2016;86:192-219.
- [34] Silling SA, Parks ML, Kamm JR, Weckner O, Rassaian M. Modeling shockwaves and impact phenomena with Eulerian peridynamics. *Int J Impact Eng.* 2017;107:47-57.

- [35] Xu Z, Zhang G, Chen Z, Bobaru F. Elastic vortices and thermally-driven cracks in brittle materials with peridynamics. *Int J Fracture*. 2018;209:203-22.
- [36] Wang YT, Zhou XP, Kou MM. A coupled thermo-mechanical bond-based peridynamics for simulating thermal cracking in rocks. *Int J Fracture*. 2018;211:13-42.
- [37] Mehrmashhadi J, Wang L, Bobaru F. Uncovering the dynamic fracture behavior of PMMA with peridynamics: The importance of softening at the crack tip. *Eng Fract Mech*. 2019;219:106617.
- [38] Bobaru F, Duangpanya M. A peridynamic formulation for transient heat conduction in bodies with evolving discontinuities. *J Comput Phys*. 2012;231:2764-85.
- [39] Chen ZG, Bobaru F. Peridynamic modeling of pitting corrosion damage. *J Mech Phys Solids*. 2015;78:352-81.
- [40] Zhao JM, Chen ZG, Mehrmashhadi J, Bobaru F. Construction of a peridynamic model for transient advection-diffusion problems. *Int J Heat Mass Tran*. 2018;126:1253-66.
- [41] Jafarzadeh S, Chen Z, Bobaru F. Peridynamic Modeling of Repassivation in Pitting Corrosion of Stainless Steel. *Corrosion*. 2018;74:393-414.
- [42] Jafarzadeh S, Chen Z, Bobaru F. Peridynamic Modeling of Intergranular Corrosion Damage. *J Electrochem Soc*. 2018;165:C362-C74.
- [43] Jafarzadeh S, Chen Z, Zhao J, Bobaru F. Pitting, lacy covers, and pit merger in stainless steel: 3D peridynamic models. *Corros Sci*. 2019;150:17-31.
- [44] Li W, Guo L. A mechanical-diffusive peridynamics coupling model for meso-scale simulation of chloride penetration in concrete under loadings. *Constr Build Mater*. 2020;241:118021.
- [45] Jafarzadeh S, Chen ZG, Li SM, Bobaru F. A peridynamic mechano-chemical damage model for stress-assisted corrosion. *Electrochim Acta*. 2019;323.
- [46] De Meo D, Diyaroglu C, Zhu N, Oterkus E, Siddiq MA. Modelling of stress-corrosion cracking by using peridynamics. *International Journal of Hydrogen Energy*. 2016;41:6593-609.
- [47] Silling SA, Askari E. A meshfree method based on the peridynamic model of solid mechanics. *Comput Struct*. 2005;83:1526-35.
- [48] Gerstle W, Sau N, Silling S. Peridynamic modeling of plain and reinforced concrete structures. In: 18th International Conference on Structural Mechanics in Reactor Technology (SMiRT 18), Beijing, China, SMiRT18-B01-2. 2005.
- [49] Gerstle W, Sau N, Silling S. Peridynamic modeling of concrete structures. *Nucl Eng Des*. 2007;237:1250-8.
- [50] Yaghoobi A, Chorzepa MG. Fracture analysis of fiber reinforced concrete structures in the micropolar peridynamic' analysis framework. *Eng Fract Mech*. 2017;169:238-50.

- [51] Lammi CJ, Vogler TJ. A nonlocal peridynamic plasticity model for the dynamic flow and fracture of concrete. Report SAND2014-18257, Sandia National Laboratories. 2014.
- [52] Yang D, Dong W, Liu X, Yi S, He X. Investigation on mode-I crack propagation in concrete using bond-based peridynamics with a new damage model. *Eng Fract Mech.* 2018;199:567-81.
- [53] Anderson TL. *Fracture mechanics: fundamentals and applications*: CRC press; 2017.
- [54] Chen ZG, Niazi S, Bobaru F. A peridynamic model for brittle damage and fracture in porous materials. *Int J Rock Mech Min.* 2019;122.
- [55] Mehrmashhadi J, Chen Z, Zhao J, Bobaru F. A Stochastically Homogenized Peridynamic Model for Intraply Fracture in Fiber-Reinforced Composites. *Composite Science and Technology.* 2019;182:107770.
- [56] Li W, Guo L. Meso-fracture simulation of cracking process in concrete incorporating three-phase characteristics by peridynamic method. *Constr Build Mater.* 2018;161:665-75.
- [57] Delale F, Erdogan F. The Crack Problem for a Nonhomogeneous Plane. *Journal of Applied Mechanics.* 1983;50:609-14.
- [58] Chen Z, Niazi S, Zhang G, Bobaru F. Peridynamic Functionally Graded and Porous Materials: Modeling Fracture and Damage. *Handbook of Nonlocal Continuum Mechanics for Materials and Structures.* 2017:1-35.
- [59] Chen ZG, Bakenhus D, Bobaru F. A constructive peridynamic kernel for elasticity. *Comput Method Appl M.* 2016;311:356-73.
- [60] Ha YD, Bobaru F. Studies of dynamic crack propagation and crack branching with peridynamics. *Int J Fracture.* 2010;162:229-44.
- [61] Bobaru F. Influence of van der Waals forces on increasing the strength and toughness in dynamic fracture of nanofibre networks: a peridynamic approach. *Model Simul Mater Sc.* 2007;15:397-417.
- [62] Chen X, Gunzburger M. Continuous and discontinuous finite element methods for a peridynamics model of mechanics. *Comput Method Appl M.* 2011;200:1237-50.
- [63] Macek RW, Silling SA. Peridynamics via finite element analysis. *Finite Elem Anal Des.* 2007;43:1169-78.
- [64] Kilic B, Madenci E. Coupling of Peridynamic Theory and the Finite Element Method. *J Mech Mater Struct.* 2010;5:707-33.
- [65] Liu WY, Hong JW. A coupling approach of discretized peridynamics with finite element method. *Comput Method Appl M.* 2012;245:163-75.
- [66] Jafarzadeh S, Larios A, Bobaru F. Efficient Solutions for Nonlocal Diffusion Problems Via Boundary-Adapted Spectral Methods. *Journal of Peridynamics and Nonlocal Modeling.* 2020.

- [67] Hu W, Wang Y, Yu J, Yen C-F, Bobaru F. Impact damage on a thin glass plate with a thin polycarbonate backing. *Int J Impact Eng.* 2013;62:152-65.
- [68] Bobaru F, Ha YD. Adaptive Refinement and Multiscale Modeling in 2d Peridynamics. *Int J Multiscale Com.* 2011;9:635-59.
- [69] Henke SF, Shanbhag S. Mesh sensitivity in peridynamic simulations. *Comput Phys Commun.* 2014;185:181-93.
- [70] Gu X, Zhang Q, Xia X. Voronoi-based peridynamics and cracking analysis with adaptive refinement. *Int J Numer Meth Eng.* 2017;112:2087-109.
- [71] Seleson P. Improved one-point quadrature algorithms for two-dimensional peridynamic models based on analytical calculations. *Comput Method Appl M.* 2014;282:184-217.
- [72] Polak E, Ribiere G. Note sur la convergence de méthodes de directions conjuguées. *Revue française d'informatique et de recherche opérationnelle Série rouge.* 1969;3:35-43.
- [73] Hu Y, Storey C. Global convergence result for conjugate gradient methods. *J Optim Theory Appl.* 1991;71:399-405.
- [74] Kilic B, Madenci E. An adaptive dynamic relaxation method for quasi-static simulations using the peridynamic theory. *Theor Appl Fract Mec.* 2010;53:194-204.
- [75] Prakash N, Seidel GD. Computational electromechanical peridynamics modeling of strain and damage sensing in nanocomposite bonded explosive materials (NCBX). *Eng Fract Mech.* 2017;177:180-202.
- [76] Le QV, Chan WK, Schwartz J. A two-dimensional ordinary, state-based peridynamic model for linearly elastic solids. *Int J Numer Meth Eng.* 2014;98:547-61.
- [77] Mehrmashhadi J, Tang Y, Zhao X, Xu Z, Pan JJ, Le QV, et al. The Effect of Solder Joint Microstructure on the Drop Test Failure—A Peridynamic Analysis. *IEEE T Comp Pack Man.* 2019;9:58-71.
- [78] Van Mier JG. *Fracture processes of concrete*: CRC press; 2017, Chapter 2, p49.
- [79] Rao GA, Prasad BKR. Influence of type of aggregate and surface roughness on the interface fracture properties. *Mater Struct.* 2004;37:328-34.
- [80] Bobaru F, Yang MJ, Alves LF, Silling SA, Askari E, Xu JF. Convergence, adaptive refinement, and scaling in 1D peridynamics. *Int J Numer Meth Eng.* 2009;77:852-77.
- [81] Tran KK, Nakamura H, Kawamura K, Kunieda M. Analysis of crack propagation due to rebar corrosion using RBSM. *Cement Concrete Comp.* 2011;33:906-17.
- [82] Du YG, Chan AHC, Clark LA. Finite element analysis of the effects of radial expansion of corroded reinforcement. *Comput Struct.* 2006;84:917-29.
- [83] Michel A, Pease BJ, Peterova A, Geiker MR, Stang H, Thybo AEA. Penetration of corrosion products and corrosion-induced cracking in reinforced cementitious materials: Experimental investigations and numerical simulations. *Cement Concrete Comp.* 2014;47:75-86.

- [84] Le Q, Bobaru F. Surface corrections for peridynamic models in elasticity and fracture. *Comput Mech.* 2018;61:499-518.
- [85] Mengesha T, Du Q. The bond-based peridynamic system with Dirichlet-type volume constraint. *P Roy Soc Edinb A.* 2014;144:161-86.
- [86] Amalia Z, Qiao D, Nakamura H, Miura T, Yamamoto Y. Development of simulation method of concrete cracking behavior and corrosion products movement due to rebar corrosion. *Constr Build Mater.* 2018;190:560-72.
- [87] John R, Shah SP. Mixed-Mode Fracture of Concrete Subjected to Impact Loading. *J Struct Eng-Asce.* 1990;116:585-602.
- [88] Ren WY, Yang ZJ, Sharma R, Zhang C, Withers PJ. Two-dimensional X-ray CT image based meso-scale fracture modelling of concrete. *Eng Fract Mech.* 2015;133:24-39.
- [89] Ren HL, Zhuang XY, Cai YC, Rabczuk T. Dual-horizon peridynamics. *Int J Numer Meth Eng.* 2016;108:1451-76.
- [90] Nguyen QT, Millard A, Caré S, L'Hostis V, Berthaud Y. Fracture of concrete caused by the reinforcement corrosion products. *Journal de Physique IV (Proceedings): EDP sciences; 2006.* p. 109-20.
- [91] Xi X, Yang S. Time to surface cracking and crack width of reinforced concrete structures under corrosion of multiple rebars. *Constr Build Mater.* 2017;155:114-25.
- [92] Fischer C. Auswirkungen der Bewehrungskorrosion auf den Verbund zwischen Stahl und Beton. 2012.
- [93] Bobaru F, Duangpanya M. The peridynamic formulation for transient heat conduction. *Int J Heat Mass Tran.* 2010;53:4047-59.
- [94] Dong W, Murakami Y, Oshita H, Suzuki S, Tsutsumi T. Influence of Both Stirrup Spacing and Anchorage Performance on Residual Strength of Corroded RC Beams. *J Adv Concr Technol.* 2011;9:261-75.

Chapter 3 A Peridynamic Model for Galvanic Corrosion and Fracture

3.1 Introduction

Corrosion induced by galvanic coupling can cause deep and rough trenches at the material interface, leading to dangerous situations like other types of localized corrosion, such as pitting corrosion. As stresses rise at these locations, cracks can easily initiate and grow catastrophically. Efficient and accurate predictions of galvanic corrosion problems can help evaluate their effect on engineering structures and provide insights on solutions to prevent it. Due to the simultaneous influence of multiple physical mechanisms involved in galvanic corrosion, computational models are necessary for this purpose. A comparison between different computational models for corrosion can be found in [1]. Major recent advances in galvanic corrosion modeling comes with models based on finite element method (FEM) [2–4] or phase field (PF) method [5,6].

A FEM-based model was developed for galvanic corrosion using the commercial software COMSOL MultiPhysics® (COMSOL hereafter) [2] and validated against the experimental results in [3]. For the galvanic couple between steel and magnesium alloy, although the initial current density and the final corrosion depth obtained by the model have similar patterns to the measured data, the maximum current density and corrosion depth, as well as the transition across the material interface, present nontrivial deviations from the experimental data. A similar model was used in [4] to investigate the effect of mechanical loading on the galvanic corrosion behavior by including stress/strain-dependent electric potential. However, the corrosion pattern obtained by this model, when the mechanical loading is absent, agree even less with those from the experiments

shown in [3]. This deviation possibly comes from the linear, instead of piecewise linear, fitting of the polarization curve. The authors of [4] also studied crack initiation in the galvanic couple under uniaxial tension loading by computing the stress intensity factor, approximating the specimen as a side edge notched tensile specimen. As the corrosion front progresses, it departs from such an idealization of the geometry, and these approximations may not be sufficiently accurate. Corrosion depths closer to experimental observations in [3] were obtained in [7][8] by taking into account the effect of corrosion deposition on the corrosion rate.

A PF model for corrosion in galvanic couples was introduced in [5]. However, in the simulation results, the current density distribution does not match well a reference solution given by the FEM-based COMSOL simulation [3]. In addition, the corrosion depth at the junction of the galvanic couple deviates from experimental observation [3] significantly. A different PF model was developed in [6] and was verified against a FEM-based model built in COMSOL, but the polarization was neglected along the corroding interface and no validation tests against experimental data were presented.

One notes that, for these FEM-based /PF models, when corrosion happens at the interface between two joined metal parts, an artificial step-down on the anode side needs to be introduced because of mathematical and numerical inconsistencies [5,6]. As we shall see, in the absence of such a step, an incorrect evolution of the corrosion front is obtained (see discussion in Section 3.4.2 below). Determining a proper height of this artificial step has not been examined in the published literature. Moreover, with these models based on partial differential equations (PDEs), there is, so far, no attempt to couple galvanic corrosion in a couple with that of crack initiation and propagation. This is partly due to

difficulties in being able to simulate the complex interactions of these two critical mechanisms: singularities (in classical models), moving-boundary problem, arbitrary geometries, etc.

Recently, the peridynamic (PD) method has been applied to corrosion modeling [9,10]. PD models view corrosion as material damage caused by the dissolution of metal into the electrolyte, coupled with the diffusion of metal ions in the electrolyte [9,10]. A concentration-dependent damage index monitors the evolving corrosion front (phase changes from solid to electrolyte) and the gradual changes in material degradation across the Diffusion-based Corrosion Layer (DCL) [9]. This provides us a better understanding of the factors that lead to the degradation of mechanical properties (strength, ductility, etc.) observed in corroded samples. The PD model has been especially advantageous in simulating stress-corrosion cracking, as shown in the results for pit-to-crack transition obtained in [11].

The existing PD corrosion models, however, use an important simplification: for activation-controlled corrosion, one assumes a constant potential along the corrosion front. The constant potential determines a constant current density from the polarization curve which is measured experimentally. This approach avoids solving for the electric potential distribution along the corrosion front and is acceptable for pitting corrosion cases in which the potential distribution (and therefore the current density) along the pit surface is close to uniform [12]. To cover situations like salt layer formation or passivation at the corrosion front when diffusion-controlled conditions dominate (and the potential distribution varies significantly along the corrosion front), the existing PD models include concentration-based rules that can cause pausing/stopping of metal

dissolution as specific locations along the corrosion front [10,13], effectively leading to non-uniform corrosion rates (even if the input corrosion rate is constant). Under activation-controlled conditions, however, these mechanisms are not triggered, and the existing PD corrosion models would not apply to galvanic corrosion problems [14], in which activation-controlled conditions are critical and the electric potential (or the corrosion rate) varies significantly along the corrosion front. Moreover, these variations can also change drastically as the corrosion front evolves. This is the reason why one needs to compute the distribution of the electric potential along the corrosion front in order to predict the evolution of galvanic corrosion.

For galvanic corrosion problems, FEM-based and PF models first evaluate the electric potential by solving the Laplace's/Poisson's equation, with the boundary condition (BC) given by the corresponding metals'/alloys' polarization curves (Tafel's equations). The electric potential determines the current density, which is related to corrosion rate by Faraday's law [2,6,15]. Following a similar procedure, in this paper we introduce a PD electric potential model, and couple it with the existing PD corrosion model [10]. This model is an important extension compared with the previous PD model and will be applicable to a larger class of corrosion problems, including galvanic corrosion. When solving for the electric potential, in order to apply the nonlinear Robin BCs at the arbitrarily-shaped corrosion front and reduce the PD surface effect in the PD electric potential solver, we use a recently introduced autonomous fictitious nodes method (FNM) ([16]).

In addition to introducing the PD electrostatic solver to compute the electric potential, we reformulate the PD corrosion dissolution model in [9,10] based on electrochemistry, and

replace the previous numerical calibration stage (which required a trial solution in the pre-processing step) with an analytical one. By eliminating the numerical calibration, the model is significantly more efficient in problems with highly non-uniform current densities along an arbitrary-shape corroding surface, which is often the case in galvanic corrosion problems. The damage-dependent corrosion model used in the original PD corrosion model in [9] is no longer needed. The new model eliminates the required (in order to match the experimental observations) artificial changes to the given geometry of a galvanic couple in models based on PDEs (e.g., COMSOL, phase-field).

We verify the new model for a uniform corrosion 2D case against a classical analytical solution in terms of the electric potential and current density at the beginning of the corrosion process, as well as the evolution of the corrosion depth in time. The model is validated against experimental galvanic corrosion results available in the literature for a mild steel-AE44 galvanic couple. The results for the initial current density distribution and final corrosion profile are also compared with those from a model built using COMSOL. A coupled corrosion-fracture problem is solved to show the potential of the new PD model in resolving failure caused by the combination of sharp corrosion damage (induced by galvanic corrosion) and mechanical loading.

3.2 Kinetics of galvanic corrosion

In galvanic corrosion, the metal/alloy with lower corrosion potential is the anode and corrodes first. The ordering of corrosion potential (the galvanic series) for metals/alloys, for a specific environment, is determined from experiments (see pages 171-172 in [17]). However, the galvanic series only gives information about the corrosion tendency. The actual corrosion rates of the anode must be determined by separate experiments and the

mixed potential theory by overlaying the polarization curves of the constituent individual metals/alloys [2], as schematically shown in Figure 3.1.

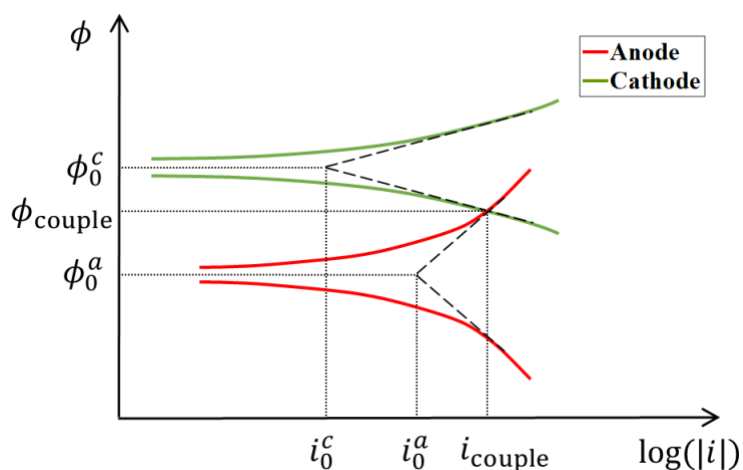


Figure 3.1. Schematic polarization curves of anode and cathode in a galvanic couple (see page 177 in [17]). ϕ_0^c and ϕ_0^a are the uncoupled corrosion potential and i_0^c and i_0^a are the uncoupled exchange current density for the cathode and anode, respectively.

ϕ_{couple} and i_{couple} are the coupled corrosion potential and current density, respectively.

Electrochemical polarization is the change in electrode potential due to the flow of current (see page 127 in [14]). When the overpotential is small, the corrosion process is activation controlled. In this corrosion type, the current density is governed by Tafel's law:

$$i_a = i_0 \times 10^{\frac{\phi - \phi_0}{\beta}} \quad (3.1)$$

where i_0 is the uncoupled exchange current density, ϕ is the electrode potential, ϕ_0 is the uncoupled corrosion potential and β is the geometric slope of the linear portion of the semi-logarithmic plot of the polarization curve.

When the overpotential is large, the resulting high anodic dissolution rate saturates the electrolyte near the anode surface, and the corrosion process becomes diffusion

controlled. In this case, the current density is determined by concentration changes in reactants or products near an electrode surface. Between these two corrosion types, there exists a transition corrosion type called IR controlled corrosion which is caused by resistance of the electrolyte to the current flow. It happens because there is a finite distance between the reference electrode and the metal surface to be investigated (see pages 130-131 in [14]). There are other factors which can affect the corrosion rate, such as the pH field, temperature field, formation of corrosion products, etc. In real corrosion problems, the corrosion rate is simultaneously influenced by multiple factors and can be determined from the polarization curve measured from corresponding experiments.

For the computational modeling of galvanic corrosion in this work, we focus on the anodic reaction (metal dissolution). The cathodic reaction and the mass transfer in the electrolyte will not be included. Consider an anodic reaction: $M \rightarrow M^{q+} + qe^-$, the current density is formulated by Eq. (3.1) in which the unknown coefficients are determined by the polarization curve obtained from experiments.

Note that i_a scales linearly with the magnitude of the molar dissolution flux ($|\mathbf{J}_{\text{diss}}|$) at the corrosion front via Faraday's law [18]:

$$i_a = qF|\mathbf{J}_{\text{diss}}|. \quad (3.2)$$

where q is the charge number and F is the Faraday's constant. To use Eq. (3.1) to determine the distribution of current density at the electrode surface, we have to solve for the potential distribution in the electrolyte domain. The electrostatic field satisfies the following Poisson equation [19,20]:

$$\nabla^2 \phi = \frac{\rho}{\varepsilon_0} = \frac{\dot{\rho}}{\sigma} \quad (3.3)$$

where ϕ is the electric potential, ρ is the charge density, ε_0 and σ are the electric permittivity and conductivity of the medium, respectively. For problems in this work, electroneutrality is satisfied in the electrolyte domain, therefore, Poisson's equation reduces to the Laplace's equation:

$$\nabla^2 \phi = 0. \quad (3.4)$$

Rather than using this classical model (Laplace's equation) to approximate the electric potential in the electrolyte for the examples shown in Section 3.4, we will use the corresponding nonlocal (PD) version of this equation because it will be easier to couple it with the mechanical PD model that we seek to employ for simulating the corrosion and fracture of the sample exposed to galvanic conditions and mechanical loadings. The PD model for the electrostatic solver is given in Section 3.3.2.1.

3.3 A coupled PD model for electric potential-driven corrosion and fracture

The PD theory is a nonlocal extension of the classical continuum mechanics [21]. The PD formulation is in the form of integro-differential equations (IDEs) rather than PDEs used in classical local theories. In PD models, discontinuities such as cracks/damages can initiate and propagate naturally and autonomously [22–25]. While the PD method has been primarily used to deal with mechanical behaviors [22,24,26–29], it has also been employed in diffusion-type problems involving cracks and damage, including thermal diffusion [30–33] and mass transport (e.g. corrosion) [1,9,10,13,34–36].

Consider a PD body occupying the domain $\Omega \in \mathbb{R}^k$, $k = 2$ or 3 , in which a point $\mathbf{x} \in \Omega$ interacts with points $\hat{\mathbf{x}} \in \Omega \setminus \mathbf{x}$ in a neighborhood $H_{\mathbf{x}}$ (called the horizon region of \mathbf{x} , usually selected to be a disk in 2D, sphere in 3D, centered at \mathbf{x}). The radius of $H_{\mathbf{x}}$ is called the horizon size (or simply, the horizon) and denoted by δ . Objects that carry the pairwise nonlocal interactions between points are called bonds. Figure 3.2 schematically shows a PD body with a generic point \mathbf{x} , its family and its horizon.

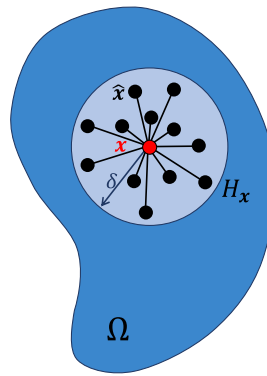


Figure 3.2. Nonlocal interaction between point \mathbf{x} and an arbitrary point located in the horizon of \mathbf{x} .

In this section we first briefly review the PD mechanical (for fracture) model and then introduce an extended PD corrosion model. Finally, we show how these models are coupled together into a PD corrosion-fracture model. For further discussion on the model the following definitions for solid and liquid domains are useful:

$$\begin{aligned}
 \Omega_s(t) &= \{\mathbf{x} \in \Omega | C(\mathbf{x}, t) > C_{\text{sat}}\} \\
 \Omega_{\text{diss}}(t) &= \{\mathbf{x} \in \Omega | C_{\text{sat}} < C(\mathbf{x}, t) < C_{\text{solid}}\} \\
 \Omega_l(t) &= \{\mathbf{x} \in \Omega | C(\mathbf{x}, t) \leq C_{\text{sat}}\}
 \end{aligned} \tag{3.5}$$

where C_{solid} refers to the concentration of metal atoms in the intact solid phase, and C_{sat} is the saturation value for dissolved metal atoms in electrolyte.

3.3.1 Bond-based PD mechanical model

The equations of motion for the bond-based PD mechanical model, at each $\mathbf{x} \in \Omega_s$, can be written as [22]:

$$\rho(\mathbf{x})\ddot{\mathbf{u}}(\mathbf{x}, t) = \int_{H_{\mathbf{x}} \cap \Omega_s} \mathbf{f}(\mathbf{u}(\hat{\mathbf{x}}, t) - \mathbf{u}(\mathbf{x}, t), \hat{\mathbf{x}} - \mathbf{x}) dV_{\hat{\mathbf{x}}} + \mathbf{b}(\mathbf{x}, t) \quad (3.6)$$

where t is the time, ρ is the density field, \mathbf{u} is the displacement vector field, \mathbf{f} is the pairwise force in the PD bond $\mathbf{x} - \hat{\mathbf{x}}$, and \mathbf{b} is the body force field. $dV_{\hat{\mathbf{x}}}$ is the volume (area in 2D, length in 1D) associated with $\hat{\mathbf{x}}$ that is covered by $H_{\mathbf{x}}$. The pairwise force for a prototype micro-elastic brittle material is defined as [22]:

$$\mathbf{f} = cs\mu \frac{\boldsymbol{\xi} + \boldsymbol{\eta}}{\|\boldsymbol{\xi} + \boldsymbol{\eta}\|} \quad (3.7)$$

where $\boldsymbol{\xi} = \hat{\mathbf{x}} - \mathbf{x}$ is the relative position of $\hat{\mathbf{x}}$ and \mathbf{x} in the reference configuration, $\boldsymbol{\eta} = \mathbf{u}(\hat{\mathbf{x}}, t) - \mathbf{u}(\mathbf{x}, t)$ is the relative displacement with respect to the reference configuration, c is the micro-modulus function or the elastic stiffness of the bond which can take different forms depending on the required horizon-scale behavior [37], $s = \frac{\|\boldsymbol{\xi} + \boldsymbol{\eta}\| - \|\boldsymbol{\xi}\|}{\|\boldsymbol{\xi}\|}$ is the relative deformation or bond strain. PD bonds break when they reach the critical relative deformation s_0 and the state of a bond is tracked by the bond damage factor μ as [22]:

$$\mu(\mathbf{x}, \hat{\mathbf{x}}, t) = \begin{cases} 1 & \text{if } s(\mathbf{x}, \hat{\mathbf{x}}, t') < s_0 \text{ for all } 0 \leq t' \leq t \\ 0 & \text{otherwise} \end{cases} \quad (3.8)$$

which means once a bond breaks, it does not carry bond force anymore. With the breakage of bonds, failure starts to accumulate, and cracks begin to initiate and propagate. The damage index d is used to measure the damage level at a point:

$$d(\mathbf{x}, t) = 1 - \frac{\int_{H_x} \mu(\hat{\mathbf{x}}, \mathbf{x}, t) dV_{\hat{\mathbf{x}}}}{\int_{H_x} dV_{\hat{\mathbf{x}}}}. \quad (3.9)$$

After spatial discretization, $d(\mathbf{x}, t)$ is the ratio of the number of broken bonds to that of total bonds connected to point \mathbf{x} at time t . When all bonds connected to point \mathbf{x} are broken, $d(\mathbf{x}, t) = 1$ and point \mathbf{x} becomes a free point. In this work, we consider the constant micro-modulus function [27]. For plane stress conditions, we have $c = \frac{9E}{\pi\delta^3}$ and

$$s_0 = \sqrt{\frac{4\pi G_0}{9E\delta}} \quad (E \text{ and } G_0 \text{ are Young's modulus and energy release rate, respectively), \text{ while}$$

$$\text{for plane strain conditions, we have } c = \frac{48E}{5\pi\delta^3} \text{ and } s_0 = \sqrt{\frac{5\pi G_0}{12E\delta}}.$$

For mechanical equilibrium problems with no body forces, but in which damage may evolve in time because of corrosion, Eq. (3.6) becomes:

$$\int_{H_x} \mathbf{f}(\mathbf{u}(\hat{\mathbf{x}}, t) - \mathbf{u}(\mathbf{x}, t), \hat{\mathbf{x}} - \mathbf{x}) dV_{\hat{\mathbf{x}}} = 0 \quad (3.10)$$

where t is the time when equilibrium is tested/enforced after a certain evolution of the corrosion process. Appropriate conditions on the boundaries (volume constraints) have to be assigned to this equation for specific problems. In many cases, it is convenient to enforce these nonlocal BCs to approximate as close as possible the local BCs one would

use in a classical model. For each of the examples solved below we describe these conditions in detail.

3.3.2 PD corrosion model

Corrosion is the result of an electrochemical process. In the presence of electrolytes, metal corrosion can be represented as a dissolution process of the solid material (metal) into the liquid medium (electrolyte). The diffusion of metal ions in the electrolyte can affect the dissolution rate. This process can be effectively described by the original PD corrosion model [9,10], which treats corrosion as a diffusion-type problem in a bi-material system, with specific diffusivities assigned to the solid (an effective diffusivity, not its actual one), liquid and interface phases. Later it was recognized ([10]) that important savings can be achieved by focusing only on the dissolution layer part of the solid (the DCL, Diffusion-based Corrosion Layer [38]) and the electrolyte, as the rest of the solid (with its very small actual diffusivity) does not directly participate in the corrosion process. Specifically, the dissolution flux of metal ions crossing the solid-liquid interface is used in the PD diffusion equation to solve for the metal ion concentration in the bi-material system. The nonlocality in PD models introduces a length scale which facilitates modeling of the dissolution flux, which cannot be defined in local models when jump-discontinuities are present at the interface [10].

The dissolution process causes mechanical damage through a thin layer (several micrometers-thick) at the corroding surface [38–41]. To model mass transport and material damage simultaneously in the PD corrosion model, the material damage definition (d) in Eq. (3.9) is employed and two sets of bonds are overlaid: transport bonds and mechanical bonds. Transport bonds are responsible for diffusion/dissolution of metal

ions/atoms, while mechanical bonds provide the link between strain- and corrosion-induced damage. The corrosion damage process is the progression of material damage/disintegration into the intact material. When the concentration at a solid point drops below the saturated concentration, the point suffers a phase change from solid to electrolyte (its diffusivity is switched to that of the electrolyte), and all of its mechanical bonds are broken (its damage value becomes 1). Material points with a damage value lower than 1 are part of the solid phase: intact ($d = 0$, no broken bonds) or partially damaged ($0 < d < 1$).

Existing PD models for corrosion can capture important changes that happen near the corrosion front (on the solid side) and offer a more complete description of corrosion damage than was possible before [1,9,10,13]. However, in these models, an important simplification is used for activation-controlled corrosion, namely that the overpotential is a constant value (independent of location) along the corrosion front. This value can be measured from experiments and determines the current density from corresponding polarization curves. This treatment avoids solving for the electric potential distribution along the corrosion front and is acceptable for pitting corrosion cases in which the potential distribution (and therefore the current density) along the pit surface is close to uniform [12]. To cover situations like salt layer formation or passivation at the corrosion front when diffusion-controlled conditions dominate (and the potential distribution varies significantly along the corrosion front), the existing PD models include concentration-based rules that lead to the pausing/stopping of metal dissolution [10,13]. Under activation-controlled conditions, these mechanisms are not triggered, and the existing PD corrosion models would not apply to galvanic corrosion problems [14], in which

activation-controlled conditions are critical and the electric potential (or the corrosion rate) varies significantly along the corrosion front. Moreover, these variations also change drastically as the corrosion front evolves. Therefore, to predict galvanic corrosion, it is necessary to compute and update the potential distribution throughout the corrosion process, so that the distribution of corrosion rates along the corrosion front can be updated accordingly.

To achieve this goal, we introduce a PD electrostatic solver to compute the electric potential distribution in the electrolyte domain. In addition to that, we reformulate the PD corrosion dissolution model in [10] based on electrochemistry to substitute the numerical calibration with an analytical one. This change makes the model more reliable for problems with highly non-uniform current densities along arbitrary corroding surface, as in the case of galvanic corrosion. Moreover, we show that the damage-dependent corrosion model which was used in the original PD concentration-dependent damage model is no longer needed.

3.3.2.1 PD electrostatic model

In galvanic corrosion, one can use the classical model (Laplace's equation) shown in Eq. (3.4) to find the electric potential. However, because we would like to couple the electric potential solver with the PD corrosion model, it is more convenient (for a seamless integration) to formulate and solve the corresponding PD problem of Laplace's equation in Eq. (3.4) to find the electric potential needed in the corrosion model. The PD model for finding the electric potential is identical to that for steady state diffusion, with a constant micro-diffusivity:

$$\int_{H_x} \frac{\phi(\hat{\mathbf{x}}) - \phi(\mathbf{x})}{\|\hat{\mathbf{x}} - \mathbf{x}\|^2} dV_{\hat{\mathbf{x}}} = 0. \quad (3.11)$$

When using Eq. (3.11) to solve for the electric potential in the electrolyte, the BCs away from the metal surfaces can be approximated as homogeneous Neumann-type conditions (zero flux across those boundaries). The BC that has to be specified on the metal surfaces, according to the Ohm's law, is:

$$i(\mathbf{p}, t) = -\sigma \nabla_{\mathbf{n}} \phi(\mathbf{p}, t) \quad (3.12)$$

in which \mathbf{p} is a point at the metal surface, σ is the electric conductivity, i is the current density and $\nabla_{\mathbf{n}} \phi = \nabla \phi \cdot \mathbf{n}$, where \mathbf{n} is the outward unit normal. The relation between i and ϕ can be measured experimentally and expressed using Tafel's equation (see Eq. (3.1)). This makes Eq. (3.12) a nonlinear Robin type BC [2], written as:

$$i_0 \times 10^{\frac{\phi(\mathbf{p}, t) - \phi_0}{\beta}} = -\sigma \nabla_{\mathbf{n}} \phi(\mathbf{p}, t). \quad (3.13)$$

To enforce the local Robin BC on the metal surfaces in the PD model, we use an autonomous mirror-type fictitious nodes method (FNM) [16], which has been designed to handle boundaries of arbitrary shape. Implementation details are provided in Appendix A. Once the electric potential is obtained, the current density at each point $\mathbf{p} \in \partial\Omega$ can be determined by Eq. (3.13) or the Ohm's law (see Section 3.3.2.2). For simplicity of implementation, along the zero-flux boundaries, we do not use fictitious nodes, and these conditions are then, approximately, but naturally, represented in the model.

3.3.2.2 A modified PD corrosion dissolution model

PD corrosion models use a phase-dependent nonlocal diffusion equation on a domain that contains both liquid (electrolyte) and solid (metal) phases. Diffusion of metal ions/atoms in the liquid/solid, and the dissolution of solid into liquid at the solid-liquid interface can all be represented using the PD corrosion model as discussed in [9,10]. In this work, however, we assume activation-controlled conditions, i.e., corrosion rate is not influenced by mass transport in the liquid domain Ω_l (all liquid points are set to always have zero metal-ion concentration). In addition ([10]), mass transport in the solid Ω_s is too slow relative to the interfacial mass transport (dissolution). Therefore, for these conditions we ignore diffusion in Ω_l and Ω_s . Consequently, as shown in Figure 3.3 for pitting corrosion, only transport bonds connecting solid and liquid points across the anode surface (pit wall) are involved in the dissolution of solid into liquid. These are called dissolution bonds.

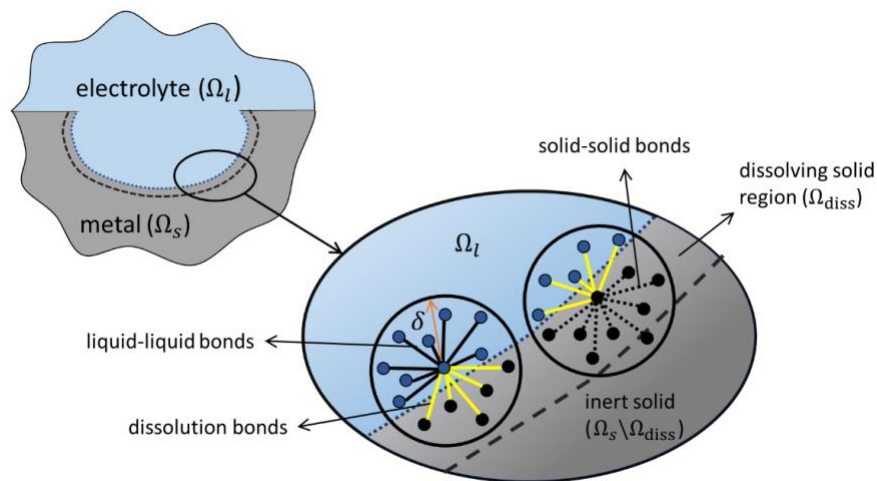


Figure 3.3. A schematic of different regions and bonds defined in the PD corrosion model at the corrosion front (redrawn from [10]). The PD horizon size is δ . Solid-solid bonds are considered as inert here, and diffusion in liquid is also ignored (by enforcing zero concentration at all times on liquid nodes).

Based on the above assumptions, the PD corrosion dissolution model can be written as:

$$\frac{\partial C(\mathbf{x}_d, t)}{\partial t} = \int_{H_{\mathbf{x}_d} \cap \Omega_l} J(\hat{\mathbf{x}}, \mathbf{x}_d, t) dV_{\hat{\mathbf{x}}} \quad (3.14)$$

where $C(\mathbf{x}_d, t)$ is the concentration at a dissolving point $\mathbf{x}_d \in \Omega_{\text{diss}}$ at time t , and the integrand $J(\hat{\mathbf{x}}, \mathbf{x}_d, t)$ is the mass flow density from \mathbf{x}_d to a point $\hat{\mathbf{x}} \in H_{\mathbf{x}_d} \cap \Omega_l$. In the model presented in [10], J was assumed to depend on the concentration gradient between the ends of a transport bond, \mathbf{x}_d and $\hat{\mathbf{x}}$:

$$J(\hat{\mathbf{x}}, \mathbf{x}_d, t) = \kappa_d \frac{C(\hat{\mathbf{x}}, t) - C(\mathbf{x}_d, t)}{\|\hat{\mathbf{x}} - \mathbf{x}_d\|^2} \quad (3.15)$$

where κ_d is the constant micro-dissolvability, a parameter that needs to be calibrated such that the dissolution rate in the PD model matches the measured/given activation-controlled corrosion rate. Since there is a linear correlation between κ_d and the current density i [9], i.e., $\kappa_d = \lambda i$, one can find the correlation constant λ by using a trial simulation as follows [10]: a simulation of uniform corrosion under activation-controlled regime is performed with a trial micro-dissolvability κ_d^{trial} ; if the resulting current density is denoted by i^{trial} , we have $\lambda = \kappa_d^{\text{trial}}/i^{\text{trial}}$. For cases like galvanic corrosion where i is location-dependent, this would lead to a location-dependent κ_d in Eq. (3.15), which could be computed from $\lambda i(\mathbf{p}(\mathbf{x}_d), t)$ (since the electrostatic solver gives the current density value at each point along the metal surface), where $\mathbf{p}(\mathbf{x}_d)$ is the point in Γ_f (the corrosion front/surface, see Figure 3.4) that minimizes the distance to \mathbf{x}_d . One still would have to find λ , through a calibration procedure. Each set of \mathbf{x}_d which share the same \mathbf{p} are denoted by $\chi(\mathbf{p})$, as shown in Figure 3.4 for the case of a smooth boundary.

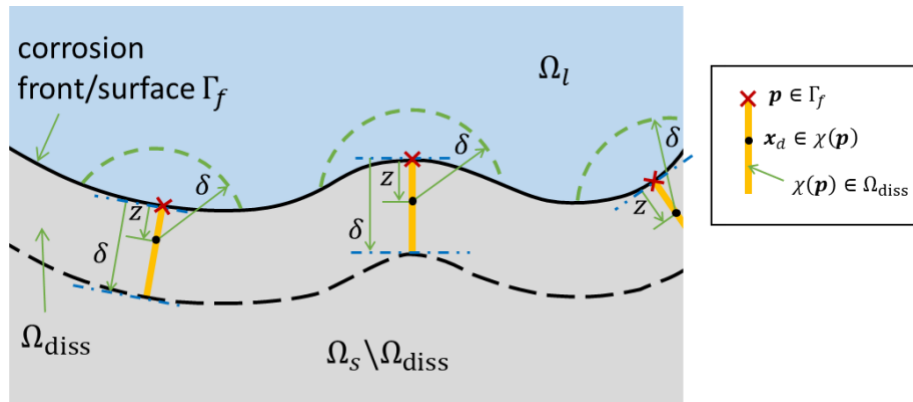


Figure 3.4. Examples of dissolving points (that form the set $\chi(\mathbf{p})$) which share the current density of point $\mathbf{p} \in \Gamma_f$, for an arbitrary, but smooth, boundary.

Since the calibration procedure described above was based on a trial simulation that assumed uniform corrosion for a flat surface, the calibrated value would not be valid on anode surfaces with high curvature (where the radius of curvature is in the order of the horizon size). Such high curvatures are likely to appear in galvanic corrosion in which the corrosion rate can vary significantly along the anode surface, especially near the anode-cathode joint. Moreover, even for flat anode surfaces, this calibration approach would fail to predict the corrosion rate accurately at locations near a corner of the anode (e.g., anode-cathode joint), since dissolving points located near a corner have significantly smaller number of dissolution bonds compared with those which are located elsewhere. This would result in unrealistically slow dissolution rates at locations which can be critical in the evolution of material damage and failure. For example, the corrosion rate at the anode-cathode joint in galvanic corrosion plays a significant role in material failure since these joints are likely to become stress concentration locations once corrosion starts.

While these issues could be overcome with a series of calibrations performed on a sufficient number of different geometrical configurations of the anode surface, that would

lead to a rather complex algorithm/implementation, as well as an increase in the computational cost of the simulation. A preferred option is an analytical, instead of a numerical, calibration for this model parameter. Recall that most PD models are setup using analytical relationships between bond parameters, such as micro-modulus and micro-diffusivity, and material properties, like elastic modulus and diffusivity [22,30].

Furthermore, the dependency of mass flow density in Eq. (3.15) on concentration distribution becomes less reliable for problems with highly non-uniform current densities along an arbitrary corroding surface, which is the case of galvanic corrosion, for example. From electrochemistry, we know that anodic dissolution is driven by the corrosion reaction (directly related to the current density), which is determined by the potential distribution at the anode surface, and is only indirectly dependent on the concentration distribution near the corrosion front. Therefore, we modify the definition of the PD mass flow density in Eq. (3.15) to make it directly depend on the current density distribution (determined by the PD electrostatic model, see Section 3.3.2.1) at the corrosion front, as follows:

$$J(\hat{\mathbf{x}}, \mathbf{x}_d, t) = \omega \frac{i(\mathbf{p}(\mathbf{x}_d), t)}{\|\hat{\mathbf{x}} - \mathbf{x}_d\|} \quad (3.16)$$

where ω is a constant that will be calibrated analytically for a certain curvature at \mathbf{p} by matching the PD flux $J_{\text{diss}}^{\text{PD}}(\mathbf{p}, t)$ (see below) with a given constant dissolution flux $J_{\text{diss}}(\mathbf{p}, t)$. Note that here we use a constant ω , but other options are not precluded, for example one could choose $\omega = \omega(\|\hat{\mathbf{x}} - \mathbf{x}_d\|)$.

Consider a flat surface as shown in Figure 3.5, $J_{\text{diss}}^{\text{PD}}(\mathbf{p}, t)$ is contributed from all dissolution bonds connected to $\mathbf{x}_d \in \chi(\mathbf{p})$ and can be computed as [25]:

$$\begin{aligned} J_{\text{diss}}^{\text{PD}}(\mathbf{p}, t) &= \int_0^\delta \int_0^\xi \int_0^{\cos^{-1}\left(\frac{z}{\xi}\right)} J(\hat{\mathbf{x}}, \mathbf{x}_d, t) \xi d\theta d\xi dz \\ &= \int_0^\delta \int_0^\xi \int_0^{\cos^{-1}\left(\frac{z}{\xi}\right)} \omega \frac{i(\mathbf{p}, t)}{\xi} \xi d\theta d\xi dz = \omega i(\mathbf{p}, t) \delta^2 \end{aligned} \quad (3.17)$$

where ξ is the bond length, θ is the angle between the bond and the surface, and z is the distance between \mathbf{x}_d and the surface (or $\mathbf{p}(\mathbf{x}_d)$). Since $J_{\text{diss}}(\mathbf{p}, t) = i(\mathbf{p}, t)/qF$ according to Faraday's law, by letting $J_{\text{diss}}^{\text{PD}}(\mathbf{p}, t) = J_{\text{diss}}(\mathbf{p}, t)$, we obtain:

$$\omega = \frac{1}{qF\delta^2}. \quad (3.18)$$

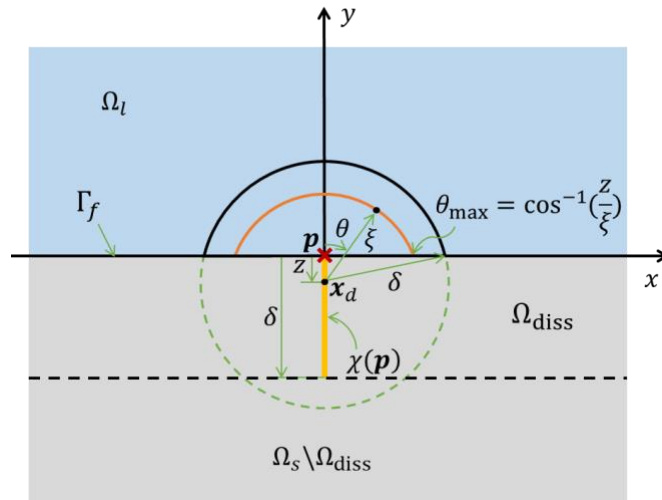


Figure 3.5. Computation of the PD flux at a point \mathbf{p} at a flat anode surface.

One more step is required to make this model applicable for general corrosion problems, including galvanic corrosion. The PD flux definition in Eq. (3.17) assumes a flat surface (see Figure 3.5). In order to have this analytical calibration process work for the PD

transport equation in Eq. (3.14) independent on the curvature of the anodic surface, we modify the transport equation as described next.

In general, uniform corrosion (same current density i everywhere) on a metal surface of arbitrary shape, as shown in Figure 3.4, should evolve perpendicular to the surface and progress with the same speed everywhere. In the PD framework, this means that points \mathbf{x}_d with the same distance to the surface (z) should have the same rate of concentration loss, independent of the curvature of the surface at $\mathbf{p}(\mathbf{x}_d)$ and the number of dissolution bonds connected to \mathbf{x}_d (the shape of the horizon region contained in the electrolyte domain, $H_{\mathbf{x}_d} \cap \Omega_l$). Therefore, we can write $\frac{\partial C(\mathbf{x}_d, t)}{\partial t} = f(z(\mathbf{x}_d))$, where $f(z(\mathbf{x}_d))$ is the integral of the mass flow density of all dissolution bonds connected to \mathbf{x}_d , that should not depend on the shape of $H_{\mathbf{x}_d} \cap \Omega_l$. Since we calibrated ω for a flat surface, we need to compute $f(z(\mathbf{x}_d))$ over a flat surface:

$$\begin{aligned} f(z(\mathbf{x}_d)) &= \int_z^\delta \int_0^{\cos^{-1}\left(\frac{z}{\xi}\right)} \omega \frac{i(\mathbf{p}(\mathbf{x}_d), t)}{\xi} \xi d\theta d\xi \\ &= 2\omega i(\mathbf{p}(\mathbf{x}_d), t) \left\{ \delta \cos^{-1} \frac{z}{\delta} - z \ln \left[\frac{\delta}{z} + \tan \left(\cos^{-1} \frac{z}{\delta} \right) \right] \right\}. \end{aligned} \quad (3.19)$$

The modification to the PD model for corrosion dissolution defined by Eqs. (3.14) and (3.15) is:

$$\frac{\partial C(\mathbf{x}_d, t)}{\partial t} = 2\omega i(\mathbf{p}(\mathbf{x}_d), t) \left\{ \delta \cos^{-1} \frac{z}{\delta} - z \ln \left[\frac{\delta}{z} + \tan \left(\cos^{-1} \frac{z}{\delta} \right) \right] \right\}. \quad (3.20)$$

Therefore, we replace the integro-differential model in Eqs. (3.14) and (3.15) with an ordinary differential model (Eq. (3.20)) in which $z(\mathbf{x}_d)$ for each $\mathbf{x}_d \in \Omega_{\text{diss}}$, together with $i(\mathbf{p}(\mathbf{x}_d), t)$, determines the dissolution flux. Note that computing the distance $z(\mathbf{x}_d)$

is, in a sense, computationally equivalent to evaluating the integral in Eq. (3.14), because it involves, after discretization, searching through the nodes in $H_{\mathbf{x}_d} \cap \Omega_l$ for the one closest to \mathbf{x}_d .

We remark that if we wanted to calibrate ω using a surface different than a flat one, we would have to use that same geometry for computing $f(z(\mathbf{x}_d))$. Eq. (3.20) works naturally for cases where i is highly location-dependent, or when the curvature of the corrosion surface is high (at corners, for example). In Section 3.4.1, we will use the discrete version of Eq. (3.20) to estimate the numerical error of resulting current density introduced by the discretization, for a problem with a known (classical) analytical solution.

We now explain how to find the corresponding \mathbf{p} and the distance to the surface z , for a given \mathbf{x}_d . With the meshfree-type (one-point Gaussian quadrature) spatial discretization of the domain (see Figure 3.6), the corrosion surface Γ_f is located between the solid nodes and liquid nodes and can be approximated by those liquid nodes $\tilde{\mathbf{p}}$ which are closest to solid nodes, as shown in Figure 3.6. To determine $\mathbf{p}(\mathbf{x}_d)$, we search all $\mathbf{x} \in H_{\mathbf{x}_d} \cap \Omega_l$ for the one closest to \mathbf{x}_d . If there are multiple such points, we select the one which makes the angle between $\overline{\mathbf{x}_d \tilde{\mathbf{p}}}$ and the nonlocal outward unit “normal” at \mathbf{x}_d , $\mathbf{n}(\mathbf{x}_d)$, the smallest. The nonlocal outward unit “normal” at \mathbf{x}_d (which approximates the classical outward normal on the boundary of a domain) is [16]:

$$\mathbf{n}(\mathbf{x}_d) = \frac{\int_{H_{\mathbf{x}_d} \cap \Omega_l} (\hat{\mathbf{x}} - \mathbf{x}_d) d\hat{\mathbf{x}}}{\left\| \int_{H_{\mathbf{x}_d} \cap \Omega_l} (\hat{\mathbf{x}} - \mathbf{x}_d) d\hat{\mathbf{x}} \right\|} \quad (3.21)$$

Since we are not tracking the corrosion front with a moving mesh (we use a fixed and uniform discretization), to improve the approximation of current density distribution along Γ_f , we take $z(\mathbf{x}_d) \approx \|\mathbf{x}_d - \tilde{\mathbf{p}}\| - \frac{\Delta x}{2}$, and used it in Eq. (3.20).

We compute the current density $i(\tilde{\mathbf{p}}, t)$ from Ohm's law:

$$i(\tilde{\mathbf{p}}, t) = \sigma \frac{|\phi(\tilde{\mathbf{p}}, t) - \phi(\tilde{\mathbf{p}}^R, t)|}{\|\tilde{\mathbf{p}}^R - \tilde{\mathbf{p}}\|}. \quad (3.22)$$

Here, $\tilde{\mathbf{p}}^R$ is the reflection/mirror node of $\tilde{\mathbf{p}}$ (see Appendix A) through Γ_f and $\phi(\tilde{\mathbf{p}}^R, t)$ is the electric potential assigned at $\tilde{\mathbf{p}}_m$ to enforce the local BC for the electric potential solver as discussed in Section 3.3.2.1 and Appendix A. If the polarization curve (or Tafel's equation) is used, we can also compute $i(\tilde{\mathbf{p}}, t)$ using Eq. (3.13) with $\phi(\tilde{\mathbf{p}}, t) = \frac{1}{2}[\phi(\tilde{\mathbf{p}}, t) + \phi(\tilde{\mathbf{p}}^R, t)]$.

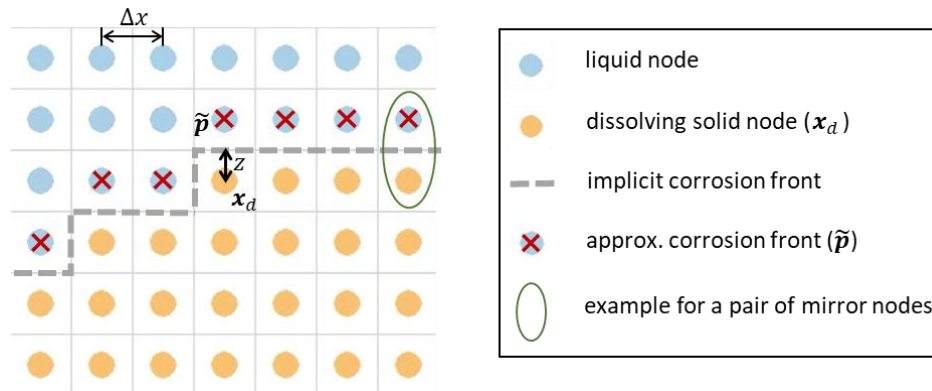


Figure 3.6. A schematic of corrosion front after spatial discretization.

3.3.2.3 Concentration-dependent damage models in PD simulation of corrosion

Modeling of corrosion-induced damage is important in understanding stress-corrosion cracking [42]. In the combined action of mechanical loading and environmental attack, material damage can be caused by strain- or chemically-induced atomic bond rupturing.

In the corresponding PD model, we will account for damage accumulation (see Eq. (3.9)) from both sources: corrosion-induced damage (monitored by $d_c(\mathbf{x}, t)$) and mechanical strain-triggered damage (monitored by $d_s(\mathbf{x}, t)$). Note that, in the context of corrosion, Eq. (3.8) is augmented so that the condition for $\mu = 0$ includes corrosion-induced bond breaking.

A concentration-dependent damage (CDD) model was introduced in [9] to establish a relationship between corrosion and the damage of mechanical bonds. Given the intrinsic randomness of the corrosion reaction (partly due to the variations in the microstructure of the material), one can assign a probability $P(\mathbf{x}, t)$ of the bonds connected at $\mathbf{x} \in \Omega_s$ at time t to break, based on the concentration drop at \mathbf{x} , for all (intact) mechanical bonds connected to \mathbf{x} . In order to determine $P(\mathbf{x}, t)$, a linear dependency between the corrosion-induced damage $d_c(\mathbf{x}, t)$ and the concentration $C(\mathbf{x}, t)$ was proposed in [9]:

$$d_c(\mathbf{x}, t) = \begin{cases} 1 & , C(\mathbf{x}, t) \leq C_{\text{sat}} \\ \frac{C_{\text{solid}} - C(\mathbf{x}, t)}{C_{\text{solid}} - C_{\text{sat}}} & , C_{\text{sat}} < C(\mathbf{x}, t) \leq C_{\text{solid}} \end{cases} \quad (3.23)$$

where C_{solid} refers to the concentration of metal atoms in the intact solid phase, and C_{sat} is the saturation concentration for metal ions in electrolyte. Reaching C_{sat} was assumed as a good approximation for when the solid-to-liquid phase-change takes place. Note that for activation-controlled corrosion, we assume that if a nodal concentration reaches below C_{sat} , that concentration is set to zero. The change in damage (from one time-step to the next, at a point) can then be expressed in terms of the probability $P(\mathbf{x}, t)$ as [9]:

$$\Delta d_c(\mathbf{x}, t_i) = d_c(\mathbf{x}, t_i) - d_c(\mathbf{x}, t_{i-1}) = (1 - d_c(\mathbf{x}, t_{i-1}))P(\mathbf{x}, t_i) \quad (3.24)$$

Combining Eqs. (3.23) and (3.24), one finds an expression for the probability of corrosion damage at $\mathbf{x} \in \Omega_s$ and t_i in terms of the concentration drop at that point:

$$P(\mathbf{x}, t_i) = \frac{1}{1 - d_c(\mathbf{x}, t_{i-1})} \left(\frac{C(\mathbf{x}, t_{i-1}) - C(\mathbf{x}, t_i)}{C_{\text{solid}} - C_{\text{sat}}} \right) = \frac{C(\mathbf{x}, t_{i-1}) - C(\mathbf{x}, t_i)}{C(\mathbf{x}, t_{i-1}) - C_{\text{sat}}} \quad (3.25)$$

This quantity now allows us to break a corresponding number of mechanical bonds connected to \mathbf{x} so that the damage evolves (stochastically) according to Eq. (3.23). The stochastic procedure for selecting which mechanical bond breaks at a given time $\forall \mathbf{x} \in \Omega_s$ is as follows [9]:

Appendix B. Compute/update the concentration field at this time step.

Appendix C. Loop over all $\mathbf{x} \in \Omega_s$.

- a. Compute the probability of breaking P at \mathbf{x} ; if $P = 0$, then skip this \mathbf{x} , else continue.
- b. Loop over all $\hat{\mathbf{x}} \in H_{\mathbf{x}} \cap \Omega_s$.
 - i. If the mechanical bond connecting \mathbf{x} and $\hat{\mathbf{x}}$ is already broken, then skip this bond, else continue.
 - ii. Generate a random number $R(\mathbf{x}, \hat{\mathbf{x}})$ from a uniform distribution in interval $[0,1]$; if $R(\mathbf{x}, \hat{\mathbf{x}})$ is smaller than or equal to P , then break the bond (note that each bond connects two points, thus, once a bond breaks, it is considered broken for both points).
- c. End loop over all $\hat{\mathbf{x}} \in H_{\mathbf{x}} \cap \Omega_s$.

Appendix D. End loop over all $\mathbf{x} \in \Omega_s$.

Note that Eq. (3.23) gives the expected corrosion-induced damage value d_c at point \mathbf{x} , based on the concentration drop at that point only. After performing the bond-breaking procedure for all $\mathbf{x} \in \Omega_{\text{diss}}$, the damage index d at each $\mathbf{x} \in \Omega_s$ is computed from Eq.

(3.9). However, as we can see in this procedure, a mechanical bond $\mathbf{x} - \hat{\mathbf{x}}$ can be broken due to either \mathbf{x} or $\hat{\mathbf{x}}$, which means that the damage index at a point $\mathbf{x} \in \Omega_s$, at the end of a time step, can also be affected by bond-breaking events due to concentration drop at $\hat{\mathbf{x}} \in H_{\mathbf{x}} \cap \Omega_{\text{diss}}$. This means that the damage index computed by Eq. (3.9) may have a slightly larger values than what is expected from Eq. (3.23). As a result, there could be material points that reach $d = 1$ (totally detached from other solid points) that still have $C > C_{\text{sat}}$. Physically, this would mean that a small part of the solid (a speck, defined by a node) is now surrounded by electrolyte and would dissolve rather instantaneously. This leads to the conclusion that we can assume this location to, effectively, now be electrolyte phase. This was the reason for the damage-dependent corrosion (DDC) model to be used in [9], where such nodes were switched from the solid phase to the liquid phase (by changing the micro-diffusivity of transport bonds connected to them). In the absence of DDC, given the “effective” diffusion in solid used in [9] to calibrate the model to a given corrosion rate, one obtains an ever expanding corrosion-affected layer, which is not physically observed (see [38]).

An important update to the CDD+DDC model in [9] has appeared in [10]. There, it was recognized that it was sufficient to monitor changes in the Diffusion-based Corrosion Layer (DCL, a layer of thickness δ at the corrosion surface), and only model transport through PD transport bonds whose end nodes are either solid-liquid or liquid-liquid. The numerical calibration to match a certain corrosion rate for the model in [10] was performed to determine the micro-dissolvability of an dissolution (anode-liquid) bond, as explained above in the paragraph after Eq. (3.15). While the DDC part of the coupled corrosion-damage model was still used in [10], it had become redundant. Because of the

numerical calibration procedure, the model in [10] can work with or without the DDC part. However, the new PD formulation for corrosion dissolution, see Eq. (3.20), introduced here, does not work with DDC because it uses an analytical calibration, which assumes dissolution happens only through dissolution bonds, and phase-change takes place only when the concentration at a node drops below C_{sat} :

$$\begin{cases} \text{if } C(\mathbf{x}, t) \leq C_{\text{sat}} \text{ then } \mathbf{x} \in \Omega_l \\ \text{if } C_{\text{sat}} < C(\mathbf{x}, t) \leq C_{\text{solid}} \text{ then } \mathbf{x} \in \Omega_s \end{cases} \quad (3.26)$$

In the context of the new coupled corrosion-damage model, Eqs. (3.20) and (3.25), adding the DDC part would artificially speed up the corrosion rate. Therefore, the coupled corrosion-induced damage model we use here is based on Eqs. (3.20), (3.25), and (3.26).

3.3.3 PD corrosion-fracture model

In previous sections, we reviewed the mechanical fracture model and introduced different ingredients of the modified corrosion model. In this section, we introduce the coupling strategy for these models and discuss their numerical implementation.

The elasticity (with fracture), electrostatics, and mass transfer (with damage and phase-change) models are coupled into a PD model called the PD corrosion-fracture (PD-CF) model and consists of the following set of equations:

Elasticity (Eqs. (3.7) and (3.10)):

$$\int_{H_{\mathbf{x}}} cs\mu \frac{\xi+\eta}{\|\xi+\eta\|} dV_{\hat{\mathbf{x}}} = 0 \quad \forall \mathbf{x} \in \Omega_s \text{ (displacement)} \quad (3.27)$$

where $s = \frac{\|\xi+\eta\|-\|\xi\|}{\|\xi\|}$ (bond strain)

Electrostatics (Eqs. (3.11) and (3.22)):

$$\int_{H_x} \frac{\phi(\hat{x}) - \phi(x)}{\|\hat{x} - x\|^2} dV_{\hat{x}} = 0 \quad \forall x \in \Omega_l \text{ (electric potential)} \quad (3.28)$$

$$i(\tilde{\mathbf{p}}, t) = \sigma \frac{|\phi(\tilde{\mathbf{p}}, t) - \phi(\tilde{\mathbf{p}}^R, t)|}{\|\tilde{\mathbf{p}}^R - \tilde{\mathbf{p}}\|} \text{ (current density)}$$

Corrosion (Eqs. (3.20), (3.25) and (3.26)):

$$\frac{\partial C(x, t)}{\partial t} = 2\omega i(\mathbf{p}(x), t) \left\{ \delta \cos^{-1} \frac{z}{\delta} - z \ln \left[\frac{\delta}{z} + \tan \left(\cos^{-1} \frac{z}{\delta} \right) \right] \right\} \quad \forall x \in \Omega_{\text{diss}}$$

(mass transport)

$$P(x, t_i) = \frac{C(x, t_{i-1}) - C(x, t_i)}{C(x, t_{i-1}) - C_{\text{sat}}} \quad \forall x \in \Omega_s \text{ (bond-breaking probability)} \quad (3.29)$$

$$\begin{cases} \text{if } C(x, t) \leq C_{\text{sat}} & \text{then } x \in \Omega_l \\ \text{if } C_{\text{sat}} < C(x, t) \leq C_{\text{solid}} & \text{then } x \in \Omega_s \end{cases} \text{ (phase-change)}$$

Bond damage (corrosion- and strain-induced bond breaking) is defined as:

$$\mu(x, \hat{x}, t) = \begin{cases} 1 & \text{if } x, \hat{x} \in \Omega_s \text{ and } s(x, \hat{x}, t') < s_0 \text{ and } R(x, \hat{x}, t') > P(x, t') \\ & \forall t' \in [0, t] \\ 0 & \text{otherwise} \end{cases} \quad (3.30)$$

where R is the random number generated for each bond in the algorithm given in the previous section.

These equations are accompanied by appropriate initial and BCs. The initial concentration distribution for the corrosion and the local BCs to be enforced for electrostatics and elasticity are specified for each of the examples considered here in Sections 3.4 and 3.5. In Appendix A, we explain how we enforce local BCs in PD models.

In the PD-CF model, the elasticity model (Eq. (3.27)) computes the displacements field (\mathbf{u}) and bond strains (s) in the solid; the electrostatic model (Eq. (3.28)) computes the electric potential distribution (ϕ) in the electrolyte and current density distribution (i) on

electrode surfaces; the corrosion model (Eq. (3.29)) updates the distribution of metal concentrations (C), computes the corrosion-induced bond-breaking probability (P) and determines the necessary phase changes from the dissolution process; the damage model (Eq. (3.30)) updates the strain- and corrosion-induced bond-failure in the solid. To visualize damage results, in a post-processing phase, we determine the total nodal damage index value (d) by Eq. (3.9). Note that in the PD-CF model, $d(\mathbf{x}, t) \approx d_s(\mathbf{x}, t) + (1 - d_s) \times d_c(\mathbf{x}, t)$ in which d_c represents the corrosion-induced damage index and d_s is mechanical strain-triggered damage index.

The implementation of the PD-CF model is shown in Figure 3.7. In the main solver, the corrosion solvers are called at each time-step, and the electric potential and displacement fields are updated at the first time-step and any time step if any of the solid nodes becomes liquid in the previous time step. In the electrostatic solver, because the FNM is used to impose BCs, the electric potential needs to be solved iteratively, with the solution in the domain and constraint in the fictitious region updated after each iteration, until two sequential solutions differ by less than a given tolerance. Since this system is linear, we use the Conjugate Gradient (CG) method to solve it. The Euclidean norm is used to measure the difference between two solutions, and the tolerance is set to 1e-6. The displacement field is solved by the Nonlinear Conjugate Gradient (NCG) method [43,44] and, ideally, should be updated every time new corrosion damage happens. However, in this work, to save computational time, we update it as frequently as the electric potential field. The influence of this treatment on the stress corrosion cracking behavior is insignificant [11]. If any mechanical bond breaks after we updated the displacement field, the update needs to be repeated until equilibrium is satisfied and no more bonds break in

the process. The simulation stops when the final time-step is reached, or when the number of successive updates of displacement field exceed a certain value, e.g., 50, since this would be an indication of unstable crack growth, and a different solver (e.g., explicit) may need to be used.

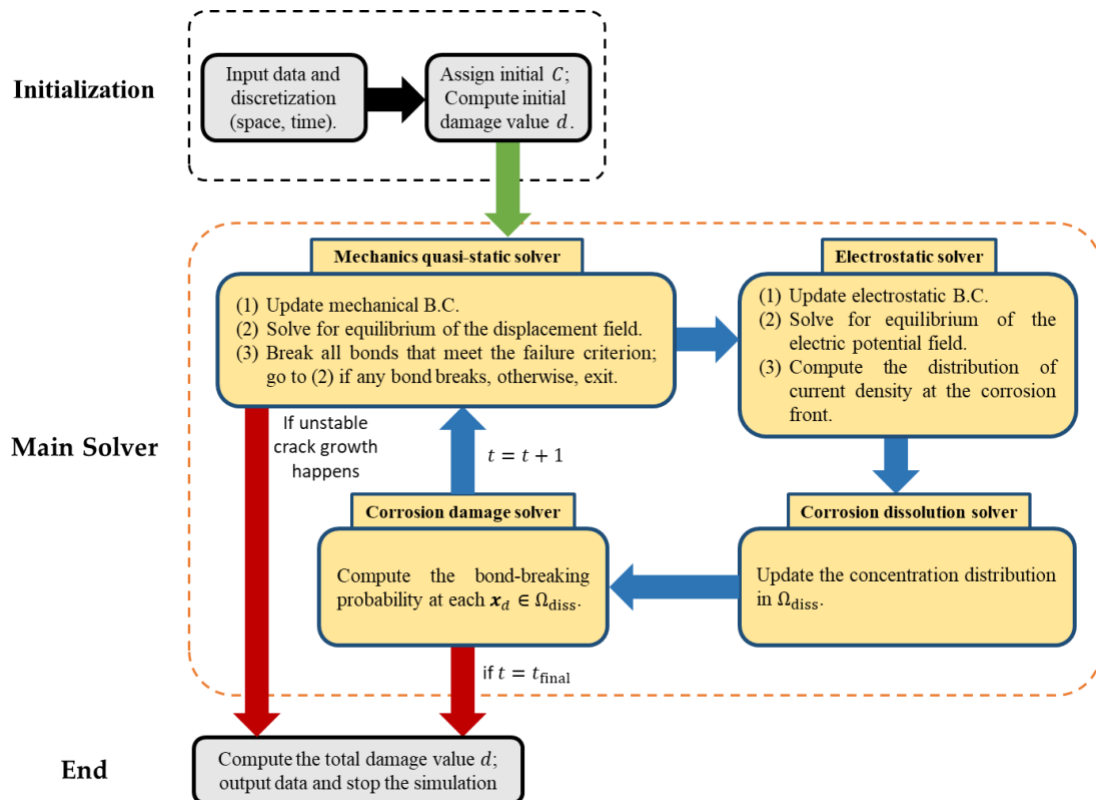


Figure 3.7. Workflow of the PD corrosion-fracture (PD-CF) model.

The corrosion rate may depend on the stress field [36]. While we will show an example solving a coupled corrosion-fracture problem (in which changes in sample geometry induced by the galvanic dissolution process leads to higher tensile stresses/strains and fracture) in Section 3.5, here we assume the corrosion rate to be independent of the stress field. It is, however, possible to introduce the stress-dependent corrosion rate model into a PD model of corrosion, as has been presented in [36]. The examples shown in Section

3.4 do not employ the mechanical solver, because no mechanical loadings are involved.

The full model is used in the example in Section 3.5, where we simulate the combined effects of galvanic corrosion and failure induced by corrosion and mechanical loadings.

To discretize the PD IDEs, we use the meshfree method with one-point Gaussian quadrature, in which handling damage and fracture is natural [24]. Uniform grids are used to discretize the domain, both electrolyte and solid regions. Detailed descriptions of the discretization used can be found in [10].

3.4 Verification and validation of the PD corrosion model

In this section, we first verify the new PD corrosion model against a problem with the corresponding classical analytical solution. Then, validation against experimental data is provided. We only consider activation-controlled corrosion, therefore mass transport between any two points in the electrolyte domain is ignored.

3.4.1 Verification of the new PD formulation for galvanic corrosion

To verify the new corrosion model for galvanic corrosion, we consider the example shown in Figure 3.8. The cathode and anode are in electric contact by a perfect conductor, in the presence of an electrolyte with conductivity σ . The electrode potential of cathode and anode are ϕ_c and ϕ_a , respectively. The whole domain is infinite in the x direction and the electrolyte region has an initial height of h_0 .

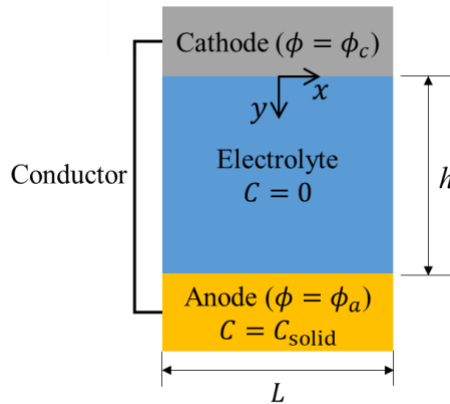


Figure 3.8. Sketch of the example used to verify the PD galvanic corrosion model (redrawn from [6]).

If both electrodes are nonpolarizable, the classical formulation for the electric potential distribution in the electrolyte domain is:

$$\begin{cases} \nabla^2 \phi = 0 \\ \phi(x, y = 0, t) = \phi_c \\ \phi(x, y = h(t), t) = \phi_a \end{cases} \quad (3.31)$$

where $h(t)$ is the height of the electrolyte domain at time t . The classical solution of Eq. (3.31) is:

$$\phi(y) = \phi_a - \frac{y}{h(t)}(\phi_a - \phi_c) \quad (3.32)$$

and the mass flux at the anode surface is:

$$J = \frac{\sigma(\phi_a - \phi_c)}{qFh(t)} \quad (3.33)$$

where q is charge number of a metal ion and F is Faraday's constant. Values for these parameters are provided in Table 3.1. Note that the width of the domain is set to L in the PD simulation, and periodic BCs are imposed at $x = \pm \frac{L}{2}$, to effectively make the domain

infinite in the x direction. To accomplish this, two fictitious regions (\tilde{A} and \tilde{B}), with their width equal to the horizon size, are added outside the domain, as shown in Figure 3.9.

The electric potential in these fictitious regions is mapped from that of the corresponding subdomains (A and B) in the solution domain, so that the left and right boundaries of the solution domain are effectively connected by periodicity.

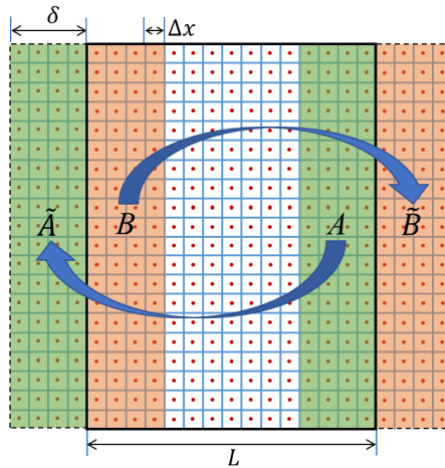


Figure 3.9. Schematic of the implementation of periodic BCs in PD simulations.

Table 3.1. Parameter values for the example shown in Figure 3.8.

Parameters	Value	Parameters	Value
ϕ_a	0.6 V	F	96,485 C/mol
ϕ_c	0.1 V	h_0	0.1 m
σ	2.5 S/m	L	0.1 m
C_{solid}	143 mol/L	q	2

We first compute the electric potential in the electrolyte domain to verify our PD electrostatic model. We choose $\delta = 4$ mm and $\Delta x = 1$ mm for the simulation. The relative difference (using the Euclidean norm) of the electric potential compared to the classical solution (see Eq. (3.32)) is $1.67\text{e-}6$, when the tolerance for convergence is set to

1e-6. The uniform current density at the anode surface computed by Eq. (3.22) is 12.50183 A/m², while the classical solution is 12.5 A/m², leading to a relative difference of 1.46e-4. Note that the convergence study on the electric potential is not needed for this problem, because the exact solution has a linear distribution and the FNM enforces the local BCs exactly, i.e., the PD solution matches the analytical classical solution exactly regardless of the grid density. In fact, a finer grid leads to a larger error due to accumulation of round-off numerical errors.

Next, we analyze the numerical error introduced by using the discretized form of Eq. (3.20) to update the concentration in the corrosion dissolution model. Assuming that at a point on the anode surface the given current density (e.g., obtained from the electric potential) is i_0 , the relative difference between i_0 and the resulting current density i_{PD}^m generated by using the discrete form of Eq. (3.20) can be written as:

$$\left| \frac{i_{PD}^m - i_0}{i_0} \right| = \left| 1 - \frac{2}{m^2} \sum_{k=1}^m \left\{ m \cos^{-1} \frac{z_k}{m} - z_k \ln \left[\frac{m}{z_k} + \tan \left(\cos^{-1} \frac{z_k}{m} \right) \right] \right\} \right| \quad (3.34)$$

where m is the ratio of horizon size and grid size ($\delta/\Delta x$), and $z_k = k - 1/2$. This relative error only depends on the value of m and should drop as m increases (or as $1/m$ decreases). The error for different m -values is given in Table 3.2; as expected, larger m -value leads to smaller error (with a convergence rate close to quadratic). However, as we increase the m -value (with δ fixed), the scaling of the total computational cost also increases significantly, since with this type of numerical solution, the scaling is $O(N^2)$, where N is the total number of nodes used in the discretization [45]. Note also that a larger m -value does not necessarily improve the accuracy because of concurrent increase

in round-off error. It is possible to choose different m -values for each model in the coupled PD-CF model to balance cost and accuracy. When a large m -value is needed to capture some fine details, the fast convolution-based PD method recently introduced, may be used as an alternative approach, since it has been shown to lead to significant computational efficiencies [45,46]. Here, considering that the relative error in i_{PD} is acceptable when $m = 4$, we use this value. Note that since we calibrated the PD models, for any horizon size, to match a given current density (see Eq. (3.18)), these numerical errors are independent of the horizon size.

Table 3.2. Numerical errors (for different values of m) for the resulting current density when the discrete version of Eq. (3.20) is used to update the concentration in the corrosion dissolution model.

m -value	$\left \frac{i_{\text{PD}}^m - i_0}{i_0} \right $
2	7.15e-2
4	2.18e-2
8	6.4e-3
16	1.8e-3
32	5.2e-4

To verify the coupling of the electrostatic model and the corrosion dissolution model, we test the corrosion evolution for the problem in Figure 3.8 by checking the corrosion depth $z_h = (h - h_0)$ as a function of time t . The solution for the corrosion depth in the classical model is [6]:

$$z_h = \sqrt{\frac{2\sigma t(\phi_a - \phi_c)}{qFc_{\text{solid}}} + h_0^2} - h_0 \quad (3.35)$$

The evolution of corrosion depth obtained by the PD corrosion model (using effective corrosion depth, see Appendix A) agrees with the classical solution, as shown in Figure 3.10. The relative difference of the final depth between them is 2.07%, which is close to the numerical error in the effective current density for $m = 4$ shown in Table 3.2. Note that the relative difference in electric potential between the PD and classical solutions, and the approximation of the current density by Eq. (3.22), also contribute to the relative difference in corrosion depth between the PD and classical models.

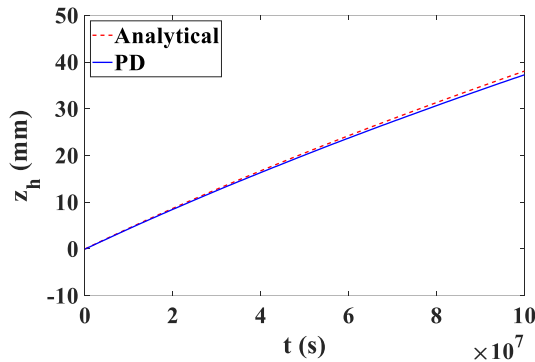


Figure 3.10. Comparison of the corrosion depth vs. time between PD solution and classical solution (Eq. (3.35)) for the problem shown in Figure 3.8. Computing the effective corrosion depth in PD corrosion model is described in Appendix A.

3.4.2 Validation against experimental results from the literature

The previous example verified the PD electrostatic model and the modified corrosion dissolution model. In this subsection, we validate the model against a galvanic corrosion experiment which appeared in [3]. We compare the PD results with experimental observations, as well as with results obtained by a FEM-based model built in COMSOL (see Appendix B) for the classical formulation of the problem. The model in COMSOL

uses the Arbitrary Lagrangian-Eulerian method to track the corrosion front as a moving boundary [2].

The setup of the problem is shown in Figure 3.11 (a). The classical formulation for the electric potential distribution in the electrolyte domain is:

$$\left\{ \begin{array}{l} \nabla^2 \phi = 0 \\ \nabla_{\mathbf{n}} \phi(x = 0, 10 < y < 20, t) = 0 \\ \nabla_{\mathbf{n}} \phi(x = 20, 10 < y < 20, t) = 0 \\ \nabla_{\mathbf{n}} \phi(0 < x < 20, y = 15, t) = 0 \\ \nabla_{\mathbf{n}} \phi(0 < x < 10, y = 5, t) = -i_c/\sigma \\ \nabla_{\mathbf{n}} \phi(10 < x < 20, y = 5, t) = -i_a/\sigma \end{array} \right. \quad (3.36)$$

in which $\nabla_{\mathbf{n}} \phi = \nabla \phi \cdot \mathbf{n}$, i_a and i_c are defined by the Tafel's equation (see Eq. (3.13))

which can be determined by fitting the polarization curves of corresponding galvanic

couples. The polarization curves we use for the mild steel-AE44 couple are shown in

Figure 3.11 (b) which are (piecewise) linear interpolations of the experimentally obtained

curves in [2]. The coefficients in the Tafel's equation are given in Table 3.3. Note that the

sign of cathodic and anodic current densities is negative and positive, respectively. Other

material properties for this problem are provided in Table 3.4. These parameters are used

in both PD and COMSOL simulations.

(a)

(b)

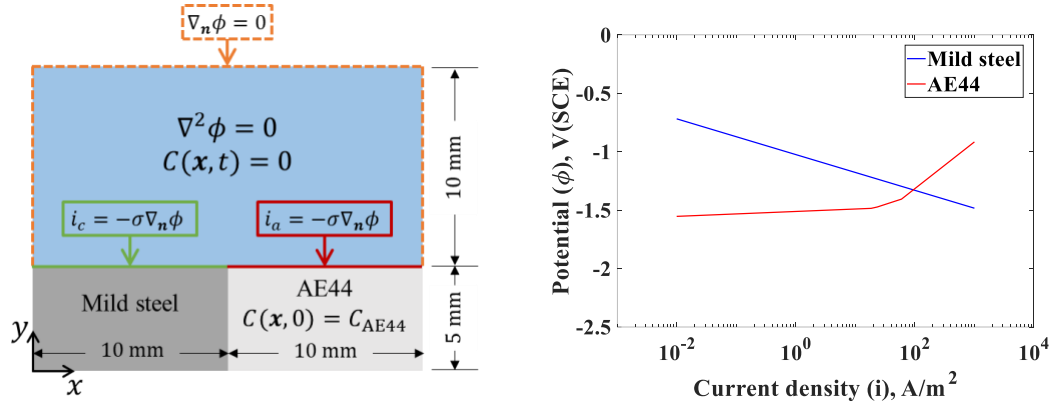


Figure 3.11. (a) Geometry and BCs for the galvanic corrosion problem (adapted from [2]); (b) piecewise linear interpolation of the experimentally obtained polarization curves for mild steel and AE44 in [2] (details are given in Table 3.3).

Table 3.3. Data used in the piecewise linear interpolation of the polarization curves from [2] (to be used in the Tafel's equation).

	Alloy	ϕ (V, SCE)	i_0 (A/m ²)	β (V)	ϕ_0 (V, SCE)
Anode	AE44	$(-\infty, -1.48)$	0.014	0.021	-1.55
		$[-1.48, -1.41]$	21.145	0.166	-1.48
		$(-1.41, \infty)$	58.107	0.400	-1.41
Cathode	Mild steel		0.00125	-0.153	-0.58

Table 3.4. Material properties for the galvanic problem shown in Figure 3.11 (a).

Parameters	σ	$C_{\text{solid}}^{\text{AE44}}$	q
Value	2.5 S/m	67860 mol/m ³	2

The comparison between COMSOL results and PD results (with $\delta = 0.4$ mm) in terms of the initial potential distribution is shown in Figure 3.12. The COMSOL result is selected after a convergence study with respect to the mesh size (see Appendix B for details on the COMSOL model) and then, before plotting, post-processed by the Kriging interpolation (necessary because of the adaptive mesh used in COMSOL) and plotting

that at the nodes of the uniform grid used in the PD model. The agreement between the two solutions is very good.

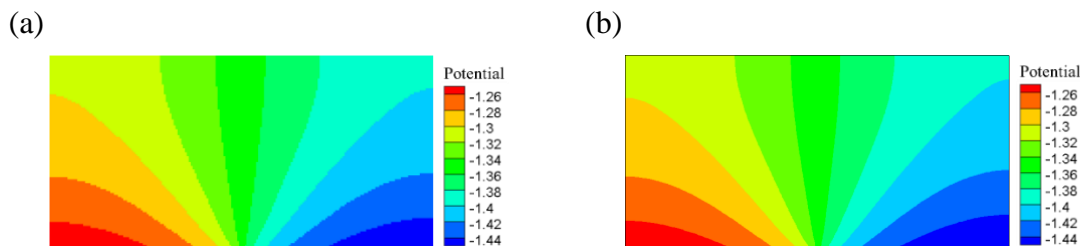


Figure 3.12. Electric potential distribution for mild steel-AE44 galvanic couple obtained by (a) PD; (b) COMSOL.

For a quantitative comparison, we plot the initial current density distribution along the electrode surface in Figure 3.13. From the zoom-in images, we can see that the PD solution, as the horizon size decreases (m -value is fixed to be 4), approaches the result found by COMSOL. In the experimental results, there is a smooth transition of current density at the galvanic joint, and its minimum value is around -50 A/m^2 , while the PD and COMSOL results show much smaller values (around -120 A/m^2), and a sudden jump at the galvanic joint. We notice that, in the experiment (see [2]), the spatial resolution of the current density variation at the joint is highly dependent on the scan rate, or the data acquisition time at each measurement point, but the author did not perform a convergence study on the scan rate. A slower scan rate may lead to sharper transition at the joint. Another possible factor is that, in the real physical system, there exists a transition zone between different materials, while in our models, we assumed a sudden material change at the joint. Note that the difference between the PD and COMSOL results near the interface is due to the finer discretization used by COMSOL near the interface (automatic adaptive refinement).

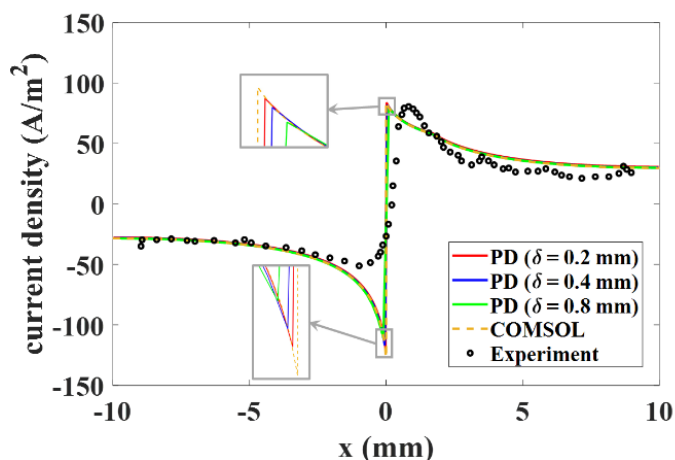


Figure 3.13. Initial current density along the electrode surface for mild steel-AE44 couple: PD solutions, COMSOL (our work), and experimental results from [3].

The experimental profile and that obtained by the PD model for the mild steel-AE44 galvanic couple after 3 days of corrosion are shown in Figure 3.14 (a) and (b), respectively. Although the magnitude of corrosion depth obtained by PD simulation is slightly smaller than that from the experiment, their patterns agree very well.

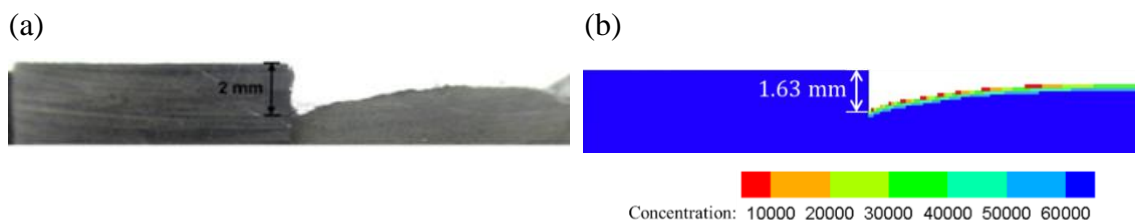


Figure 3.14. Corrosion profiles for the mild steel-AE44 galvanic couple obtained from (a) experiments [3]; (b) PD corrosion model ($\delta = 0.4$ mm).

The comparison for the final corrosion depth between experimental measurements, COMSOL and PD results, is shown in Figure 3.15. In Appendix A we explain how we computed the effective corrosion depth in the PD corrosion model. The corrosion profile obtained by the COMSOL model differs considerably from the experimental one or the one found by the PD corrosion model. Notice, however, that the results presented in

references [5,6,47] show patterns similar to experimental measurements. That is because an artificial step in the geometry of the galvanic joint was used in producing those results. While this artificial step is mentioned in reference [31], it was not mentioned in [32] but its insertion is obvious from the plots shown there. To obtain COMSOL results closer to those measured in experiments, we therefore modify the geometry and insert the small step at the galvanic joint before the start of the COMSOL simulation. This extra treatment, which reduces the generality of the COMSOL model, is necessary because of difficulties with assigning proper BCs in the classical model at the interface, and it allows the corrosion front to start moving in a way similar to what is observed experimentally (see Appendix B). The size of the artificial step determines the smallest mesh size used, and, as its size goes to zero, the maximum corrosion depth obtained appears to converge, as results shown in Appendix B indicate. Note also that in [2,4], the authors did not specify whether or not they inserted this artificial step into their COMSOL model. However, the corrosion depth profiles for the mild steel-AE44 galvanic couple obtained there show a pattern close to our COMSOL results that use the artificial step, and it is, therefore, reasonable to assume that they made use of the step there as well.

As shown in Figure 3.15, both PD and the modified-geometry COMSOL models generate slightly smaller maximum corrosion depths than measured in experiments. Some possible explanations are: 1) the geometry of the electrolyte domain used in simulations is different from the real conditions (our electrolyte “bath” has “walls” at the ends of the sample, while the electrochemical cell used in experiments is likely larger than the sample; also, our model is a 2D approximation of an actual 3D experiment); 2) other corrosion mechanisms, not included here (e.g. crevice or micro-galvanic corrosion,

stress-dependent corrosion rate), may accelerate the corrosion at the interface between the anode and the cathode, as well as at the edge of the anode; 3) the deposition of corrosion products on the corrosion surface (not considered here), can affect the dissolution of metal atoms into the electrolyte and the electric potential around the surface and thus impact the evolution of corrosion [7,8]. Note that the specific shape at the bottom of the trench carved by the galvanic corrosion process is very important when mechanical loadings are involved because it affects the stress profile in that critical region, from which cracks can initiate and propagate (see next section). Microscale experimentation that can quantify, in detail, the shape of the bottom of the trench as galvanic corrosion attack progresses, could be used for further validation of the PD models presented here.

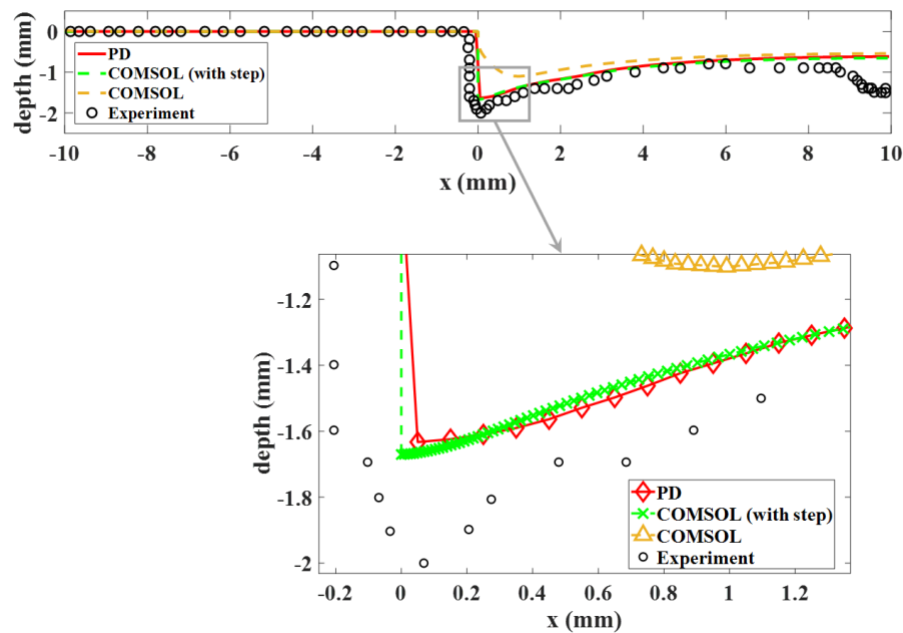


Figure 3.15. Corrosion depths obtained from the PD corrosion model ($\delta = 0.4$ mm), COMSOL with and without the artificial step (our work), and experiments from [3] for mild steel-AE44 galvanic couple. See Appendix A for how we computed the corrosion depth in the PD corrosion model.

The COMSOL curve obtained with the artificial step (see Figure 3.15), appears to be slightly steeper and deeper at the galvanic interface than the PD curves. This is because: (1) the adaptive mesh refinement technique the COMSOL model employs generates a much finer mesh near the interface than the uniform grid used in PD models, leading to a slightly larger current density at the interface than that obtained by the PD corrosion model (see Figure 3.13); and (2), the discretized PD corrosion dissolution model effectively induces a slightly slower corrosion rate, as demonstrated in Section 3.4.1, that could be mitigated by using a larger m -value (not pursued here due to increasing computational cost).

Note that our galvanic corrosion model is general and work for any kind of galvanic joints, as long as the corrosion processes are well described by the mechanisms included in the model. An additional validation for the AE44-AA6063 galvanic couple is provided in Appendix C.

The DCL formed below the corrosion front can degrade material's performance, and can play a significant role in material failure when mechanical loadings are applied to the galvanic couple [48]. In the next section, we investigate the coupling of galvanic corrosion and fracture, when both corrosion attack and mechanical loadings are present. Such a multi-physical problem can be easily treated with PD models but is difficult to simulate using classical models.

3.5 Application of the PD-CF model to galvanic corrosion-induced fracture

In this section, we investigate the coupling effect between galvanic corrosion and mechanical loading on material failure. Galvanic corrosion usually generates localized

and deep trenches at a material interface. As stresses rise/concentrate at these locations, cracks can easily initiate and grow catastrophically. To date, no model has attempted to predict the coupling of these two critical mechanisms involved in material degradation and failure. Such a multi-physical problem can be easily treated using PD models.

We consider the 2D thin plate galvanic couple (mild steel and AE44, see Figure 3.11 (a)) under plane stress conditions and subject to the mechanical loadings and environmental conditions shown in Figure 3.16. As galvanic corrosion progresses at the interface, bending creates a region a higher tensile stresses at the corrosion trench, and a crack may initiate and propagate, if conditions meet the brittle fracture criterion discussed in Section 3.3.1. Note that the loading conditions and geometry have significant effects on the stress concentration at the joint of the galvanic couple. In addition, once a crack initiates in the region damaged by galvanic corrosion, its stress intensity factor also depends on the loading conditions and geometry [49]. In actual 3D structures, conditions along the crack front vary from plane stress near its edges to plane strain in its central part [49]. The thin plate couple we chose here is only for demonstrating our models' capabilities to handle the coupled effect of galvanic corrosion and fracture induced by it. A full 3D example will be pursued once experimental data for this coupled problem become available.

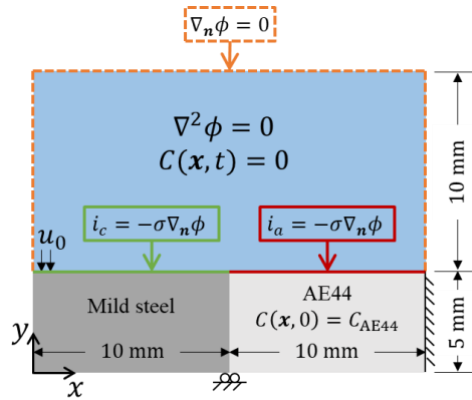


Figure 3.16. Geometry and BCs for the galvanic couple under combined mechanical loading and galvanic corrosion attack.

The local mechanical BCs to be enforced are:

$$\begin{cases} u_y(0 < x < \delta, y = 5, t) = u_0 \\ u_y\left(-\frac{\delta}{2} < x < \frac{\delta}{2}, y = 0, t\right) = 0 \\ u_x(x = 20, 0 < y < 5, t) = 0 \\ u_y(x = 20, 0 < y < 5, t) = 0 \end{cases} \quad (3.37)$$

In the corresponding PD mechanical model, the displacement on the right side is fixed in all directions through a thickness equal to the horizon size δ . At the left top of the cathode domain, a $\delta \times \delta$ square region is displaced at the start of the simulation by a fixed amount ($u_0 = 50 \mu\text{m}$) and is kept constant in time, while another square region (of same dimension) at the central bottom location of the couple is fixed in the vertical direction. In this example, we choose $\delta = 4 \text{ mm}$ and $\Delta x = 1 \text{ mm}$.

Since we did not find experimental data for this type of problem to compare our PD results with, we simply assume a certain fracture toughness (100 J/m^2) for the interface between the metals, to allow a crack to propagate at some point (not too early, not too late) during the formation of the galvanic corrosion trench in our particular example.

Material properties for the alloys and the interface are given in Table 3.5. The Young's modulus for the interface is assumed to be the average of the two alloys [50], i.e., 125 GPa.

Table 3.5. Mechanical properties for materials in the galvanic couple (Figure 3.16).

Parameters	Steel	AE44	Interface
Young's modulus (GPa)	205 [51]	45 [52]	125
Fracture energy (kJ/m ²)	65 [53]	1.5 [54]	0.1

As mentioned previously, the DCL reduces the material properties at the corrosion front. According to experimental measurements (performed on a number of material systems, such as Mg and Al alloys), the DCL can be several micrometers thick and is seamlessly attached to the bulk with gradual change of properties [38–40]. Under external loadings, microcracks can accumulate in the DCL in a brittle fashion and grow into the bulk, leading to significant loss of overall ductility in the structure.

Contours of the damage index obtained by the PD simulation for the problem setup seen in Figure 3.16 are given in Figure 3.17. A simulation movie is also included in Supplementary Materials. The system does not crack under the applied bending loads before corrosion starts, as shown in Figure 3.17 (a). As galvanic corrosion progresses, the geometry changes gradually, creating higher and higher tensile stresses at the bottom of the trench. A few PD bonds start to break because of reaching their critical strain (see Section 3.3.1), but once they do, strains nearby relax and any potential crack growth arrests, and the next call to the corrosion solver is made. After about 41.6 hrs. of corrosion time, as shown in Figure 3.17 (c), a crack suddenly initiates and propagates

along the interface. The crack arrests at some point before reaching the bottom of the interface, because of the displacement-controlled BCs. Note that here we only considered a brittle fracture model. Plastic deformations can also strongly influence crack growth but were not considered in this work.

While galvanic corrosion influences the state of stress in our model (by changing the geometry of the sample as the corrosion trench increases), we did not consider here stress-dependent corrosion rate, the possible direct effect tensile stresses could have on the corrosion itself. A PD model that uses a stress-dependent corrosion rate has been introduced and validated in [11,36]. We do not consider it here for simplicity, but once experimental data on the coupled corrosion-fracture problems become available, such a model can easily be tested. For the same reason, we do not account for the conditions that are specific to crevice corrosion, which has been recently investigated with a PD model in [55]. The example chosen here is demonstrate that possible coupling of degradation due to galvanic corrosion and that due to critical strains that take place in the trench created by the galvanic corrosion process.

Note also that temperature can have a significant influence on the corrosion rate, as well as on the mechanical properties (elasticity, plasticity, fracture). Our model can incorporate such dependencies easily and examples of such effects in thermomechanical fracture have been shown using PD formulations in, , e.g. [44]. Such dependencies are, however, beyond the scope of the present work.

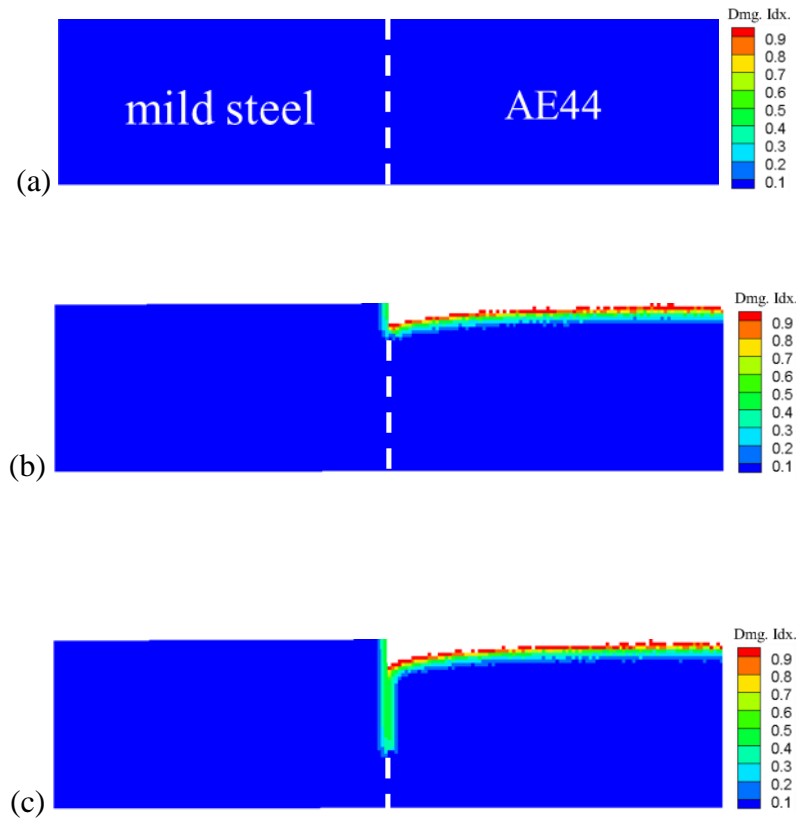


Figure 3.17. Damage index for the mild steel-AE44 galvanic couple under stress corrosion cracking at (a) $t = 0$ hrs, (b) $t = 36$ hrs, and (c) $t = 41.6$ hrs. See also the movie in Supplementary Materials.

To solve this coupled problem using COMSOL or other PDE-based classical models, one needs to consider a model for crack growth. One option is to use cohesive elements with their corresponding damage models defined throughout the domain of interest. Beside the complexity of coupling these physical mechanisms, introducing cohesive elements can significantly increase the computational cost by creating new nodes and increasing the bandwidth of matrices. The PD model, on the other hand, simplifies this process and allows treatment of complex problems with little effort. For realistic, complex problems, the advantages of PD formulations over traditional methods stand out.

3.6 Conclusions

A new peridynamic (PD) model for coupled galvanic corrosion and fracture was introduced. The coupled model consists of a PD electrostatic solver to compute the electric potential distribution over the electrolyte domain, a reformulated PD corrosion dissolution model which is applicable to problems with highly non-uniform current densities along arbitrary-shape corroding surfaces (a common occurrence in galvanic corrosion problems), and a linear elastic-brittle fracture PD model.

The reformulated PD corrosion dissolution model was established based on the electrochemical view of the corrosion process. This change enabled an analytical calibration for the corrosion rate and replaced the original integro-differential equation for corrosion dissolution with an ordinary differential equation, leading to a simplified algorithm/implementation and decreased computational cost of simulation compared to the original PD corrosion model. The new model works well even in cases where the current density is highly location-dependent, or when the curvature of the corrosion surface is high (near reentrant corners, for example), as in the case of galvanic corrosion.

The model was verified for a 2D uniform corrosion case in terms of the initial electric potential and current density, and time-dependent corrosion depth. Validating the model against experimental results available from the literature for two galvanic couples (mild steel-AE44 and AE44-AA6063) was performed. Results obtained with an FEM-based model built using COMSOL were compared with the PD results. It was found that for FEM-based or phase-field models of corrosion in galvanic couples, a “step-down” needs to be artificially inserted in the geometry at the material interface of the couple in order for these models to produce reasonable results. The step appears to be necessary in

models based on partial differential equations because of difficulties in assigning proper boundary conditions at the galvanic couple interface, to correctly initialize the motion of the corrosion front. The need for introducing such geometrical artifacts in a model reduces its generality. Moreover, such artificial modifications to the sample geometry may lead to erroneous results when mechanical loadings are applied to a galvanic couple system, because the stress profile near the interface would be different from the actual one, at least in the early stages of the corrosion process. If there is a strong stress-dependency of the corrosion rate, the likelihood of obtaining wrong results for coupled problems (e.g., galvanic corrosion and fracture) may be further enhanced. The PD model introduced here does not require the artificial change in geometry at the interface to obtain results that match the experimental observations.

A coupled corrosion-fracture problem was solved using the new PD model, demonstrating how fracture can initiate and grow from the sharp trench created by galvanic corrosion. This showed the model's potential for simulating failure caused by the combined galvanic corrosion attack and mechanical loadings.

Acknowledgments

This work has been supported in part by the US National Science Foundation CMMI CDS&E Grant No. 1953346 (program manager Joanne Culbertson) and by a Nebraska System Science award. This work was completed utilizing the Holland Computing Center of the University of Nebraska, which receives support from the Nebraska Research Initiative.

Appendix A. Boundary conditions in PD elastic and electrostatic solvers

Unlike classical local methods, the BCs in peridynamic models are intrinsically nonlocal. However, when solving practical problems, imposing local-type BCs in nonlocal/PD models is usually desired/needed because, in reality, conditions (on the unknown function values or its flux) are imposed at the surfaces of a body, not through a finite layer near the surface. The natural representation of such conditions (based on measurements) is via local BCs. Various methods to impose local BCs in PD models have been investigated in [32,56,57].

For the elastic solver in this work, the local BCs involved (see the example in Section 3.5) is of the Dirichlet type, and the accuracy of the BCs is not a major concern considering the purpose of the example. Therefore, we assign the value of the Dirichlet BCs directly to those PD nodes nearby, as described in Section 3.5.

The electrostatic solver, however, involves Robin-type BCs and requires more accurate representation of the local BCs to be enforced. Therefore, we use the fictitious nodes method (FNM) [32,57,58]. In FNM for PD models, certain constraints are specified on the fictitious region $\tilde{\Omega} = \{\mathbf{x} \notin \Omega \mid \text{distance}(\mathbf{x}, \partial\Omega) < \delta\}$ (the “collar” outside of the solution domain Ω shown in Figure 3.18), so that desired local BCs on $\partial\Omega$ are satisfied or approximately satisfied. There are a couple of different FNMs to enforce local BCs in PD models. In this paper, we use the autonomous mirror-based one (or mirror FNM) [16], which is designed to handle arbitrary boundary shapes, to enforce the local BCs at metal surfaces for the electrostatic solver. The fictitious region overlaps a solid region with thickness δ below the metal surface, as shown in Figure 3.19. A brief review of the

autonomous mirror FNM and a simplification performed for the problem in this work are provided next.

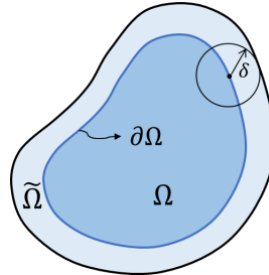


Figure 3.18. Schematic of a PD domain (Ω), its boundary ($\partial\Omega$), and its fictitious region ($\tilde{\Omega}$).

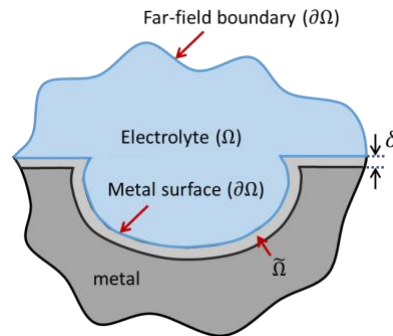


Figure 3.19. An illustration of the electrolyte domain (Ω), boundaries ($\partial\Omega$) and fictitious region in the PD electrostatic model for a general corrosion problem. The PD horizon size is δ .

Consider a body occupying the domain $\Omega \in \mathbb{R}^d$, $d = 2$ or 3 , and an extended fictitious region $\tilde{\Omega} = \{\mathbf{x} \in \mathbb{R}^d \setminus \Omega \mid \text{distance}(\mathbf{x}, \partial\Omega) < \delta\}$. The mirror FNM assigns the constraint $\tilde{u}(\mathbf{x})$ at each $\mathbf{x} \in \tilde{\Omega}$ based on $u(\mathbf{x}^R)$ and $u(\mathbf{x}^P)$ in which $\mathbf{x}^P = O\text{Proj}_{\partial\Omega}(\mathbf{x})$ is the orthogonal projection of \mathbf{x} onto $\partial\Omega$ and $\mathbf{x}^R = \text{Ref}_{\partial\Omega}(\mathbf{x}) = \mathbf{x} + 2(\mathbf{x}^P - \mathbf{x})$ is the reflection, or mirror point, of \mathbf{x} through/across $\partial\Omega$. For $\mathbf{x} \in \tilde{\Omega}$, when $\partial\Omega_{\mathbf{x}} = \{\partial\Omega \cap \mathcal{H}_{\mathbf{x}}\}$ is continuous and the normal to $\partial\Omega_{\mathbf{x}}$ at each $\mathbf{y} \in \partial\Omega_{\mathbf{x}}$ is unique (i.e., $\partial\Omega_{\mathbf{x}} \in G^1$), we have $\overline{\mathbf{x}\mathbf{x}^P} = \alpha \mathbf{n}(\mathbf{x}^P)$, in which $\alpha \in \mathbb{R}^-$ and $\mathbf{n}(\mathbf{x}^P)$ is the outward unit normal vector at \mathbf{x}^P .

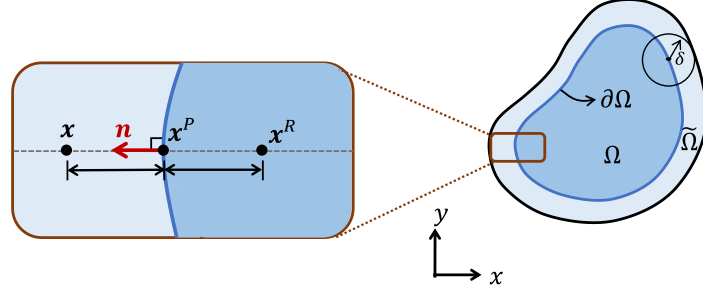


Figure 3.20. A schematic of orthogonal projection of \mathbf{x} onto $\partial\Omega$ and the reflection of \mathbf{x} through/across $\partial\Omega$ in mirror-based FNM [32].

In the mirror FNM, to impose the local Dirichlet BC $u(\mathbf{x}) = u_D(\mathbf{x})$ for $\mathbf{x} \in \partial\Omega_D$ and the Neumann BC $\nabla_n u(\mathbf{x}) = q$ for $\mathbf{x} \in \partial\Omega_N$, $\tilde{u}(\mathbf{x})$ at $\mathbf{x} \in \tilde{\Omega}_D$ is assigned as:

$$\tilde{u}(\mathbf{x}) = 2u(\mathbf{x}^P) - u(\mathbf{x}^R) \quad (3.38)$$

and $\tilde{u}(\mathbf{x})$ at $\mathbf{x} \in \tilde{\Omega}_N$ is assigned as:

$$\tilde{u}(\mathbf{x}) = u(\mathbf{x}^R) + \|\mathbf{x} - \mathbf{x}^R\|q \quad (3.39)$$

respectively. For the local Robin BC $\nabla_n u(\mathbf{x}) = f(u(\mathbf{x}))$ for $\mathbf{x} \in \partial\Omega_R$, we have, for $\mathbf{x} \in \tilde{\Omega}_R$:

$$\begin{aligned} \tilde{u}(\mathbf{x}) &= u(\mathbf{x}^R) + \|\mathbf{x} - \mathbf{x}^R\|f(u(\mathbf{x}^P)) \\ &= u(\mathbf{x}^R) + \|\mathbf{x} - \mathbf{x}^R\|f\left(\frac{u(\mathbf{x}^R) + \tilde{u}(\mathbf{x})}{2}\right) \end{aligned} \quad (3.40)$$

in which the approximation $u(\mathbf{x}^P) = \frac{u(\mathbf{x}^R) + \tilde{u}(\mathbf{x})}{2}$ is made by assuming that the value of u , or \tilde{u} , between \mathbf{x} and \mathbf{x}^R are close to a linear distribution. $\tilde{u}(\mathbf{x})$ in Eq. (3.40) requires to be solved using a nonlinear solver if function f is nonlinear. Constraints applied on fictitious nodes vary with the solution step. See Figure 3.21 for illustrations of how local Dirichlet BCs are enforced in the mirror FNM at each solution step.

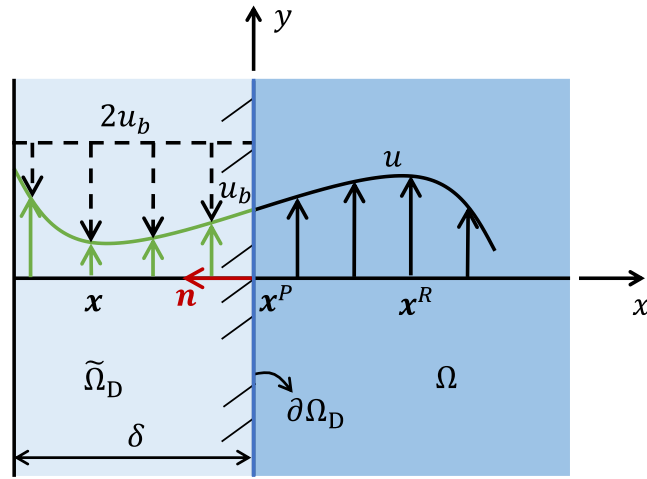


Figure 3.21. Illustration of enforcing a local Dirichlet BC in the mirror FNM (redrawn from [32]).

For the nonlinear robin boundary condition (at the electrode surfaces) in the galvanic corrosion problem we are solving (see Section 3.4.2), instead of using a nonlinear solver to solve Eq. (3.40), one can replace Eq. (3.40) by:

$$\tilde{\phi}(x) = \phi(x^R) - \frac{W(w_0)}{b} \quad (3.41)$$

for $x \in \tilde{\Omega}_R$ where $y = W(w_0)$ is the Lambert W function which satisfies $ye^y = w_0$ and

$$w_0 = -\frac{i_0 \ln 10}{2\sigma\beta} \times \|\overrightarrow{xx^R}\| \times 10^{\left(\frac{\phi(x^R) + \tilde{\phi}(x)}{2} - \phi_0\right)} \quad (3.42)$$

where i_0 , σ , β and ϕ_0 are parameters determined by the polarization curve and given in Table 3.3.

Appendix A. Computing effective corrosion depth

The corrosion depth distribution for a problem with general geometry is usually measured, when available, in the direction normal to the original surface. For the

problems considered in this work, that direction is the vertical direction. Therefore, we will measure the depth at each horizontal coordinate x . For a fair comparison of corrosion depth obtained by our PD model and by a classical model (analytical or numerical) or experiments, we will consider both the fully corroded region ($d(\mathbf{x}, t) = 1$) and the diffusion-based corrosion layer ($d(\mathbf{x}, t) \in (0,1)$) when computing the total mass loss.

The effective corrosion depth can then be computed at $x = x_0$ as:

$$z_h(x_0, t) = \frac{1}{C_{\text{solid}} - C_{\text{sat}}} \int_{\psi(x_0, t)} [C_{\text{solid}} - C(x_0, y, t)] dy \quad (3.43)$$

where $\psi(x_0, t) = \{\mathbf{x}(x, y) | x = x_0 \text{ and } d(\mathbf{x}, t = 0) = 0 \text{ and } d(\mathbf{x}, t) > 0\}$. The nodes with $d(\mathbf{x}, t = 0) = 0$ are those solid at the initial time, while nodes with $d(\mathbf{x}, t) > 0$ include liquid and partially damaged ones at the current time. The schematic of $\psi(x_0)$ is shown in Figure 3.22.

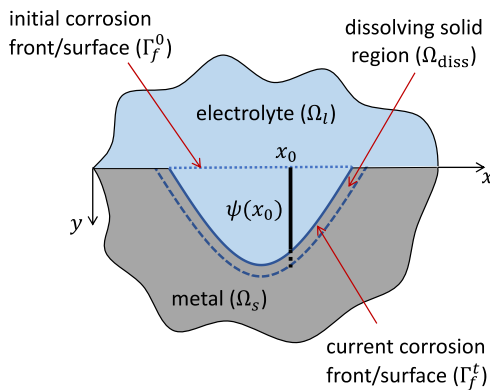


Figure 3.22. A schematic of $\psi(x_0)$ over which the PD effective corrosion depth is computed in this work.

Appendix B. COMSOL modeling of galvanic corrosion

In COMSOL MultiPhysics[®], the dissolution/corrosion process is modeled through the deformation of the boundary using the Arbitrary Lagrangian-Eulerian Method [47]. The

deformation is determined by relating the boundary velocity to the electrode corrosion velocity, by the following equation:

$$V_{\text{diss,tot}} = \frac{\partial \mathbf{y}}{\partial t} \cdot \mathbf{n} \Big|_{\text{anode}} = \sum_j \frac{M_j}{\rho_j} \sum_k \frac{\vartheta_{j,k} i_k}{q_k F} \quad (3.44)$$

where \mathbf{n} is the normal vector to the boundary, M_j and ρ_j are molar mass and density of the species j , respectively, $\vartheta_{j,k}$, i_k and q_k are the stoichiometric coefficient of species j , local current density, and the number of participating electrons, respectively, associated with the electrode reactions of index k .

While Eq. (3.44) assumes that deformation/dissolution occurs only in the normal direction of the dissolving electrode (anode) boundary, a pointwise constraint is applied to non-dissolving boundaries (cathode) to prevent any dissolution in their normal directions (zero normal displacement):

$$d\mathbf{y} \cdot \mathbf{n} \Big|_{\text{Cathode}} = 0. \quad (3.45)$$

Such treatments may cause challenges for cases with shared nodes at the anode-cathode interface (e.g., the galvanic corrosion shown in Figure 3.11 (a)), where the deformation/dissolution may grow into the cathode. To resolve this issue, one may extend the cathode boundary by introducing a small geometric step at the cathode-anode interface, as shown in Figure 3.23.

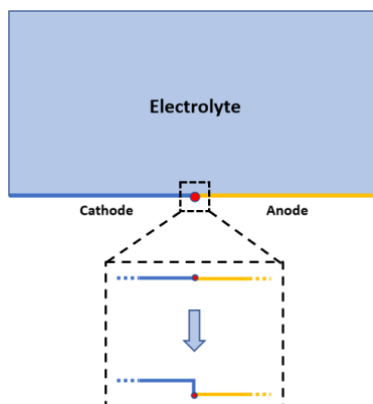


Figure 3.23. A schematic of the artificial geometric step at the interface between the anode and the cathode.

To build the geometry with small step incorporated at the anode-cathode interface the whole domain was constructed using two separate shapes with a difference in height. The two shapes were then connected using the *Booleans and Partitions* module. For the physics of the problem, the *secondary current distribution* and *deformed geometry* modules were used. Then, the electrolyte domain and two electrode surfaces were defined in the model. The cathodic reduction reaction was assigned to the cathode electrode surface, while the anodic corrosion reaction and the resulting boundary movement were defined at the anode electrode surface. The stoichiometric coefficients for dissolving-depositing species were defined for the anode part. To apply a constraint for the planar non-depositing walls in order to enforce a zero boundary movement in the normal direction of surfaces other than the anode, zero normal displacement BC was used in the Multiphysics setting.

For the COMSOL modeling of the galvanic corrosion problem in Figure 3.11 (a), the FE mesh at the initial stage is shown in Figure 3.24. There are in total 7 one-node vertex elements, 183 two-node edge elements and 7189 three-node triangular elements, while

the number of mesh points is 3687. As we explained above, the small step-down (0.1 mm) at the interface between the anode and the cathode is necessary.

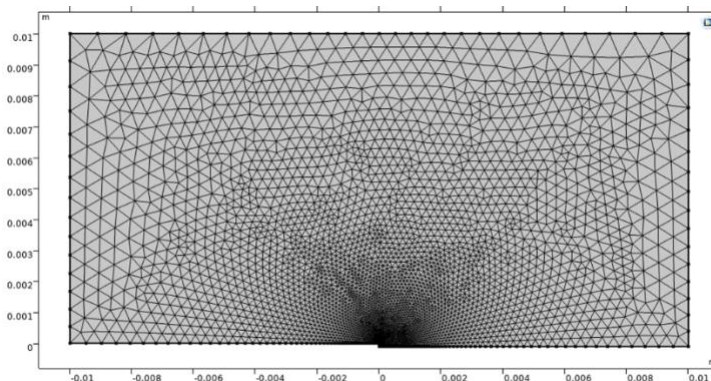


Figure 3.24. Finite element mesh in COMSOL for the galvanic cell shown in Figure 3.11 (a). Notice the artificial step on the bottom side.

The height of this vertical geometric step controls the mesh resolution. Table 3.6 represents the result for maximum corrosion depth as the height of the step decreases, for the AE44-AA6063 galvanic couple.

Table 3.6. Convergence study on the maximum corrosion depth as the height of the initial step decreases, for the AE44-AA6063 galvanic couple.

Step height (mm)	No. of elements	Max. corrosion depth (mm)
1	1001	0.236905914
0.5	1040	0.240754949
0.2	1078	0.249791228
0.1	1180	0.255897817
0.01	1886	0.259696086
0.001	3850	0.260926697
0.0001	8464	0.261126347

Appendix C. Galvanic corrosion of a AE44-AA6063 couple

In this appendix, we use the AE44-AA6063 galvanic couple test the PD and COMSOL models and compare their results with the experimental data provided in [3]. The coefficients used to fit the polarization curve for AA6063 are shown in Table 3.7, while those for AE44 can be found in Table 3.3.

Table 3.7. Data used in the Tafel's equation for AA6063 [2].

		i_0 (A/m ²) (V)	b_c (V)	φ_0 (V, SCE)
AA6063	$\phi \leq -1.363$	0.142	-0.0701	-1.363
	$\phi > -1.363$	0.142	-0.0051	-1.363

The quantitative comparison of the final corrosion depth between experimental measurement, PD simulation and COMSOL simulation (with the artificial step at the joint included), after 3 days of corrosion, is shown in Figure 3.25. As we can see, the corrosion depth obtained from PD simulation agrees with that from the COMSOL simulation. However, they have two significant differences compared with the corrosion depth from the experiment. First, in the experiment, the corrosion does not take place exactly along the interface between two materials. Some part of the AA6063 (which is supposed to be cathode) is also corroded. Second, in the experiment, the corrosion trench is localized near the interface, and is very deep, while the computations show a much shallower trench and considerable reach of corrosion along the AE44 surface. It is highly possible that some other forms of corrosion, such as crevice and micro-galvanic corrosions, take place at the interface and play a significant role here. While we did not consider these mechanisms into our model here, some of them have been separately

investigated with PD formulations (see [35,55]), and future developments will include them.

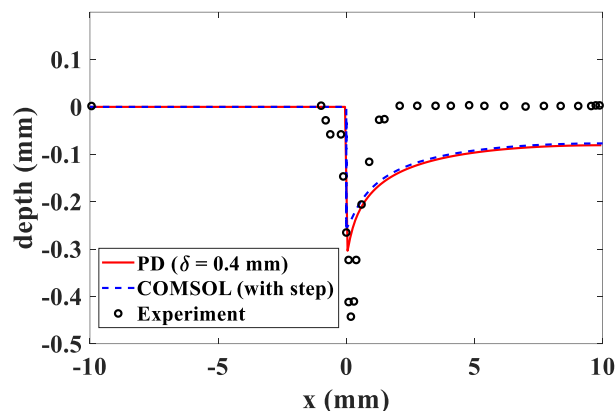


Figure 3.25. Quantitative comparison of the final corrosion depth for AE44-AA6063 galvanic couple between experimental measurement [3], PD simulation and COMSOL simulation.

References

- [1] S. Jafarzadeh, Z. Chen, F. Bobaru, Computational modeling of pitting corrosion, *Corros. Rev.* 37 (2019) 419–439. <https://doi.org/10.1515/correv-2019-0049>.
- [2] K.B. Deshpande, Validated numerical modelling of galvanic corrosion for couples: Magnesium alloy (AE44)–mild steel and AE44–aluminium alloy (AA6063) in brine solution, *Corros. Sci.* 52 (2010) 3514–3522. <https://doi.org/10.1016/j.corsci.2010.06.031>.
- [3] K.B. Deshpande, Experimental investigation of galvanic corrosion: Comparison between SVET and immersion techniques, *Corros. Sci.* 52 (2010) 2819–2826. <https://doi.org/10.1016/j.corsci.2010.04.023>.
- [4] I. Adlakha, B.G. Bazehhour, N.C. Muthegowda, K.N. Solanki, Effect of mechanical loading on the galvanic corrosion behavior of a magnesium–steel structural joint, *Corros. Sci.* 133 (2018) 300–309. <https://doi.org/10.1016/j.corsci.2018.01.038>.
- [5] A. Imanian, M. Amiri, Phase field modeling of galvanic corrosion, (2018) arXiv preprint. <http://arxiv.org/abs/1804.08517>.
- [6] W. Mai, S. Soghrati, New phase field model for simulating galvanic and pitting corrosion processes, *Electrochim. Acta.* 260 (2018) 290–304. <https://doi.org/10.1016/j.electacta.2017.12.086>.

- [7] W. Sun, G. Liu, L. Wang, T. Wu, Y. Liu, An arbitrary Lagrangian–Eulerian model for studying the influences of corrosion product deposition on bimetallic corrosion, *J. Solid State Electrochem.* 17 (2013) 829–840. <https://doi.org/10.1007/s10008-012-1935-9>.
- [8] K. Wang, C. Li, Y. Li, J. Lu, Y. Wang, X. Luo, Multi-physics analysis of the galvanic corrosion of Mg-steel couple under the influence of time-dependent anisotropic deposition film, *J. Magnes. Alloy.* (2021). <https://doi.org/10.1016/j.jma.2020.11.022>.
- [9] Z. Chen, F. Bobaru, Peridynamic modeling of pitting corrosion damage, *J. Mech. Phys. Solids.* 78 (2015) 352–381. <https://doi.org/10.1016/j.jmps.2015.02.015>.
- [10] S. Jafarzadeh, Z. Chen, J. Zhao, F. Bobaru, Pitting, lacy covers, and pit merger in stainless steel: 3D peridynamic models, *Corros. Sci.* 150 (2019) 17–31. <https://doi.org/10.1016/j.corsci.2019.01.006>.
- [11] Z. Chen, S. Jafarzadeh, J. Zhao, F. Bobaru, A coupled mechano-chemical peridynamic model for pit-to-crack transition in stress-corrosion cracking, *J. Mech. Phys. Solids.* 146 (2021) 104203. <https://doi.org/10.1016/j.jmps.2020.104203>.
- [12] R. Duddu, N. Kota, S.M. Qidwai, An extended finite element method based approach for modeling crevice and pitting corrosion, *J. Appl. Mech.* 83 (2016) 081003. <https://doi.org/10.1115/1.4033379>.
- [13] S. Jafarzadeh, Z. Chen, F. Bobaru, Peridynamic modeling of repassivation in pitting corrosion of stainless steel, *Corrosion.* 74 (2018) 393–414. <https://doi.org/10.5006/2615>.
- [14] E. McCafferty, *Introduction to Corrosion Science*, Springer New York, New York, NY, 2010. <https://doi.org/10.1007/978-1-4419-0455-3>.
- [15] C. Lin, H. Ruan, S.-Q. Shi, Phase field study of mechanico-electrochemical corrosion, *Electrochim. Acta.* 310 (2019) 240–255. <https://doi.org/10.1016/j.electacta.2019.04.076>.
- [16] J. Zhao, S. Jafarzadeh, Z. Chen, F. Bobaru, An algorithm for imposing local boundary conditions in peridynamic models on arbitrary domains, *EngrXiv.* (2020). <https://doi.org/10.31224/osf.io/7z8qr>.
- [17] D.A. Jones, *Principles and prevention of corrosion*, Macmillan, 1992.
- [18] A.J. Bard, L. Faulkner, *Electrochemical Methods, Fundamental Applications*, John Wiley & Sons, Inc., 2001.
- [19] S.M. Sharland, C.P. Jackson, A.J. Diver, A finite-element model of the propagation of corrosion crevices and pits, *Corros. Sci.* 29 (1989) 1149–1166. [https://doi.org/10.1016/0010-938X\(89\)90051-6](https://doi.org/10.1016/0010-938X(89)90051-6).
- [20] C. Tsuyuki, A. Yamanaka, Y. Ogimoto, Phase-field modeling for pH-dependent general and pitting corrosion of iron, *Sci. Rep.* 8 (2018) 12777. <https://doi.org/10.1038/s41598-018-31145-7>.
- [21] S.A. Silling, Reformulation of elasticity theory for discontinuities and long-range

- forces, *J. Mech. Phys. Solids*. 48 (2000) 175–209. [https://doi.org/10.1016/S0022-5096\(99\)00029-0](https://doi.org/10.1016/S0022-5096(99)00029-0).
- [22] S.A. Silling, E. Askari, A meshfree method based on the peridynamic model of solid mechanics, *Comput. Struct.* 83 (2005) 1526–1535. <https://doi.org/10.1016/j.compstruc.2004.11.026>.
- [23] E. Madenci, E. Oterkus, *Peridynamic Theory and Its Applications*, Springer New York, New York, NY, 2014. <https://doi.org/10.1007/978-1-4614-8465-3>.
- [24] F. Bobaru, G. Zhang, Why do cracks branch? A peridynamic investigation of dynamic brittle fracture, *Int. J. Fract.* 196 (2015) 59–98. <https://doi.org/10.1007/s10704-015-0056-8>.
- [25] F. Bobaru, J.T. Foster, P.H. Geubelle, S.A. Silling, *Handbook of Peridynamic Modeling*, CRC press, 2016. <https://doi.org/10.1201/9781315373331>.
- [26] S.A. Silling, R.B. Lehoucq, Peridynamic theory of solid mechanics, in: *Adv. Appl. Mech.*, 2010: pp. 73–168. [https://doi.org/10.1016/S0065-2156\(10\)44002-8](https://doi.org/10.1016/S0065-2156(10)44002-8).
- [27] Y.D. Ha, F. Bobaru, Studies of dynamic crack propagation and crack branching with peridynamics, *Int. J. Fract.* 162 (2010) 229–244. <https://doi.org/10.1007/s10704-010-9442-4>.
- [28] J.T. Foster, S.A. Silling, W.W. Chen, Viscoplasticity using peridynamics, *Int. J. Numer. Methods Eng.* 81 (2010) 1242–1258. <https://doi.org/10.1002/nme.2725>.
- [29] Y.L. Hu, N. V. De Carvalho, E. Madenci, Peridynamic modeling of delamination growth in composite laminates, *Compos. Struct.* 132 (2015) 610–620. <https://doi.org/10.1016/j.compstruct.2015.05.079>.
- [30] F. Bobaru, M. Duangpanya, The peridynamic formulation for transient heat conduction, *Int. J. Heat Mass Transf.* 53 (2010) 4047–4059. <https://doi.org/10.1016/j.ijheatmasstransfer.2010.05.024>.
- [31] F. Bobaru, M. Duangpanya, A peridynamic formulation for transient heat conduction in bodies with evolving discontinuities, *J. Comput. Phys.* 231 (2012) 2764–2785. <https://doi.org/10.1016/j.jcp.2011.12.017>.
- [32] S. Oterkus, E. Madenci, A. Agwai, Peridynamic thermal diffusion, *J. Comput. Phys.* 265 (2014) 71–96. <https://doi.org/10.1016/j.jcp.2014.01.027>.
- [33] J. Zhao, Z. Chen, J. Mehrmashadi, F. Bobaru, Construction of a peridynamic model for transient advection-diffusion problems, *Int. J. Heat Mass Transf.* 126 (2018) 1253–1266. <https://doi.org/10.1016/j.ijheatmasstransfer.2018.06.075>.
- [34] Z. Chen, G. Zhang, F. Bobaru, The influence of passive film damage on pitting corrosion, *J. Electrochem. Soc.* 163 (2016) C19–C24. <https://doi.org/10.1149/2.0521602jes>.
- [35] S. Jafarzadeh, Z. Chen, F. Bobaru, Peridynamic modeling of intergranular corrosion damage, *J. Electrochem. Soc.* 165 (2018) C362–C374. <https://doi.org/10.1149/2.0821807jes>.

- [36] S. Jafarzadeh, Z. Chen, S. Li, F. Bobaru, A peridynamic mechano-chemical damage model for stress-assisted corrosion, *Electrochim. Acta.* 323 (2019) 134795. <https://doi.org/10.1016/j.electacta.2019.134795>.
- [37] Z. Chen, D. Bakenhus, F. Bobaru, A constructive peridynamic kernel for elasticity, *Comput. Methods Appl. Mech. Eng.* 311 (2016) 356–373. <https://doi.org/10.1016/j.cma.2016.08.012>.
- [38] S. Li, Z. Chen, F. Wang, B. Cui, L. Tan, F. Bobaru, Analysis of corrosion-induced diffusion layer in ZK60A magnesium alloy, *J. Electrochem. Soc.* 163 (2016) C784–C790. <https://doi.org/10.1149/2.1001613jes>.
- [39] S. Li, Z. Chen, L. Tan, F. Bobaru, Corrosion-induced embrittlement in ZK60A Mg alloy, *Mater. Sci. Eng. A.* 713 (2018) 7–17. <https://doi.org/10.1016/j.msea.2017.12.053>.
- [40] R. Vallabhaneni, T.J. Stannard, C.S. Kaira, N. Chawla, 3D X-ray microtomography and mechanical characterization of corrosion-induced damage in 7075 aluminium (Al) alloys, *Corros. Sci.* 139 (2018) 97–113. <https://doi.org/10.1016/j.corsci.2018.04.046>.
- [41] D. Yavas, P. Mishra, A. Alshehri, P. Shrotriya, K.R. Hebert, A.F. Bastawros, Nanoindentation study of corrosion-induced grain boundary degradation in a pipeline steel, *Electrochem. Commun.* 88 (2018) 88–92. <https://doi.org/10.1016/j.elecom.2018.02.001>.
- [42] J.T. Burns, S. Kim, R.P. Gangloff, Effect of corrosion severity on fatigue evolution in Al–Zn–Mg–Cu, *Corros. Sci.* 52 (2010) 498–508. <https://doi.org/10.1016/j.corsci.2009.10.006>.
- [43] J.R. Shewchuk, An Introduction to the Conjugate Gradient Method Without the Agonizing Pain, Tech. Rep. C. Carnegie Mellon Univ. (1994). [ftp://ftp.unicauca.edu.co/Facultades/.FIET_serepiteencuentasyocupaespaacio/DEIC/docs/Materias/computacion inteligente/parte II/semana12/gradient/painless-conjugate-gradient.pdf](ftp://ftp.unicauca.edu.co/Facultades/.FIET_serepiteencuentasyocupaespaacio/DEIC/docs/Materias/computacion%20inteligente/parte%20II/semana12/gradient/painless-conjugate-gradient.pdf).
- [44] Z. Xu, G. Zhang, Z. Chen, F. Bobaru, Elastic vortices and thermally-driven cracks in brittle materials with peridynamics, *Int. J. Fract.* 209 (2018) 203–222. <https://doi.org/10.1007/s10704-017-0256-5>.
- [45] S. Jafarzadeh, A. Larios, F. Bobaru, Efficient solutions for nonlocal diffusion problems via boundary-adapted spectral methods, *J. Peridynamics Nonlocal Model.* 2 (2020) 85–110. <https://doi.org/10.1007/s42102-019-00026-6>.
- [46] S. Jafarzadeh, L. Wang, A. Larios, F. Bobaru, A fast convolution-based method for peridynamic transient diffusion in arbitrary domains, *Comput. Methods Appl. Mech. Eng.* 375 (2021) 113633. <https://doi.org/10.1016/j.cma.2020.113633>.
- [47] COMSOL, Corrosion Module User’s Guide, 2018. <https://doc.comsol.com/5.4/doc/com.comsol.help.corr/CorrosionModuleUsersGuide.pdf>.
- [48] H. Tada, P.C. Paris, G.R. Irwin, *The Stress Analysis of Cracks Handbook*, Third

- Edition, ASME Press, 2000. <https://doi.org/10.1115/1.801535>.
- [49] T.L. Anderson, *Fracture Mechanics*, CRC Press, 2017. <https://doi.org/10.1201/9781315370293>.
- [50] A. Katiyar, J.T. Foster, H. Ouchi, M.M. Sharma, A peridynamic formulation of pressure driven convective fluid transport in porous media, *J. Comput. Phys.* 261 (2014) 209–229. <https://doi.org/10.1016/j.jcp.2013.12.039>.
- [51] J.B. Yan, J.Y.R. Liew, M.H. Zhang, J.Y. Wang, Mechanical properties of normal strength mild steel and high strength steel S690 in low temperature relevant to Arctic environment, *Mater. Des.* 61 (2014) 150–159. <https://doi.org/10.1016/j.matdes.2014.04.057>.
- [52] M.M. Avedesian, H. Baker, *ASM specialty handbook: magnesium and magnesium alloys*, ASM Int. (1999).
- [53] K. Prasad, M. Srinivas, S.V. Kamat, Influence of mixed mode I/III loading on dynamic fracture toughness of mild steel at room and low temperatures, *Mater. Sci. Eng. A.* 590 (2014) 54–59. <https://doi.org/10.1016/j.msea.2013.09.099>.
- [54] N. Winzer, A. Atrens, G. Song, E. Ghali, W. Dietzel, K.U. Kainer, N. Hort, C. Blawert, A critical review of the stress corrosion cracking (SCC) of magnesium alloys, *Adv. Eng. Mater.* 7 (2005) 659–693. <https://doi.org/10.1002/adem.200500071>.
- [55] S. Jafarzadeh, J. Zhao, M. Shakouri, F. Bobaru, A peridynamic model for crevice corrosion damage, submitted, (2021).
- [56] Q. Du, M. Gunzburger, R.B. Lehoucq, K. Zhou, A nonlocal vector calculus, nonlocal volume-constrained problems, and nonlocal balance laws, *Math. Model. Methods Appl. Sci.* 23 (2013) 493–540. <https://doi.org/10.1142/S0218202512500546>.
- [57] Y. Tao, X. Tian, Q. Du, Nonlocal diffusion and peridynamic models with Neumann type constraints and their numerical approximations, *Appl. Math. Comput.* 305 (2017) 282–298. <https://doi.org/10.1016/j.amc.2017.01.061>.
- [58] Q. V. Le, F. Bobaru, Surface corrections for peridynamic models in elasticity and fracture, *Comput. Mech.* 61 (2018) 499–518. <https://doi.org/10.1007/s00466-017-1469-1>.

Chapter 4 Construction of a Peridynamic Model for Transient Advection-diffusion Problems

4.1 Introduction and motivation

The classical advection-diffusion equation (ADE) is present in the mathematical description of many phenomena related to heat transfer, fluid dynamics, chemistry, biology, environmental sciences, etc. Some of the common practical problems include the spread of pollutants in groundwater [1], the transport of drugs in body tissue [2-4].

Analytical solutions of the ADE are limited to only a few special cases, while for most of such problems one needs to obtain approximate solutions. Various numerical techniques have been used to approximately solve the ADE, such as Finite Element Method (FEM) [5-9], Finite Difference Method (FDM) [10, 11] and Boundary Element Method (BEM) [12, 13]. The classical ADE, however, cannot capture some more general environmental conditions such as anomalous diffusion observed in heterogeneous environments, in which nonlocal effects play an important role [14].

In recent years, peridynamics, a nonlocal method, has received much attention. The theory of peridynamics was introduced by Silling [15] as a reformulation of the classical continuum mechanics for modeling mechanical behavior in solid materials. The term peridynamics comes from the Greek roots for “near” and “force”. An important generalization of the theory has appeared in [16]. In the peridynamic model, spatial integration rather than differentiation is used, and this leads to a mathematically consistent formulation, even when strong discontinuities appear due to breaking and fragmentation of the material.

The peridynamic (PD) theory has been successfully applied to model fracture in brittle materials [17-24], rupture of membranes and nanofiber networks [25, 26], damage in composite materials [27-32], fatigue failure [33-35], pitting corrosion [36-38], phase transformations [39], plastic and viscoplastic deformation [40-42] and hydraulic fracturing [43].

Gerstle et al. [44], Bobaru and Duangpanya [45, 46], extended the ideas of Silling to diffusion problems. These models use the bond-based version of peridynamics. Generic forms of PD diffusion models have been analyzed mathematically as well [47, 48]. A formal derivation for a state-based PD model [49] of heat diffusion appeared in [50], but the bond-based approach was adopted for numerical examples. As a generalization of the work by Bobaru and Duangpanya, a state-based PD formulation was given in [51] for convective single-phase flow in heterogeneous porous media, in which the flow potential difference was assumed to cause the fluid to flow only along the bond (pressure driven flow). Recently, a state-based peridynamic heat conduction model which considers the non-Fourier and nonlocal effects was developed [52].

To model problems in which both diffusion and flow are involved, the advection-diffusion equations need to be considered. A nonlocal model for *steady-state* advection-diffusion problems has been introduced in [53] where several examples were solved numerically using finite element discretization and results were compared with analytical solutions of both the nonlocal model and the corresponding local model. The nonlocal upwind kernel proposed in [53] was further discussed in [54].

In this paper, we **construct** a PD model for the *transient* advection-diffusion problem, following a similar procedure to that used in [45]. In this way we arrive at a different PD kernel from the one postulated in [53]. We test our model with examples in both 1D and 2D and compare PD results with classical solutions. We also evaluate the effectiveness of the hybrid model compared with the upwind and central models and find it to perform well even in advection-dominated cases. Convergence studies in the limit of the PD horizon going to zero show convergence to the classical results. Finally, we use the new model to simulate advection-diffusion in complex heterogeneous media, with little extra effort.

4.2 The peridynamic formulation for advection-diffusion problems

4.2.1 Peridynamic equation for diffusion problems

The PD equation for diffusion without any sources or sinks has been given in [55]:

$$\frac{\partial \theta(\mathbf{x}, t)}{\partial t} = \int_{H_{\mathbf{x}}} J_n(\mathbf{x}', \mathbf{x}, t) dV_{\mathbf{x}'}, \quad (4.1)$$

where $\theta(\mathbf{x}, t)$ is the concentration at point \mathbf{x} at time t , $H_{\mathbf{x}}$ is the horizon region of \mathbf{x} , \mathbf{x}' is a point inside $H_{\mathbf{x}}$, $V_{\mathbf{x}'}$ is the volume (area in 2D, length in 1D) belongs to \mathbf{x}' , and the integrand $J_n(\mathbf{x}', \mathbf{x}, t)$ usually takes the following form:

$$J_n(\mathbf{x}', \mathbf{x}, t) = \begin{cases} d(\|\mathbf{x}' - \mathbf{x}\|) \frac{\theta(\mathbf{x}', t) - \theta(\mathbf{x}, t)}{\|\mathbf{x}' - \mathbf{x}\|^n} & \|\mathbf{x}' - \mathbf{x}\| \leq \delta, \\ 0 & \|\mathbf{x}' - \mathbf{x}\| > \delta \end{cases}, \quad (4.2)$$

where δ is the horizon size, n is a real number (smaller than or equal to 2, see [55]) usually selected to be 0, 1, or 2, and $d(\|\mathbf{x}' - \mathbf{x}\|)$ is the micro-diffusivity function.

The constructive approach proposed in [45] gives $n = 2$, while the other usually employed values in the literature ($n = 1$ and $n = 0$) are postulated. According to Chen and Bobaru (see [55]), with one-point Gaussian quadrature used for discretization, when the horizon size approaches zero and the ratio m between the horizon size and grid spacing is maintained constant (this is the so-called δ -convergence, see [56]), only the form with $n = 2$ leads to results that converge to the classical solution. For other values of n , δ -convergence happens but to different values other than the classical one. Notice that other forms of discretization (see the asymptotically compatible discretizations in [47]), may lead to δ -convergence for other values of n . In this work, however, we only consider the one-point Gaussian quadrature since it leads to a meshfree model, which is naturally well suited for capturing damage evolution (see [55]). With $n = 2$, the PD diffusion equation reads:

$$\frac{\partial \theta(\mathbf{x}, t)}{\partial t} = \int_{H_{\mathbf{x}}} d(\mathbf{x}', \mathbf{x}) \frac{\theta(\mathbf{x}', t) - \theta(\mathbf{x}, t)}{\|\mathbf{x}' - \mathbf{x}\|^2} dV_{\mathbf{x}'}. \quad (4.3)$$

The micro-diffusivity function can have different forms with different horizon-scale behaviors. Two popular choices are the “constant” micro-diffusivity:

$$d(\mathbf{x}', \mathbf{x}) = \begin{cases} d_0 & \|\mathbf{x}' - \mathbf{x}\| \leq \delta \\ 0 & \|\mathbf{x}' - \mathbf{x}\| > \delta \end{cases} \quad (4.4)$$

which means the interaction between points (when $\|\mathbf{x}' - \mathbf{x}\| \leq \delta$) is independent of the distance between them, and the “linear” (also called “triangular”) micro-diffusivity, in which the interaction is linearly dependent on the distance (when $\|\mathbf{x}' - \mathbf{x}\| \leq \delta$):

$$d(\mathbf{x}', \mathbf{x}) = \begin{cases} d_1 \left(1 - \frac{\|\mathbf{x}' - \mathbf{x}\|}{\delta}\right) & \|\mathbf{x}' - \mathbf{x}\| \leq \delta \\ 0 & \|\mathbf{x}' - \mathbf{x}\| > \delta \end{cases}. \quad (4.5)$$

By matching the PD solution with the classical one for the case of linear concentration profile, one obtains the parameters above as follows: for the one-dimensional case, $d_0 = \frac{D}{\delta}$ and $d_1 = \frac{2D}{\delta}$; for two-dimensional case, $d_0 = \frac{4D}{\pi\delta^2}$ and $d_1 = \frac{12D}{\pi\delta^2}$ (see [55]); For 3-dimensional case, $d_0 = \frac{9D}{2\pi\delta^3}$ and $d_1 = \frac{18D}{\pi\delta^3}$.

According to [55], the rate of convergence of the nonlocal solution to the classical one, under δ -convergence, is better with the linear micro-diffusivity, which will be used in the following sections.

4.2.2 Derivation of peridynamic transient advection equation

For the derivation of PD advection equation, we assume that diffusion is negligible and use the constructive approach similar to the one used in [45].

Consider a cylinder bounded by two parallel planes P and P' with different mass concentration θ and θ' , as shown in Figure 4.1. The cross-sectional area equals s . It is assumed that no mass transfer takes place through the cylinder's side surface A and the cylinder is short enough so that the flow field is uniform along it. The quantity of mass which flows into the cylinder per unit time equals:

$$s(\theta - \theta')\mathbf{V} \cdot \mathbf{e}_{\mathbf{x}\mathbf{x}'}, \quad (4.6)$$

where \mathbf{V} is the flow velocity of the flow field at \mathbf{x} , in the conventional sense, and $\mathbf{e}_{\mathbf{x}\mathbf{x}'}$ is the unit vector along the cylinder's longitudinal axis.

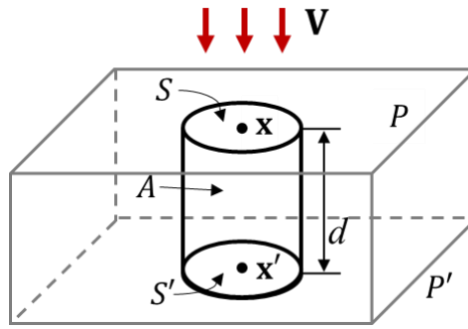


Figure 4.1. Mass transfer under a uniform fluid flow in a cylinder bounded by two planes which are at different concentrations (redrawn from [45]).

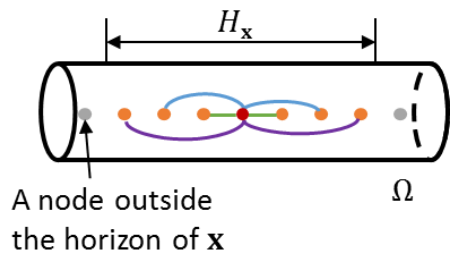
If θ_a is defined as the average concentration in the cylinder, then the rate of mass change equals

$$ds \frac{\partial \theta_a}{\partial t}. \quad (4.7)$$

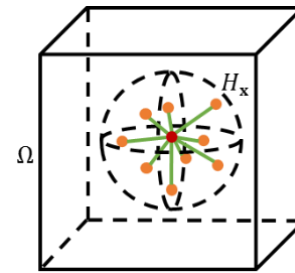
From mass conservation, Eqs. (4.6) and (4.7) give:

$$\frac{\partial \theta_a}{\partial t} = - \frac{\theta_{x'} - \theta_x}{\|\mathbf{x}' - \mathbf{x}\|} \mathbf{V} \cdot \mathbf{e}_{xx'}. \quad (4.8)$$

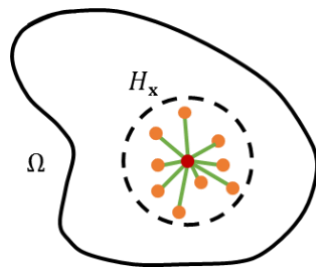
To derive the PD advection equation, a body occupying a region Ω (in 1D, 2D or 3D) is considered (see Figure 4.2). The body is composed of material points associated with mass and volume. Each point is connected to other points in the body through “concentration bonds”. The following derivation is for one-dimensional pure advection in a tube. It can be easily extended to multi-dimensional cases.



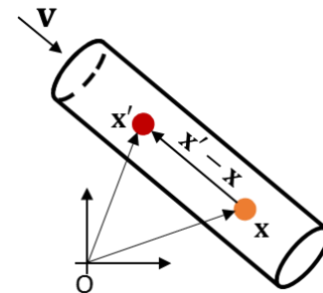
(a) Horizon and bonds connected to a node in 1D.



(c) Horizon region and some PD bonds for a node in a 3D body.



(b) Horizon region and some PD bonds for a node in a 2D body.



(d) A PD concentration bond.

Figure 4.2. The PD description of a body (a, b, c) and the concentration bond (d) (redrawn from [45]).

It is reasonable to assume that point \mathbf{x} only interacts with points located in a certain neighborhood of \mathbf{x} (denoted by $H_{\mathbf{x}}$), called the horizon region (or simply “the horizon”) of \mathbf{x} . For convenience, $H_{\mathbf{x}}$ is taken to be a sphere/circle of radius δ (or a line segment with length 2δ in 1D), centered at \mathbf{x} (see Figure 4.2).

Considering that all bonds are “insulated” from each other so that no mass transfer happens between them, and making the analogy with the cylinder that lead to Eq. (4.8), then for the bond $(\mathbf{x}, \mathbf{x}')$ we can write:

$$\frac{\partial \theta_a(\mathbf{x}, \mathbf{x}', t)}{\partial t} = -\mathbf{V}(\mathbf{x}, t) \cdot \mathbf{e}_{\mathbf{x}\mathbf{x}'} \frac{\theta(\mathbf{x}', t) - \theta(\mathbf{x}, t)}{\|\mathbf{x}' - \mathbf{x}\|}, \quad (4.9)$$

where $\theta_a(\mathbf{x}, \mathbf{x}', t)$ is the average concentration along the bond. Integrating over the horizon region of point \mathbf{x} on both sides of Eq. (4.9) gives

$$\int_{H_x} \frac{\partial \theta_a(\mathbf{x}, \mathbf{x}', t)}{\partial t} dV_{\mathbf{x}'} = - \int_{H_x} \mathbf{V}(\mathbf{x}, t) \cdot \mathbf{e}_{\mathbf{x}\mathbf{x}'} \frac{\theta(\mathbf{x}', t) - \theta(\mathbf{x}, t)}{\|\mathbf{x}' - \mathbf{x}\|} dV_{\mathbf{x}'}. \quad (4.10)$$

We assume the following relation between the concentration at point \mathbf{x} and the average concentration of all bonds connected to \mathbf{x} :

$$\int_{H_x} \theta_a(\mathbf{x}, \mathbf{x}', t) dV_{\mathbf{x}'} = \theta(\mathbf{x}, t) V_{H_x}. \quad (4.11)$$

Then we have

$$\int_{H_x} \frac{\partial \theta_a(\mathbf{x}, \mathbf{x}', t)}{\partial t} dV_{\mathbf{x}'} = \frac{\partial \theta(\mathbf{x}, t)}{\partial t} V_{H_x}, \quad (4.12)$$

where V_{H_x} is the volume/area/length of the horizon region for point \mathbf{x} . Then Eq. (4.10)

becomes:

$$\frac{\partial \theta(\mathbf{x}, t)}{\partial t} = - \int_{H_x} \mathbf{v}(\mathbf{x}, \|\mathbf{x}' - \mathbf{x}\|, t) \cdot \mathbf{e}_{\mathbf{x}\mathbf{x}'} \frac{\theta(\mathbf{x}', t) - \theta(\mathbf{x}, t)}{\|\mathbf{x}' - \mathbf{x}\|} dV_{\mathbf{x}'}, \quad (4.13)$$

where $\mathbf{v}(\mathbf{x}, \|\mathbf{x}' - \mathbf{x}\|, t) = w(\|\mathbf{x}' - \mathbf{x}\|) \mathbf{V}(\mathbf{x}, t) / V_{H_x}$ is a weighted flow velocity density at \mathbf{x} over its horizon region. We call it the “micro-velocity” vector at \mathbf{x} , and its dot product with the bond direction $\mathbf{e}_{\mathbf{x}\mathbf{x}'}$ gives the “micro-velocity” function of the $(\mathbf{x}, \mathbf{x}')$ bond, $v(\mathbf{x}, \mathbf{x}', t)$. The function $w(\|\mathbf{x}' - \mathbf{x}\|)$ is a weighting function which controls the “shape”

of the micro-velocity vector function over the horizon region, and it will be discussed in Section 4.2.4. The units for the bond micro-velocity are velocity per length, area or volume for the 1D, 2D or 3D cases, respectively. Once a weighting function is selected, the micro-velocity can be explicitly found by matching the PD and the classical models for the case of constant flow velocity. This is also explained in Section 4.2.4 below.

The equation above is the PD equation for advection without any sources. If a mass source $b(\mathbf{x}, t)$ is present, Eq. (4.13) becomes:

$$\frac{\partial \theta(\mathbf{x}, t)}{\partial t} = - \int_{H_{\mathbf{x}}} \mathbf{v}(\mathbf{x}, \mathbf{x}', t) \frac{\theta(\mathbf{x}', t) - \theta(\mathbf{x}, t)}{\|\mathbf{x}' - \mathbf{x}\|} dV_{\mathbf{x}'} + b(\mathbf{x}, t). \quad (4.14)$$

By combining Eqs. (4.3) and (4.13), the PD diffusion-advection equation without sources can be written as:

$$\begin{aligned} \frac{\partial \theta(\mathbf{x}, t)}{\partial t} = & \int_{H_{\mathbf{x}}} d(\mathbf{x}, \mathbf{x}') \frac{\theta(\mathbf{x}', t) - \theta(\mathbf{x}, t)}{\|\mathbf{x}' - \mathbf{x}\|^2} dV_{\mathbf{x}'} \\ & - \int_{H_{\mathbf{x}}} \mathbf{v}(\mathbf{x}, \mathbf{x}', t) \frac{\theta(\mathbf{x}', t) - \theta(\mathbf{x}, t)}{\|\mathbf{x}' - \mathbf{x}\|} dV_{\mathbf{x}'} . \end{aligned} \quad (4.15)$$

For steady flow, which is assumed in all of the examples solved below, $\mathbf{v}(\mathbf{x}, \mathbf{x}', t)$ becomes $\mathbf{v}(\mathbf{x}, \mathbf{x}')$. For problems with time-dependent input flow velocity field, one replaces the constant velocity vector with its instantaneous value.

Compared to the kernels given in [53, 54], our kernels have both δ (contained in the micro-diffusivity and the micro-velocity functions, see Section 4.2.4) and $\|\mathbf{x} - \mathbf{x}'\|$ in the denominator, while the kernels in [53, 54] only have δ in the denominator.

4.2.3 Peridynamic advection-diffusion models

For the advection part of Eq. (4.15), two basic kernels can be considered: the central kernel and the upwind kernel. They came from the classical schemes (see, for example, [57]). The upwind type kernel depicted in Figure 4.4 was first considered in a nonlocal setting in [53, 54] by Tian et al. With the central kernel, the whole horizon region influences the concentration at \mathbf{x} , just as Figure 4.3 shows, and we obtain a central peridynamic advection-diffusion model (central model). With the upwind kernel, the concentration at \mathbf{x} is only influenced by the “upwind” region which is only half of $H_{\mathbf{x}}$ (see the shaded area in Figure 4.4), and we obtain an upwind peridynamic advection-diffusion model (upwind model). To determine the upwind region, we compute the dot product of the given flow direction \mathbf{e}_V at each node \mathbf{x} and the direction $\mathbf{e}_{\mathbf{x}\mathbf{x}'}$ of each bond connected to \mathbf{x} . If the result is negative, then \mathbf{x}' is in the upwind region of \mathbf{x} .

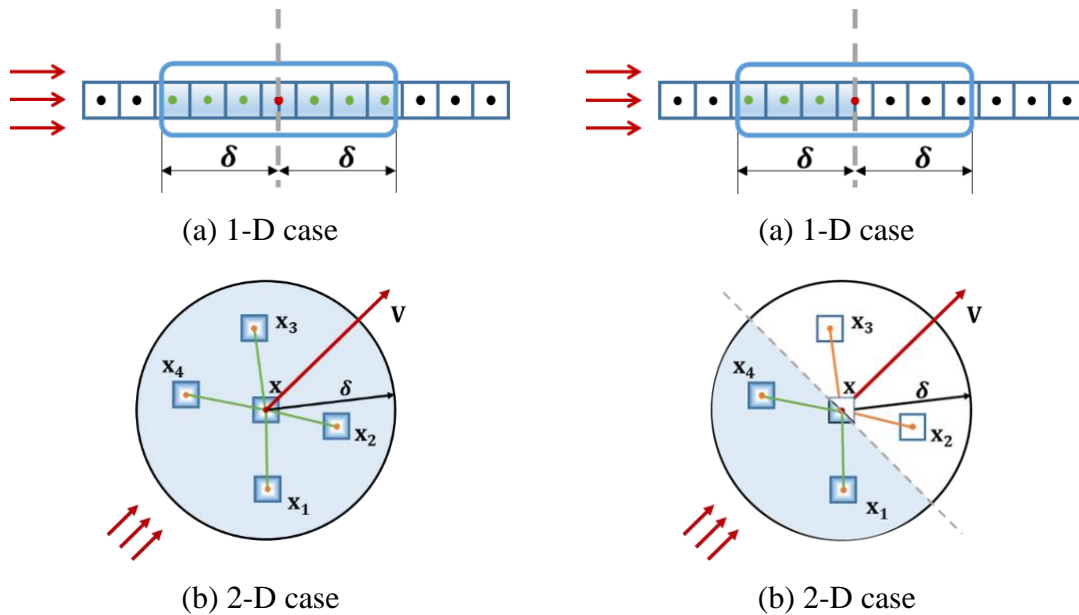


Figure 4.3. Illustration of the central kernel.

Figure 4.4. Illustration of the upwind kernel (shaded area is the upwind region $\tilde{H}_{\mathbf{x}}$).

4.2.4 Calibration of micro-velocity parameters

For any point \mathbf{x}' within the horizon of a given node \mathbf{x} , the micro-velocity for the bond connecting them can take different forms through the selection of the weighting function $w(\xi)$. The simplest ones are the “constant” and the “linear” types shown in Figure 4.5.

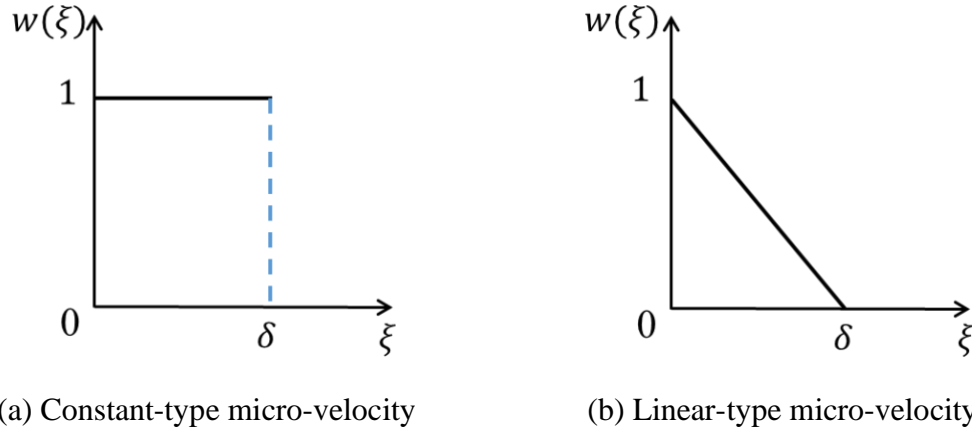


Figure 4.5. Two possible types of the weighting function and their variations over the PD horizon.

From the physical perspective, a specific weighting function for a material should be possible to be obtained by experiments. Here, we determine the micro-velocity in terms of the velocity of the flow field through a match or calibration between the PD results and the classical solution for a simple case: mass transfer under one-dimensional constant flow.

Consider a one-dimensional constant flow (without diffusion) defined by the velocity V and an initial linear concentration $\theta(x, t = 0) = ax + b$, with given constants a and b (see Figure 4.6). Then the concentration distribution with respect to time is $\theta(x, t) = a(x - Vt) + b$.

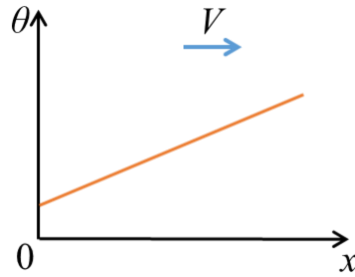


Figure 4.6. A constant concentration flux for one dimensional steady flow in the absence of diffusion.

With the classical model, at some point x along the tube, we can write:

$$\frac{\partial \theta}{\partial t} = -aV. \quad (4.16)$$

The PD model, assuming the constant-type micro-velocity, can be written as:

$$\frac{\partial \theta}{\partial t} = - \int_{H_x} \frac{\theta(x', t) - \theta(x, t)}{x' - x} v_0 dx'. \quad (4.17)$$

If the micro-velocity is taken to be the linear-type [45], then the equation will be:

$$\frac{\partial \theta}{\partial t} = - \int_{H_x} \frac{\theta(x', t) - \theta(x, t)}{x' - x} v_1 \left(1 - \frac{|x' - x|}{\delta} \right) dx'. \quad (4.18)$$

By enforcing a match between Eqs. (4.17) or (4.18) with (4.16), one can obtain the undetermined micro-velocity parameters v_0 and v_1 .

For the 2D and 3D cases, the micro-velocity parameters/vectors can be obtained in a similar way (see Appendix A). The table below summarizes the micro-velocity parameters in different conditions.

Remark: It is important to note that the micro-velocity parameter for the upwind kernel will be **twice** that used in the central kernel because the integration in Eqs. (4.17) or

(4.18) is over half the horizon region while it still has to match the same rate of change of concentration in Eq. (4.16).

Table 4.1. The micro-velocity parameters for different types of weighting functions (constant and linear) under the flow field defined by velocity \mathbf{V} (V in 1D), where $\hat{\mathbf{v}}$ and $\tilde{\mathbf{v}}$ are for the central and upwind kernels, respectively.

Function “shape”	Micro-velocity parameters for the central kernel	Micro-velocity parameters for the upwind kernel	
1D	constant	$\hat{v}_0 = \frac{V}{2\delta}$	$\tilde{v}_0 = \frac{V}{\delta}$
	linear	$\hat{v}_1 = \frac{V}{\delta}$	$\tilde{v}_1 = \frac{2V}{\delta}$
2D	constant	$\hat{\mathbf{v}}_0 = \frac{2\mathbf{V}}{\pi\delta^2}$	$\tilde{\mathbf{v}}_0 = \frac{4\mathbf{V}}{\pi\delta^2}$
	linear	$\hat{\mathbf{v}}_1 = \frac{6\mathbf{V}}{\pi\delta^2}$	$\tilde{\mathbf{v}}_1 = \frac{12\mathbf{V}}{\pi\delta^2}$
3D	constant	$\hat{\mathbf{v}}_0 = \frac{9\mathbf{V}}{4\pi\delta^3}$	$\tilde{\mathbf{v}}_0 = \frac{9\mathbf{V}}{2\pi\delta^3}$
	linear	$\hat{\mathbf{v}}_1 = \frac{9\mathbf{V}}{\pi\delta^3}$	$\tilde{\mathbf{v}}_1 = \frac{18\mathbf{V}}{\pi\delta^3}$

4.3 Numerical methods

To numerically integrate Eq. (4.15), we discretize the domain using a uniform grid with grid spacing Δx . Each node has a “volume” (length in 1D and area in 2D). Figure 4.7 shows the 2D discretization around a node \mathbf{x}_i . Non-uniform grids are possible in peridynamics [58-60], but it is not pursued here.

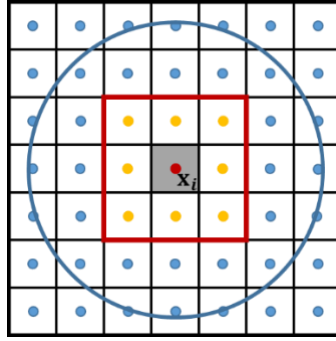


Figure 4.7. Numerical discretization around a node \mathbf{x}_i . The nearest-neighbor nodes to \mathbf{x}_i are used to account for the advection-diffusion within the volume of itself. The circular region is the horizon region of \mathbf{x}_i .

The spatial discretization of Eq. (4.15), using the mid-point rule, is

$$\begin{aligned} \dot{\theta}(\mathbf{x}_i, t) = & \sum_p d(\mathbf{x}_i, \mathbf{x}_p) \frac{\theta(\mathbf{x}_p, t) - \theta(\mathbf{x}_i, t)}{\|\mathbf{x}_p - \mathbf{x}_i\|^2} V_{ip} \\ & - \sum_p v(\mathbf{x}_i, \mathbf{x}_p) \frac{\theta(\mathbf{x}_p, t) - \theta(\mathbf{x}_i, t)}{\|\mathbf{x}_p - \mathbf{x}_i\|} V_{ip}, \end{aligned} \quad (4.19)$$

where the first summation is after all nodes \mathbf{x}_p inside the horizon of node \mathbf{x}_i , and V_{ip} is the portion of volume of node \mathbf{x}_p covered by the horizon of node \mathbf{x}_i . The partial volume integration, which was first proposed by [61] and then further discussed by [62, 63], is used to approximate the covered portion of V_{ip} . The second summation is different between the central model ($v = \hat{v}$, the micro-velocity for the central model) and the upwind model ($v = \tilde{v}$, the micro-velocity for the upwind model)

Note that special care must be taken when computing the term for $p = i$. Mathematically, this term can be computed by taking the limit $\mathbf{x}_p \rightarrow \mathbf{x}_i$, but note that this can be done only if the corresponding volumes of these nodes go to zero, otherwise the principle of non-interpenetration of matter will be violated. Instead of using the limit approach, we

approximate these values as follows: for the 1D dimensional case, we calculate the average value from the nearest-neighbors:

$$\begin{aligned}
& \frac{1}{2} \left[d(x_{i-1}, x_i) \frac{\theta(x_{i-1}, t) - \theta(x_i, t)}{(x_{i-1} - x_i)^2} V_{i,i-1} \right. \\
& \quad + d(x_{i+1}, x_i) \frac{\theta(x_{i+1}, t) - \theta(x_i, t)}{(x_{i+1} - x_i)^2} V_{i,i+1} \\
& \quad - \hat{v}(x_{i-1}, x_i) \frac{\theta(x_{i-1}, t) - \theta(x_i, t)}{x_{i-1} - x_i} V_{i,i-1} \\
& \quad \left. - \hat{v}(x_{i+1}, x_i) \frac{\theta(x_{i+1}, t) - \theta(x_i, t)}{x_{i+1} - x_i} V_{i,i+1} \right]
\end{aligned} \tag{4.20}$$

for the central model, and:

$$\begin{aligned}
& \frac{1}{2} \left[d(x_{i-1}, x_i) \frac{\theta(x_{i-1}, t) - \theta(x_i, t)}{(x_{i-1} - x_i)^2} V_{i,i-1} \right. \\
& \quad + d(x_{i+1}, x_i) \frac{\theta(x_{i+1}, t) - \theta(x_i, t)}{(x_{i+1} - x_i)^2} V_{i,i+1} \\
& \quad \left. - \tilde{v}(x_{i-1}, x_i) \frac{\theta(x_{i-1}, t) - \theta(x_i, t)}{x_{i-1} - x_i} V_{i,i-1} \right]
\end{aligned} \tag{4.21}$$

for the upwind model if the flow direction is from left to right. If the flow direction is from right to left, then the x_{i-1} in the third term is replaced by x_{i+1} .

For 2-D case, we also only employ the nearest (eight or three, see Figure 4.7) neighbors of node \mathbf{x}_i , and the approximation is given by:

$$\begin{aligned} & \frac{1}{8} \sum_{j=1}^8 d(\mathbf{x}_j, \mathbf{x}_i) \frac{\theta(\mathbf{x}_j, t) - \theta(\mathbf{x}_i, t)}{\|\mathbf{x}_j - \mathbf{x}_i\|^2} A_i \\ & - \frac{1}{8} \sum_{j=1}^8 \hat{v}(\mathbf{x}_j, \mathbf{x}_i) \frac{\theta(\mathbf{x}_j, t) - \theta(\mathbf{x}_i, t)}{\|\mathbf{x}_j - \mathbf{x}_i\|} \cos(\alpha) A_i, \end{aligned} \quad (4.22)$$

for the central model, and by:

$$\begin{aligned} & \frac{1}{8} \sum_{j=1}^8 d(\mathbf{x}_j, \mathbf{x}_i) \frac{\theta(\mathbf{x}_j, t) - \theta(\mathbf{x}_i, t)}{\|\mathbf{x}_j - \mathbf{x}_i\|^2} A_i \\ & - \frac{1}{3} \sum_{j=1}^3 \tilde{v}(\mathbf{x}_j, \mathbf{x}_i) \frac{\theta(\mathbf{x}_j, t) - \theta(\mathbf{x}_i, t)}{\|\mathbf{x}_j - \mathbf{x}_i\|} \cos(\alpha) A_i, \end{aligned} \quad (4.23)$$

for the upwind model. The extension to 3D of this procedure is obvious.

In a body that undergoes damage, if a mechanical bond (x_i, x_p) gets broken and advection and diffusion are both interrupted (or modified in a prescribed way), then the contribution from this bond is skipped (or modified in a prescribed way) in the summations in Eq. (4.19).

For the time integration of Eq. (4.19), we use the forward Euler method:

$$\theta_i^{n+1} = \theta_i^n + \Delta t \dot{\theta}_i^n. \quad (4.24)$$

To compare PD solution with the classical solution, we use the relative difference defined as:

$$\frac{\|\theta_{\text{classical}} - \theta_{\text{PD}}\|_2}{\|\theta_{\text{classical}}\|_2} = \frac{\sqrt{\sum_{i=1}^n (\theta_i^{\text{classical}} - \theta_i^{\text{PD}})^2}}{\sqrt{\sum_{i=1}^n (\theta_i^{\text{classical}})^2}}, \quad (4.25)$$

and the convergence rate defined as:

$$p \approx \frac{\log \frac{e_{\text{new}}}{e_{\text{old}}}}{\log \frac{h_{\text{new}}}{h_{\text{old}}}}, \quad (4.26)$$

where e is the relative difference and h is the grid spacing.

The time step has to satisfy the condition of stability [17, 50] defined as:

$$\Delta t < \frac{1}{\sum_{j=1}^n \frac{d}{\|\mathbf{x}_j - \mathbf{x}_i\|^2} V_j}. \quad (4.27)$$

Imposing Dirichlet (concentration) boundary conditions

For the uniform discretization mentioned at the beginning of this section, the Dirichlet boundary conditions can be imposed by assigning the given concentration value to the end node/nodes. Another method is adding a boundary layer (with a thickness of δ) outside the real boundary. When the horizon size is relatively small (relative to geometrical features) there is little difference between these two methods. With the horizon size approaching zero (in a d -convergence approach, which induces the nodal volumes to go to zero as well), the PD Dirichlet condition converges to the classical boundary condition [64].

Imposing Neumann (mass flux) boundary conditions

The implementation of heat-flux boundary conditions in PD was discussed in [46].

Imposing mass-flux conditions is identical to the heat-flux conditions.

4.4 Numerical tests and convergence to classical solutions

In this section, two examples (1D and 2D, for which analytical solutions for the classical model exist) are used to verify the PD model and discuss convergence to the classical

solution. We assume a given uniform steady velocity field, and the linear micro-diffusivity is used. To impose the PD boundary conditions, we add a boundary layer (with a thickness of δ) outside the real boundary and assign the given concentration values to this boundary layer.

4.4.1 Test example in 1D

When the diffusion coefficient is constant, the velocity field describes a uniform steady flow, and no sources or sinks exist, classical advection-diffusion equation in 1D can be written as:

$$\frac{\partial \theta(x, t)}{\partial t} = D \frac{\partial^2 \theta(x, t)}{\partial x^2} - V \frac{\partial \theta(x, t)}{\partial x}, \quad (4.28)$$

where $\theta(x, t)$ is the concentration of the substance of interest at position x at time t , D is the diffusion coefficient and V is the velocity of the flow field.

The initial and boundary conditions of the first example are:

$$\begin{cases} \theta(x, 0) = 0 & x > 0 \\ \theta(0, t) = C_0 & t \geq 0 \\ \theta(\infty, t) = 0 & t \geq 0 \end{cases} \quad (4.29)$$

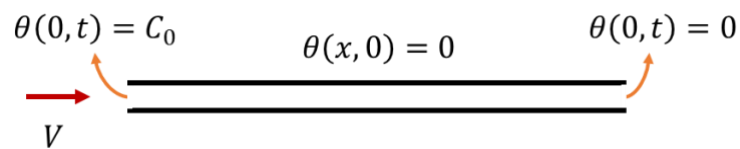


Figure 4.8. Boundary and initial conditions for 1D advection-diffusion in a semi-infinite tube.

The classical solution for this problem can be found in [65] as:

$$\theta(x, t) = \frac{C_0}{2} \left[\operatorname{erfc} \left(\frac{x - Vt}{2\sqrt{Dt}} \right) + \exp \left(\frac{Vx}{D} \right) \operatorname{erfc} \left(\frac{x + Vt}{2\sqrt{Dt}} \right) \right], \quad (4.30)$$

where $\operatorname{erfc}(\dots)$ is the complementary error function given by:

$$\operatorname{erfc}(x) = \frac{2}{\sqrt{\pi}} \int_x^\infty e^{-t^2} dt. \quad (4.31)$$

4.4.1.1 Case 1: Neither diffusion nor advection is dominant

When the diffusion coefficient $D = 1 \text{ cm}^2/\text{s}$ and the flow velocity $V = 1 \text{ cm/s}$, the exact classical solution and the PD solutions (with central and upwind models, and the constant-type micro-velocity function) for the 1D example shown above are plotted in Figure 4.9 at times $t = 1 \text{ s}, 2 \text{ s}, 3 \text{ s}, 4 \text{ s}$. The PD solutions shown were obtained with a horizon size of 0.05 cm and m value (the ratio of δ and Δx) of 4.

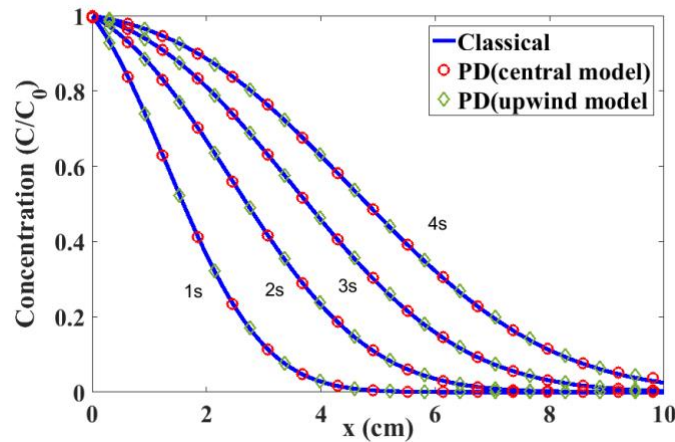


Figure 4.9. The comparison between classical solution and PD solutions for the 1D example case 1.

The match between the PD results (with either central or upwind models) and the classical result is excellent, because of the small horizon size used. Section 4.4.3.1 discusses the δ -convergence in detail and gives reasons for using these values for the horizon size and the m value.

4.4.1.2 Case 2: Advection-dominated

In case 1, only the constant-type micro-velocity function was used. When the diffusion coefficient $D = 0.001 \text{ cm}^2/\text{s}$ and the flow velocity $V = 1 \text{ cm/s}$ (advection-dominated case), we compare results between the constant-type and the linear-type micro-velocity functions. From Figure 4.10, the results with the linear type of micro-velocity function are closer to the classical result, for both upwind and central models. The results with the central model have oscillations (numerical instabilities) near the concentration front, while those from the upwind model exhibit no oscillations but some numerical diffusion.

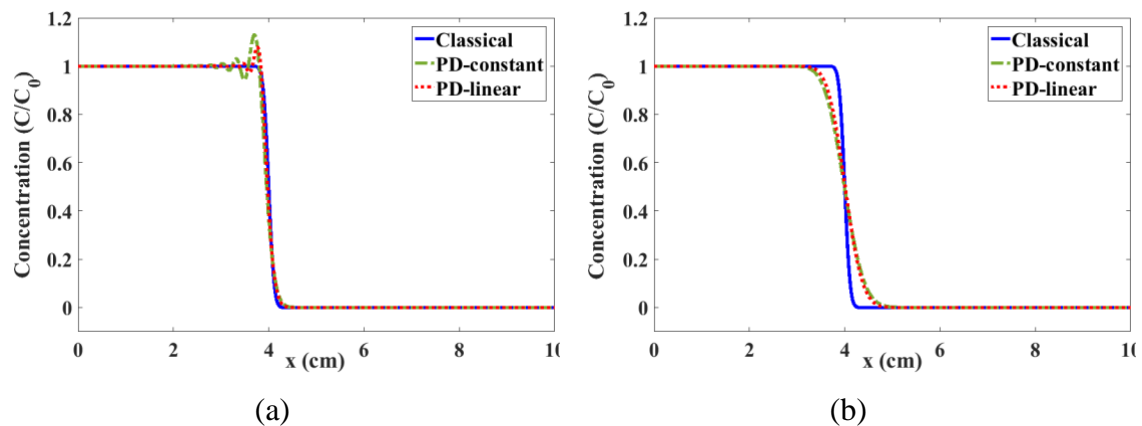


Figure 4.10. Concentration over the tube obtained with PD for the constant-type and linear-type micro-velocity functions for the 1D example case 2 (advection-dominated) at time $t = 4 \text{ s}$. (a) with central model, (b) with upwind model.

The hybrid model

Because of the observed oscillations (central model) and numerical diffusion (upwind model) when solving advection-dominated cases, we now test a hybrid model [57], which combines the two basic models. To do so, the parameter $\omega (\in [0,1])$ is introduced [66] to control the weight of each model. Thus, Eq. (4.15) becomes:

$$\begin{aligned}
\frac{\partial \theta(\mathbf{x}, t)}{\partial t} &= \int_{H_x} d(\mathbf{x}, \mathbf{x}') \frac{\theta(\mathbf{x}', t) - \theta(\mathbf{x}, t)}{\|\mathbf{x}' - \mathbf{x}\|^2} dV_{\mathbf{x}'} \\
&\quad - \omega \int_{H_x} \hat{v}(\mathbf{x}, \mathbf{x}') \frac{\theta(\mathbf{x}', t) - \theta(\mathbf{x}, t)}{\|\mathbf{x}' - \mathbf{x}\|} dV_{\mathbf{x}'} \\
&\quad - (1 - \omega) \int_{H_x} \tilde{v}(\mathbf{x}, \mathbf{x}') \frac{\theta(\mathbf{x}', t) - \theta(\mathbf{x}, t)}{\|\mathbf{x}' - \mathbf{x}\|} dV_{\mathbf{x}'} .
\end{aligned} \tag{4.32}$$

The pure central model and the pure upwind model can be obtained by setting $\omega = 1$ and $\omega = 0$, respectively. Through an optimal choice of ω , it is possible to control the oscillations and minimize the numerical diffusion.

For the advection-dominant case in example 1, we test results with $\omega = 0, 0.5, 0.8, 1$, and compare them with the classical solution in Figure 4.11 and Figure 4.12, for the constant-type micro-velocity and the linear-type micro-velocity, respectively. Table 4.2 gives the relative differences computed using Eq. (4.25).

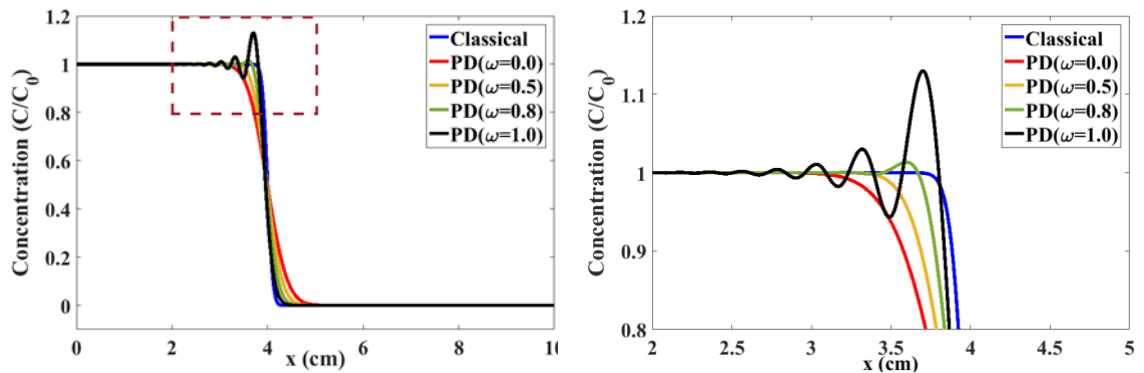


Figure 4.11. The PD results with different ω using the *constant-type* micro-velocity function compared to classical results (zoomed-in pictures on the right) for example 1, advection-dominated case, at time $t = 4$ s.

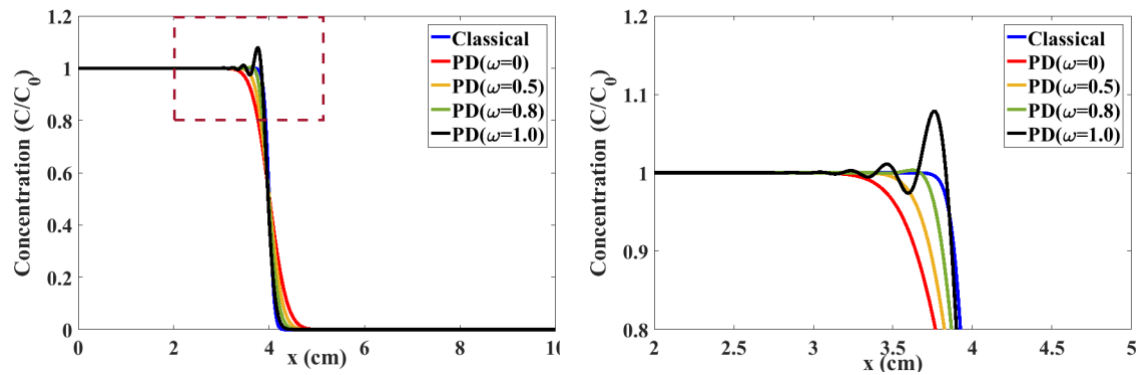


Figure 4.12. The PD results with different ω using the *linear-type* micro-velocity function compared to classical results (zoomed-in pictures on the right) for example 1, advection-dominated case, at time $t = 4$ s.

Table 4.2. Relative differences in concentration along the tube between the classical model and PD solutions at time $t = 4$ s, (advection-dominated case), with $\delta=0.05$ cm ($\Delta x = 0.0125$ cm) for different ω .

ω	Constant-type micro-velocity	Linear-type micro-velocity
0.0	0.095617	0.083922
0.5	0.070083	0.05935
0.8	0.046846	0.035418
1.0	0.043525	0.022552

The figures show, as expected, that oscillations are most severe when $\omega = 1$, and especially for the constant-type micro-velocity function. By successively decreasing the value of ω , the oscillation can be reduced, and are almost completely suppressed when $\omega < 0.8$. Thus, with an appropriate choice of ω , overshooting can be completely avoided with only little decrease in numerical accuracy. The optimal selection of ω depends on the Peclet number which is the ratio of the strengths of advection and diffusion [57]. The convergence study for this advection-dominated case is given in Section 4.4.3.2.

4.4.2 Test example in 2D

Transport in a homogeneous and isotropic medium during one-dimensional uniform steady flow with two-dimensional diffusion in classical form can be given by:

$$\frac{\partial \theta(x, y, t)}{\partial t} = D \left(\frac{\partial^2 \theta(x, y, t)}{\partial x^2} + \frac{\partial^2 \theta(x, y, t)}{\partial y^2} \right) - V \frac{\partial \theta(x, y, t)}{\partial x}, \quad (4.33)$$

where D is the diffusion coefficient; V is the velocity of the one-dimensional flow; x and y are positions along the coordinate axes parallel and perpendicular to the direction of flow, respectively.

Assume the solution domain is a half plane with $x \geq 0$ and the other boundaries at infinity. The initial and boundary conditions are:

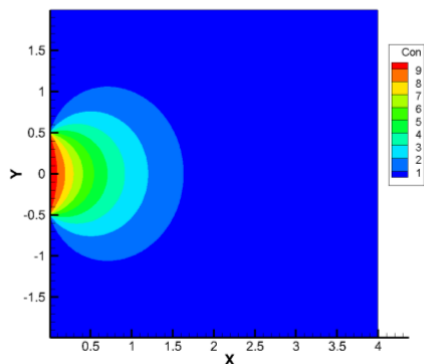
$$\begin{cases} \theta(x, y, 0) = 0 & 0 < x < \infty \quad -\infty < y < \infty \\ \left. \frac{\partial \theta}{\partial x} \right|_{x \rightarrow \infty} = 0 & -\infty < y < \infty \quad t > 0 \\ \left. \frac{\partial \theta}{\partial y} \right|_{y \rightarrow \pm \infty} = 0 & 0 < x < \infty \quad t > 0 \\ \theta(0, y, t) = C_0 & |y| \leq a \quad t > 0 \\ \theta(0, y, t) = 0 & |y| > a \quad t > 0 \end{cases}, \quad (4.34)$$

with prescribed concentration at $x = 0$. The classical solution was given in [67] as:

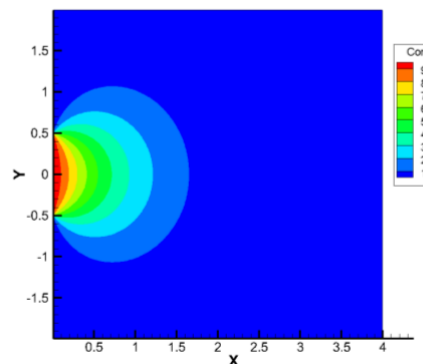
$$\begin{aligned} \theta(x, y, t) = \frac{x C_0}{(16\pi D_L)^{\frac{1}{2}}} \int_0^t \tau^{-\frac{3}{2}} \left\{ \operatorname{erf} \left[\frac{a + y}{(4D_T \tau)^{\frac{1}{2}}} \right] \right. \\ \left. + \operatorname{erf} \left[\frac{a - y}{(4D_T \tau)^{\frac{1}{2}}} \right] \right\} \exp \left\{ - \left[\frac{x - V\tau}{(4D_T \tau)^{\frac{1}{2}}} \right]^2 \right\} d\tau, \end{aligned} \quad (4.35)$$

which can be computed using Chebyshev–Gauss quadrature.

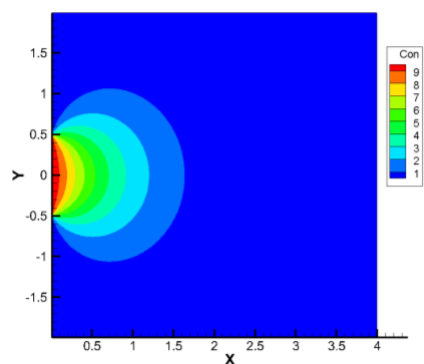
contour of the whole domain and the solution along the center line are given in Figure 4.15 and Figure 4.16 respectively.



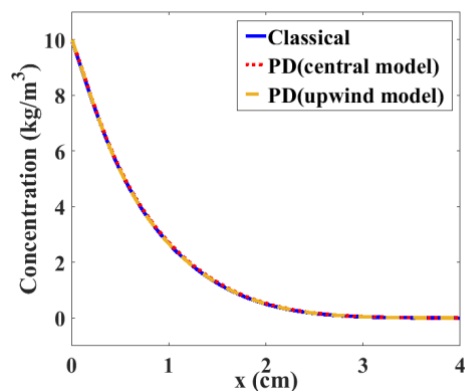
(a) Classical solution.



(b) PD solution (central model).

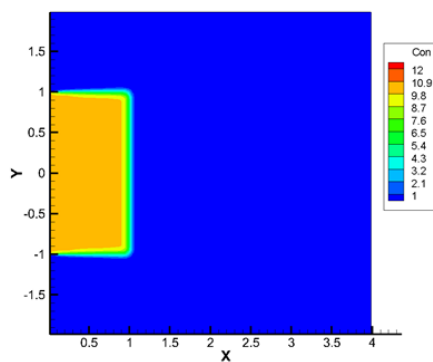


(c) PD solution (upwind model).

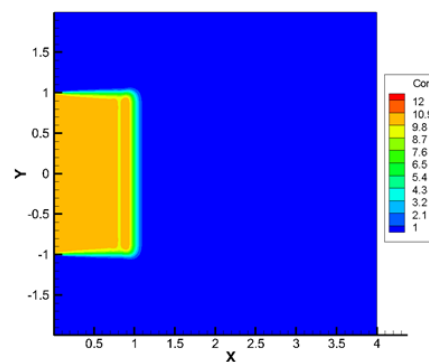


(d) Comparison of solutions along the center line

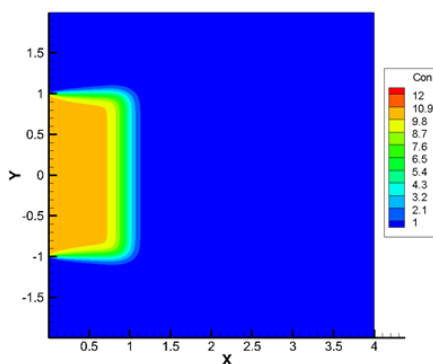
Figure 4.14. Classical and PD solutions for $D = 1 \text{ cm}^2/\text{s}$ and $V = 1 \text{ cm/s}$.



(a) Classical solution.



(b) PD solution (central model).



(c) PD solution (upwind model).

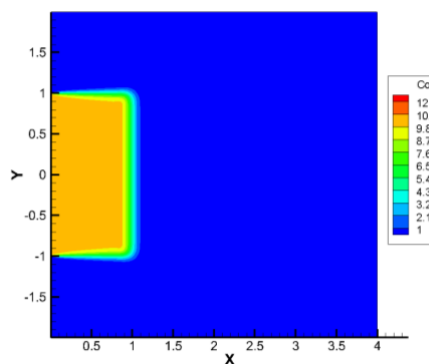
(d) PD Solution (hybrid model, $\omega = 0.8$).

Figure 4.15. Classical and PD solutions for advection-dominant case ($D = 0.001 \text{ cm}^2/\text{s}$ and $V = 1 \text{ cm/s}$).

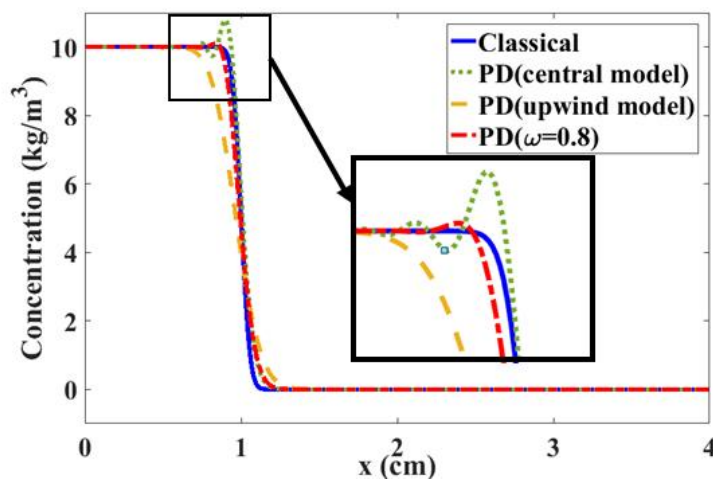


Figure 4.16. Comparison between classical and PD solutions along the center line for advection-dominant case.

4.4.3 Convergence study

We focus the analysis on two types of convergence defined in [56]: the m -convergence (m is defined as $\delta/\Delta x$), and the δ -convergence. In the m -convergence, we consider the horizon δ to be fixed and take $m \rightarrow \infty$, then the numerical PD approximation will converge to the exact nonlocal PD solution for the given δ . In the case of δ -convergence, the horizon $\delta \rightarrow 0$ while m is fixed. For problems with no singularities, the numerical PD approximation converges to the classical local solution [47, 55, 68, 69]. The results in this section justify the horizon size and m value used in Sections 4.4.1 and 4.4.2.

4.4.3.1 Convergence with central model in 1D, case 1

m -convergence: For several different horizon sizes ($\delta = L/10, L/20, L/40, L/80$), we perform the m -convergence test. In Figure 4.17, we plot the relative difference of the PD solutions compared with the classical solution at $t = 3s$, for values of m equal to 2, 4, 8 and 16, for case 1. We see that, when δ is fixed, the relative difference decreases as m increases, but it converges to a value that is not zero. That can be explained by the fact that the nonlocal exact solution, for a given horizon size, is not equal to the classical local solution. The smaller the horizon size, the closer the nonlocal solution is to the classical local solution, as can be seen from Figure 4.17 by looking at the relative difference for decreasing values of the horizon size δ and a fixed m value.

δ -convergence: Table 4.3 in **Appendix B** shows the detailed data for fixed m and varying node spacing (varying horizon size). For a fixed m value, as δ decreases (thus, node spacing decreases), the relative difference decreases gradually, with an increasing convergence rate, to zero.

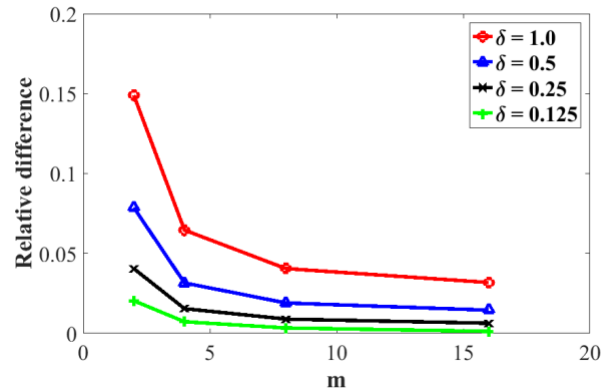


Figure 4.17. The convergence study of the 1D example, case 1.

4.4.3.2 Convergence with hybrid model in 1D, case 2 with $\omega = 0.8$

From the convergence study shown in Table 4.4 in Appendix B we can see that the hybrid model with $\omega = 0.8$ performs very well. The fact that central model (with $\omega = 1.0$) converges faster for a fixed m is reasonable because the relative difference over the whole tube can be very small even with the presence of obvious oscillation at the concentration front. However, the local relative difference inside the oscillation region can be much larger, according to Figure 4.12 which is the result obtained with $\delta = 0.05$ cm and $m = 4$. Through the hybrid model, the local oscillation can be reduced with a little sacrifice to the global relative difference. Thus, advection-dominated problems can be handled well using PD method with the hybrid model.

4.4.3.3 Convergence for the 2D example

Figure 4.18 shows the convergence study of the whole domain for example 2, with $D = 1 \text{ cm}^2/\text{s}$ and $V = 1 \text{ cm/s}$ (the central and upwind models give almost the same result). It can be observed that, for every horizon size, as m increases, the relative difference between the PD and the classical solution (which is the limit of the PD solution when the horizon goes to zero) decreases at first but then increases when m keeps growing. This is

similar to what happened in [55], where it was suggested that simply finding a certain horizon and a certain m -value for which there is a good match between the nonlocal model and the classical result is a misleading procedure. Instead, when the problem under consideration does not have a material length-scale that requires a particular horizon size, the δ -convergence and m -convergence need to be tested. Recall that, for a fixed horizon size, the numerical approximation of the PD formulation converges, under grid refinement (m -convergence) to the exact solution of the analytical nonlocal problem. It can easily happen that, for a fixed horizon size, the difference between the PD numerical solution and the classical solution is low for some values of m and it becomes larger when increasing the m -value (see Figure 4.19). This should come as no surprise, since we know that in the limit of m going to infinity we need to approach the analytical solution of the nonlocal problem for that particular horizon size, not the classical solution.

In [55], Chen showed with one dimensional diffusion examples that all m -convergence curves, if they cross with the classical solution, should cross at the same point. From Figure 4.19 we notice the same behavior for the advection-diffusion problem, and the three m -convergence curves cross with the classical solution at the same point, which guarantees δ -convergence to the classical solution, for any m value. Notice that this behavior is not conserved in the case of elastic wave propagation (see [70]) because of the nonlocal wave dispersion.

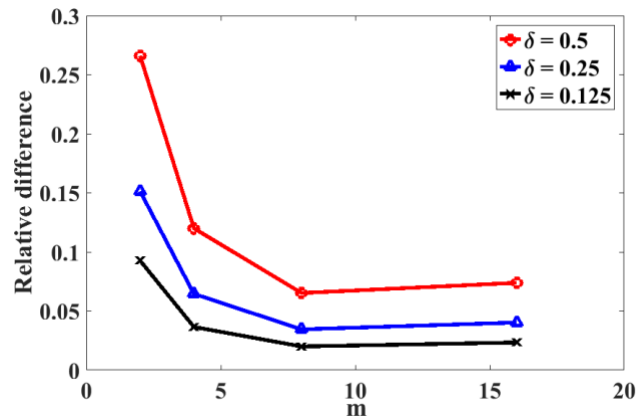


Figure 4.18. Relative difference for the whole domain with different horizon sizes and m values, at $t = 0.5$ s ($D = 1$ cm²/s and $V = 1$ cm/s).

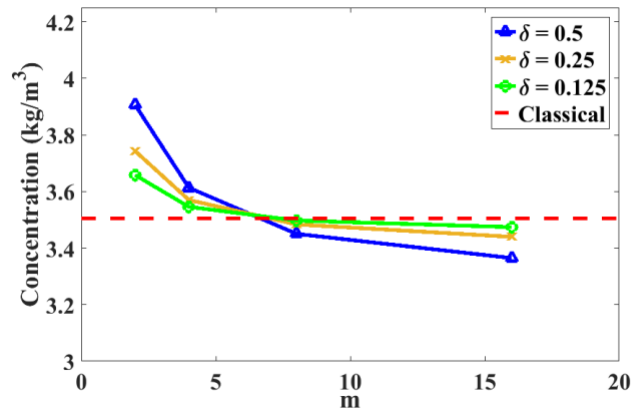


Figure 4.19. Concentration at $x = 0.5$ cm, $y = 0.5$ cm with different horizon sizes and m values, at $t = 0.5$ s ($D = 1$ cm²/s and $V = 1$ cm/s).

4.5 Mass flow over a 2-D heterogeneous medium

In this section, we use some examples to show the capability of our PD diffusion-advection model in the analysis of mass flow in heterogeneous media. Two potential applications of this capability include:

1. Environmental engineering example: flow of polluted water into ground, a heterogeneous porous structure with many inclusions (permeable/impermeable stones, rocks). The inclusions' presence influences the flow as well, and the

distribution of pollutants can be dramatically different from the homogeneous case.

2. Drug therapy example: delivery of drugs in cancer treatments. The lower transport rates through the tumor interstitium influences the distribution of drugs, which affects the efficacy of therapy.

Note that for heterogeneous material, special values for the micro-diffusivity and the micro-velocity should be assigned for bonds that cross over different regions. Several strategies can be selected for such purpose. One of them uses the arithmetic average values of the two nodes connected by the bond. Another option is the harmonic average [71], which is more appropriate in this case.

To demonstrate the ability of the proposed PD model in solving problems set in heterogeneous media, we consider the mass flow problem in a 2D domain with randomly distributed inclusions (circles or ellipses) as shown in Figure 4.20. The initial concentration of the whole domain is zero and there is an inlet for mass flow at the middle of the left boundary. Zero flux of concentration is imposed along the other boundaries. For simplicity, we set the diffusion coefficient and a 1D uniform steady flow velocity to be $1 \text{ cm}^2/\text{s}$ and $1 \text{ cm}/\text{s}$ in the matrix, respectively. This is a non-physical flow (because the flow would be influenced by the inclusions, in reality), but our model can use any given flow field. We solve the problem using a horizon size $\delta = 0.1 \text{ cm}$ and $m = 4$.

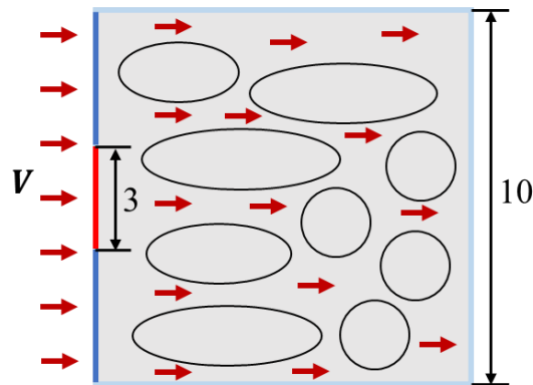


Figure 4.20. Example 3: flow in a heterogeneous medium. Same boundary conditions as in Figure 4.13.

First, for the case with permeable inclusions, we generate five randomly distributed circular inclusions with smaller diffusion coefficients and flow velocities than the matrix. For each inclusion, we use a random number (from a uniform distribution) within the (0, 0.1) range to decide its diffusion coefficient and flow velocity (still 1D uniform steady, in each inclusion). Figure 4.21 shows the concentration in the domain at $t = 6$ s. The dash-dot curves indicate the location of inclusions. The randomly assigned diffusion coefficients and flow velocities lead to various penetration levels in different inclusions.

Next, with impermeable inclusions, we generate elliptical inclusions and assign to them zero diffusion coefficient and zero flow velocity. Figure 4.22 shows the distribution of concentration at $t = 6$ s. We can see that the flow path is restricted to the gaps between inclusions.

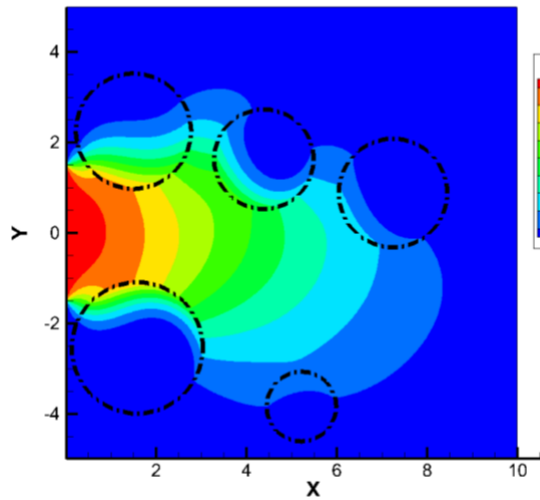


Figure 4.21. Concentration distribution for permeable circular inclusions (with smaller diffusion coefficients and flow velocities) at $t = 6$ s.

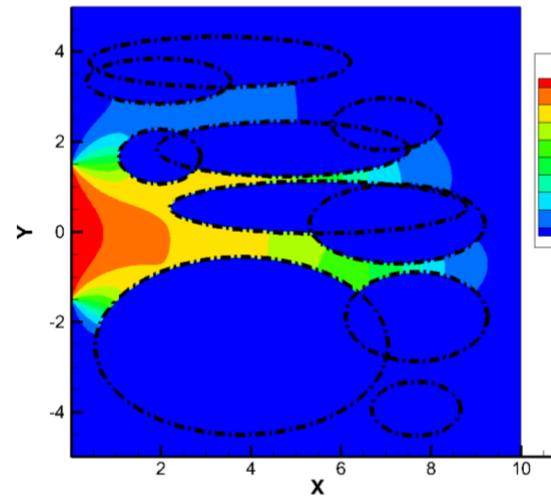


Figure 4.22. Concentration distribution for impermeable random elliptical inclusions at $t = 6$ s.

We note that in these examples, a simple uniform grid (non-conforming to the geometry of the inclusions) was used, and that no change in the model was required other than changing the input data to account for the heterogeneity in the system.

4.6 Conclusions

In this paper we provided a constructive approach to obtain a peridynamic (PD) formulation for transient advection-diffusion problems. The advantage of the PD kernel we obtained here by construction from physical principles is that, compared with the ones postulated in the literature, convergence to the classical model in the limit of the nonlocal region size going to zero is guaranteed independent of the fineness of the discretization.

The model presented here was employed to solve transient advection-diffusion examples in 1D and 2D, including transport in heterogeneous media with permeable and impermeable random inclusions. The model is versatile in the treatment of complex

problems and we demonstrated that by using a simple uniform grid, non-conforming to the microstructure geometry.

We presented two integration kernels for advection: the central kernel and the upwind kernel, leading to the central and upwind peridynamic advection-diffusion models, respectively. We also introduced a weighted combination between these two models and observed elimination of the oscillations at the high-gradient front compared with the central model, and reduction of numerical diffusion compared with the upwind model. Furthermore, we performed thorough convergence analyses (δ -convergence and m -convergence) for both 1D and 2D examples.

In the future, we plan to extend our model to advection-diffusion-reaction problems.

Acknowledgements

This work was supported, in part, by the ONR project “Stress-Corrosion Cracking: the Importance of Damage Evolution in the Layer Affected by Corrosion” (program manager William Nickerson), and the AFOSR MURI Center for Materials Failure Prediction through Peridynamics (program managers: Jaimie Tiley, Ali Sayir, David Stargel, and Fariba Fahroo). The work of the first author was partly done as a visiting scholar at University of Nebraska-Lincoln supported by the Northwestern Polytechnic University in Xi’an, China. This work was completed utilizing the Holland Computing Center of the University of Nebraska, which receives support from the Nebraska Research Initiative.

Appendix A. Derivation of the micro-velocity parameters for steady flow

In 2D condition, Eq. (4.8) becomes:

$$\frac{\partial \theta_a}{\partial t} = -\frac{(\theta' - \theta)}{\|\mathbf{x}' - \mathbf{x}\|} (V_x \cos \alpha + V_y \sin \alpha), \quad (4.36)$$

where V_x and V_y are the components of the velocity in x and y direction, respectively, and α is the angle between $\mathbf{e}_{\mathbf{x}'}$ and the flow direction at \mathbf{x} . Assuming linear-type micro-velocity (like the one used in Eq. (4.18) and shown in Figure 4.5 (b)), we have:

$$\begin{aligned} \frac{\partial \theta}{\partial t} &= -\int_{\hat{H}_x} \frac{(\theta' - \theta)}{\|\mathbf{x}' - \mathbf{x}\|} \left(1 - \frac{\|\mathbf{x}' - \mathbf{x}\|}{\delta}\right) (v_x \cos \alpha + v_y \sin \alpha) dA_{\mathbf{x}'} \\ &= -\int_{\hat{H}_x} \frac{(\theta' - \theta)}{x' - x} \left(1 - \frac{\|\mathbf{x}' - \mathbf{x}\|}{\delta}\right) v_x \cos^2 \alpha dA_{\mathbf{x}'} \\ &\quad - \int_{\hat{H}_x} \frac{(\theta' - \theta)}{y' - y} \left(1 - \frac{\|\mathbf{x}' - \mathbf{x}\|}{\delta}\right) v_y \sin^2 \alpha dA_{\mathbf{x}'}. \end{aligned} \quad (4.37)$$

If we only consider one dimensional uniform steady flow in x direction, we have $v_y = 0$, thus,

$$\frac{\partial \theta}{\partial t} = -\int_{\hat{H}_x} \frac{(\theta' - \theta)}{x' - x} v_x \left(1 - \frac{\|\mathbf{x}' - \mathbf{x}\|}{\delta}\right) \cos^2 \alpha dA_{\mathbf{x}'}. \quad (4.38)$$

Assuming that $\theta = a(x - V_x t) + b$, we have:

$$aV_x = av_x \int_{\hat{H}_x} \left(1 - \frac{\|\mathbf{x}' - \mathbf{x}\|}{\delta}\right) \cos^2 \alpha dA_{\mathbf{x}'}. \quad (4.39)$$

Finally, we obtain the parameter for a linear-type micro-velocity:

$$v_x = \frac{V_x}{\int_{\hat{H}_x} \left(1 - \frac{\|\mathbf{x}' - \mathbf{x}\|}{\delta}\right) \cos^2 \alpha dA_{\mathbf{x}'}} = \frac{6V_x}{\pi\delta^2}, \quad (4.40)$$

where a conversion between Cartesian coordinate and polar coordinate is used. Similarly, if we consider the same one-dimensional uniform steady flow in y direction, we have:

$$v_y = \frac{V_y}{\int_{\hat{H}_x} \left(1 - \frac{\|\mathbf{x}' - \mathbf{x}\|}{\delta}\right) \sin^2 \alpha dA_{x'}} = \frac{6V_y}{\pi\delta^2}. \quad (4.41)$$

For a constant-type micro-velocity, the parameters can be obtained in a similar way:

$$v_x = \frac{V_x}{\int_{\hat{H}_x} \cos^2 \alpha dA_{x'}} = \frac{2V_x}{\pi\delta^2}, \quad (4.42)$$

$$v_y = \frac{V_y}{\int_{\hat{H}_x} \sin^2 \alpha dA_{x'}} = \frac{2V_y}{\pi\delta^2}. \quad (4.43)$$

In 3D condition, Eq. (4.8) becomes:

$$\begin{aligned} \frac{\partial \theta_a}{\partial t} \cdot d &= -(\theta' - \theta) \mathbf{V} \cdot \mathbf{e} \\ &= -(\theta' - \theta)(V_x \sin \alpha \cos \beta + V_y \sin \alpha \sin \beta + V_z \cos \alpha), \end{aligned} \quad (4.44)$$

where V_x , V_y and V_z are the components of the velocity in x , y and z direction, respectively, α is the angle between $\mathbf{e}_{xx'}$ and z axis, β is the angle between the projection of $\mathbf{e}_{xx'}$ on xy -plane and x axis, as shown in Figure 4.230. Assuming linear-type micro-velocity, we have:

$$\begin{aligned} \frac{\partial \theta}{\partial t} &= - \int_{H_x} \frac{(\theta' - \theta)}{\|\mathbf{x}' - \mathbf{x}\|} \left(1 \right. \\ &\quad \left. - \frac{\|\mathbf{x}' - \mathbf{x}\|}{\delta}\right) (v_x \sin \alpha \cos \beta + v_y \sin \alpha \sin \beta + v_z \cos \alpha) dV_{x'} \end{aligned} \quad (4.45)$$

$$\begin{aligned}
&= - \int_{H_x} \frac{(\theta' - \theta)}{x' - x} \left(1 - \frac{\|\mathbf{x}' - \mathbf{x}\|}{\delta}\right) v_x \sin^2 \alpha \cos^2 \beta dV_{\mathbf{x}'} \\
&\quad - \int_{H_x} \frac{(\theta' - \theta)}{y' - y} \left(1 - \frac{\|\mathbf{x}' - \mathbf{x}\|}{\delta}\right) v_y \sin^2 \alpha \sin^2 \beta dV_{\mathbf{x}'} \\
&\quad - \int_{H_x} \frac{(\theta' - \theta)}{z' - z} \left(1 - \frac{\|\mathbf{x}' - \mathbf{x}\|}{\delta}\right) v_z \cos^2 \alpha dV_{\mathbf{x}'} .
\end{aligned}$$

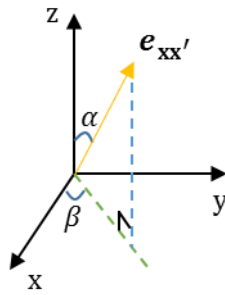


Figure 4.23. The decomposition of vector $\mathbf{e}_{\mathbf{x}\mathbf{x}'}$.

Assuming that $\theta = a(x - V_x t) + b$, we have

$$v_x = \frac{V_x}{\int_{\hat{H}_x} \left(1 - \frac{\|\mathbf{x}' - \mathbf{x}\|}{\delta}\right) \sin^2 \alpha \cos^2 \beta dV_{\mathbf{x}'}} = \frac{9V_x}{\pi\delta^3}, \quad (4.46)$$

and similarly:

$$v_y = \frac{V_y}{\int_{\hat{H}_x} \left(1 - \frac{\|\mathbf{x}' - \mathbf{x}\|}{\delta}\right) \sin^2 \alpha \sin^2 \beta dV_{\mathbf{x}'}} = \frac{9V_y}{\pi\delta^3}, \quad (4.47)$$

$$v_z = \frac{V_z}{\int_{\hat{H}_x} \left(1 - \frac{\|\mathbf{x}' - \mathbf{x}\|}{\delta}\right) \cos^2 \alpha dV_{\mathbf{x}'}} = \frac{9V_z}{\pi\delta^3}. \quad (4.48)$$

For the constant micro-velocity, we have

$$v_x = \frac{V_x}{\int_{\hat{H}_x} \sin^2 \alpha \cos^2 \beta dV_{x'}} = \frac{9V_x}{4\pi\delta^3}, \quad (4.49)$$

$$v_y = \frac{V_y}{\int_{\hat{H}_x} \sin^2 \alpha \sin^2 \beta dV_{x'}} = \frac{9V_y}{4\pi\delta^3}, \quad (4.50)$$

$$v_z = \frac{V_z}{\int_{\hat{H}_x} \cos^2 \alpha dV_{x'}} = \frac{9V_z}{4\pi\delta^3}, \quad (4.51)$$

where a conversion between Cartesian coordinate and spherical coordinate is used.

Appendix B. Convergence study for the 1D example

Table 4.3. δ -convergence results on relative differences and convergence rates between classical model and peridynamic using central model (p is the convergence rate) for 1D example, case 1.

$m = 2$			$m = 4$		
$dx/(\text{cm})$	$\ e\ _{L^2}$	p	$dx/(\text{cm})$	$\ e\ _{L^2}$	p
0.5	0.148968	-	0.25	0.064594	-
0.25	0.078692	0.920713576	0.125	0.031553	1.033622982
0.125	0.040502	0.958223825	0.0625	0.015472	1.028117481
0.0625	0.020422	0.987868989	0.03125	0.007267	1.090227888
$m = 8$			$m = 16$		
$dx/(\text{cm})$	$\ e\ _{L^2}$	p	$dx/(\text{cm})$	$\ e\ _{L^2}$	p
0.125	0.040538	-	0.0625	0.031824	-
0.0625	0.019032	1.090847736	0.03125	0.014514	1.132670006
0.03125	0.008935	1.090887542	0.015625	0.006346	1.193525749
0.015625	0.003405	1.391812931	0.0078125	0.001277	2.313088996

Table 4.4. Numerical results on relative differences between classical model and peridynamics using the hybrid model for 1D example, advection-dominated case.

$\omega = 0.8$	$\delta = 0.5$ cm	$\delta = 0.25$ cm	$\delta = 0.125$ cm	$\delta = 0.05$ cm
$m = 2$	0.182509	0.123537	0.083056	0.044723
$m = 4$	0.157839	0.109418	0.071526	0.036613
$m = 8$	0.154758	0.106673	0.068958	0.034448
$m = 16$	0.154052	0.106002	0.068262	0.033732
$\omega = 1.0$	$\delta = 0.5$ cm	$\delta = 0.25$ cm	$\delta = 0.125$ cm	$\delta = 0.05$ cm
$m = 2$	0.207338	0.145666	0.094438	0.036809
$m = 4$	0.185651	0.131226	0.080393	0.027198
$m = 8$	0.184953	0.129620	0.078200	0.025340
$m = 16$	0.185304	0.129369	0.077631	0.024428
$\omega = 0.0$	$\delta = 0.5$ cm	$\delta = 0.25$ cm	$\delta = 0.125$ cm	$\delta = 0.05$ cm
$m = 2$	0.224266	0.174730	0.137277	0.095286
$m = 4$	0.199299	0.158561	0.123241	0.083729
$m = 8$	0.193931	0.153892	0.119161	0.080401
$m = 16$	0.192562	0.152679	0.118098	0.079566

References

- [1] V. Givanasen, R.E. Volker, Numerical-Solutions for Solute Transport in Unconfined Aquifers, *Int J Numer Meth Fl*, 3(2) (1983) 103-123.
- [2] S.J. Chapman, R.J. Shipley, R. Jawad, Multiscale Modeling of Fluid Transport in Tumors, *B Math Biol*, 70(8) (2008) 2334-2357.
- [3] C. Pozrikidis, D.A. Farrow, A model of fluid flow in solid tumors, *Ann Biomed Eng*, 31(2) (2003) 181-194.
- [4] J. Naghipoor, N. Jafary, T. Rabczuk, Mathematical and computational modeling of drug release from an ocular iontophoretic drug delivery device, *Int J Heat Mass Tran*, 123 (2018) 1035-1049.
- [5] P. Siegel, R. Mose, P. Ackerer, J. Jaffre, Solution of the advection-diffusion equation using a combination of discontinuous and mixed finite elements, *Int J Numer Meth Fl*, 24(6) (1997) 595-613.
- [6] L.P. Franca, S.L. Frey, T.J. Hughes, Stabilized finite element methods: I. Application to the advective-diffusive model, *Comput Method Appl M*, 95(2) (1992) 253-276.

- [7] T.J. Hughes, L.P. Franca, G.M. Hulbert, A new finite element formulation for computational fluid dynamics: VIII. The Galerkin/least-squares method for advective-diffusive equations, *Comput Method Appl M*, 73(2) (1989) 173-189.
- [8] P. Huang, J. Zhao, X. Feng, Highly efficient and local projection-based stabilized finite element method for natural convection problem, *Int J Heat Mass Tran*, 83 (2015) 357-365.
- [9] P. Wang, u. Rizwan, A modified, hybrid nodal-integral/finite-element method for 3D convection-diffusion problems in arbitrary geometries, *Int J Heat Mass Tran*, 122 (2018) 99-116.
- [10] M. Dehghan, Weighted finite difference techniques for the one-dimensional advection-diffusion equation, *Appl Math Comput*, 147(2) (2004) 307-319.
- [11] S. Savović, A. Djordjević, Finite difference solution of the one-dimensional advection-diffusion equation with variable coefficients in semi-infinite media, *Int J Heat Mass Tran*, 55(15) (2012) 4291-4294.
- [12] C.L.N. Cunha, J.A.M. Carrer, M.F. Oliveira, V.L. Costa, A study concerning the solution of advection-diffusion problems by the Boundary Element Method, *Eng Anal Bound Elem*, 65 (2016) 79-94.
- [13] D.L. Young, Y.F. Wang, T.I. Eldho, Solution of the advection-diffusion equation using the Eulerian-Lagrangian boundary element method, *Eng Anal Bound Elem*, 24(6) (2000) 449-457.
- [14] R. Metzler, J. Klafter, The random walk's guide to anomalous diffusion: a fractional dynamics approach, *Phys Rep*, 339(1) (2000) 1-77.
- [15] S.A. Silling, Reformulation of elasticity theory for discontinuities and long-range forces, *J Mech Phys Solids*, 48(1) (2000) 175-209.
- [16] F. Bobaru, J.T. Foster, P.H. Geubelle, S.A. Silling, *Handbook of peridynamic modeling*, CRC Press, 2016.
- [17] S.A. Silling, E. Askari, A meshfree method based on the peridynamic model of solid mechanics, *Comput Struct*, 83(17-18) (2005) 1526-1535.
- [18] R.W. Macek, S.A. Silling, Peridynamics via finite element analysis, *Finite Elem Anal Des*, 43(15) (2007) 1169-1178.
- [19] W. Gerstle, N. Sau, S. Silling, Peridynamic modeling of concrete structures, *Nucl Eng Des*, 237(12) (2007) 1250-1258.
- [20] Y.D. Ha, F. Bobaru, Studies of dynamic crack propagation and crack branching with peridynamics, *Int J Fracture*, 162(1) (2010) 229-244.
- [21] F. Bobaru, W. Hu, The Meaning, Selection, and Use of the Peridynamic Horizon and its Relation to Crack Branching in Brittle Materials, *Int J Fracture*, 176(2) (2012) 215-222.
- [22] D. Huang, G. Lu, P. Qiao, An improved peridynamic approach for quasi-static elastic deformation and brittle fracture analysis, *Int J Mech Sci*, 94-95 (2015) 111-122.

- [23] G. Zhang, G.A. Gazonas, F. Bobaru, Supershear damage propagation and sub-Rayleigh crack growth from edge-on impact: A peridynamic analysis, *Int J Impact Eng*, 113 (2018) 73-87.
- [24] Z. Xu, G. Zhang, Z. Chen, F. Bobaru, Elastic vortices and thermally-driven cracks in brittle materials with peridynamics, *Int J Fracture*, 209(1) (2018) 203-222.
- [25] S.A. Silling, F. Bobaru, Peridynamic modeling of membranes and fibers, *Int J Nonlin Mech*, 40(2-3) (2005) 395-409.
- [26] F. Bobaru, Influence of van der Waals forces on increasing the strength and toughness in dynamic fracture of nanofibre networks: a peridynamic approach, *Model Simul Mater Sc*, 15(5) (2007) 397-417.
- [27] J.F. Xu, A. Askari, O. Weckner, S. Silling, Peridynamic analysis of impact damage in composite laminates, *J Aerospace Eng*, 21(3) (2008) 187-194.
- [28] B. Kilic, A. Agwai, E. Madenci, Peridynamic theory for progressive damage prediction in center-cracked composite laminates, *Compos Struct*, 90(2) (2009) 141-151.
- [29] W.K. Hu, Y.D. Ha, F. Bobaru, Modeling Dynamic Fracture and Damage in a Fiber-Reinforced Composite Lamina with Peridynamics, *Int J Multiscale Com*, 9(6) (2011) 707-726.
- [30] E. Oterkus, E. Madenci, Peridynamic Analysis of Fiber-Reinforced Composite Materials, *J Mech Mater Struct*, 7(1) (2012) 45-84.
- [31] W.K. Hu, Y.D. Ha, F. Bobaru, Peridynamic model for dynamic fracture in unidirectional fiber-reinforced composites, *Comput Method Appl M*, 217 (2012) 247-261.
- [32] Y.-I. Hu, Y. Yu, H. Wang, Peridynamic analytical method for progressive damage in notched composite laminates, *Compos Struct*, 108 (2014) 801-810.
- [33] E. Oterkus, I. Guven, E. Madenci, Fatigue failure model with peridynamic theory, in: 2010 12th IEEE Intersociety Conference on Thermal and Thermomechanical Phenomena in Electronic Systems, 2010, pp. 1-6.
- [34] S.A. Silling, A. Askari, Peridynamic model for fatigue cracking, SAND2014-18590. Albuquerque: Sandia National Laboratories, (2014)
<http://prod.sandia.gov/techlib/access-control.cgi/2014/1418590.pdf>.
- [35] G. Zhang, Q. Le, A. Loghin, A. Subramaniyan, F. Bobaru, Validation of a peridynamic model for fatigue cracking, *Eng Fract Mech*, 162 (2016) 76-94.
- [36] Z.G. Chen, F. Bobaru, Peridynamic modeling of pitting corrosion damage, *J Mech Phys Solids*, 78 (2015) 352-381.
- [37] Z.G. Chen, G.F. Zhang, F. Bobaru, The Influence of Passive Film Damage on Pitting Corrosion, *J Electrochem Soc*, 163(2) (2016) C19-C24.
- [38] S. Jafarzadeh, Z. Chen, F. Bobaru, Peridynamic Modeling of Repassivation in Pitting Corrosion of Stainless Steel, *CORROSION*, 74(4) (2018) 393-414.

- [39] K. Dayal, K. Bhattacharya, Kinetics of phase transformations in the peridynamic formulation of continuum mechanics, *J Mech Phys Solids*, 54(9) (2006) 1811-1842.
- [40] T.L. Warren, S.A. Silling, A. Askari, O. Weckner, M.A. Epton, J. Xu, A non-ordinary state-based peridynamic method to model solid material deformation and fracture, *Int J Solids Struct*, 46(5) (2009) 1186-1195.
- [41] J.T. Foster, S.A. Silling, W.W. Chen, Viscoplasticity using peridynamics, *Int J Numer Meth Eng*, 81(10) (2010) 1242-1258.
- [42] E. Madenci, S. Oterkus, Ordinary state-based peridynamics for plastic deformation according to von Mises yield criteria with isotropic hardening, *J Mech Phys Solids*, 86 (2016) 192-219.
- [43] H. Ouchi, A. Katiyar, J. York, J. Foster, M.M. Sharma, A fully coupled porous flow and geomechanics model for fluid driven cracks: a peridynamics approach, *Comput Mech*, 55(3) (2015) 561-576.
- [44] W. Gerstle, S. Silling, D. Read, V. Tewary, R. Lehoucq, Peridynamic Simulation of Electromigration, *Cmc-Comput Mater Con*, 8(2) (2008) 75-92.
- [45] F. Bobaru, M. Duangpanya, The peridynamic formulation for transient heat conduction, *Int J Heat Mass Tran*, 53(19-20) (2010) 4047-4059.
- [46] F. Bobaru, M. Duangpanya, A peridynamic formulation for transient heat conduction in bodies with evolving discontinuities, *J Comput Phys*, 231(7) (2012) 2764-2785.
- [47] X.C. Tian, Q. Du, Analysis and Comparison of Different Approximations to Nonlocal Diffusion and Linear Peridynamic Equations, *Siam J Numer Anal*, 51(6) (2013) 3458-3482.
- [48] Q. Du, M. Gunzburger, R.B. Lehoucq, K. Zhou, Analysis and Approximation of Nonlocal Diffusion Problems with Volume Constraints, *Siam Rev*, 54(4) (2012) 667-696.
- [49] S.A. Silling, M. Epton, O. Weckner, J. Xu, E. Askari, Peridynamic states and constitutive modeling, *J Elasticity*, 88(2) (2007) 151-184.
- [50] S. Oterkus, E. Madenci, A. Agwai, Peridynamic thermal diffusion, *J Comput Phys*, 265 (2014) 71-96.
- [51] A. Katiyar, J.T. Foster, H. Ouchi, M.M. Sharma, A peridynamic formulation of pressure driven convective fluid transport in porous media, *J Comput Phys*, 261 (2014) 209-229.
- [52] L. Wang, J. Xu, J. Wang, A peridynamic framework and simulation of non-Fourier and nonlocal heat conduction, *Int J Heat Mass Tran*, 118 (2018) 1284-1292.
- [53] H. Tian, L.L. Ju, Q. Du, Nonlocal convection-diffusion problems and finite element approximations, *Comput Method Appl M*, 289 (2015) 60-78.
- [54] H. Tian, L.L. Ju, Q. Du, A conservative nonlocal convection-diffusion model and asymptotically compatible finite difference discretization, *Comput Method Appl M*, 320 (2017) 46-67.

- [55] Z.G. Chen, F. Bobaru, Selecting the kernel in a peridynamic formulation: A study for transient heat diffusion, *Comput Phys Commun*, 197 (2015) 51-60.
- [56] F. Bobaru, M.J. Yang, L.F. Alves, S.A. Silling, E. Askari, J.F. Xu, Convergence, adaptive refinement, and scaling in 1D peridynamics, *Int J Numer Meth Eng*, 77(6) (2009) 852-877.
- [57] S. Patankar, *Numerical heat transfer and fluid flow*, CRC Press, 1980, Chapter 5.
- [58] F. Bobaru, Y.D. Ha, Adaptive refinement and multiscale modeling in 2D peridynamics, *Int J Multiscale Com*, 9(6) (2011) 635-659.
- [59] S.F. Henke, S. Shanbhag, Mesh sensitivity in peridynamic simulations, *Comput Phys Commun*, 185(1) (2014) 181-193.
- [60] X. Gu, Q. Zhang, X. Xia, Voronoi-based peridynamics and cracking analysis with adaptive refinement, *Int J Numer Meth Eng*, 112(13) (2017) 2087-2109.
- [61] W. Hu, Y. Ha, F. Bobaru, Numerical integration in peridynamics, Technical report, University of Nebraska-Lincoln, Department of Mechanical and Materials Engineering, (2010).
- [62] F. Bobaru, G. Zhang, Why do cracks branch? A peridynamic investigation of dynamic brittle fracture, *Int J Fracture*, 196(1) (2015) 59-98.
- [63] P. Seleson, Improved one-point quadrature algorithms for two-dimensional peridynamic models based on analytical calculations, *Comput Method Appl M*, 282 (2014) 184-217.
- [64] T. Mengesha, Q. Du, The bond-based peridynamic system with Dirichlet-type volume constraint, *Proceedings of the Royal Society of Edinburgh: Section A Mathematics*, 144(1) (2014) 161-186.
- [65] A. Ogata, R.B. Banks, A solution of the differential equation of longitudinal dispersion in porous media, 411A, 1961 <http://pubs.er.usgs.gov/publication/pp411A>.
- [66] C.V. Ramakrishnan, Upwind Finite-Element Scheme for the Unsteady Convective Diffusive Transport-Equation, *Appl Math Model*, 3(4) (1979) 280-284.
- [67] F.J. Leij, J.H. Dane, Analytical solutions of the one-dimensional advection equation and two- or three-dimensional dispersion equation, *Water Resour Res*, 26(7) (1990) 1475-1482.
- [68] X. Tian, Q. Du, Asymptotically Compatible Schemes and Applications to Robust Discretization of Nonlocal Models, *Siam J Numer Anal*, 52(4) (2014) 1641-1665.
- [69] Q. Du, X. Tian, Asymptotically compatible schemes for peridynamics based on numerical quadratures, in: *ASME 2014 International Mechanical Engineering Congress and Exposition*, American Society of Mechanical Engineers, 2014, pp. V001T001A058-V001T001A058 doi:010.1115/IMECE2014-39620.
- [70] Z. Chen, D. Bakenhus, F. Bobaru, A constructive peridynamic kernel for elasticity, *Comput Method Appl M*, 311 (2016) 356-373.
- [71] S. Patankar, *Numerical heat transfer and fluid flow*, CRC Press, 1980, 44-47.

Chapter 5 Construction of a Peridynamic Model for Viscous Flow

5.1 Introduction

Nonlocality plays important roles in many phenomena, including anomalous diffusion [1,2] and turbulence in fluid motion [3–5], and effects of microstructure in the deformation and fracture of solid materials [6,7]. Classical models based on PDEs have difficulties dealing with problems involving nonlocal effects. Fractional calculus is a powerful mathematical tool that can describe nonlocal behavior. However, models based on fractional calculus are computationally costly because the integrals in fractional calculus are defined over the entire space [8]. The peridynamic (PD) theory, which was introduced as a nonlocal extension of the classical continuum mechanics [9], provides an alternative to fractional calculus. It has been shown that PD operators converge to corresponding classical and fractional operators as the nonlocal size δ approaches zero and infinity, respectively [8,10]. Therefore, both classical and fractional operators can be seen as limiting cases of PD operators.

In addition to describing anomalous phenomena, PD models can be advantageous in simulating regular/common but complex physical/chemical problems. For example, classical local models have difficulties dealing with problems involving discontinuities or moving boundaries, such as those occurring in fracture, corrosion, etc. PD models, however, do not have such issues because they employ integro-differential equations (IDEs) rather than partial differential equations (PDEs), and thus cracks and other forms of damage can initiate and propagate naturally and autonomously [9,11,12]. Classical formulations also encounter significant challenges for problems that involve complex interactions between fluids and solids, such as erosion corrosion and hydraulic fracture,

while PD models, due to their generality/flexibility, have the potential to better deal with such problems [13,14].

While the PD method has been used extensively for mechanical and diffusion-type problems involving cracks and damage [15,16], there is very little existing literature on formulations or applications of the PD method to fluid mechanics. State-based PD models for fluid flow in porous media are presented in [13,14,17] and are coupled with mechanical models to simulate the fluid-driven cracks [13,14]. These models are limited to porous flows in which the flow is driven by the pressure gradient. Later, more general models for fluid flow based on the Navier-Stokes equations (NSEs) have been developed in the PD framework to simulate laminar fluid flows at low Reynold numbers. Some of them use the PD correspondence model [18], such as the updated Lagrangian particle hydrodynamics (ULPH) [19,20] and the PD Moving Particle Semi-implicit (MPS) model [21]. According to [22,23], the discretized PD correspondence models are equivalent to SPH and RKPM under certain conditions, and thus share some common numerical issues such as zero-energy modes. We also note the use of the “PD differential operators” [24,25] and the “peridynamic D operators” [26] to compute derivatives using integral operators. Integro-differential equations obtained in this way are “translations” of classical PDE-based models (like the NSEs), rather than being constructions of nonlocal formulations of viscous flow. In other words, the “nonlocality” introduced in the translations of PDE-based models to integro-differential ones is merely a computational parameter, whereas in true nonlocal formulation, the nonlocal region introduces a length-scale in the model.

It is worth noting that a PD formulation of the Navier-Stokes equations is perhaps a more natural model for fluids. First, we note that it is more general (at least formally), in the sense that it contains the classical Navier-Stokes equations as a special case (again, at least formally) by making a special choice of the PD kernel. Second, while proving (or disproving) the existence and uniqueness of global strong solutions to the classical incompressible 3D Navier-Stokes equations remains a challenging open problem, there is at least some hope that for a nonlocal PD formulation, such as the one presented in the present work, will allow for a proof of existence and uniqueness, at least for certain kernels. For instance, by analogy, it has been proven in [27] that a certain non-local version of the inviscid Burgers equation is globally well-posed, even though the classical version develops a singularity in finite time (see also [28] and the references therein). Third, on a deeper level, it may be that certain fluid regimes are more accurately described by taking into account non-local interactions rather than insisting that a strict local balance be maintained at every point in space and time, which in turn necessitates that solutions have at least some degree of smoothness (possibly in a weak sense) in order to make sense of the equations. For instance, it was noted by Ciprian Foias [29] that since (i) one can prove global well-posedness for the (modified) Navier-Stokes equations with higher-order diffusion added, (ii) higher-order diffusion modifications have been used with some success in certain ocean models, and (iii) higher-order derivatives have larger stencils (one pictures larger horizon sizes), there is some indication that including non-local interactions (in addition to the nonlocal effects of the pressure) could perhaps provide a model that more realistically captures the true dynamics of the flow.

In this work, we construct, for the first time, a PD bond-based model using the Eulerian description for viscous flow, starting from fundamental conservation principles, in order to arrive at a PD counterpart of the classical Navier-Stokes equation. A similar constructive approach has been used to formulate PD diffusion equations [30,31], advection-diffusion equations [32], and elastodynamic equations [33]. We investigate the convergence of the terms in the PD continuity equation to their classical counterparts as the nonlocal size in PD equations approaches zero. (In forthcoming works, e.g., [34], we will study the convergence of solutions of the PD equations to solutions of the classical equations.) We test the PD model numerically using examples for which (classical) analytical or numerical solutions are available in the literature. This paper is organized as follows: in Section 5.2 we introduce the constructive approach to arrive at the PD formulation for viscous flow; in Section 5.3 we explain the numerical discretization used; in Section 5.4 we verify our model for several problems with classical analytical/SPH solutions; conclusions are given in Section 5.5.

5.2 Peridynamic constructive model for viscous flow

In the classical theory of fluid mechanics, the motion of Newtonian fluids, in its Eulerian form, is described by the following NSEs [35]:

$$\frac{\partial \rho}{\partial t} = -\nabla \cdot (\rho \mathbf{v}) \quad (5.1)$$

$$\frac{\partial(\rho \mathbf{v})}{\partial t} = -\nabla \cdot (\rho \mathbf{v} \otimes \mathbf{v}) - \nabla p + \mu \nabla^2 \mathbf{v} + \rho \mathbf{b} \quad (5.2)$$

where ρ is the density, \mathbf{v} is the velocity, p is the pressure, μ is the viscosity and \mathbf{b} is the body acceleration. These equations are derived from conservation principles of mass and

momentum [35]. Note that an appropriate constitutive law is required to solve the above NSEs (e.g., constant ρ for incompressible fluids or equation of state for compressible fluids).

In this section, we derive an Eulerian PD model for viscous flow from a general PD continuity equation, following a procedure similar to that used in the derivation of the classical Eulerian Navier-Stokes equations.

Consider $d = 2$ or 3 , and let Ω denote an open bounded subset of \mathbb{R}^d . Points in \mathbb{R}^d are denoted by the vectors \mathbf{x} or $\hat{\mathbf{x}}$. Functions from Ω , or subsets of Ω , and time $t \in [0, T]$ into \mathbb{R} or \mathbb{R}^d are denoted by Roman or Greek letters, plain-face italic for scalars and lower-case bold italic for vectors, e.g., $\theta(\mathbf{x}, t)$ and $\mathbf{v}(\mathbf{x}, t)$. For notation simplicity, in much of the rest of the paper, we omit the spatial and temporal dependencies of these functions. For example, we denote θ and $\hat{\theta}$ for $\theta(\mathbf{x}, t)$ and $\theta(\hat{\mathbf{x}}, t)$, respectively.

In PD models, each material point $\mathbf{x} \in \Omega$ interacts with other points within its neighborhood $\mathcal{H}_{\mathbf{x}}$, which is called the horizon region of \mathbf{x} and is usually selected to be a disk when $d = 2$ (or sphere when $d = 3$) centered at \mathbf{x} . For a modification of this formulation to allow use of non-spherical horizons, please see [36] The radius of $\mathcal{H}_{\mathbf{x}}$ is called the horizon size (or simply “the horizon”) and denoted by δ . Objects that carry the pairwise nonlocal interactions between points are called PD bonds. Figure 5.1 schematically shows a peridynamic body with a generic point \mathbf{x} , its family and its horizon.

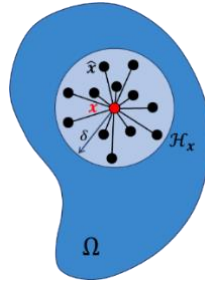


Figure 5.1. A peridynamic body with a generic point \mathbf{x} and its horizon. Nonlocal interactions exist through the bond between two points, e.g., point \mathbf{x} and an arbitrary point $\hat{\mathbf{x}}$ located in its horizon $\mathcal{H}_{\mathbf{x}}$.

5.2.1 The peridynamic continuity equation

To construct a bond-based PD model for fluid motion, we first consider an imaginary cylinder in a fluid domain with two points \mathbf{x} and $\hat{\mathbf{x}}$ located at the top and bottom of the cylinder, respectively, as shown in Figure 5.2. It is assumed that no mass transfer takes place through the cylinder's side surface. Even if the flow velocity has a component perpendicular to the axial direction of the cylinder, it does not participate in the transport of mass through the cylinder. Then, the continuity equation for some integrated property θ (mass, linear momentum, etc.) associated with the fluid, in the Eulerian form, can be expressed by:

$$hs \frac{\partial \theta_a}{\partial t} + s(\hat{\theta} \hat{\mathbf{v}} - \theta \mathbf{v}) \cdot \mathbf{e} = hsr_a \quad (5.3)$$

where h and s are the height and cross-sectional area of the cylinder, respectively; θ_a and r_a are the average θ and source/sink (taking the source as positive) in the cylinder, respectively; \mathbf{v} is the flow velocity of the fluid; \mathbf{e} is the unit vector $\frac{\hat{\mathbf{x}} - \mathbf{x}}{\|\hat{\mathbf{x}} - \mathbf{x}\|}$. Since $h = \|\hat{\mathbf{x}} - \mathbf{x}\|$, dividing Eq. (5.3) by both h and s gives us:

$$\frac{\partial \theta_a}{\partial t} + \frac{\hat{\theta} \hat{\mathbf{v}} - \theta \mathbf{v}}{\|\hat{\mathbf{x}} - \mathbf{x}\|} \cdot \mathbf{e} = r_a. \quad (5.4)$$

By taking $\hat{\mathbf{x}}$ to \mathbf{x} , we would recover the classical derivation of the conservation equation.

Instead, we assume the equation to hold for finite distances $\|\hat{\mathbf{x}} - \mathbf{x}\|$.

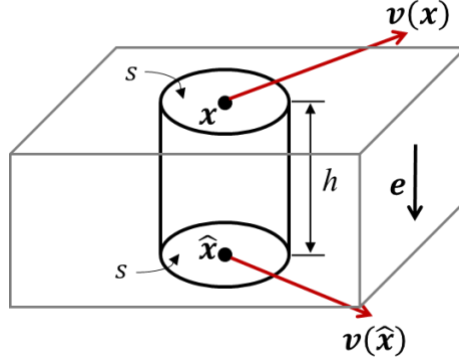


Figure 5.2. A cylinder in the fluid domain with two points located at the top and bottom. It is assumed that nothing can transfer through the cylinder's side surface.

In the peridynamic framework, each material point $\mathbf{x} \in \Omega$ interacts with points located in $\mathcal{H}_{\mathbf{x}}$ through PD bonds. For each of these PD bonds, we assume that there is only mass transfer between PD points, which allows us to use Eq. (5.4). For the bond connecting $\hat{\mathbf{x}}$ and \mathbf{x} , we can then write:

$$\frac{\partial \theta_a}{\partial t} + \alpha \frac{\hat{\theta} \hat{\mathbf{v}} - \theta \mathbf{v}}{\|\hat{\mathbf{x}} - \mathbf{x}\|} \cdot \mathbf{e} = r_a \quad (5.5)$$

where α is a coefficient which connects the macroscale flow velocity to the bond-level flow velocity. It will be determined later by requiring that the PD equation/solution converges (see Section 5.2.2) to the classical one as δ goes to zero. Note that α can be selected as a function of $\|\hat{\mathbf{x}} - \mathbf{x}\|$ as well [30], but this is not considered in this work for simplicity. Integrating Eq. (5.5) over the horizon of point \mathbf{x} we get:

$$\int_{\mathcal{H}_x} \frac{\partial \theta_a}{\partial t} d\hat{\mathbf{x}} + \alpha \int_{\mathcal{H}_x} \frac{\hat{\theta} \hat{\mathbf{v}} - \theta \mathbf{v}}{\|\hat{\mathbf{x}} - \mathbf{x}\|} \cdot \mathbf{e} d\hat{\mathbf{x}} = \int_{\mathcal{H}_x} r_a d\hat{\mathbf{x}} \quad (5.6)$$

We assume the following relation between θ at point \mathbf{x} and time t and the average θ in all the PD bonds connected at \mathbf{x} :

$$\int_{\mathcal{H}_x} \theta_a d\hat{\mathbf{x}} = \theta V_{\mathcal{H}} \quad (5.7)$$

where $V_{\mathcal{H}}$ is the volume (area in 2D and length in 1D) of the horizon region, a constant in this paper. Then we can write:

$$\int_{\mathcal{H}_x} \frac{\partial \theta_a}{\partial t} d\hat{\mathbf{x}} = \frac{\partial \theta}{\partial t} V_{\mathcal{H}} \quad (5.8)$$

Similarly, we have:

$$\int_{\mathcal{H}_x} r_a d\hat{\mathbf{x}} = r V_{\mathcal{H}} \quad (5.9)$$

Therefore, Eq. (5.6) becomes:

$$\frac{\partial \theta(\mathbf{x}, t)}{\partial t} = -\frac{\alpha}{V_{\mathcal{H}}} \int_{\mathcal{H}_x} \frac{\theta(\hat{\mathbf{x}}, t) \mathbf{v}(\hat{\mathbf{x}}, t) - \theta(\mathbf{x}, t) \mathbf{v}(\mathbf{x}, t)}{\|\hat{\mathbf{x}} - \mathbf{x}\|} \cdot \mathbf{e}(\mathbf{x}, \hat{\mathbf{x}}) d\hat{\mathbf{x}} + r(\mathbf{x}, t) \quad (5.10)$$

which is the general PD continuity equation in Eulerian form.

In the next section, we first show that the classical continuity equation is a limiting case of the PD form in Eq. (5.6). This is achieved by showing that the PD continuity equation converges to that of the classical one as $\delta \rightarrow 0$.

5.2.2 Convergence of the peridynamic continuity equation to its classical counterpart

To simplify the writing, we use the following notation for the weight function:

$$\omega = \omega(\mathbf{x}, \hat{\mathbf{x}}) = \frac{\alpha}{V_{\mathcal{H}} \|\hat{\mathbf{x}} - \mathbf{x}\|} \quad (5.11)$$

and for the nonlocal gradient and divergence operators:

$$\mathcal{G}_\omega(\phi)(\mathbf{x}) = \int_{\mathcal{H}_x} \omega(\phi(\hat{\mathbf{x}}, t) - \phi(\mathbf{x}, t)) \mathbf{e} d\hat{\mathbf{x}} \quad (5.12)$$

$$\mathcal{D}_\omega(\boldsymbol{\varphi})(\mathbf{x}) = \int_{\mathcal{H}_x} \omega(\boldsymbol{\varphi}(\hat{\mathbf{x}}, t) - \boldsymbol{\varphi}(\mathbf{x}, t)) \cdot \mathbf{e} d\hat{\mathbf{x}} \quad (5.13)$$

where ϕ and $\boldsymbol{\varphi}$ are some arbitrary scalar and vector fields in L^2 , respectively. The weighted nonlocal operators $\mathcal{G}_\omega(\phi)$ and $\mathcal{D}_\omega(\boldsymbol{\varphi})$ have been shown (see Section 5.2 in [37]) to converge (in the L^2 norm) to their differential counterparts $\nabla\phi$ and $\nabla \cdot \boldsymbol{\varphi}$, respectively, as $\delta \rightarrow 0$ (δ -convergence), if the weight function satisfies the following condition:

$$\int_{\mathcal{H}_x} \omega \|\hat{\mathbf{x}} - \mathbf{x}\| d\hat{\mathbf{x}} = d \quad (5.14)$$

in which d is the dimension. Substitute Eq. (5.11) into Eq. (5.14) leads to $\alpha = d$. In Appendix A, as an illustration, we use simple Taylor expansions to show that $\mathcal{G}_\omega(\phi)$ converges to $\nabla\phi$ when $\alpha = d$. For more detailed proofs of convergence in the L^2 norm for both nonlocal gradient and divergence, the reader is referred to [37].

Using the nonlocal operators defined in Eqs. (5.12) and (5.13), the integral in Eq. (5.10) can be written as:

$$\begin{aligned}
\mathcal{D}_\omega(\theta \mathbf{v}) &= \int_{\mathcal{H}_x} \omega(\hat{\theta} \hat{\mathbf{v}} - \theta \mathbf{v}) \cdot \mathbf{e} d\hat{\mathbf{x}} \\
&= \int_{\mathcal{H}_x} \omega(\hat{\theta}(\hat{\mathbf{v}} - \mathbf{v}) - \theta(\hat{\mathbf{v}} - \mathbf{v}) + \theta(\hat{\mathbf{v}} - \mathbf{v}) + \mathbf{v}(\hat{\theta} - \theta)) \cdot \mathbf{e} d\hat{\mathbf{x}} \\
&= \mathbf{v} \cdot \mathcal{G}_\omega(\theta) + \theta \mathcal{D}_\omega(\mathbf{v}) + \mathcal{A}_\omega(\theta, \mathbf{v})
\end{aligned} \tag{5.15}$$

in which the last term is

$$\mathcal{A}_\omega(\theta, \mathbf{v}) = \int_{\mathcal{H}_x} \omega(\hat{\theta} - \theta)(\hat{\mathbf{v}} - \mathbf{v}) \cdot \mathbf{e} d\hat{\mathbf{x}} \tag{5.16}$$

Therefore, Eq. (10) can be written as:

$$\frac{\partial \theta(\mathbf{x}, t)}{\partial t} = -\mathbf{v} \cdot \mathcal{G}_\omega(\theta) - \theta \mathcal{D}_\omega(\mathbf{v}) + \mathcal{A}_\omega(\theta, \mathbf{v}) + r(\mathbf{x}, t) \tag{5.17}$$

We show that $\mathcal{A}_\omega(\theta, \mathbf{v}) \rightarrow 0$ as $\delta \rightarrow 0$, as follows:

$$\begin{aligned}
\mathcal{A}_\omega(\theta, \mathbf{v}) &= \int_{\mathcal{H}_x} \omega(\hat{\theta} - \theta)(\hat{\mathbf{v}} - \mathbf{v}) \cdot \mathbf{e} d\hat{\mathbf{x}} \\
&\leq \int_{\mathcal{H}_x} |\omega(\hat{\theta} - \theta)(\hat{\mathbf{v}} - \mathbf{v}) \cdot \mathbf{e}| d\hat{\mathbf{x}} \\
&\leq \int_{\mathcal{H}_x} |\omega| |(\hat{\theta} - \theta)| \|\hat{\mathbf{v}} - \mathbf{v}\| d\hat{\mathbf{x}} \\
&\leq \frac{d}{V_{\mathcal{H}}} \int_{\mathcal{H}_x} \frac{1}{\|\hat{\mathbf{x}} - \mathbf{x}\|} |(\hat{\theta} - \theta)| \|\hat{\mathbf{v}} - \mathbf{v}\| d\hat{\mathbf{x}}
\end{aligned} \tag{5.18}$$

According to Taylor's theorem and the Cauchy-Schwarz inequality, we have on \mathcal{H}_x :

$$\begin{aligned}
\frac{|\hat{\theta} - \theta|}{\|\hat{\mathbf{x}} - \mathbf{x}\|} &\leq \|\nabla \theta\| + \frac{1}{2} \|\nabla^2 \theta\| \|\hat{\mathbf{x}} - \mathbf{x}\| + O(\|\hat{\mathbf{x}} - \mathbf{x}\|) \\
&\leq \|\nabla \theta\| + \frac{\delta}{2} \|\nabla^2 \theta\| + O(\delta)
\end{aligned} \tag{5.19}$$

and

$$\|\widehat{\mathbf{v}} - \mathbf{v}\| \leq \|D\mathbf{v}\| \|\widehat{\mathbf{x}} - \mathbf{x}\| + O(\|\widehat{\mathbf{x}} - \mathbf{x}\|) \leq \|D\mathbf{v}\| \delta + O(\delta) \quad (5.20)$$

where

$$D\mathbf{v} = \frac{\partial v^i}{\partial x^j} \mathbf{e}_i \otimes \mathbf{e}^j \quad (5.21)$$

If $D\mathbf{v}$ and $\nabla\theta$ are bounded in Ω , we have:

$$\begin{aligned} \mathcal{A}_\omega(\theta, \mathbf{v}) &\leq d \left(\|\nabla\theta(\mathbf{x})\| + \frac{\delta}{2} \|\nabla^2\theta(\mathbf{x})\| + O(\delta) \right) (\|D\mathbf{v}(\mathbf{x})\| \delta + O(\delta)) \rightarrow \\ 0 &\text{ as } \delta \rightarrow 0 \end{aligned} \quad (5.22)$$

Comparing the PD form of continuity equation in Eq. (5.17) with its classical form:

$$\frac{\partial \theta}{\partial t} = -\mathbf{v} \cdot \nabla\theta - \theta \nabla \cdot \mathbf{v} + r, \quad (5.23)$$

and considering that $\mathcal{G}_\omega(\theta) \rightarrow \nabla\theta$ and $\mathcal{D}_\omega(\mathbf{v}) \rightarrow \nabla \cdot \mathbf{v}$ in the sense of L^2 as $\delta \rightarrow 0$, we conclude that the PD continuity equation converges to the classical version as $\delta \rightarrow 0$.

5.2.3 The peridynamic formulation for viscous flow

Starting from the general continuity equation given in Eq. (5.10), we now derive the PD governing equations for viscous flow. When the property θ in Eq. (5.10) is mass, by taking $r = 0$, we obtain the PD mass continuity equation without sources/sinks:

$$\frac{\partial \rho}{\partial t} = -\frac{d}{V_{\mathcal{H}}} \int_{\mathcal{H}_x} \frac{\widehat{\rho\mathbf{v}} - \rho\mathbf{v}}{\|\widehat{\mathbf{x}} - \mathbf{x}\|} \cdot \mathbf{e} d\widehat{\mathbf{x}} \quad (5.24)$$

where ρ is the mass density. When the property θ is the linear momentum, we have the following PD equation of motion:

$$\frac{\partial(\rho\mathbf{v})}{\partial t} = -\frac{d}{V_{\mathcal{H}}} \int_{\mathcal{H}_x} \frac{\hat{p}\hat{\mathbf{v}} \otimes \hat{\mathbf{v}} - \rho\mathbf{v} \otimes \mathbf{v}}{\|\hat{\mathbf{x}} - \mathbf{x}\|} \cdot \mathbf{e} d\hat{\mathbf{x}} + \mathbf{r} \quad (5.25)$$

in which the generic momentum source \mathbf{r} consists of internal and external forces. The internal forces can be decomposed into pressure and viscous forces. To find the expression for these forces in the PD framework, we consider again the cylinder shown in Figure 5.2. As shown in Figure 5.3, in a viscous flow, the force exerted on the cylinder along its axial direction is:

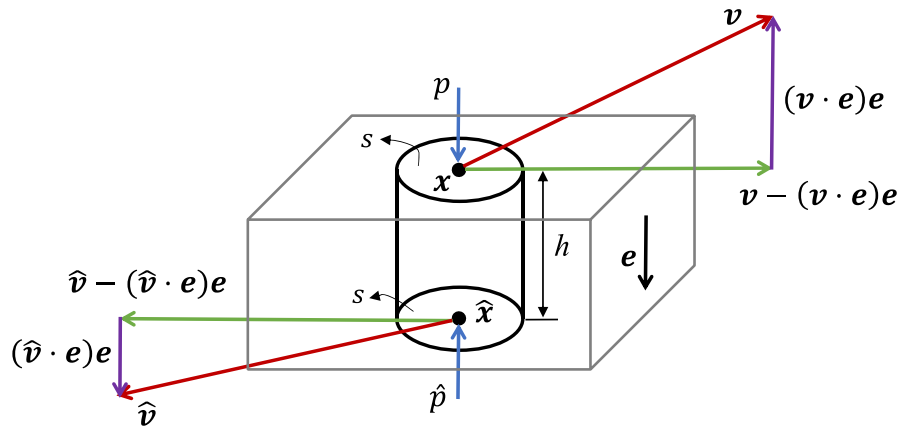


Figure 5.3. Velocity decomposition at \mathbf{x} and $\hat{\mathbf{x}}$ located at the top and bottom, respectively, for an imaginary cylinder in the fluid domain.

$$s(\hat{p} - p)\mathbf{e} \quad (5.26)$$

The viscous force, inspired by the shear bond force introduced in PD bond-based mechanical models [38,39], can be formulated as the shear force exerted on the cylinder due to the velocity difference between the two ends of the cylinder:

$$\mu s \frac{(\mathbf{I} - \mathbf{e} \otimes \mathbf{e})(\hat{\mathbf{v}} - \mathbf{v})}{\|\hat{\mathbf{x}} - \mathbf{x}\|} \quad (5.27)$$

in which μ is the viscosity of the fluid, and $(\mathbf{I} - \mathbf{e} \otimes \mathbf{e})(\hat{\mathbf{v}} - \mathbf{v})$ is the portion of velocity difference, between the two ends of the cylinder, that is perpendicular to the cylinder's axial direction \mathbf{e} .

Following a similar procedure used to derive the general PD continuity equation as shown in Section 5.2.1, we have:

$$\mathbf{r} = -\frac{\alpha_p}{V_{\mathcal{H}}} \int_{\mathcal{H}_x} \frac{\hat{p} - p}{\|\hat{\mathbf{x}} - \mathbf{x}\|} \cdot \mathbf{e} d\hat{\mathbf{x}} + \frac{\mu\alpha_\mu}{V_{\mathcal{H}}} \int_{\mathcal{H}_x} \frac{((\mathbf{I} - \mathbf{e} \otimes \mathbf{e})(\hat{\mathbf{v}} - \mathbf{v}))}{\|\hat{\mathbf{x}} - \mathbf{x}\|^2} d\hat{\mathbf{x}} + \rho \mathbf{b} \quad (5.28)$$

Therefore, the PD governing equations for viscous flow are established as follows:

$$\frac{\partial \rho(\mathbf{x}, t)}{\partial t} = -\frac{d}{V_{\mathcal{H}}} \int_{\mathcal{H}_x} \frac{\hat{\rho}\hat{\mathbf{v}} - \rho(\mathbf{x}, t)\mathbf{v}(\mathbf{x}, t)}{\|\hat{\mathbf{x}} - \mathbf{x}\|} \cdot \mathbf{e}(\mathbf{x}, \hat{\mathbf{x}}) d\hat{\mathbf{x}} \quad (5.29)$$

$$\begin{aligned} & \frac{\partial(\rho(\mathbf{x}, t)\mathbf{v}(\mathbf{x}, t))}{\partial t} \\ &= -\frac{d}{V_{\mathcal{H}}} \int_{\mathcal{H}_x} \frac{\rho(\hat{\mathbf{x}}, t)\mathbf{v}(\hat{\mathbf{x}}, t) \otimes \mathbf{v}(\hat{\mathbf{x}}, t) - \rho(\mathbf{x}, t)\mathbf{v}(\mathbf{x}, t) \otimes \mathbf{v}(\mathbf{x}, t)}{\|\hat{\mathbf{x}} - \mathbf{x}\|} \cdot \mathbf{e}(\mathbf{x}, \hat{\mathbf{x}}) d\hat{\mathbf{x}} \\ & - \frac{\alpha_p}{V_{\mathcal{H}}} \int_{\mathcal{H}_x} \frac{p(\hat{\mathbf{x}}, t) - p(\mathbf{x}, t)}{\|\hat{\mathbf{x}} - \mathbf{x}\|} \cdot \mathbf{e}(\mathbf{x}, \hat{\mathbf{x}}) d\hat{\mathbf{x}} \\ & + \frac{\mu\alpha_\mu}{V_{\mathcal{H}}} \int_{\mathcal{H}_x} \frac{((\mathbf{I} - \mathbf{e}(\mathbf{x}, \hat{\mathbf{x}}) \otimes \mathbf{e}(\mathbf{x}, \hat{\mathbf{x}}))(\mathbf{v}(\hat{\mathbf{x}}, t) - \mathbf{v}(\mathbf{x}, t)))}{\|\hat{\mathbf{x}} - \mathbf{x}\|^2} d\hat{\mathbf{x}} + \rho(\mathbf{x}, t)\mathbf{b}(\mathbf{x}, t) \end{aligned} \quad (5.30)$$

The PD model for viscous flow contains the pressure field which does not have an explicit equation yet. For incompressible Newtonian fluids, because directly solving the original incompressible equations creates numerical difficulties in terms of accuracy and efficiency, the artificial compressibility method is commonly used in the literature to handle the pressure term (see, e.g., [40–42]). This approach treats the incompressible fluid as a weakly compressible one and adopts an equation of state to explicitly determine the pressure field from the density field [41,43] as follows:

$$p = \frac{\rho_0 c_0^2}{\gamma} \left(\left(\frac{\rho^*}{\rho_0} \right)^\gamma - 1 \right) \quad (5.31)$$

where ρ_0 is the initial density, ρ^* is the predicted density at the current step, γ is the material constant which is 7 for water and c_0 is the sound speed in the initial density. The real sound speed is usually not used as it would require a significantly small timestep for stability of the numerical model (see Section 5.3). Instead, an artificial, lower sound speed c , which ensures sufficiently accurate solution, is preferred. To keep the density variation of fluid to less than 1% of the initial density, the Mach number ($M = v/c$) must be smaller than 0.1 [41]. This requires the artificial sound speed to be higher than 10 times of the maximum fluid velocity.

The PD equations for viscous flow still require determination of the unknown parameters in the weight functions. We already know that $\alpha = d$ from Section 5.2.2. Since α_p in Eq. (5.30) is also a constant coefficient in the PD gradient operator, we have $\alpha_p = \alpha = d$.

We find α_μ by calibration for a simple flow problem, that ensures linear consistency of the formulation [31,32]. Consider a steady-state shear-driven fluid flow parallel to the x -axis and with a linear distribution of velocity magnitude, i.e., $v = v_0 y$. According to Newton's law of viscosity, we have $\tau_{xx} = \mu v_0$. The counterpart of τ_{xx} in PD can be formulated as $\tau_{xx}^{\text{PD}} = \frac{\alpha_\mu \mu v_0}{10}$ for 3D and $\tau_{xx}^{\text{PD}} = \frac{3}{16} \alpha_\mu \mu v_0$ for 2D. The detailed derivation of τ_{xx}^{PD} is provided in Appendix A. By letting $\tau_{xx}^{\text{PD}} = \tau_{xx}$, it leads to $\alpha_\mu = 10$ for 3D and $\alpha_\mu = \frac{16}{3}$ for 2D.

5.2.4 Boundary conditions

Unlike classical local methods, “boundary conditions” in peridynamics are “volume constraints”, acting through a finite layer under the surface of a body. However, in practice, measurements are normally achievable only at the surfaces of a body, thus the normal local representation of boundary conditions. For these reasons, imposing local-type boundary conditions in peridynamic models is usually desired/needed. Various methods to impose local boundary conditions in PD models have been investigated in [37,44,45]. One such method is the fictitious nodes method (FNM) [44–46]. In FNM for peridynamics, certain constraints are specified on the fictitious region $\tilde{\Omega} = \{x \notin \Omega | \text{distance}(x, \partial\Omega) < \delta\}$ (the “collar” outside of the solution domain Ω shown in Figure 5.4), so that desired local boundary conditions imposed at $\partial\Omega$ are satisfied or approximately satisfied. Figure 5.4 schematically shows the solution domain Ω , its boundary $\partial\Omega$, and the fictitious region, $\tilde{\Omega}$.

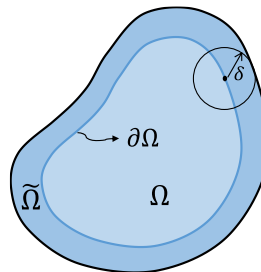


Figure 5.4. Schematic of a peridynamic domain (Ω), its boundary ($\partial\Omega$), and its fictitious region, $\tilde{\Omega}$.

In fluid dynamics, there are a number of different boundaries conditions, such as inlet/outlet, free and solid wall boundaries [47]. Various treatments are required for each of these types. In this work, we only consider no-slip solid wall boundaries. The corresponding boundary conditions then are:

$$\begin{aligned} \mathbf{v} \cdot \mathbf{n} &= 0 \\ \mathbf{v} \cdot \mathbf{t} &= 0 \end{aligned} \tag{5.32}$$

where \mathbf{n} and \mathbf{t} are vectors normal and tangential to the boundary, respectively. We use the naïve-type FNM (because of its ease of implementation, see [48]) to enforce the above boundary conditions, i.e., the velocity assigned to the fictitious points $\mathbf{x} \in \tilde{\Omega}$ are the same as that of the solid wall:

$$\mathbf{v}(\mathbf{x}) = \mathbf{v}_{\text{wall}} = \mathbf{0} \tag{5.33}$$

5.3 Numerical implementation

For the spatial discretization, we discretize the domain uniformly [49] into cells with nodes in the center of those cells. Figure 5.5 shows a 2D uniform discretization with grid spacing Δx around a node \mathbf{x}_i . Non-uniform grids are also possible [50–52], and very useful when having to conform to round boundaries [7][53], but this is not pursued in this work.

To discretize the peridynamic integro-differential equations, we use a meshfree method with one-point Gaussian quadrature [49] for the approximation of the integral term. For the time integration we select the forward-Euler method for simplicity.

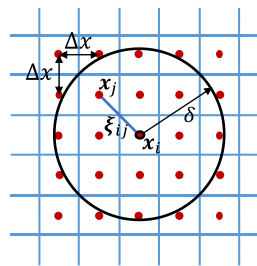


Figure 5.5. Uniform discretization for the 2D PD model. The circular region is the horizon region of node \mathbf{x}_i .

The discretized PD equations for viscous flow (Eqs. (5.29) and (5.30)) are as follows:

$$\rho_i^{n+1} = \rho_i^n - \frac{d\Delta t}{\pi\delta^2} \sum_{\substack{j \in \mathcal{H}_i \\ j \neq i}} \left(\frac{\rho_j^n \mathbf{v}_j^n - \rho_i^n \mathbf{v}_i^n}{\xi_{ij}} \cdot \frac{\mathbf{x}_j - \mathbf{x}_i}{\xi_{ij}} V_{ij} \right) \quad (5.34)$$

$$\begin{aligned} \mathbf{v}_i^{n+1} = \mathbf{v}_i^n + \frac{\Delta t}{\rho_i^n} & \left[-\frac{d}{V_{\mathcal{H}}} \left(\sum_{\substack{j \in \mathcal{H}_i \\ j \neq i}} \frac{(\rho_j^n \mathbf{v}_j^n \otimes \mathbf{v}_j^n - \rho_i^n \mathbf{v}_i^n \otimes \mathbf{v}_i^n)}{\xi_{ij}} \cdot \xi_{ij} V_{ij} \right) \right. \\ & - \frac{d}{V_{\mathcal{H}}} \sum_{\substack{j \in \mathcal{H}_i \\ j \neq i}} \left(\frac{(p_j^n - p_i^n) \xi_{ij}}{\xi_{ij}^2} V_{ij} \right) \\ & \left. + \frac{\mu\alpha_\mu}{V_{\mathcal{H}}} \sum_{\substack{j \in \mathcal{H}_i \\ j \neq i}} \frac{1}{\xi_{ij}^2} \left(\mathbf{I} - \frac{\xi_{ij} \otimes \xi_{ij}}{\xi_{ij}^2} \right) \cdot (\mathbf{v}_j^n - \mathbf{v}_i^n) V_{ij} + \rho_i^n \mathbf{b}_i^n \right] \end{aligned} \quad (5.35)$$

where $\xi_{ij} = \mathbf{x}_j - \mathbf{x}_i$ and $\xi_{ij} = \|\xi_{ij}\|$. The superscript n means n^{th} load step. The subscripts i and j denote the current node \mathbf{x}_i and its family node \mathbf{x}_j respectively, in the discretized domain. \mathcal{H}_i is the horizon region of node \mathbf{x}_i , $j \in \mathcal{H}_i$ includes all the nodes covered by \mathcal{H}_i (fully or partially), V_{ij} is the area of node \mathbf{x}_j covered by \mathcal{H}_i . Note that the partial volume integration, which was first proposed in [54] and then further discussed in [55,56], is used to approximate V_{ij} .

For stability of the time-integrator, the time step needs to satisfy several criteria. Here we use similar criteria as those in SPH models [42], including a CFL condition [57], the additional constraints due to the magnitude of nodal accelerations a [58] and the viscous diffusion, as follows:

$$\Delta t \leq 0.25 \frac{\Delta x}{c} \quad (5.36)$$

$$\Delta t \leq 0.25 \left(\frac{\Delta x}{a} \right)^{\frac{1}{2}} \quad (5.37)$$

$$\Delta t \leq 0.125 \frac{\rho \Delta x^2}{\mu} \quad (5.38)$$

where the value of each right-hand side is the minimum over all nodes.

A detailed study of the stability, consistency, and convergence of the numerical scheme, and higher-order schemes, as well as simulations in the higher Reynolds number case, will be the subject of forthcoming work. Our purpose here is just to demonstrate that a straight-forward implementation agrees with some standard benchmark cases to a reasonable level of accuracy—a first step toward validation of the model.

5.4 Computational validation

In this section, we first verify our PD model for viscous flow using the Couette and Poiseuille flow problems. We test whether the PD solution converges, in the limit of horizon going to zero, to the classical analytical solutions. We also study the flow through a periodic array of cylinders to test the wall boundary condition for curved geometries and compare with an SPH solution (of the corresponding classical model) from the literature.

5.4.1 Couette flow

Consider two infinite, parallel plates separated by a distance h . The top one, moves with a constant velocity v_0 in its own plane. This generates a unidirectional fluid motion,

called Couette flow. The series solution for the classical model of this problem, in terms of the velocity in the horizontal direction, is given by [42]:

$$v_x(y, t) = \frac{v_0}{h} y + \sum_{n=1}^{\infty} \frac{2v_0}{n\pi} (-1)^n \sin\left(\frac{n\pi}{h} y\right) \exp\left(-\frac{\mu n^2 \pi^2}{\rho h^2} t\right) \quad (5.39)$$

In our PD simulation of this Couette flow problem, we choose $v_0 = 10 \mu\text{m/s}$, $h = 1 \text{ mm}$, $\rho = 10^3 \text{ kg/m}^3$ and $\mu = 10^{-3} \text{ kg} \cdot \text{m}^{-1} \cdot \text{s}^{-1}$. We make the domain periodic in the x direction to mimic the infinite domain (see Fig. 16 in [59] for an illustration of how this can be achieved). Figure 5.6 shows the comparison of the velocity profile along y -axis between the PD solution (for $\delta = 40 \mu\text{m}$ and $m = 4$) and the analytical series solution of the classical model at different times. A δ -convergence study is then performed, and results are shown in Table 5.1. Note that the convergence rate of δ -convergence is linear because we use the naïve FNM to impose the local boundary condition [48]. Higher convergence rate should be possible with the mirror-based FNM, for example, but this is not pursued here.

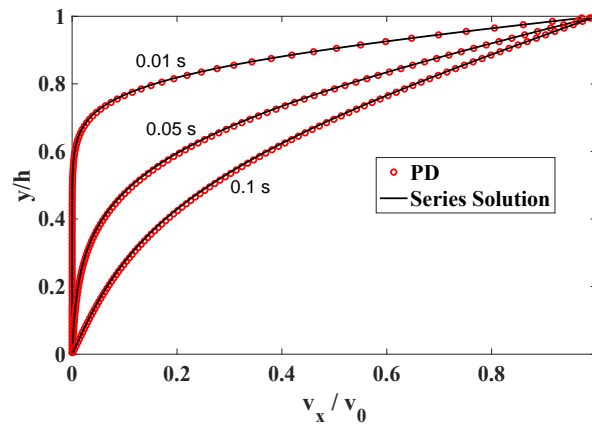


Figure 5.6. Comparison of PD solutions (for $\delta = 40 \mu\text{m}$ and $m = 4$) and series solutions of the corresponding classical model (using the first 50 terms in the series) for Couette flow.

Table 5.1. δ -convergence study for the PD solution of Couette flow.

$t = 0.1 \text{ s}$	$\delta = 80 \mu\text{m}$	$\delta = 40 \mu\text{m}$	$\delta = 20 \mu\text{m}$
ε_r	0.0419	0.0184	0.0075

where $\varepsilon_r = \frac{\sqrt{\sum_{i=1}^n (u_i^{\text{classical}} - u_i^{\text{PD}})^2}}{\sqrt{\sum_{i=1}^n (u_i^{\text{classical}})^2}}$, and n is the total number of nodes in the computation.

5.4.2 Poiseuille flow

The second test case is Poiseuille flow between stationary infinite plates at $y = 0$ and $y = h$. The fluid is initially at rest and is driven by an applied body force b_x parallel to the x -axis for $t \geq 0$. The series solution of the classical model for this problem give the velocity in the horizontal direction as [42]:

$$v_x(y, t) = \frac{\rho b_x}{2\mu} y(h - y) + \sum_{n=0}^{\infty} \frac{4\rho b_x h^2}{\mu\pi^3(2n+1)^3} \sin\left(\frac{\pi y}{h}(2n+1)\right) \exp\left(-\frac{(2n+1)^2\pi^2\mu}{\rho h^2}t\right) \quad (5.40)$$

We choose $h = 1 \text{ mm}$, $\rho = 10^3 \text{ kg/m}^3$, $\mu = 10^{-3} \text{ kg} \cdot \text{m}^{-1} \cdot \text{s}^{-1}$ and $b_x = 1 \times 10^{-4} \text{ m/s}^2$. Again, the PD solution matches the series solution very well, as shown in Figure 5.7.

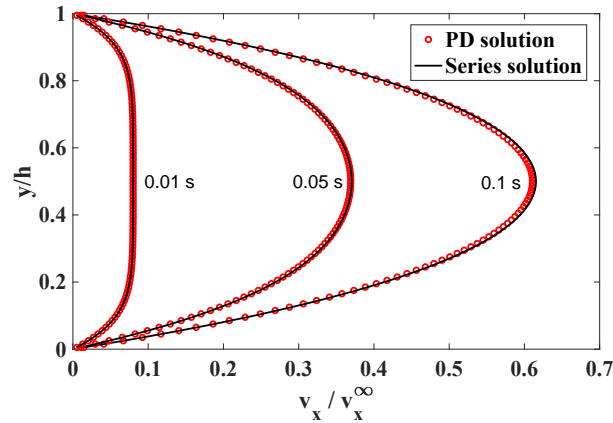


Figure 5.7. Comparison of PD (for $\delta = 40 \mu\text{m}$ and $m = 4$) and classical series solutions (using the first 50 terms in the series) for Poiseuille flow. Note that $v_x^\infty =$

$$v_x\left(\frac{h}{2}, \infty\right) = \frac{\rho b_x h^2}{8\mu}.$$

5.4.3 Flow through a Periodic Lattice of Cylinders

The previous examples have shown the performance of our method for fluid flow confined by straight channel walls. Now we verify the model for flow through a periodic array of disks/cylinders [42] (see Figure 5.8), to test the wall boundary condition for curved geometries. For implementing periodic BCs in PD models, please see [59]. The parameters used in this example are given in Table 5.2. Figure 5.9 shows the comparison for the velocity magnitude and velocity contour lines at steady state between PD results (100×100 discretization nodes) and SPH results (50×50 particles, plus extra particles placed on the circular disk to conform better to the actual geometry) from [60]. In spite of using a uniform discretization grid that does not conform with the circular disk geometry, the PD results track the SPH solution very well. As mentioned in Section 5.3, PD can also be implemented on non-uniform, conforming grids (see, e.g., [53]), but this is not pursued here for simplicity.

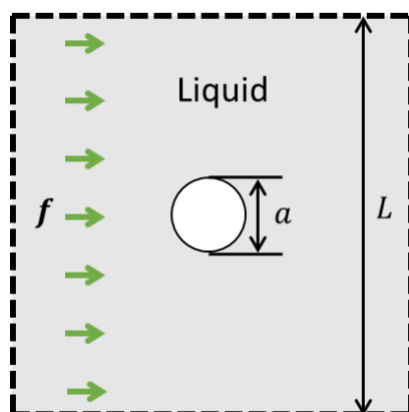


Figure 5.8. Schematic of fluid flow driven by a body force around a disk. The cell is repeated by symmetry to represent flow around a periodic array of disks.

Table 5.2. Parameters for flow through periodic lattice of disks.

Parameters	Value	Parameters	Value
L	0.1 m	a	4×10^{-2} m
μ	$10^{-3} \text{ kg} \cdot \text{m}^{-1} \cdot \text{s}^{-1}$	f	$1.5 \times 10^{-7} \text{ m} \cdot \text{s}^{-2}$
ρ	$1 \text{ kg} \cdot \text{m}^{-3}$	c	$5.77 \times 10^{-4} \text{ m} \cdot \text{s}^{-1}$

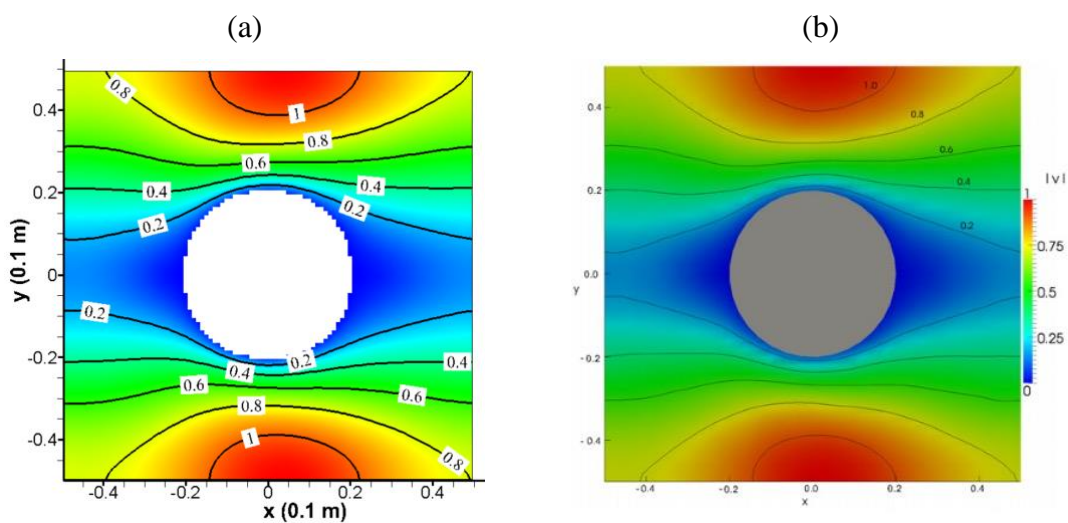


Figure 5.9. Contour plots of velocity magnitude by (a) PD model (for $\delta = 40 \mu\text{m}$ and $m = 4$); (b) SPH model [60] (contour lines are labeled in units of 10^{-4} m/s).

5.5 Conclusions

In this paper, we constructed a peridynamic (PD) alternative of the classical Navier-Stokes equations (in Eulerian formulation) from fundamental conservation principles. The formulation is different from “re-casting” of the classical Navier-Stokes equations using the so-called “PD differential operator” found in the literature. We showed that the classical continuity equation is a limiting case of the PD one with selected weight functions. We formulated the viscous force from PD shear bond forces. We determined the weight function present in the viscous force by enforcing linear consistency of the viscous stress provided by a PD model with that from a corresponding classical model. We verified the model against analytical solutions of the classical model for Couette and Poiseuille flows, as well as against an SPH approximation of the classical model for incompressible flow past a regular lattice of cylinders at low Reynolds numbers. The new model can be used to solve fluid-structure interaction problems involving damage and degradation, such as erosion, erosion-corrosion and hydraulic fracture, by coupling with existing PD models for corrosion and fracture.

Acknowledgments

This work has been supported in part by the US National Science Foundation Grant No. 1953346. This work was completed utilizing the Holland Computing Center of the University of Nebraska, which receives support from the Nebraska Research Initiative.

Appendix A. Convergence of the PD gradient operator to the classical one

To show the convergence of PD gradient operator $\mathcal{G}_\omega(u)$ to the classical one ∇u , we follow a procedure similar to the one used in [61]. Consider an incompressible

Newtonian fluid motion in which θ is sufficiently smooth in Ω , one can write, for any $\mathbf{x} \in \Omega$ and $\hat{\mathbf{x}} \in \mathcal{H}_{\mathbf{x}}$ that:

$$\hat{u} - u = \xi_i u_{,i} + \frac{1}{2} \xi_i \xi_j u_{,ij} + \frac{1}{3!} \xi_i \xi_j \xi_k u_{,ijk} + \dots \quad i, j, k \in [1, d] \quad (5.41)$$

where $\boldsymbol{\xi} = (\hat{\mathbf{x}} - \mathbf{x}) = \xi \mathbf{e} = \xi_i \mathbf{e}_i$ and d is the space dimension. Substitute Eq. (5.41),

without the remaining terms, into $\mathcal{G}_{\omega}(u)$ and consider symmetry of $\mathcal{H}_{\mathbf{x}}$, we get:

$$\begin{aligned} \mathcal{G}_{\omega}(u) &= \int_{\mathcal{H}_{\mathbf{x}}} \omega(\hat{u} - u) \mathbf{e} d\hat{\mathbf{x}} = \frac{\alpha}{V_{\mathcal{H}}} \int_{\mathcal{H}_{\mathbf{x}}} \frac{1}{\xi} \left\{ \xi_i u_{,i} + \frac{1}{3!} \xi_i \xi_j \xi_k u_{,ijk} \right\} \mathbf{e} d\hat{\mathbf{x}} \\ &= \frac{\alpha}{V_{\mathcal{H}}} \int_{\mathcal{H}_{\mathbf{x}}} \frac{\xi_i}{\xi} u_{,i} \mathbf{e} d\hat{\mathbf{x}} + \frac{\alpha}{6V_{\mathcal{H}}} \int_{\mathcal{H}_{\mathbf{x}}} \frac{\xi_i \xi_j \xi_k}{\xi \xi \xi} u_{,ijk} \mathbf{e} \xi^2 d\hat{\mathbf{x}} \end{aligned} \quad (5.42)$$

If $d = 2$, we have

$$\begin{aligned} \mathcal{G}_{\omega}(u) &= \frac{\alpha}{V_{\mathcal{H}}} \int_{\mathcal{H}_{\mathbf{x}}} \frac{\xi_i}{\xi} u_{,i} \mathbf{e} d\hat{\mathbf{x}} + \frac{\alpha}{6V_{\mathcal{H}}} \int_{\mathcal{H}_{\mathbf{x}}} \frac{\xi_i \xi_j \xi_k}{\xi \xi \xi} u_{,ijk} \mathbf{e} \xi^2 d\hat{\mathbf{x}} \\ &= \frac{\alpha}{\pi \delta^2} \int_0^{2\pi} \int_0^{\delta} \left(\cos \theta \frac{\partial u}{\partial x}(\mathbf{x}) + \sin \theta \frac{\partial u}{\partial y}(\mathbf{x}) \right) \begin{bmatrix} \cos \theta \\ \sin \theta \end{bmatrix} r dr d\theta \\ &\quad + \frac{\alpha}{6\pi \delta^2} \int_0^{2\pi} \int_0^{\delta} \left(\cos^3 \theta \frac{\partial^3 u}{\partial x^3}(\mathbf{x}) + 3 \cos^2 \theta \sin \theta \frac{\partial^3 u}{\partial x^2 \partial y}(\mathbf{x}) \right. \\ &\quad \left. + 3 \cos \theta \sin^2 \theta \frac{\partial^3 u}{\partial x \partial y^2}(\mathbf{x}) \right. \\ &\quad \left. + \sin^3 \theta \frac{\partial^3 u}{\partial y^3}(\mathbf{x}) \right) \begin{bmatrix} \cos \theta \\ \sin \theta \end{bmatrix} r^3 dr d\theta \\ &= \frac{\alpha}{\pi \delta^2} \frac{\pi \delta^2}{2} \nabla \rho(\mathbf{x}) + O(\delta^2) = \frac{\alpha}{2} \nabla \rho(\mathbf{x}) + O(\delta^2) \end{aligned} \quad (5.43)$$

Similarly, for $d = 3$, we can show that

$$\mathcal{G}_{\omega}(u) = \frac{\alpha}{3} \nabla \rho(\mathbf{x}) + O(\delta^2) \quad (5.44)$$

Therefore, if we set $\alpha = d$, the PD operator will converge to the classical one pointwise as $\delta \rightarrow 0$. For more details, and a proof of convergence in the L^2 norm, the reader is referred to [37].

Note that boundary effects are not considered here. For those PD points near the boundary which do not have a complete horizon region, the above convergence does not stand unless special treatments are provided (e.g., fictitious nodes methods [46,48]).

Appendix B. Computing PD stress component from bond force densities

To compute the shear stress at an arbitrary point \mathbf{p} in the PD model, we first consider a plane intersecting \mathbf{p} and normal to the y -axis and a thin cylinder below \mathbf{p} with cross-sectional area dA and length δ , where δ is the horizon of the PD model. Force through the plane on the cylinder is carried through the bonds that have one end in the cylinder and the other end on the other side of the plane. A typical point \mathbf{x} in the cylinder is located a distance z to the bottom of the plane, with $0 < z \leq \delta$. The force density (per unit volume square) in a typical bond connecting this point to the other side of the plane is given by $\mathbf{f}(\mathbf{x}, \hat{\mathbf{x}})$. Using a spherical coordinate system in which ϕ is the angle from the y -axis, and ξ is the bond length, the total force on the cylinder is then (in 3D) [12]:

$$d\mathbf{F} = dA \int_0^{2\pi} \int_0^\delta \int_0^\xi \int_0^{\cos^{-1}\left(\frac{z}{\xi}\right)} \mathbf{f}(\xi, \phi, \theta) \xi^2 \sin \phi \, d\phi \, dz \, d\xi \, d\theta \quad (5.45)$$

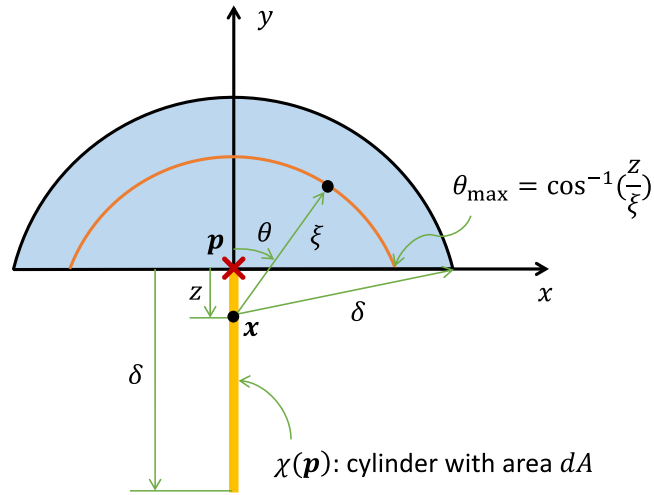


Figure 5.10. Computation of force per unit area, at a generic point \mathbf{p} , from bond force densities (redrawn from [12]).

The shear stress component at \mathbf{p} is then given by:

$$\tau_{xx}^{PD} = \frac{dF_x}{dA} = \int_0^{2\pi} \int_0^\delta \int_0^\xi \int_0^{\cos^{-1}\left(\frac{z}{\xi}\right)} f_x(\xi, \phi, \theta) \xi^2 \sin \phi \, d\phi \, dz \, d\xi \, d\theta \quad (5.46)$$

From Section 5.2.3, we know that:

$$\mathbf{f} = \frac{\mu\alpha_\mu}{V_{\mathcal{H}}} \frac{(\mathbf{I} - \mathbf{e} \otimes \mathbf{e})(\hat{\mathbf{v}} - \mathbf{v})}{\|\hat{\mathbf{x}} - \mathbf{x}\|^2} \quad (5.47)$$

For the fluid flow parallel to the x -axis and with a magnitude of $v_0 y$, we have

$$f_x = \frac{\mu\alpha_\mu}{V_{\mathcal{H}}} \frac{(1 - \sin^2 \theta)}{\|\hat{\mathbf{x}} - \mathbf{x}\|^2} v_0 (\hat{y} - y) \quad (5.48)$$

Therefore, we can compute the PD shear stress (flux) from the PD bond density of shear force as follows:

$$\begin{aligned}
\tau_{xx}^{\text{PD}} &= \frac{\mu\alpha_\mu}{V_{\mathcal{H}}} \int_0^{2\pi} \int_0^\delta \int_0^\xi \int_0^{\cos^{-1}\left(\frac{z}{\xi}\right)} \frac{1}{\xi^2} (1 - \sin^2 \theta) v_0 (\hat{y} \\
&\quad - y) \xi^2 \sin \phi \, d\phi dz d\xi d\theta \\
&= -\frac{3\alpha_\mu \mu v_0}{2\delta^3} \int_0^\delta \int_0^\xi \int_0^{\cos^{-1}\left(\frac{z}{\xi}\right)} \xi \cos^3 \phi \, d \cos \phi \, dz d\xi \\
&= -\frac{3\alpha_\mu \mu v_0}{8\delta^3} \int_0^\delta \xi \int_0^\xi \left(\frac{z^4}{\xi^4} - 1 \right) dz d\xi = \frac{3\alpha_\mu \mu v_0}{10\delta^3} \int_0^\delta \xi^2 d\xi = \frac{\alpha_\mu \mu v_0}{10}
\end{aligned} \tag{5.49}$$

Similarly, for 2D, we have:

$$\begin{aligned}
\tau_{xx}^{\text{PD}} &= \int_0^\delta \int_0^\xi \int_0^{\cos^{-1}\left(\frac{z}{\xi}\right)} f_x \xi d\theta dz d\xi \\
&= \frac{\mu\alpha_\mu}{V_{\mathcal{H}}} \int_0^\delta \int_0^\xi \int_0^{\cos^{-1}\left(\frac{z}{\xi}\right)} \frac{1}{\xi^2} (1 - \sin^2 \theta) v_0 (\hat{y} - y) \xi d\theta dz d\xi \\
&= \frac{\alpha_\mu \mu v_0}{\pi\delta^2} \int_0^\delta \int_0^\xi \int_0^{\cos^{-1}\left(\frac{z}{\xi}\right)} \cos^3 \theta \, d\theta dz d\xi \\
&= \frac{\alpha_\mu \mu v_0}{\pi\delta^2} \int_0^\delta \int_0^\xi \left(\left(\frac{1}{3} \sin \theta (2 + \cos^2 \theta) \right) \Big|_0^{\cos^{-1}\left(\frac{z}{\xi}\right)} \right) d\theta dz d\xi \\
&= \frac{2\alpha_\mu \mu v_0}{\pi\delta^2} \int_0^\delta \int_0^\xi \left(\frac{1}{3} \sqrt{1 - \left(\frac{z}{\xi}\right)^2} \left(2 + \left(\frac{z}{\xi}\right)^2 \right) \right) dz d\xi \\
&= \frac{2\alpha_\mu \mu v_0}{\pi\delta^2} \int_0^\delta \xi \int_0^1 \left(\frac{1}{3} \sqrt{1 - x^2} (2 + x^2) \right) dx d\xi \\
&= \frac{2\alpha_\mu \mu v_0}{\pi\delta^2} \int_0^\delta \xi \int_0^{\frac{\pi}{2}} \left(\frac{\cos^2 \alpha}{3} (2 + \sin^2 \alpha) \right) d\alpha d\xi \\
&= \frac{2\alpha_\mu \mu v_0}{3\pi\delta^2} \int_0^\delta \xi \int_0^{\frac{\pi}{2}} (\cos^2 \alpha (3 - \cos^2 \alpha)) d\alpha d\xi \\
&= \frac{\alpha_\mu \mu v_0}{3\pi\delta^2} \frac{9}{16} \pi \int_0^\delta \xi d\xi = \frac{2\alpha_\mu \mu v_0}{3\pi\delta^2} \frac{9}{16} \pi \frac{1}{2} \delta^2 = \frac{3}{16} \alpha_\mu \mu v_0
\end{aligned} \tag{5.50}$$

References

- [1] R. Metzler, J. Klafter, The random walk's guide to anomalous diffusion: A fractional dynamics approach, Phys. Rep. 339 (2000) 1–77.

[https://doi.org/10.1016/S0370-1573\(00\)00070-3](https://doi.org/10.1016/S0370-1573(00)00070-3).

- [2] R. Metzler, J. Klafter, The restaurant at the end of the random walk: Recent developments in the description of anomalous transport by fractional dynamics, *J. Phys. A. Math. Gen.* 37 (2004). <https://doi.org/10.1088/0305-4470/37/31/R01>.
- [3] M. Samiee, A. Akhavan-Safaei, M. Zayernouri, A fractional subgrid-scale model for turbulent flows: Theoretical formulation and a priori study, *Phys. Fluids.* 32 (2020) 055102. <https://doi.org/10.1063/1.5128379>.
- [4] M.F. Shlesinger, B.J. West, J. Klafter, Lévy dynamics of enhanced diffusion: Application to turbulence, *Phys. Rev. Lett.* 58 (1987) 1100–1103. <https://doi.org/10.1103/PhysRevLett.58.1100>.
- [5] B.A. Carreras, V.E. Lynch, G.M. Zaslavsky, Anomalous diffusion and exit time distribution of particle tracers in plasma turbulence model, *Phys. Plasmas.* 8 (2001) 5096–5103. <https://doi.org/10.1063/1.1416180>.
- [6] S.A. Silling, Origin and effect of nonlocality in a composite, *J. Mech. Mater. Struct.* 9 (2014) 245–258. <https://doi.org/10.2140/jomms.2014.9.245>.
- [7] J. Zhao, Z. Chen, J. Mehrmashhadi, F. Bobaru, A stochastic multiscale peridynamic model for corrosion-induced fracture in reinforced concrete, *Eng. Fract. Mech.* 229 (2020) 106969. <https://doi.org/10.1016/j.engfracmech.2020.106969>.
- [8] S. Duo, H. Wang, Y. Zhang, A comparative study on nonlocal diffusion operators related to the fractional Laplacian, *Discret. Contin. Dyn. Syst. - B.* 24 (2019) 231–256. <https://doi.org/10.3934/dcdsb.2018110>.
- [9] S.A. Silling, Reformulation of elasticity theory for discontinuities and long-range forces, *J. Mech. Phys. Solids.* 48 (2000) 175–209. [https://doi.org/10.1016/S0022-5096\(99\)00029-0](https://doi.org/10.1016/S0022-5096(99)00029-0).
- [10] M. D'Elia, M. Gunzburger, The fractional Laplacian operator on bounded domains as a special case of the nonlocal diffusion operator, *Comput. Math. with Appl.* 66 (2013) 1245–1260. <https://doi.org/10.1016/j.camwa.2013.07.022>.
- [11] E. Madenci, E. Oterkus, *Peridynamic Theory and Its Applications*, Springer New York, New York, NY, 2014. <https://doi.org/10.1007/978-1-4614-8465-3>.
- [12] F. Bobaru, J.T. Foster, P.H. Geubelle, S.A. Silling, *Handbook of Peridynamic Modeling*, CRC press, 2016. <https://doi.org/10.1201/9781315373331>.
- [13] H. Ouchi, A. Katiyar, J. York, J.T. Foster, M.M. Sharma, A fully coupled porous flow and geomechanics model for fluid driven cracks: a peridynamics approach, *Comput. Mech.* 55 (2015) 561–576. <https://doi.org/10.1007/s00466-015-1123-8>.
- [14] S. Oterkus, E. Madenci, E. Oterkus, Fully coupled poroelastic peridynamic formulation for fluid-filled fractures, *Eng. Geol.* 225 (2017) 19–28.

<https://doi.org/10.1016/j.enggeo.2017.02.001>.

- [15] E. Askari, F. Bobaru, R.B. Lehoucq, M.L. Parks, S.A. Silling, O. Weckner, Peridynamics for multiscale materials modeling, *J. Phys. Conf. Ser.* 125 (2008) 012078. <https://doi.org/10.1088/1742-6596/125/1/012078>.
- [16] A. Javili, R. Morasata, E. Oterkus, S. Oterkus, Peridynamics review, *Math. Mech. Solids.* 24 (2019) 3714–3739. <https://doi.org/10.1177/1081286518803411>.
- [17] A. Katiyar, J.T. Foster, H. Ouchi, M.M. Sharma, A peridynamic formulation of pressure driven convective fluid transport in porous media, *J. Comput. Phys.* 261 (2014) 209–229. <https://doi.org/10.1016/j.jcp.2013.12.039>.
- [18] S.A. Silling, Stability of peridynamic correspondence material models and their particle discretizations, *Comput. Methods Appl. Mech. Eng.* 322 (2017) 42–57. <https://doi.org/10.1016/j.cma.2017.03.043>.
- [19] Q. Tu, S. Li, An updated Lagrangian particle hydrodynamics (ULPH) for Newtonian fluids, *J. Comput. Phys.* 348 (2017) 493–513. <https://doi.org/10.1016/j.jcp.2017.07.031>.
- [20] J. Yan, S. Li, A.M. Zhang, X. Kan, P.N. Sun, Updated Lagrangian Particle Hydrodynamics (ULPH) modeling and simulation of multiphase flows, *J. Comput. Phys.* 393 (2019) 406–437. <https://doi.org/10.1016/j.jcp.2019.05.017>.
- [21] J. Wang, X. Zhang, Improved Moving Particle Semi-implicit method for multiphase flow with discontinuity, *Comput. Methods Appl. Mech. Eng.* 346 (2019) 312–331. <https://doi.org/10.1016/j.cma.2018.12.009>.
- [22] M.A. Bessa, J.T. Foster, T. Belytschko, W.K. Liu, A meshfree unification: reproducing kernel peridynamics, *Comput. Mech.* 53 (2014) 1251–1264. <https://doi.org/10.1007/s00466-013-0969-x>.
- [23] G.C. Ganzenmüller, S. Hiermaier, M. May, On the similarity of meshless discretizations of Peridynamics and Smooth-Particle Hydrodynamics, *Comput. Struct.* 150 (2015) 71–78. <https://doi.org/10.1016/j.compstruc.2014.12.011>.
- [24] Y. Gao, S. Oterkus, Nonlocal numerical simulation of low Reynolds number laminar fluid motion by using peridynamic differential operator, *Ocean Eng.* 179 (2019) 135–158. <https://doi.org/10.1016/j.oceaneng.2019.03.035>.
- [25] Y. Gao, S. Oterkus, Multi-phase fluid flow simulation by using peridynamic differential operator, *Ocean Eng.* 216 (2020) 108081. <https://doi.org/10.1016/j.oceaneng.2020.108081>.
- [26] Y. Mikata, Peridynamics for fluid mechanics and acoustics, *Acta Mech.* 232 (2021) 3011–3032. <https://doi.org/10.1007/s00707-021-02947-0>.
- [27] Q. Du, J.R. Kamm, R.B. Lehoucq, M.L. Parks, A new approach for a nonlocal, nonlinear conservation law, *SIAM J. Appl. Math.* 72 (2012) 464–487. <https://doi.org/10.1137/110833233>.

- [28] C. Imbert, R. Shvydkoy, F. Vigneron, Global well-posedness of a non-local Burgers equation: the periodic case, *Ann. La Fac. Des Sci. Toulouse Mathématiques*. 25 (2016) 723–758. <https://doi.org/10.5802/afst.1509>.
- [29] C. Foias, Private Communication, College Station, TX, (2013).
- [30] F. Bobaru, M. Duangpanya, The peridynamic formulation for transient heat conduction, *Int. J. Heat Mass Transf.* 53 (2010) 4047–4059. <https://doi.org/10.1016/j.ijheatmasstransfer.2010.05.024>.
- [31] F. Bobaru, M. Duangpanya, A peridynamic formulation for transient heat conduction in bodies with evolving discontinuities, *J. Comput. Phys.* 231 (2012) 2764–2785. <https://doi.org/10.1016/j.jcp.2011.12.017>.
- [32] J. Zhao, Z. Chen, J. Mehrmashhadi, F. Bobaru, Construction of a peridynamic model for transient advection-diffusion problems, *Int. J. Heat Mass Transf.* 126 (2018) 1253–1266. <https://doi.org/10.1016/j.ijheatmasstransfer.2018.06.075>.
- [33] Z. Chen, D. Bakenhus, F. Bobaru, A constructive peridynamic kernel for elasticity, *Comput. Methods Appl. Mech. Eng.* 311 (2016) 356–373. <https://doi.org/10.1016/j.cma.2016.08.012>.
- [34] F. Bobaru, A. Larios, I. Safarik, C. Victor, J. Zhao, Convergence of solutions to a nonlinear conservation law to solutions of a local conservation law, in progress, (n.d.).
- [35] A.J. Chorin, J.E. Marsden, *A Mathematical Introduction to Fluid Mechanics*, Springer New York, New York, NY, 1993. <https://doi.org/10.1007/978-1-4612-0883-9>.
- [36] S. Jafarzadeh, J. Zhao, M. Shakouri, F. Bobaru, A peridynamic model for crevice corrosion damage, *EngrXiv*. (2021). <https://doi.org/10.31224/OSF.IO/FC7XD>.
- [37] Q. Du, M. Gunzburger, R.B. Lehoucq, K. Zhou, A nonlocal vector calculus, nonlocal volume-constrained problems, and nonlocal balance laws, *Math. Model. Methods Appl. Sci.* 23 (2013) 493–540. <https://doi.org/10.1142/S0218202512500546>.
- [38] N. Prakash, G.D. Seidel, A novel two-parameter linear elastic constitutive model for bond based peridynamics, in: *56th AIAA/ASCE/AHS/ASC Struct. Struct. Dyn. Mater. Conf.*, American Institute of Aeronautics and Astronautics, Reston, Virginia, 2015. <https://doi.org/10.2514/6.2015-0461>.
- [39] Q. Zhu, T. Ni, Peridynamic formulations enriched with bond rotation effects, *Int. J. Eng. Sci.* 121 (2017) 118–129. <https://doi.org/10.1016/j.ijengsci.2017.09.004>.
- [40] A.J. Chorin, A numerical method for solving incompressible viscous flow problems, *J. Comput. Phys.* 135 (1997) 118–125. <https://doi.org/10.1006/jcph.1997.5716>.
- [41] J.J. Monaghan, Simulating free surface flows with SPH, *J. Comput. Phys.* 110

- (1994) 399–406. <https://doi.org/10.1006/jcph.1994.1034>.
- [42] J.P. Morris, P.J. Fox, Y. Zhu, Modeling low Reynolds number incompressible flows using SPH, *J. Comput. Phys.* 136 (1997) 214–226. <https://doi.org/10.1006/jcph.1997.5776>.
- [43] G.K. Batchelor, *An Introduction to Fluid Dynamics*, Cambridge University Press, 2000. <https://doi.org/10.1017/CBO9780511800955>.
- [44] S. Oterkus, E. Madenci, A. Agwai, Peridynamic thermal diffusion, *J. Comput. Phys.* 265 (2014) 71–96. <https://doi.org/10.1016/j.jcp.2014.01.027>.
- [45] Y. Tao, X. Tian, Q. Du, Nonlocal diffusion and peridynamic models with Neumann type constraints and their numerical approximations, *Appl. Math. Comput.* 305 (2017) 282–298. <https://doi.org/10.1016/j.amc.2017.01.061>.
- [46] Q. V. Le, F. Bobaru, Surface corrections for peridynamic models in elasticity and fracture, *Comput. Mech.* 61 (2018) 499–518. <https://doi.org/10.1007/s00466-017-1469-1>.
- [47] J.F. Wendt, J.D. Anderson, J. Degroote, G. Degrez, E. Dick, R. Grundmann, J. Vierendeels, *Computational Fluid Dynamics*, Springer Berlin Heidelberg, Berlin, Heidelberg, 2009. <https://doi.org/10.1007/978-3-540-85056-4>.
- [48] J. Zhao, S. Jafarzadeh, Z. Chen, F. Bobaru, An algorithm for imposing local boundary conditions in peridynamic models on arbitrary domains, *EngrXiv*. (2020). <https://doi.org/10.31224/osf.io/7z8qr>.
- [49] S.A. Silling, E. Askari, A meshfree method based on the peridynamic model of solid mechanics, *Comput. Struct.* 83 (2005) 1526–1535. <https://doi.org/10.1016/j.compstruc.2004.11.026>.
- [50] F. Bobaru, Y.D. Ha, Adaptive refinement and multiscale modeling in 2D peridynamics, *Int. J. Multiscale Comput. Eng.* 9 (2011) 635–659. <https://doi.org/10.1615/IntJMultCompEng.2011002793>.
- [51] S.F. Henke, S. Shanbhag, Mesh sensitivity in peridynamic simulations, *Comput. Phys. Commun.* 185 (2014) 181–193. <https://doi.org/10.1016/j.cpc.2013.09.010>.
- [52] X. Gu, Q. Zhang, X. Xia, Voronoi-based peridynamics and cracking analysis with adaptive refinement, *Int. J. Numer. Methods Eng.* 112 (2017) 2087–2109. <https://doi.org/10.1002/nme.5596>.
- [53] S. Li, Z. Chen, L. Tan, F. Bobaru, Corrosion-induced embrittlement in ZK60A Mg alloy, *Mater. Sci. Eng. A.* 713 (2018) 7–17. <https://doi.org/10.1016/j.msea.2017.12.053>.
- [54] W. Hu, Y.D. Ha, F. Bobaru, Numerical integration in peridynamics, Technical report, 2010.
- [55] F. Bobaru, G. Zhang, Why do cracks branch? A peridynamic investigation of dynamic brittle fracture, *Int. J. Fract.* 196 (2015) 59–98.

<https://doi.org/10.1007/s10704-015-0056-8>.

- [56] P. Seleson, Improved one-point quadrature algorithms for two-dimensional peridynamic models based on analytical calculations, *Comput. Methods Appl. Mech. Eng.* 282 (2014) 184–217. <https://doi.org/10.1016/j.cma.2014.06.016>.
- [57] R. Courant, K. Friedrichs, H. Lewy, Über die partiellen Differenzengleichungen der mathematischen Physik, *Math. Ann.* 100 (1928) 32–74. <https://doi.org/10.1007/BF01448839>.
- [58] J.J. Monaghan, Smoothed Particle Hydrodynamics, *Annu. Rev. Astron. Astrophys.* 30 (1992) 543–574. <https://doi.org/10.1146/annurev.aa.30.090192.002551>.
- [59] J. Zhao, S. Jafarzadeh, M. Rahmani, Z. Chen, Y.-R. Kim, F. Bobaru, A peridynamic model for galvanic corrosion and fracture, *Electrochim. Acta.* 391 (2021) 138968. <https://doi.org/10.1016/j.electacta.2021.138968>.
- [60] S. Adami, X.Y. Hu, N.A. Adams, A generalized wall boundary condition for smoothed particle hydrodynamics, *J. Comput. Phys.* 231 (2012) 7057–7075. <https://doi.org/10.1016/j.jcp.2012.05.005>.
- [61] S. Prudhomme, P. Diehl, On the treatment of boundary conditions for bond-based peridynamic models, *Comput. Methods Appl. Mech. Eng.* 372 (2020) 113391. <https://doi.org/10.1016/j.cma.2020.113391>.

Chapter 6 An algorithm for imposing local boundary conditions in peridynamic models of diffusion on arbitrary domains

6.1 Introduction

The peridynamic (PD) theory [1], as a nonlocal extension of classical continuum mechanics, allows for a natural treatment of discontinuities/singularities (such as cracks/damages [2–5]) by employing integration, over a nonlocal region called the horizon region, rather than differentiation. While the PD method has been primarily used to deal with mechanical behaviors [2,4,6–9], it has also been employed in diffusion-type problems involving cracks and damages, including thermal diffusion [10–13] and mass transport (e.g. corrosion) [14–20]. For a nonlocal formulation, associated BCs are of nonlocal type as well, and they are sometimes referred to as “nonlocal volume constraints” [21,22]. In reality, however, conditions to be imposed (on values and/or derivatives of the unknown function) are known (measurable) only at the surface of a body, not through a finite thickness layer at the surface. The natural representation of such measurement-based conditions is via local boundary conditions. Therefore, imposing local BCs in nonlocal/peridynamic models is often desired/needed. Another issue caused by nonlocality is the surface effect [23] which appears because, unlike in the bulk, points near the free surface/boundary do not have a full horizon region. The surface effect leads to slightly different behavior of material points near the surface compared with those in the bulk.

A couple of strategies have been introduced to tackle these issues in the literature. One is to get rid of the nonlocality at boundaries, either by decomposing the domain into local and nonlocal subdomains where the former is placed in the neighborhood of the boundary

[24], or via using a variable horizon which decreases from a constant value in the interior of the domain to zero at the boundary [25]. This strategy, however, does not work for problems in which nonlocality/discontinuity plays important roles near the boundary (e.g., interface problems), not to mention the complexity involved to take care of the coupling of local and nonlocal models at the transition zone, or the imbalance of bond force/flux between material points induced by variable horizons [26]. Another popular strategy is to extend the solution domain by a fictitious layer which has the thickness of the PD horizon, so that each point in the solution domain has a full horizon region. Then the local BCs (including free BCs) are converted into nonlocal volume constraints to be imposed on this fictitious region. This strategy is called fictitious nodes method (FNM), or extended domain method (EDM), and can be further classified to different categories based on the rule of conversion [11,12,27–31]. Similar ideas have been used in other nonlocal numerical models [32,33]. Some of these FNMs require reformulation of governing equations for each type of problems [28,29] and are thus may not be suitable for general applications. Others which do not involve the modification of governing equations has been proven to work efficiently in problems with simple geometries, but it is still a challenge to apply them to problems with irregular geometries, such as those with curved boundaries, kinks, corners and cracks, due to a lack of algorithms to generate necessary data required by these methods. Specifically, for the mirror-based FNM which determines the volume constraint at each fictitious node based on the value of its mirror node in the solution domain [30,31,34], there is no general algorithm to find the mirror nodes (of all fictitious nodes) required by the method.

In this work, we introduce a new algorithm that helps us automatically finding mirror nodes in the mirror-based FNM for domains of arbitrary geometries, including for those with crack surfaces. This algorithm approximates, at each fictitious node, a “generalized” normal vector which is perpendicular to the boundary of the solution domain if the boundary satisfies the 1st order smooth condition. We select the PD diffusion model to test our algorithm. With small modifications, the algorithm presented here is also applicable to PD models solving other types of problems, such as fracture and corrosion damage. We also investigate two other types of FNMs and compare their results with those from the mirror-based FNM: the “naive” version [35], and the Taylor FNM [27,32,36]. We compare the performance of different FNMs in enforcing local boundary conditions using two problems: one is a simple problem without singularity and the other is the Motz’s problem with a singularity (in fluxes) along a boundary where Dirichlet and Neumann boundary conditions meet [37,38]. We show the capability of the new algorithm, used in the context of mirror-based FNM, by solving examples of diffusion in domains with crack surfaces and curved boundaries.

This paper is organized as follows: in Section 6.2 we review the PD method for diffusion-type problems; in Section 6.3 we discuss the fictitious nodes method and introduce the autonomous algorithm to generalize the mirror-based FNM for arbitrary geometries; in Section 6.4 we compare the performance of three different types of FNMs using examples with and without local singularities, then test the generality and capability of the developed algorithm on the mirror-based FNM for more complicated problems with cracks; conclusions are finally given in Section 6.5.

6.2 The peridynamic model for diffusion

Consider the diffusion of a scalar quantity u (e.g., temperature) in a homogeneous and isotropic body occupying the domain $\Omega \in \mathbb{R}^d$, $d = 1, 2$ or 3 , with constant diffusivity ν .

The classical local model describes the diffusion by using the following PDE-based formulation:

$$\begin{cases} \frac{\partial u(\mathbf{x}, t)}{\partial t} = \nu \nabla^2 u(\mathbf{x}, t) + s(\mathbf{x}, t) & \forall (\mathbf{x}, t) \in \Omega \times [0, T] \\ G(u(\mathbf{x}, t)) = 0 & \forall (\mathbf{x}, t) \in \partial\Omega \times [0, T] \end{cases} \quad (6.1)$$

where $s \in \mathbb{R}$ is the source/sink term and $G(u(\mathbf{x}, t))$ defines the BCs (which could be Dirichlet, Neumann, Robin, or mixed).

The peridynamic (PD) bond-based diffusion model [10,21,39], on the other hand, is written as:

$$\frac{\partial u(\mathbf{x}, t)}{\partial t} = \nu \mathcal{L}_\omega u(\mathbf{x}, t) + s(\mathbf{x}, t) \quad \forall (\mathbf{x}, t) \in \Omega \times [0, T] \quad (6.2)$$

where \mathcal{L}_ω is the PD Laplacian operator which can be expressed as:

$$\mathcal{L}_\omega u(\mathbf{x}, t) = \int_{\mathcal{H}_x} \omega(\mathbf{x}, \mathbf{y})(u(\mathbf{y}, t) - u(\mathbf{x}, t)) d\mathbf{y}, \quad (6.3)$$

Here \mathcal{H}_x is the (nonlocal) horizon region of \mathbf{x} and is usually selected to be a disk in 2D (a line segment in 1D or a sphere in 3D) centered at \mathbf{x} , with the radius denoted by δ (which is called horizon size, or simply horizon). Figure 6.1 schematically shows a 2D PD body with a generic point \mathbf{x} , its family and its horizon. Objects that carry the pairwise nonlocal interactions between points are called bonds. In the more generalized state-based formulation, diffusion in a bond is directly influenced by other bonds which connect to

the same point [12]. This setting may be beneficial for certain problems but is not considered here.

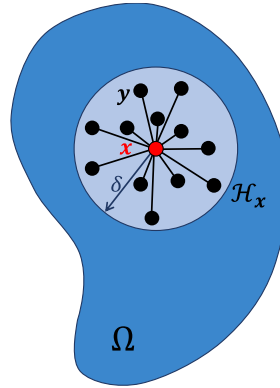


Figure 6.1. A peridynamic body with a generic point \mathbf{x} and its horizon \mathcal{H}_x . Nonlocal interactions exist through the bond between point \mathbf{x} and an arbitrary point \mathbf{y} located in its horizon \mathcal{H}_x .

The kernel function $\omega(\mathbf{x}, \mathbf{y}): \Omega \times \Omega \rightarrow \mathbb{R}$ in Eq. (6.3) denotes a nonnegative symmetric mapping, i.e., $\omega(\mathbf{x}, \mathbf{y}) = \omega(\mathbf{y}, \mathbf{x}) \geq 0$. It has been shown that for $u \in C^2(\Omega)$, $\mathcal{L}_\omega u \rightarrow \Delta u$ as $\delta \rightarrow 0$, under certain conditions [35,40,41]. A kernel function that leads to good convergence properties with the one-point Gaussian quadrature discretization of the spatial domain is [35]:

$$\omega(\mathbf{x}, \mathbf{y}) = \frac{A}{\|\mathbf{y} - \mathbf{x}\|^2} \quad (6.4)$$

where A is a constant which can be calibrated by matching PD flux to classical flux for a linearly distributed field, as shown in [11]. One can also determine A by enforcing that Eq. (6.2) recovers the classical diffusion equation as $\delta \rightarrow 0$ using the approach first provided in [25] for 1D linear elasticity, as shown below for 2D diffusion.

Suppose $u(\mathbf{x})$ is sufficiently smooth, one can write, for all $\mathbf{x} \in \Omega_l$ and $\mathbf{y} \in \mathcal{H}_x$:

$$\begin{aligned}
u(\mathbf{y}) &= u(\mathbf{x}) + \xi_x \frac{\partial u}{\partial x}(\mathbf{x}) + \xi_y \frac{\partial u}{\partial y}(\mathbf{x}) \\
&+ \frac{1}{2!} \left(\xi_x^2 \frac{\partial^2 u}{\partial x^2}(\mathbf{x}) + 2\xi_x \xi_y \frac{\partial^2 u}{\partial x \partial y}(\mathbf{x}) + \xi_y^2 \frac{\partial^2 u}{\partial y^2}(\mathbf{x}) \right) \\
&+ \frac{1}{3!} \left(\xi_x^3 \frac{\partial^3 u}{\partial x^3}(\mathbf{x}) + 3\xi_x^2 \xi_y \frac{\partial^3 u}{\partial x^2 \partial y}(\mathbf{x}) + 3\xi_x \xi_y^2 \frac{\partial^3 u}{\partial x \partial y^2}(\mathbf{x}) \right. \\
&\left. + \xi_y^3 \frac{\partial^3 u}{\partial y^3}(\mathbf{x}) \right) + o\left((\xi_x^2 + \xi_y^2)^2 \right)
\end{aligned} \tag{6.5}$$

where $\boldsymbol{\xi} = \mathbf{y} - \mathbf{x} = [\xi_x \quad \xi_y]^T$. Substitute Eq. (6.5) into Eq. (6.3) and consider symmetry, we get:

$$\begin{aligned}
\mathcal{L}_\omega u(\mathbf{x}, t) &= \frac{A}{2} \int_{\mathcal{H}_x} \frac{\xi_x^2 \frac{\partial^2 u}{\partial x^2} + \xi_y^2 \frac{\partial^2 u}{\partial y^2} + o\left((\xi_x^2 + \xi_y^2)^2 \right)}{\xi_x^2 + \xi_y^2} d\hat{\mathbf{x}} \\
&= \frac{A}{2} \left(\frac{\partial^2 u}{\partial x^2} \int_0^\delta \rho d\rho \int_0^{2\pi} \cos^2 \theta d\theta \right. \\
&\quad \left. + \frac{\partial^2 u}{\partial y^2} \int_0^\delta \rho d\rho \int_0^{2\pi} \sin^2 \theta d\theta + \delta^2 o(\delta^2) \right) \\
&= \frac{\pi \delta^2 A}{4} \left(\frac{\partial^2 u}{\partial x^2} + \frac{\partial^2 u}{\partial y^2} + o(\delta^2) \right)
\end{aligned} \tag{6.6}$$

One recovers the 2D classical diffusion equation as $\delta \rightarrow 0$ when we have:

$$A = \frac{4}{\pi \delta^2} \tag{6.7}$$

Eq. (6.7) agrees with the calibrated values given in [10,11]. With this value, the PD model converges to the classical model of order two for $\mathbf{x} \in \Omega_I$. However, using Eq. (6.7) for $\mathbf{x} \in \Omega_\varsigma$ (which does not have a full horizon region) would lead to lower diffusivity (or a lower stiffness for problems in elasticity (see [23,25])). Moreover, BCs for PD equations (e.g., Eq. (6.2)) should be nonlocal (sometimes called “volume-constraints”

[21,22]), but usually only the local BCs are available. In the next section we discuss FNMs which transforms local BCs to their nonlocal counterparts in PD models.

6.3 Fictitious nodes methods

Unlike classical local methods, the boundary conditions in peridynamics are nonlocal. However, when solving practical problems, imposing local-type boundary conditions in nonlocal/peridynamic models is usually desired/needed because, in most applications at the macroscale, conditions (on the unknown function values or its flux) are imposed at the surfaces of a body, not through a finite layer near the surface. The natural representation of such conditions (based on measurements) is via local boundary conditions. Various methods to impose local boundary conditions in PD models have been investigated in [12,22,42]. One such method is the fictitious nodes method (FNM) [12,30,42].

In FNM for peridynamics, certain volume constraints $c(u(\mathbf{x})) = 0$ are specified on the extended fictitious region $\tilde{\Omega} = \{\mathbf{x} \notin \Omega \mid \text{dist}(\mathbf{x}, \partial\Omega) < \delta\}$ (the “collar” outside of the solution domain Ω shown in Figure 6.2), so that desired local boundary conditions on $\partial\Omega$ are satisfied or approximately satisfied. Such volume-constrained PD problems are defined analogous to boundary value problems with PDEs in the local theory according to nonlocal vector calculus [22]. Volume-constrained PD steady-state diffusion (or Laplace) problem can be expressed as [22]:

$$\begin{cases} \mathcal{L}_\omega u(\mathbf{x}) = 0 & \mathbf{x} \in \Omega \\ c(u(\mathbf{x})) = 0 & \mathbf{x} \in \tilde{\Omega} \end{cases} \quad (6.8)$$

When applied to free boundaries (or crack surfaces), the FNM mitigates the peridynamic surface effect [30]. This is a common issue for numerical models using nonlocal formulations [22,33]. The surface effect appears because, unlike in the bulk, material points near the free boundary/surface do not have a full non-local neighborhood. The surface effect leads to slightly different behavior of material points near the surface compared with those in the bulk. This could mean a lower diffusivity near the surface for diffusion problems, and a lower stiffness for problems in elasticity (see [23]). These effects are reduced as one decreases δ and would be “exact” when δ is the same as the physical nonlocal interaction range, which could be atomistically small. In practical modeling, δ is usually set to match observable physical length-scales (see discussion in [43]), and not larger than relevant geometrical features of the domain (notch widths, etc.).

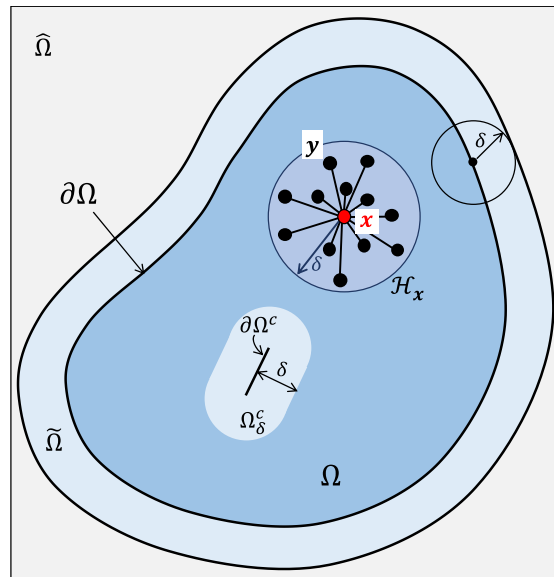


Figure 6.2. Schematic of a peridynamic domain (Ω), its boundary ($\partial\Omega$) and crack surface ($\partial\Omega^c$), its fictitious layer ($\tilde{\Omega}$), and the region affected by the crack surface (Ω_δ^c), the regular-shaped region $\hat{\Omega}$ in which $\tilde{\Omega}$ is determined.

Before implementing FNMs, the explicit $\partial\Omega$ (including crack surfaces $\partial\Omega^c$) at the initial time is needed to determine the initial configuration of discretized Ω and $\tilde{\Omega}$ (see

Appendix A). Note that if a node \mathbf{x} sits on $\partial\Omega$, we let $\mathbf{x} \in \Omega$. Then the boundary $\partial\Omega \setminus \partial\Omega^c$ will be implicitly tracked by bonds connecting points in Ω and those in $\tilde{\Omega}$, and $\partial\Omega^c$ is tracked by broken bonds. A regular-shaped region $\hat{\Omega}$ is usually placed outside Ω in which $\tilde{\Omega}$ is determined, and the $\tilde{\Omega}$ determined after discretization is usually larger than the one before discretization to assure \mathcal{H}_x is complete $\forall \mathbf{x} \in \Omega$ in the discretized configuration. In this section, we review three different types of FNM from literature.

6.3.1 Naïve FNM

A naïve type of FNM is often used in the literature to impose local Dirichlet and homogeneous Neumann (no flux) BCs. This method enforces Dirichlet BCs by assigning the same values to all fictitious points corresponding to a boundary point, while homogeneous Neumann BCs are enforced by simply neglecting all corresponding fictitious points [35]. See Figure 6.3 for an illustration of how a Dirichlet BC $u(\mathbf{x}_b) = u_b$ at $\mathbf{x}_b \in \partial\Omega_D$ (boundary subjected to **D**irichlet BC) is enforced at $\mathbf{x} \in \tilde{\Omega}_D$ (fictitious region subjected to Dirichlet volume-constraint). An even simpler version of “enforcing” local Dirichlet BCs in the nonlocal model is to dispense entirely with the fictitious points and subject only the surface points to the values of local boundary conditions [10]. Previous work has shown that results by both versions converge to local solutions as the horizon size approaches zero [13,35].

Remark: The naïve FNM has the advantage of featuring the simplest implementation and is the most efficient (see Section 6.4.1). However, a jump-discontinuity in the solution at the boundary may be generated, leading to possible errors in fluxes near the boundary (see the result in section 6.4.1 for an example).

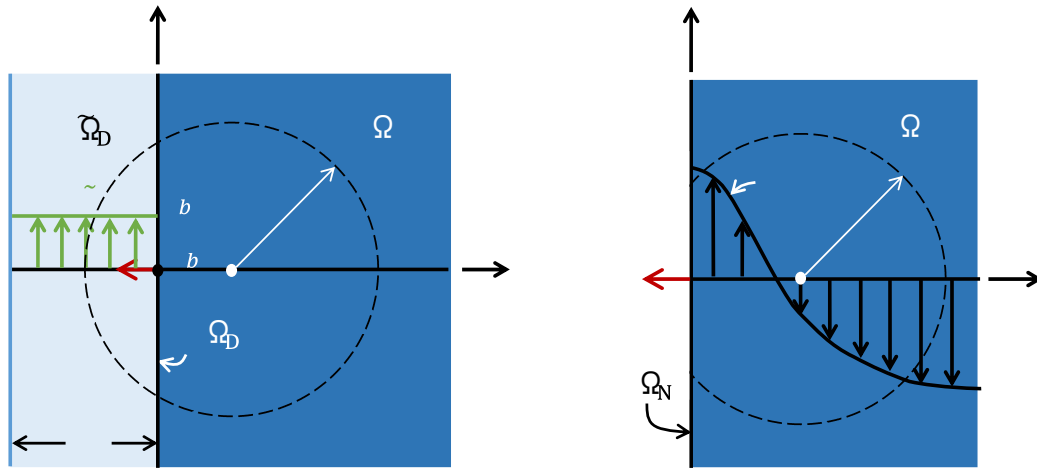


Figure 6.3. Illustration of using the naïve FNM to enforce the local (a) Dirichlet and (b) homogeneous Neumann BCs.

6.3.2 Taylor-based FNM

The second FNM, used in the PD context first in [27], requires a Taylor expansion (to linear terms) for $\mathbf{x} \in \tilde{\Omega} \cup \Omega_\delta$, in which $\Omega_\delta = \{\mathbf{x} \in \Omega \mid \text{dist}(\mathbf{x}, \partial\Omega) < \delta\}$. We call it Taylor-based FNM or simply Taylor FNM. To impose the local Dirichlet BC $u(\mathbf{x}) = u_D(\mathbf{x})$ for $\mathbf{x} \in \partial\Omega_D$ using Taylor FNM, for each $\mathbf{x} \in \Omega_\delta$, $\mathbf{y} \in \tilde{\Omega}_D \cap \mathcal{H}_x$ and $\mathbf{x}_b = \partial\Omega_D \cap \overline{\mathbf{x}\mathbf{y}}$, $\tilde{u}(\mathbf{y})$ is extrapolated from $u(\mathbf{x})$ as:

$$\tilde{u} = u + \left(\frac{\partial u}{\partial \xi}\right) \xi + \mathcal{O}(\delta^2) \approx u + \frac{(u_b - u)}{d} (d + \tilde{d}) = u_b + \frac{\tilde{d}}{d} (u_b - u) \quad (6.9)$$

where $\tilde{u} = \tilde{u}(\mathbf{y})$, $u = u(\mathbf{x})$, $u_b = u_D(\mathbf{x}_b)$, $\xi = \mathbf{y} - \mathbf{x}$, $d = \text{dist}(\mathbf{x}, \mathbf{x}_b)$ and $\tilde{d} = \text{dist}(\mathbf{y}, \mathbf{x}_b)$ (“dist” denotes distance).

$$u_b \approx u + df(u_b) \quad (6.12)$$

If $f(u_b)$ is a nonlinear function, a nonlinear equation solver, such as Newton's method, is needed to solve for u_b [44].

Remark: In this Taylor approach, in the same solution step, \tilde{u} at each $\mathbf{y} \in \tilde{\Omega}$ changes, even in the same solution step, changes and needs to be computed anew for each $\mathbf{x} \in \Omega_\delta \cap \mathcal{H}_\mathbf{y}$ at which an integration over $\mathcal{H}_\mathbf{x}$ is performed (see Eqs. (6.9) & (6.12)). This is illustrated in Figure 6.4, where for $\mathbf{x}_i \in \Omega_\delta$ and $\mathbf{x}_b \in \partial\Omega_D \cap \mathcal{H}_{\mathbf{x}_i}$, \tilde{u}_i is the distribution of $\tilde{u}(\mathbf{y}) \forall \mathbf{y} \in \{\mathbf{y} \in \tilde{\Omega}_D | \partial\Omega_D \cap \overline{\mathbf{x}_i\mathbf{y}} = \mathbf{x}_b\}$. The solution step refers to each call to the Conjugate Gradient (CG) solver (see Figure 6.24 in Appendix A for the flowchart of the simulation). Moreover, for boundaries with irregular geometries such as corners, those \mathbf{x} and \mathbf{y} nearby also have variable d and \tilde{d} associated with them, because for each pair of \mathbf{x} and \mathbf{y} , $\overline{\mathbf{x}\mathbf{y}}$ may intersect with different segments of the boundary.

6.3.3 Mirror-based FNM

If $d = \tilde{d}$ in Eqs. (6.9) and (6.12), the Taylor-based FNM degenerates to the mirror-based FNM, or simply “mirror FNM”. As shown in Figure 6.5, the mirror FNM assigns the constraint $\tilde{u}(\mathbf{x})$ at each $\mathbf{x} \in \tilde{\Omega}$ based on $u(\mathbf{x}^R)$ and $u(\mathbf{x}^P)$ in which $\mathbf{x}^P = \text{OProj}_{\partial\Omega}(\mathbf{x})$ is the orthogonal projection of \mathbf{x} onto $\partial\Omega$ and $\mathbf{x}^R = \text{Ref}_{\partial\Omega}(\mathbf{x}) = \mathbf{x} + 2(\mathbf{x}^P - \mathbf{x})$ is the reflection, or mirror point, of \mathbf{x} through/across $\partial\Omega$. For $\mathbf{x} \in \tilde{\Omega}$, when $\partial\Omega_\mathbf{x} = \{\partial\Omega \cap \mathcal{H}_\mathbf{x}\}$ is continuous and the normal to $\partial\Omega_\mathbf{x}$ at each $\mathbf{y} \in \partial\Omega_\mathbf{x}$ is unique (i.e., $\partial\Omega_\mathbf{x} \in G^1$), we have $\overline{\mathbf{x}\mathbf{x}^P} = k\mathbf{n}(\mathbf{x}^P)$, in which $k \in \mathbb{R}^-$ and $\mathbf{n}(\mathbf{x}^P)$ is the outward unit normal vector at \mathbf{x}^P .

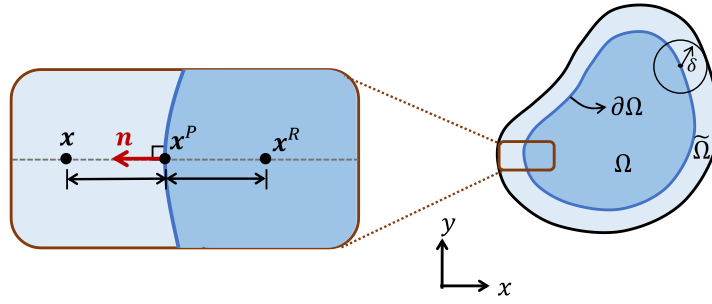


Figure 6.5. A schematic of mirror points in mirror-based FNM [12].

In the mirror FNM, to impose the local Dirichlet BC $u(\mathbf{x}) = u_D(\mathbf{x})$ for $\mathbf{x} \in \partial\Omega_D$ and the Neumann BC $\nabla_n u(\mathbf{x}) = -q(\mathbf{x})$ for $\mathbf{x} \in \partial\Omega_N$, $\tilde{u}(\mathbf{x})$ at $\mathbf{x} \in \tilde{\Omega}_D$ is assigned as:

$$\tilde{u}(\mathbf{x}) = 2u(\mathbf{x}^P) - u(\mathbf{x}^R) \quad (6.13)$$

and $\tilde{u}(\mathbf{x})$ at $\mathbf{x} \in \tilde{\Omega}_N$ is assigned as:

$$\tilde{u}(\mathbf{x}) = u(\mathbf{x}^R) - \|\mathbf{x} - \mathbf{x}^R\|q(\mathbf{x}^P) \quad (6.14)$$

respectively. For the local Robin BC $\nabla_n u(\mathbf{x}) = f(u(\mathbf{x}))$ for $\mathbf{x} \in \partial\Omega_R$, we have, for $\mathbf{x} \in \tilde{\Omega}_R$:

$$\begin{aligned} \tilde{u}(\mathbf{x}) &= u(\mathbf{x}^R) - \|\mathbf{x} - \mathbf{x}^R\|f(u(\mathbf{x}^P)) \\ &= u(\mathbf{x}^R) - \|\mathbf{x} - \mathbf{x}^R\|f\left(\frac{u(\mathbf{x}^R) + \tilde{u}(\mathbf{x})}{2}\right) \end{aligned} \quad (6.15)$$

in which the approximation $u(\mathbf{x}^P) = \frac{u(\mathbf{x}^R) + \tilde{u}(\mathbf{x})}{2}$ is made because the distribution of u should be close to linear between \mathbf{x} and \mathbf{x}^R . Note that $\tilde{u}(\mathbf{x})$ requires to be solved using a nonlinear solver if function f is nonlinear.

Remark: In the mirror FNM, $\tilde{u}(\mathbf{x})$ at each $\mathbf{x} \in \tilde{\Omega}$ does not change in the same solution step because it only depends on \mathbf{x}^R and \mathbf{x}^P which can be uniquely determined for each \mathbf{x} .

See Figure 6.6 for illustrations of how local Dirichlet BCs are enforced in the mirror FNM.

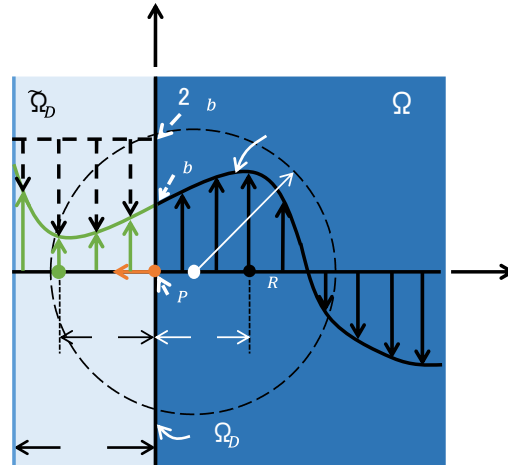


Figure 6.6. Illustration of enforcing a local Dirichlet BC in the mirror FNM (redrawn from [12]).

Remark: Note that in the Taylor and mirror FNMs described in this section, all the information for $\boldsymbol{x} \in \Omega_\delta \cup \tilde{\Omega}$, such as $\text{dist}(\boldsymbol{x}, \partial\Omega)$, $\text{Ref}_{\partial\Omega}(\boldsymbol{x})$ are considered as given, which works for simple geometries. However, for general cases, such information is not straightforward and cannot be provided as input. For example, for shapes with corners of various angles, cusps and crack tips, etc., the tangent line (and normal vector) is not well defined everywhere. While some ad-hoc choices can be made for overcoming this issue, we aim for a general strategy which assures all the information required to implement the FNM can be determined without ambiguity. Moreover, the enforcement of local BCs on surfaces of thin cracks is not considered till this point, mainly because fictitious regions are not clearly defined for such “inner” surfaces yet. In the next section we introduce an automatic algorithm specifically for the mirror FNM so that local BCs, including those

imposed on crack surfaces, can be enforced in PD for problems with arbitrary boundary/surface shapes.

6.3.4 An algorithm to find mirror nodes for the mirror-based FNM

In order to use the mirror FNM to impose local BCs on surfaces of thin cracks $\partial\Omega^c$, we let $\Omega_\delta^c = \{\mathbf{x} \in \Omega \mid \text{dist}(\mathbf{x}, \partial\Omega^c) < \delta\}$ and $\tilde{\Omega} = \tilde{\Omega} \cup \Omega_\delta^c$, so that $\mathbf{x} \in \Omega_\delta^c$ on one side of the crack surface can serve as fictitious points for $\mathbf{x} \in \Omega_\delta^c$ on the other side of the crack surface.

Using the mirror FNM for arbitrarily shaped boundaries/surfaces (with corners, cusps, etc.) requires finding both \mathbf{x}^P and $\mathbf{x}^R \forall \mathbf{x} \in \tilde{\Omega}$. Since $\mathbf{x}^R = \mathbf{x} + 2(\mathbf{x}^P - \mathbf{x})$, as shown in Figure 6.5, once \mathbf{x}^P is known, \mathbf{x}^R can be determined. Starting from $\mathbf{x} \in \tilde{\Omega}$, one could determine \mathbf{x}^P as $\arg \min_{\mathbf{y} \in \mathcal{H}_x \cap \partial\Omega} \text{dist}(\mathbf{y}, \mathbf{x})$. However, the uniqueness of the solution is not

guaranteed. Moreover, for \mathbf{x} near corners with an angle smaller than 90° (see regions $\tilde{\Omega}_1$ in Figure 6.7), it may lead to $\mathbf{x}^R \notin \Omega$.

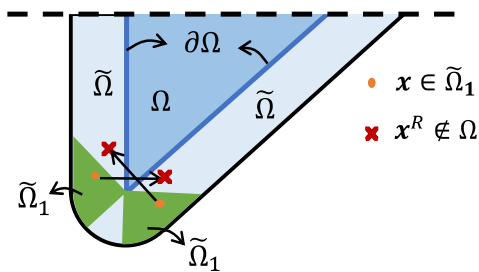


Figure 6.7. Schematic of $\tilde{\Omega}_1 \subset \tilde{\Omega}$ near an acute corner where $\mathbf{x}^R = \text{Ref}_{\partial\Omega}(\mathbf{x}) \notin \Omega$ for $\mathbf{x} \in \tilde{\Omega}_1$, when $\mathbf{x}^P = \arg \min_{\mathbf{y} \in \mathcal{H}_x \cap \partial\Omega} \text{dist}(\mathbf{y}, \mathbf{x})$

We introduce an algorithm to resolve all these issues. First, we compute $\tilde{\mathbf{n}}(\mathbf{x}) =$

$\frac{\overrightarrow{\mathbf{x}\mathbf{x}^P}}{\|\overrightarrow{\mathbf{x}\mathbf{x}^P}\|}$ for $\mathbf{x} \in \tilde{\Omega}$ using similar ideas to that of [29]:

$$\tilde{\mathbf{n}}(\mathbf{x}) = \begin{cases} \frac{\int_{\mathcal{H}_x \cap \Omega} (\mathbf{y} - \mathbf{x}) d\mathbf{y}}{\left\| \int_{\mathcal{H}_x \cap \Omega} (\mathbf{y} - \mathbf{x}) d\mathbf{y} \right\|} & \text{for } \mathbf{x} \in \tilde{\Omega} \setminus \Omega_\delta^c \\ -\frac{\int_{\mathcal{H}_x} \mu(\mathbf{x}, \mathbf{y}) (\mathbf{y} - \mathbf{x}) d\mathbf{y}}{\left\| \int_{\mathcal{H}_x} \mu(\mathbf{x}, \mathbf{y}) (\mathbf{y} - \mathbf{x}) d\mathbf{y} \right\|} & \text{for } \mathbf{x} \in \Omega_\delta^c \end{cases} \quad (6.16)$$

where $\mu(\mathbf{x}, \mathbf{y})$ is the binary function which equals 0 if the mechanical bond connecting \mathbf{x} and \mathbf{y} is broken, and 1 otherwise. $\tilde{\mathbf{n}}(\mathbf{x})$ given by Eq. (6.16) points inward (toward Ω).

Since $\tilde{\mathbf{n}}(\mathbf{x})$ is unique for each $\mathbf{x} \in \tilde{\Omega}$, it allows us to locate \mathbf{x}^P and \mathbf{x}^R uniquely. For each $\mathbf{x} \in \tilde{\Omega}$, if $\partial\Omega_x = (\partial\Omega \cap \mathcal{H}_x) \in G^1$, we have $\tilde{\mathbf{n}}(\mathbf{x}) = k\mathbf{n}(\mathbf{x}^P)$ in which $k \in \mathbb{R}^-$ and $\mathbf{n}(\mathbf{x}^P)$ is the outward unit normal vector at \mathbf{x}^P . On the other hand, if $\partial\Omega_x \notin G^1$, $\mathbf{n}(\mathbf{x}^P)$ may not exist, and even if it exists, we only have $\tilde{\mathbf{n}}(\mathbf{x}) \approx k\mathbf{n}(\mathbf{x}^P)$.

Note that for $\tilde{\Omega}$ near sharp (relative to the horizon size) convex corners, Eq. (6.16) may still lead to $\mathbf{x}^R \notin \Omega$ for $\mathbf{x} \in \tilde{\Omega}_2 \subset \tilde{\Omega}$, as shown in Figure 6.8, although $\tilde{\Omega}_2$ covers a much smaller area than that of $\tilde{\Omega}_1$ in Figure 6.7. This issue can be reduced by using smaller horizon sizes but not fully resolved. In practice, if $\mathbf{x}^R \notin \Omega$ for $\mathbf{x} \in \tilde{\Omega}_2$, we let $\mathbf{x}^R =$

$\arg \min_{\mathbf{y} \in \mathcal{H}_{\mathbf{x}^R} \cap \Omega} \text{dist}(\mathbf{y}, \mathbf{x}^R)$. Other options include approximating $\tilde{u}(\mathbf{x})$ by $u(\mathbf{y})$ at

$\arg \min_{\mathbf{y} \in \mathcal{H}_x \cap \tilde{\Omega}} \text{dist}(\mathbf{y}, \mathbf{x})$, or using Naïve FNM if it is possible. Since $\tilde{\Omega}_2$ only covers a very

small fraction of $\tilde{\Omega}$ around the corner, the error introduced by these approximations should be trivial.

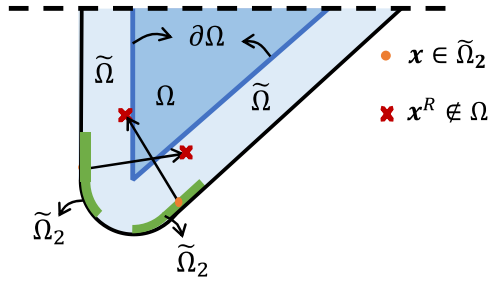


Figure 6.8. Schematic of $\tilde{\Omega}_2 \subset \tilde{\Omega}$ near an acute corner for which $\mathbf{x}^R = \text{Ref}_{\partial\Omega}(\mathbf{x}) \notin \Omega$ for $\mathbf{x} \in \tilde{\Omega}_2$, when Eq. (6.16) is used to determine \mathbf{x}^R .

Before implementing the algorithm, the explicit $\partial\Omega$ (including crack surfaces $\partial\Omega^c$) at the initial time is needed to determine the initial configuration of discretized Ω and $\tilde{\Omega}$ (see Appendix A). Note that if a node \mathbf{x} sits on $\partial\Omega$, we let $\mathbf{x} \in \Omega$. Then the boundary $\partial\Omega \setminus \partial\Omega^c$ will be implicitly tracked by bonds connecting points in Ω and those in $\tilde{\Omega}$, and $\partial\Omega^c$ is tracked by broken bonds. A regular-shaped region $\hat{\Omega}$ is usually placed outside Ω in which $\tilde{\Omega}$ is determined, and the effective $\tilde{\Omega}$ determined after discretization is usually larger than the one before discretization to assure \mathcal{H}_x is complete $\forall \mathbf{x} \in \Omega$ in the discretized configuration. Re-finding \mathbf{x}^P and \mathbf{x}^R is required every time $\tilde{\Omega}$ evolves ($\tilde{\Omega}^{\text{new}} \neq \tilde{\Omega}^{\text{old}}$), which happens in problems such as corrosion or fracture, but only for those $\mathbf{x} \in \{\mathbf{x} \in \tilde{\Omega}^{\text{new}} \mid \mathcal{H}_x \cap \{\tilde{\Omega}^{\text{new}} \cup \tilde{\Omega}^{\text{old}}\} \setminus \{\tilde{\Omega}^{\text{new}} \cap \tilde{\Omega}^{\text{old}}\} \neq \emptyset\}$.

The algorithm to find mirror nodes for each $\mathbf{x} \in \tilde{\Omega}$ is as follows:

- (1) Compute $\tilde{\mathbf{n}}(\mathbf{x})$ using Eq. (6.16).
- (2) Search for \mathbf{x}^P :
 - a. if $\mathbf{x} \in \tilde{\Omega} \setminus \Omega_\delta^c$, then search in $(\mathcal{H}_x \cap \Omega)$ in the direction of $\tilde{\mathbf{n}}(\mathbf{x})$ for the node closest to \mathbf{x} , i.e., $\mathbf{x}^P = \arg \min_{\mathbf{y} \in \mathcal{H}_x \cap \Omega} \text{dist}(\mathbf{y}, \mathbf{x})$, subject to $\text{dist}(\tilde{\mathbf{n}}(\mathbf{x}), \mathbf{y}) < \Delta x/2$; note that:

$$\text{dist}(\tilde{\mathbf{n}}(\mathbf{x}), \mathbf{y}) = \sqrt{(\mathbf{y} - \mathbf{x}) \cdot (\mathbf{y} - \mathbf{x}) - ((\mathbf{y} - \mathbf{x}) \cdot \tilde{\mathbf{n}}(\mathbf{x}))^2}; \quad (6.17)$$

- b. elseif $\mathbf{x} \in \Omega_\delta^c$, then $\mathbf{x}^P = \arg \min_{\mathbf{y} \in \mathcal{H}_x \cap \Omega} \text{dist}(\mathbf{y}, \mathbf{x})$, subject to $\text{dist}(\tilde{\mathbf{n}}(\mathbf{x}), \mathbf{y}) < \Delta x/2$ and $\mu(\mathbf{x}, \mathbf{y}) = 0$;
 - c. if \mathbf{x}^P is not found, let $\mathbf{x}^P = \arg \min_{\mathbf{y} \in \Omega} \text{dist}(\mathbf{y}, \mathbf{x})$, subject to $\text{dist}(\tilde{\mathbf{n}}(\mathbf{x}), \mathbf{y}) < \Delta x/2$;
 - d. if two or more \mathbf{x}^P are found, selecting either one of them is acceptable.
- (3) Search for \mathbf{x}^R :
- a. compute $\mathbf{x}' = \mathbf{x} + (2\|\mathbf{x}^P - \mathbf{x}\| - \Delta x)\tilde{\mathbf{n}}(\mathbf{x})$;
 - b. since \mathbf{x}' may not coincide with a node's coordinates in the domain, we have $\mathbf{x}^R = \arg \min_{\mathbf{y} \in \mathcal{H}_{\mathbf{x}'} \cap \Omega} \text{dist}(\mathbf{y}, \mathbf{x}')$.

Some examples for this searching process are shown in Figure 6.9.

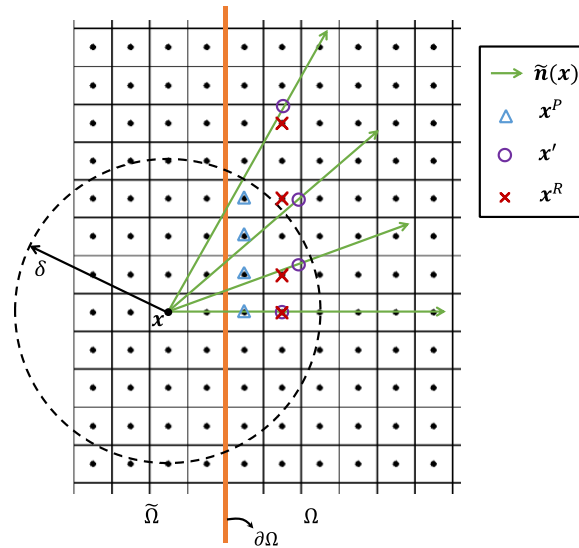


Figure 6.9. Schematic diagram of determining \mathbf{x}^P and \mathbf{x}^R for a generic $\mathbf{x} \in \tilde{\Omega}$ given four different $\tilde{\mathbf{n}}(\mathbf{x})$.

Remark: By using this algorithm, regardless of the smoothness of $\partial\Omega$, \mathbf{x}^P and \mathbf{x}^R will converge, for a certain choice of δ , as $\delta/\Delta x$ approaches infinity. If $\partial\Omega \in G^1$, the converged value will be the analytical one. Before the development of this algorithm, one needs to make assumptions (which can vary from one paper to another) about $\overline{\mathbf{x}\mathbf{x}^P}$ at

sharp corners when using the mirror FNM [12,30] and the local BCs at free crack surfaces are usually treated by the naïve FNM. Now, by using this algorithm, \mathbf{x}^P and \mathbf{x}^R are found automatically and consistently $\forall \mathbf{x} \in \tilde{\Omega}$, including \mathbf{x} near sharp corners and crack surfaces. For problems with complex shapes, the algorithm leads to important time-savings compared to manually determining \mathbf{x}^P and $\mathbf{x}^R \forall \mathbf{x} \in \tilde{\Omega}$. Since the number of fictitious nodes usually only accounts for a small portion of the total number of nodes, the computational cost to locate \mathbf{x}^P and $\mathbf{x}^R \forall \mathbf{x} \in \tilde{\Omega}$ is trivial compared with the cost of a complete simulation.

Some real examples of \mathbf{x}^R found by the algorithm are shown in Figure 6.10, where those arrows start from $\mathbf{x} \in \tilde{\Omega}$ and end at $\mathbf{x}^R \in \Omega$. Note that $\overrightarrow{\mathbf{x}\mathbf{x}^R} \approx k\tilde{\mathbf{n}}(\mathbf{x})$ (with $k \in \mathbb{R}^+$) and there is a transition of direction for $\overrightarrow{\mathbf{x}\mathbf{x}^R}$ between that of the normal vectors on two edges of the corner (or inner crack tip). The transition zone will narrow down as the horizon δ shrinks (δ -convergence) and the transition will be smoother as $m = \delta/\Delta x$ increases (m -convergence). It may be possible that this transition of the $\overrightarrow{\mathbf{x}\mathbf{x}^R}$ be used to detect/track crack tips, on the fly, but this idea will be pursued elsewhere. Although only the 2D implementation using uniform grid is considered in this work, extension of this algorithm to non-uniform grids and 3D cases and is straightforward and can be easily achieved.

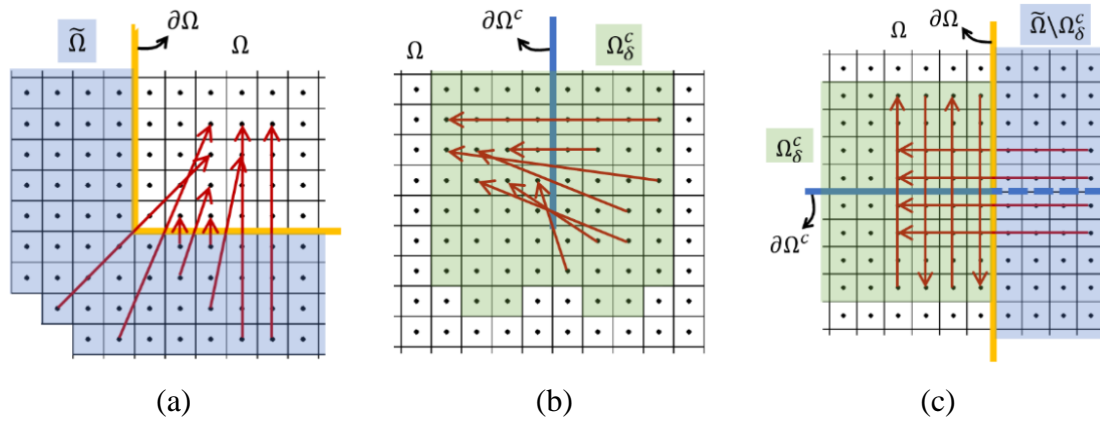


Figure 6.10. Real examples of some \mathbf{x} and their corresponding $\mathbf{x}^R \in \Omega$, connected by arrows, computed by the new algorithm: (a) at the corner; (b) at the inner crack tip; (c) at the edge crack tip. Note that the direction of arrow for each \mathbf{x} is not exactly the same as $\tilde{\mathbf{n}}(\mathbf{x})$ computed by Eq. (6.16) due to discretization.

In the following section, the performance of the mirror FNM will be compared with the naïve and the Taylor FNMs. We will also show the capability of the autonomous mirror FNM using problems with curved geometry and cracks.

6.4 Results and discussion

In this section, we first show how previously discussed three different FNMs perform in enforcing local BCs through the steady-state diffusion in a square domain. Then we will show how these FNMs perform in a problem with a singular point on its boundary.

Finally, we are going to show the capability of the autonomous mirror FNM in problems with curved geometry and cracks.

6.4.1 The performance of the three FNM versions in enforcing local BCs in peridynamics for problems without singularities

In the first problem, we consider a square domain with its side equal to 0.1, subject to the following local boundary conditions:

$$\begin{cases} u(x = -0.05, y) = 0.1 \\ u(x = 0.05, y) = 0.6 \\ \nabla_n u(x, y = \pm 0.05) = 0 \end{cases} \quad (6.18)$$

as shown in Figure 6.11. The classical solution to this problem is a linear function written as:

$$u(x, y) = 5x + 0.35 \quad (6.19)$$

In the PD simulations for this problem, we first take $\delta = 0.004$ and $\Delta x = 0.001$, respectively. This leads to about 10,000 nodes for a uniform discretization.

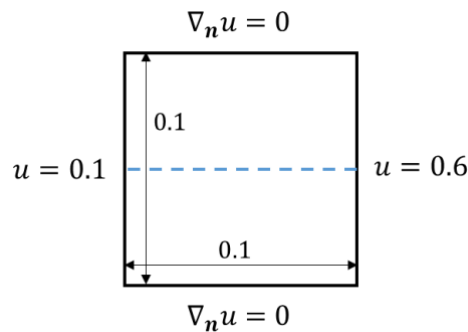


Figure 6.11. The geometry and boundary conditions for diffusion in a square domain used to compare different FNMs' capability in enforcing local BCs in the PD formulation.

The solution, obtained with the different FNMs, along the dashed mid-line in Figure 6.11 is shown in Figure 6.12. All three results match the classical solution very well. However, if we zoom in near the boundary, we can see clearly that the result obtained with the mirror FNM matches the classical analytical solution much better than results obtained with the other two FNMs. The simulation times for the three FNMs are given in Table 6.1. The simulation with the naïve FNM is at least 10 times faster than other two types of FNM, while the efficiency of Taylor and the mirror FNMs are similar to one another. Therefore, for such a simple problem, if the accuracy of the solution near the boundary is

not critical, the naïve FNM could be taken as the “best” option. If accuracy is needed, then the mirror FNM should be used.

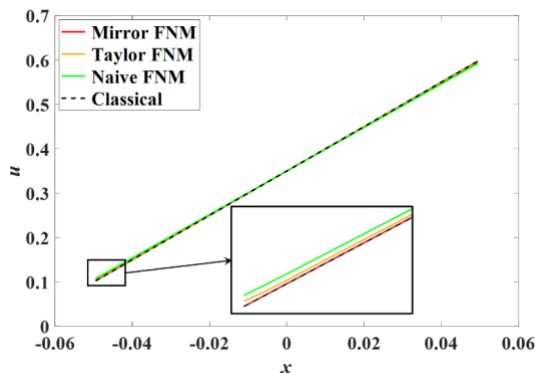


Figure 6.12. The classical analytical solution and PD solutions with different FNMs for the steady-state diffusion problem in Figure 6.11, along the dashed line shown there.

Table 6.1. Computational time of the simulation using the three different FNMs, when $\delta = 0.004$ and $\Delta x = 0.001$.

	FNM		
	naïve	Taylor-based	mirror-based
Time (s)	2.0	20.1	20.6

Notice that in [27], Eq. (6.10) is not considered in the Taylor FNM and there are no stability issues. However, for the example shown in Figure 6.11, as well as the next example shown below, the solution obtained with the Taylor FNM would diverge without using Eq. (6.10). Since a dynamic solver is used in [27] while a static one (CG solver) is employed in this work, this stability issue is possibly related to the solver being used. Another factor which might also affect the stability of the Taylor FNM is the discretization being selected. The mirror FNM, on the other hand, has not shown any stability issues and is thus more robust.

The next example has a singular point along a straight boundary, and we will use it to further test the performance of different FNMs types.

6.4.2 The performance of the three FNMs for Motz's problem

To test the capability of the different FNMs in handling local singularities along the boundary, we choose Motz's problem [37,38], which can be seen as a steady-state diffusion problem with the following local boundary conditions:

$$\begin{cases} \nabla_n u(x = -1, y) = 0 \\ \nabla_n u(x, y = 1) = 0 \\ \nabla_n u(x > 0, y = 0) = 0 \\ u(x < 0, y = 0) = 0 \\ u(x = 1, y) = 500 \end{cases} \quad (6.20)$$

as shown in Figure 6.13. This classical solution for this problem has a strong local singularity $O(\rho^{1/2})$ at the origin O .

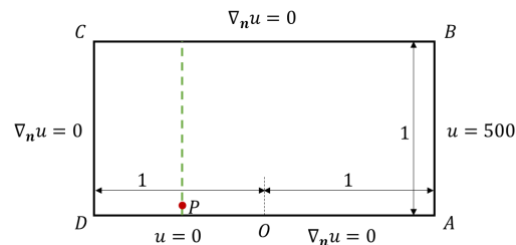


Figure 6.13. Domain and boundary conditions for an example of Motz's problem.

The classical solution for Motz's problem can be written as [38]:

$$u(\rho, \theta) = \sum_{i=0}^{\infty} D_i \rho^{i+1/2} \cos \left[\left(i + \frac{1}{2} \right) \theta \right] \quad (6.21)$$

where D_i 's are analogous to the stress intensity factors in linear elastic fracture mechanics, sometimes called "generalized flux intensity factors" [45]. Here we choose 34 terms, as in [46].

In Figure 6.14 (a) we show the contours for the classical solution. The point-wise relative differences between the PD solutions and the classical solution are given in Figure 6.14 (b)-(d). For the PD simulations, we used $\delta = 0.04$ and $\Delta x = 0.01$, respectively. Notice that for the mirror FNM, the non-trivial relative difference ($> 5\%$) is restricted to the horizon region of the singular point (point O) and the left-bottom corner (point D). As the horizon size approaches zero (with $\delta/\Delta x$ not decreasing), these areas also converge to zero. For the other two types of FNMs, the relative difference is large not only near the singular point or the corner, but also at locations far away from them. A quantitative comparison of the solutions along the vertical dash line shown in Figure 6.13 between the three types of FNMs is shown in Figure 6.15. As we can see in the zoomed-in image, the PD solution obtained with the mirror FNM matches the classical solution much better than the PD solutions obtained with other two FNMs.

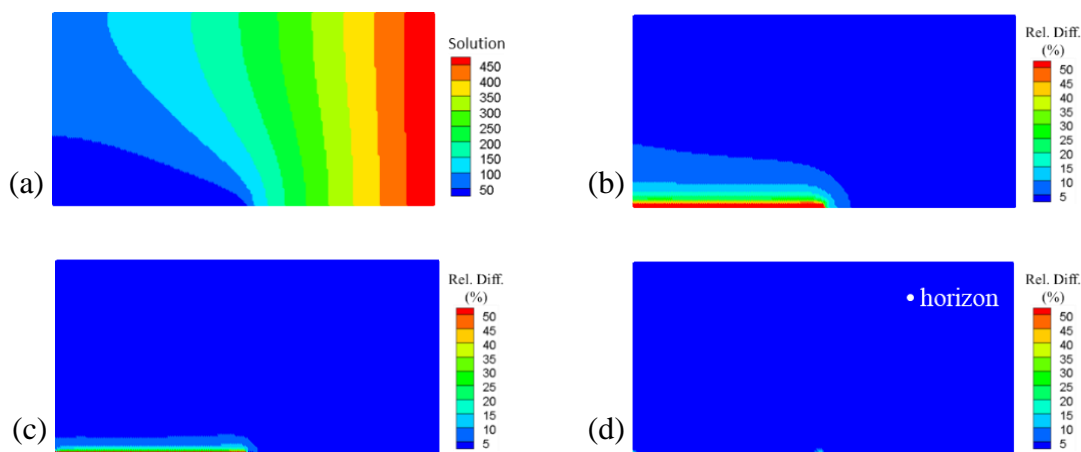


Figure 6.14. (a) Contours for the classical solution for Motz's problem; (b)-(d) Relative difference (Rel. Diff.) to classical solution of Motz's problem using the PD model with the naïve, the Taylor and the mirror FNMs, respectively.

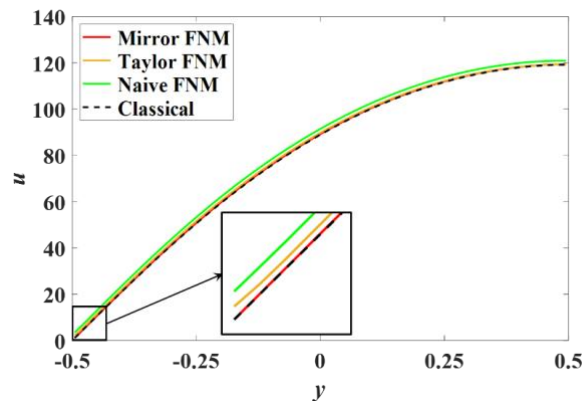


Figure 6.15. The classical and PD solutions with different FNMs for Motz's problem along the vertical dashed line at $x = -L/2 + \Delta x/2$, as shown in Figure 6.13.

The δ -convergence [47] (with $\delta/\Delta x$ fixed to be 4) to the classical solution for the three PD solutions at point P (-0.5, -0.48) (see Figure 6.13), is provided in Figure 6.16 with the relative difference in log scale. We do not choose a point on the boundary because the analytical solution there is zero (i.e., relative difference does not exist). Notice that as the horizon size changes, the grid also changes and there may not exist a node at point P. In such cases, we simply obtain the value at point P by averaging the value at four nearest nodes around P. Figure 6.16 demonstrates that, as the horizon size decreases, solutions obtained with all three types of FNM approach the classical solution. However, the mirror FNM produces relative differences from the classical solution that are two orders of magnitude smaller than those from the other two FNMs. Moreover, the mirror FNM solution exhibits a convergence rate that is increasing faster than the other two, as the horizon size decreases.

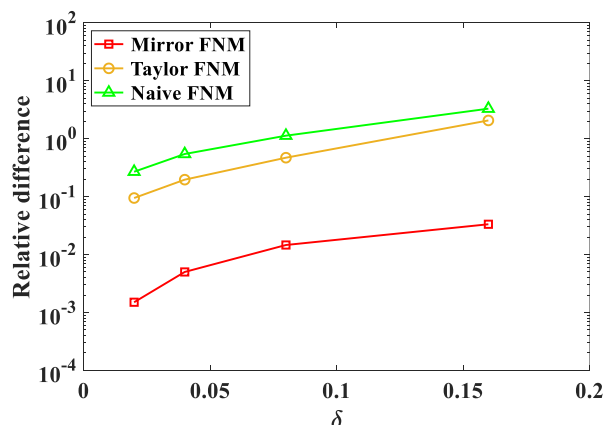


Figure 6.16. δ -convergence of PD solution (using the different FNMs) to the classical solution at point P (-0.5, -0.48) in Figure 6.16.

The above two examples show that the mirror FNM works best at accurately enforcing local boundary conditions in PD models, especially for problems with singularities (in local models) along the boundary. In the following section, we will test the autonomous algorithm developed for the mirror FNM for problems with more complex geometries.

6.4.3 Steady-state diffusion in disks with single and multiple pre-cracks

In this subsection, we will apply the autonomous mirror FNM to solve the PD formulation for diffusion in disks with cracks under Dirichlet boundary conditions. Using the algorithm developed in Section 6.3.4, the mirror FNM can be easily implemented for curved boundaries and cracks.

6.4.3.1 Disk with a single crack

We first consider a disk with a single crack and boundary conditions imposed as shown in Figure 6.17. The mirror node for each fictitious node, required by the mirror FNM, is determined by the algorithm described in Section 6.3.4. See Figure 6.10 for how mirror nodes are found for those nodes near the crack tip.

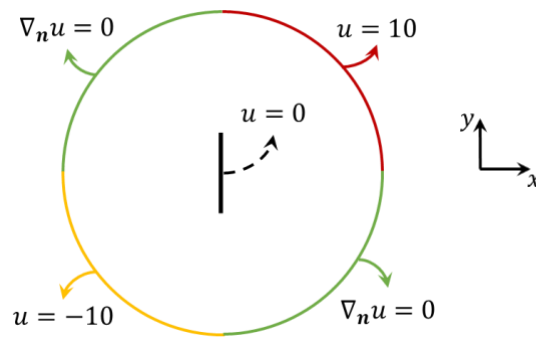


Figure 6.17. Local boundary conditions imposed for diffusion in a disk with a pre-crack at the center.

For verification, we also run a simulation of the corresponding PDE-based problem using the steady-state thermal solver in ANSYS workbench. Details of the ANSYS simulation, including how the “crack” is simulated, can be found in Appendix B. In the PD model, the crack is inserted by cutting all bonds that intersect with the pre-crack segment. The differences between the slightly different approaches as representing a crack between the two models should only have a trivial effect on the results.

Contours of the results obtained by ANSYS and PD, with zoomed-ins around the crack region, are given in Figure 6.18. The PD results match the FEM results closely, which shows that the autonomous mirror FNM works very well for problems with a curved boundary and with cracks. The jagged shape in the contours of the PD results appears because no smoothing interpolation technique is used in the visualization, we simply plot the obtained values at each PD node.

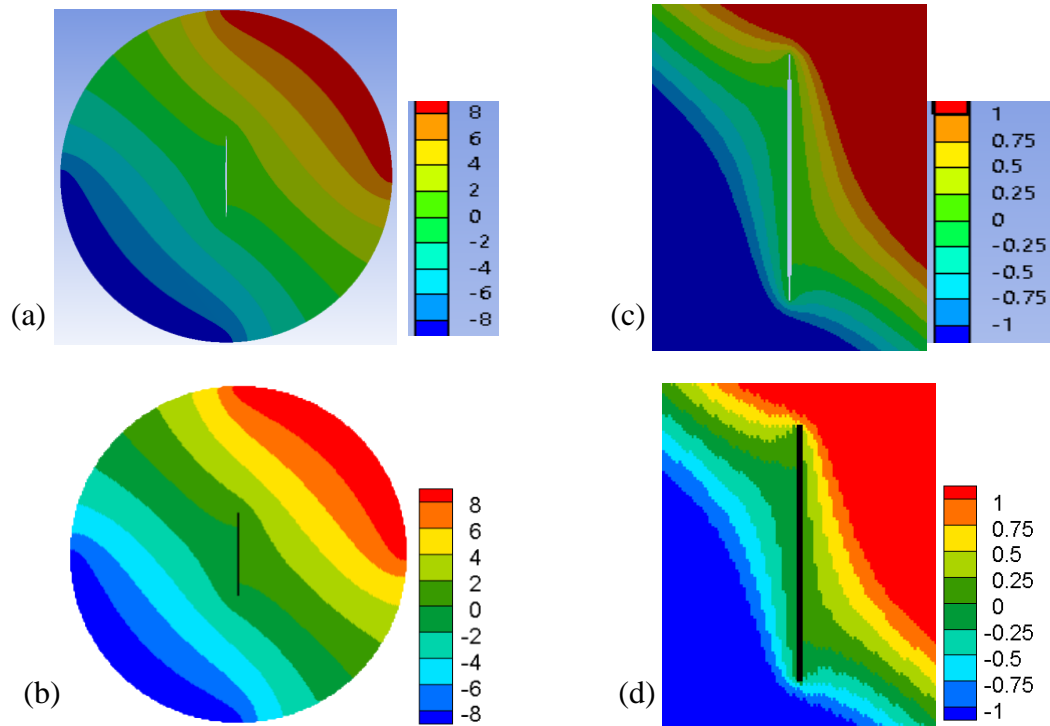


Figure 6.18. Contours for the solution to problem shown in Figure 6.17 obtained with: (a) ANSYS and (b) PD. In (c) and (d) we show zoomed-in regions around the crack for the corresponding solutions.

In practical simulations, the crack surface may have an angle with respect to the (uniform) discretization grid, whether it is a pre-crack or a new crack formed during the simulation. In order to demonstrate the generality of our algorithm for the mirror FNM, we solve the same problem but we rotate the uniform grid in the counterclockwise direction by 30° and 45° relative to the coordinates shown in Figure 6.17, respectively, as shown in Figure 6.19. Notice that when the crack is not aligned with the lattice, it may intersect with some PD nodes. These nodes are considered as free nodes (fully damaged) at which the constraint is the average of their family nodes (those not fully damaged). The PD solution with 30° -rotated and 45° -rotated grids are shown in Figure 6.20. They match very well the solution obtained with the original lattice shown in Figure 6.18.

Therefore, the autonomous algorithm can deal with arbitrarily oriented uniform grids effectively.

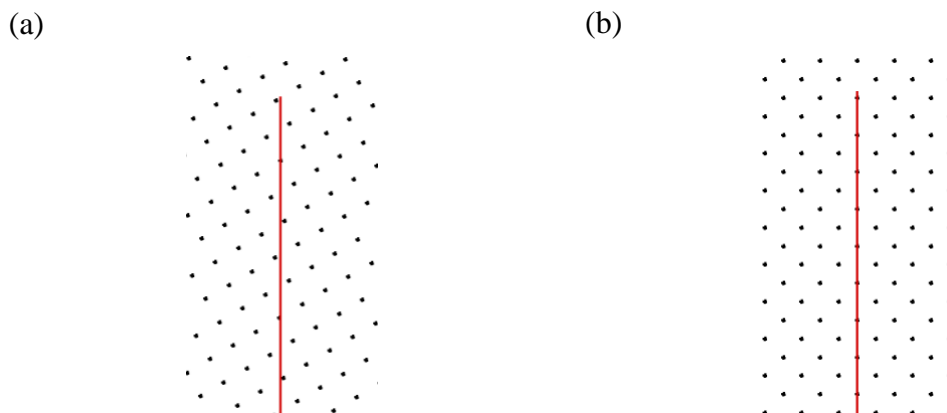


Figure 6.19. Part of the crack segment, shown by the red segment, and the PD grid after counterclockwise rotation by (a) 30° and (b) 45° .

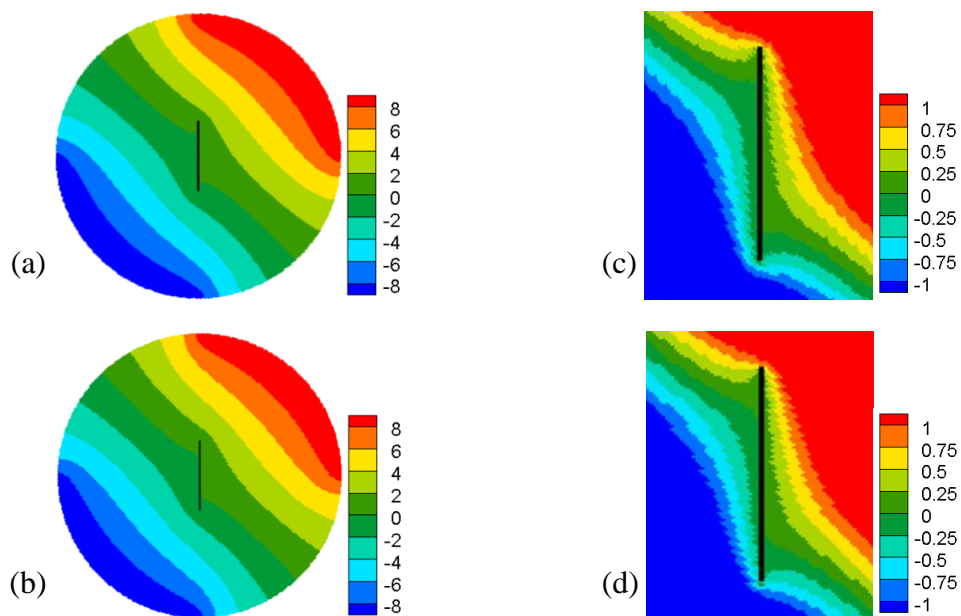


Figure 6.20. Contours of PD solutions obtained with the mirror FNM for counterclockwise-rotated grids by (a) 30° and (b) 45° . In (c) and (d) we show zoomed-in views around the crack for the corresponding solutions.

6.4.3.2 Diffusion in a disk with crossing cracks

A diffusion problem in a disk with two intersecting cracks is shown in Figure 6.21. We use the same autonomous algorithm introduced in Section 6.3.4 without any changes to treat this case. A contour-plot for the PD solution and the zoomed-in picture around the two cracks with imposed Dirichlet BCs are shown in Figure 6.22.

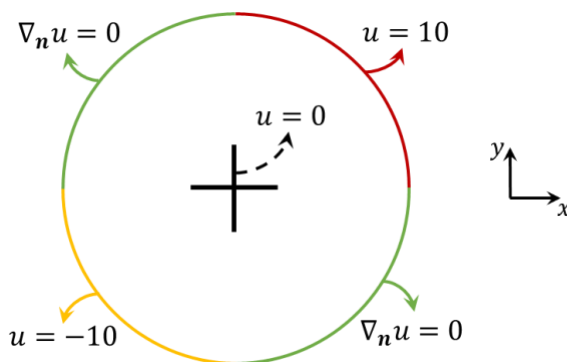


Figure 6.21. Diffusion in a disk with two intersecting cracks and associated local boundary conditions.

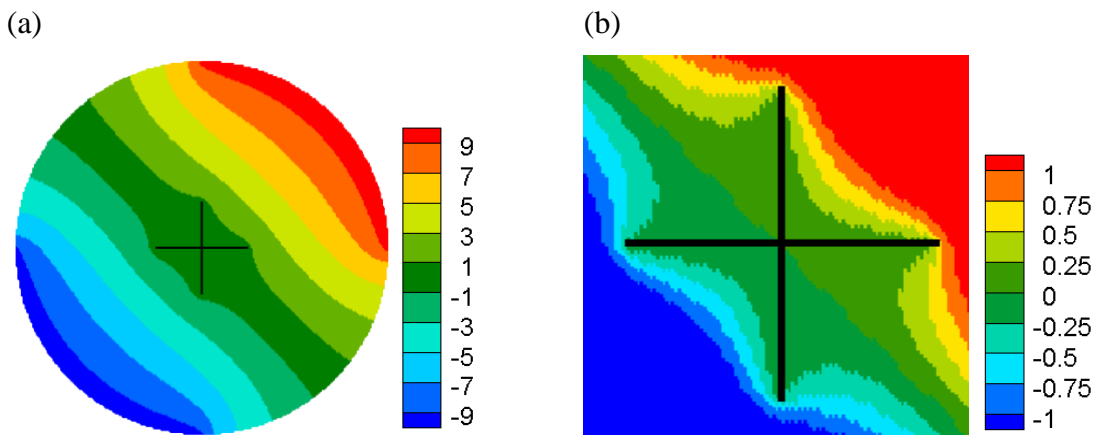


Figure 6.22. Contour-plot for the PD solution obtained with the mirror FNM (with the new algorithm) (a) over the disk and (b) over the zoomed-in area around the intersecting cracks (crack lines are drawn only approximately on top of the plot).

The examples shown in this section demonstrated that the autonomous algorithm for the mirror FNM works very well to enforce local BCs for complex geometries, including crack surfaces. Moreover, it can be readily employed for problems with moving boundaries such as corrosion damage, crack propagation, etc.

6.5 Conclusions

We introduced a new algorithm for the mirror-based fictitious nodes method (FNM) to deal with arbitrary geometries, including domains with cracks. Starting from computing, at each fictitious node, the peridynamic (PD) “generalized” normal vector which is perpendicular to the boundary of the solution domain if the boundary satisfies the 1st order smooth condition, this algorithm autonomously finds mirror nodes for all fictitious nodes. This algorithm allows us to easily generate the necessary data for mirror-based FNM in PD diffusion models to correctly impose the desired local BCs and reduce/eliminate the surface effect caused by incomplete nonlocal region near the free boundary/surface.

We compared the mirror-based FNM with the naïve and the Taylor-based FNMs for problems with or without singularities (in the corresponding local models) along the boundary, and we showed that the peridynamic solution with the mirror-based FNM agrees with the classical solution best, especially for the problem with a singularity in the corresponding classical formulation. The other two methods showed “pollution” of the solution far from the location of the singularity. We applied the new algorithm to diffusion problems in domains with a curved boundary and with cracks. In these cases too, the peridynamic solution obtained with our mirror-based FNM matched well the FE solution obtained in ANSYS. The same algorithm, with few modifications, should also

work with the mirror-based FNM for other types of PD models to enforce local-type BCs, including those with moving boundaries and growing cracks.

The new algorithm, which enables a FNM imposition of local BCs in PD models on arbitrary domains, will allow for more accurate peridynamic solutions near the boundaries. High accuracy near arbitrarily-shaped boundaries and material interfaces is crucial in, for example, problems that involve crack initiation and propagation, or evolution of corrosion fronts. In such problems, the new algorithm introduced here will have a great impact.

Acknowledgments

This work has been supported in part by the US National Science Foundation CMMI CDS&E Grant No. 1953346 (program manager Joanne Culbertson) and by a Nebraska System Science award. This work was completed utilizing the Holland Computing Center of the University of Nebraska, which receives support from the Nebraska Research Initiative.

Appendix A. Numerical implementation of peridynamic diffusion model with the fictitious nodes method

For spatial discretization, we discretize the whole PD interaction region $\Omega \cup \tilde{\Omega}$ uniformly [2] into cells with nodes in the center of those cells. Figure 6.23 shows a 2D uniform discretization with grid spacing Δx around a node \mathbf{x}_i . Non-uniform grids are also possible [23,48,49], which may conform better for shapes with, for example, rounded boundaries [50], but this is not pursued in this work. Although only 2D problems are considered here, the extension to 3D cases should be straightforward.

To discretize the peridynamic integro-differential equations, we use a meshfree method with one-point Gaussian quadrature [2] for the approximation of the integral term. Faster numerical methods such as the boundary-adapted spectral method [31][51] can be alternative options.

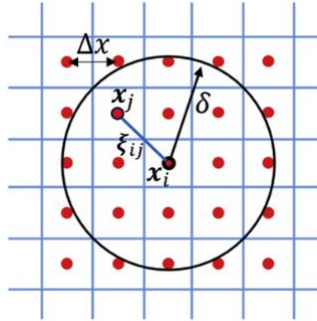


Figure 6.23. Uniform discretization for a peridynamic model. The circular region is the horizon region of node \mathbf{x}_i .

The discretized PD Laplace's equation (see Eq. (6.4)) for each $\mathbf{x}_i \in \Omega$ at n^{th} load step becomes:

$$\sum_{\substack{j \in \mathcal{H}_i \\ j \neq i}} \frac{u_j^n - u_i^n}{\xi_{ij}^2} \Delta A_{ij} = 0 \quad (6.22)$$

where the superscript n means n^{th} load step; the subscripts i and j denote the current node \mathbf{x}_i and its family node \mathbf{x}_j respectively, in the discretized domain; \mathcal{H}_i is the horizon region of node \mathbf{x}_i and $j \in \mathcal{H}_i$ includes all the nodes covered by \mathcal{H}_i (fully or partially); $\xi_{ij} = \|\mathbf{x}_j - \mathbf{x}_i\|$ and ΔA_{ij} is the area of node \mathbf{x}_j covered by \mathcal{H}_i . The discretized versions for other equations are similar to Eq. (6.22).

In Taylor-based and mirror-based fictitious nodes methods, the equilibrium system can be solved iteratively using the linear Conjugate Gradient (CG) solver combined with

additional criteria to check for the convergence of the solution. At each iteration or solution step, the CG solver is called and the solution in the domain and fictitious region is updated, respectively. For the purpose of minimizing the overall computational cost, the tolerance in the CG solver is set to be $1e-2$ at first and then decreased with solution steps by a factor until it reaches $1e-6$. This treatment could make the simulation 50% more efficient than fixing the tolerance in the CG solver to be $1e-6$ during the whole simulation. The system converges when the solution in the domain obtained between two sequential solution steps differ, in terms of norm-2 relative difference, by less than a given tolerance ($1e-6$ in this work). The detailed workflow for a complete simulation is shown in Figure 6.24.

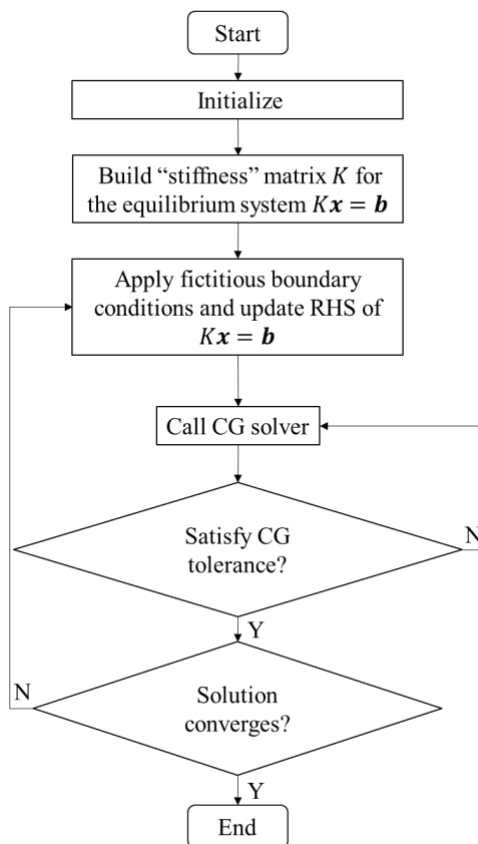


Figure 6.24. Workflow for the peridynamic simulation with Taylor/mirror FNM.

Appendix B. FEM modeling of the steady-state thermal problem

To obtain the classical FEM-based solution for the problem shown in Figure 6.17, ANSYS Workbench Steady-State Thermal solver is used. In the FE model, the two crack surfaces are generated by two arcs with the same small curvature and the maximum space between them is 0.01, which equals the grid size in the corresponding PD model. For the mesh, as shown in Figure 6.25, the element order is selected to be program controlled and all elements are triangles with the maximum size equals 0.05. The total number of nodes and elements are 9312 and 4548, respectively. All other options in the solver are set to be defaults.

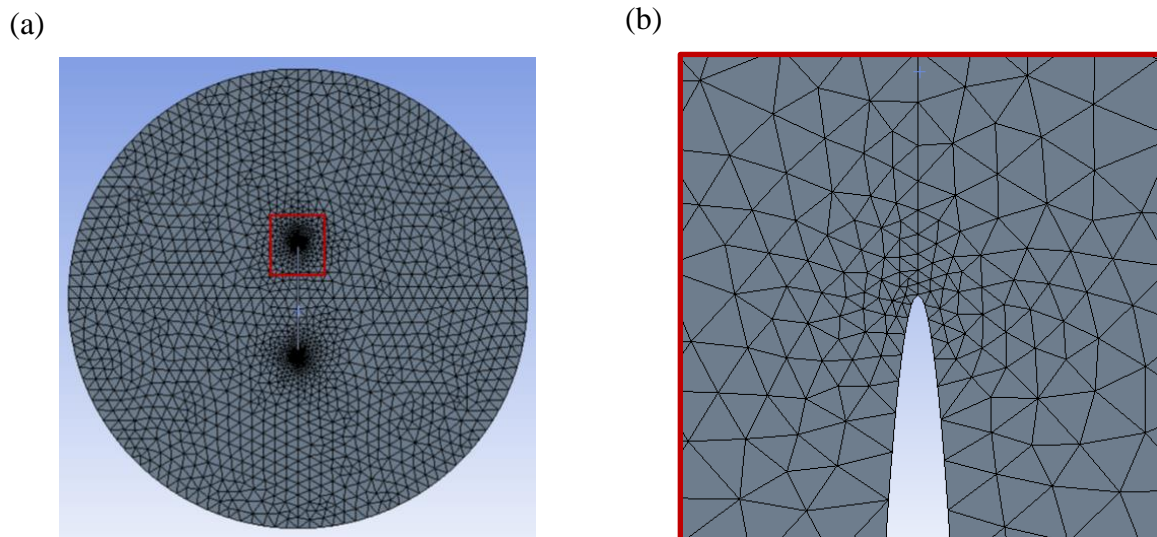


Figure 6.25. FEM mesh (a) over the whole disk; (b) near the crack tip.

References

- [1] S.A. Silling, *J. Mech. Phys. Solids* 48 (2000) 175–209.
- [2] S.A. Silling, E. Askari, *Comput. Struct.* 83 (2005) 1526–1535.
- [3] E. Madenci, E. Oterkus, *Peridynamic Theory and Its Applications*, Springer New York, New York, NY, 2014.
- [4] F. Bobaru, G. Zhang, *Int. J. Fract.* 196 (2015) 59–98.
- [5] F. Bobaru, J.T. Foster, P.H. Geubelle, S.A. Silling, *Handbook of Peridynamic*

Modeling, CRC press, 2016.

- [6] S.A. Silling, R.B. Lehoucq, in: *Adv. Appl. Mech.*, 2010, pp. 73–168.
- [7] Y.D. Ha, F. Bobaru, *Int. J. Fract.* 162 (2010) 229–244.
- [8] J.T. Foster, S.A. Silling, W.W. Chen, *Int. J. Numer. Methods Eng.* 81 (2010) 1242–1258.
- [9] Y.L. Hu, N. V. De Carvalho, E. Madenci, *Compos. Struct.* 132 (2015) 610–620.
- [10] F. Bobaru, M. Duangpanya, *Int. J. Heat Mass Transf.* 53 (2010) 4047–4059.
- [11] F. Bobaru, M. Duangpanya, *J. Comput. Phys.* 231 (2012) 2764–2785.
- [12] S. Oterkus, E. Madenci, A. Agwai, *J. Comput. Phys.* 265 (2014) 71–96.
- [13] J. Zhao, Z. Chen, J. Mehrmashhadi, F. Bobaru, *Int. J. Heat Mass Transf.* 126 (2018) 1253–1266.
- [14] Z. Chen, F. Bobaru, *J. Mech. Phys. Solids* 78 (2015) 352–381.
- [15] Z. Chen, G. Zhang, F. Bobaru, *J. Electrochem. Soc.* 163 (2016) C19–C24.
- [16] S. Jafarzadeh, Z. Chen, F. Bobaru, *Corrosion* 74 (2018) 393–414.
- [17] S. Jafarzadeh, Z. Chen, F. Bobaru, *J. Electrochem. Soc.* 165 (2018) C362–C374.
- [18] S. Jafarzadeh, Z. Chen, F. Bobaru, *Corros. Rev.* 37 (2019) 419–439.
- [19] S. Jafarzadeh, Z. Chen, S. Li, F. Bobaru, *Electrochim. Acta* 323 (2019) 134795.
- [20] S. Jafarzadeh, Z. Chen, J. Zhao, F. Bobaru, *Corros. Sci.* 150 (2019) 17–31.
- [21] Q. Du, M. Gunzburger, R.B. Lehoucq, K. Zhou, *SIAM Rev.* 54 (2012) 667–696.
- [22] Q. Du, M. Gunzburger, R.B. Lehoucq, K. Zhou, *Math. Model. Methods Appl. Sci.* 23 (2013) 493–540.
- [23] F. Bobaru, Y.D. Ha, *Int. J. Multiscale Comput. Eng.* 9 (2011) 635–659.
- [24] U. Galvanetto, T. Mudric, A. Shojaei, M. Zaccariotto, *Mech. Res. Commun.* 76 (2016) 41–47.
- [25] S. Prudhomme, P. Diehl, *Comput. Methods Appl. Mech. Eng.* 372 (2020) 113391.
- [26] H. Ren, X. Zhuang, Y. Cai, T. Rabczuk, *Int. J. Numer. Methods Eng.* 108 (2016) 1451–1476.
- [27] J. Wang, W. Hu, X. Zhang, W. Pan, *Int. J. Heat Mass Transf.* 139 (2019) 948–962.
- [28] H. You, X. Lu, N. Task, Y. Yu, *ESAIM Math. Model. Numer. Anal.* 54 (2020) 1373–1413.
- [29] Y. Yu, H. You, N. Trask, (2021).
- [30] Q. V. Le, F. Bobaru, *Comput. Mech.* 61 (2018) 499–518.
- [31] S. Jafarzadeh, A. Larios, F. Bobaru, *J. Peridynamics Nonlocal Model.* 2 (2020) 85–110.

- [32] H. Takeda, S.M. Miyama, M. Sekiya, *Prog. Theor. Phys.* 92 (1994) 939–960.
- [33] F. Macia, M. Antuono, L.M. Gonzalez, A. Colagrossi, *Prog. Theor. Phys.* 125 (2011) 1091–1121.
- [34] S. Oterkus, E. Madenci, A. Agwai, *J. Mech. Phys. Solids* 64 (2014) 1–23.
- [35] Z. Chen, F. Bobaru, *Comput. Phys. Commun.* 197 (2015) 51–60.
- [36] J.P. Morris, P.J. Fox, Y. Zhu, *J. Comput. Phys.* 136 (1997) 214–226.
- [37] H. Motz, *Q. Appl. Math.* 4 (1947) 371–377.
- [38] Z.C. Li, T.T. Lu, *Math. Comput. Model.* 31 (2000) 97–145.
- [39] P. Radu, K. Wells, *J. Integr. Equations Appl.* 31 (2019) 379–409.
- [40] X. Tian, Q. Du, *SIAM J. Numer. Anal.* 52 (2014) 1641–1665.
- [41] Q. Du, X. Tian, in: *Vol. 1 Adv. Aerosp. Technol.*, American Society of Mechanical Engineers, 2014.
- [42] Y. Tao, X. Tian, Q. Du, *Appl. Math. Comput.* 305 (2017) 282–298.
- [43] F. Bobaru, W. Hu, *Int. J. Fract.* 176 (2012) 215–222.
- [44] U.M. Ascher, C. Greif, *A First Course in Numerical Methods*, Society for Industrial and Applied Mathematics, Philadelphia, PA, 2011.
- [45] Z. Yosibash, *Singularities in Elliptic Boundary Value Problems and Elasticity and Their Connection with Failure Initiation*, Springer New York, New York, NY, 2012.
- [46] H.Y. Hu, Z.C. Li, *Comput. Methods Appl. Mech. Eng.* 195 (2006) 4139–4160.
- [47] F. Bobaru, M. Yang, L.F. Alves, S.A. Silling, E. Askari, J. Xu, *Int. J. Numer. Methods Eng.* 77 (2009) 852–877.
- [48] S.F. Henke, S. Shanbhag, *Comput. Phys. Commun.* 185 (2014) 181–193.
- [49] X. Gu, Q. Zhang, X. Xia, *Int. J. Numer. Methods Eng.* 112 (2017) 2087–2109.
- [50] J. Zhao, Z. Chen, J. Mehrmashhadi, F. Bobaru, *Eng. Fract. Mech.* 229 (2020) 106969.
- [51] S. Jafarzadeh, L. Wang, A. Larios, F. Bobaru, *Comput. Methods Appl. Mech. Eng.* 375 (2021) 113633.

Chapter 7 Conclusions and future work

In this dissertation, we introduced novel peridynamic (PD) models for fracture, corrosion, diffusion-advection and fluid flow, all of which are important ingredients involved in material degradation and the subsequent structure failure, as demonstrated by the shocking collapse of the condo building in Surfside, Florida, on June 24, 2021. Moreover, we developed a new algorithm to impose local boundary conditions in PD models to improve the accuracy. These models significantly enhanced our capability for solving complex fracture problems involving multiple physics, which are difficult for traditional PDE-based models to deal with.

The PD model for concrete fracture used the volume fraction of different phases (mortar and aggregate) in the concrete to generate a stochastic model with homogenized properties over the whole domain. This model balanced the accuracy of fracture prediction in concrete from (expensive) models that use an explicit representation of aggregates, with the efficiency of traditional homogeneous models. The model was used to simulate concrete fracture induced by the corrosion expansion of reinforced bars. For simplicity, instead of modeling the corrosion expansion process, a predefined displacement profile was used as the boundary condition around the rebar holes. In the future, the corrosion of rebars and expansion of corrosion products can be added in the model for complete multi-physics simulations. This can help us better understand the interactions between corrosion, expansion, and fracture, such that better designs of the concrete structure may be accomplished. The idea of partial or intermediate homogenization can also be easily applied to other heterogeneous materials. However, it should be noticed that some materials, unlike concrete, are not homogeneous at the larger

scale. For these materials, certain correlations between the bond type and bond features (e.g., length and angle) should be established in the IH-PD model to capture their large-scale heterogeneities.

The new PD corrosion model reformulated the existing corrosion model, leading to a simplified implementation with decreased computational cost, and integrated a PD electrostatic solver which updates, on the fly, the distribution of corrosion rate along the corrosion surface. This new model is applicable to a larger class of corrosion problems with arbitrary distribution of current densities along arbitrary-shaped corroding surfaces. The simulation results for two galvanic corrosion problems were validated against experimental results available from the literature and compared with numerical results from an FEM-based corrosion model (based on PDEs) built in COMSOL. It was found that artificial modification of the geometry at the interface of the galvanic couple is required for the COMSOL model to correctly initialize the motion of the corrosion surface, while the PD model introduced here does not require such changes. Such artificial modifications would lead to incorrect stress profile when the structure is under mechanical loadings and thus incorrect corrosion pattern when the corrosion rate depends on stress. A corrosion-fracture problem was solved by coupling this new PD corrosion model with existing PD fracture model to show how fracture can initiate and grow from the sharp trench created by galvanic corrosion. This example demonstrated the potential of PD models to simulate failure caused by the combined corrosion attack and mechanical loadings. In the future, this new corrosion model can be applied to other complex corrosion problems, especially those involving simultaneous corrosion and fracture such as the corrosion-induced concrete fracture. These problems are difficult for

traditional methods to solve but very important in terms of safety and cost in engineering industries.

The new PD formulation for transient advection-diffusion was constructed from mass conservation. The model was verified by examples with classical analytical solutions in both 1D and 2D. Thorough convergence analyses (δ -convergence and m -convergence) were also performed. Two integration kernels were presented for advection: the central kernel and the upwind kernel, leading to the central and upwind peridynamic advection-diffusion models, respectively. A weighted combination between these two models eliminated the oscillations at the high-gradient front compared with the central model, and reduction of numerical diffusion compared with the upwind model. To demonstrate the versatility of the model, mass transport in heterogeneous media with permeable and impermeable random inclusions was solved by this model using only a simple uniform grid, non-conforming to the microstructure geometry. In the future, this model can be extended to advection-diffusion-reaction and applied to simulate the mass transport in corrosion problems, because transportation rates of the substances involved in corrosion reaction can affect the corrosion rate significantly

The new PD formulation for viscous flow (in Eulerian formulation) was derived from mass and momentum conservation laws, which is different from translating the classical Navier-Stokes equations to their integro-differential forms using the “PD differential operator” in the literature. Specifically, the “nonlocality” introduced in these translations is merely a computational parameter, rather than a length-scale in true nonlocal models. The classical continuity equation was shown to be a limiting case of the constructed PD one with selected weight functions. The viscous force in the new model was formulated

from PD shear bond forces, and its weight function was determined by enforcing linear consistency of the viscous stress provided by a PD model with that from a corresponding classical model. The constructed model was verified against examples with analytical or numerical solutions of the classical model for incompressible flows at low Reynolds numbers. In the future, to extend this model for practical problems, Lagrangian formulation of this model needs to be derived, and compressible flow and flow at high Reynolds numbers should be investigated. Moreover, the new model will have advantages solving fluid-structure interaction problems such as erosion, erosion-corrosion and hydraulic fracture, by coupling with existing PD models of fracture, corrosion and mass transport. These fluid-structure interaction problems are of great interest in many areas, including aircraft industry, ocean engineering, environmental engineering, etc.

The new algorithm introduced for the mirror-based fictitious nodes method (FNM) enabled it to impose local boundary conditions more accurately in PD models for arbitrary geometries and reduce/eliminate the surface effect caused by incomplete nonlocal region near the free boundary/surface. The new algorithm introduced here will have a great impact for problems that involve crack initiation and propagation, or evolution of corrosion fronts, in which high accuracy near arbitrarily-shaped boundaries and material interfaces is crucial. We applied the new algorithm to diffusion problems in domains with a curved boundary and with cracks. The peridynamic solution matched well the FE solution obtained in ANSYS. In the future, this algorithm can be modified for other types of PD models to enforce local-type BCs, including mechanical problems with moving boundaries and growing cracks. It will help us improve the accuracy of PD simulations and promote its application in solving practical engineering problems.

All PD models in this dissertation are 2D. In the future, to solve real engineering problems, it is necessary to extend them to 3D. The extension should be straightforward, but it will significantly increase the computational cost, because both computational complexity and memory allocation of the currently used meshfree discretization scale with $O(N^2)$ in which N is the total number of discretization nodes. Fortunately, the recently developed fast convolution-based method (FCBM) for peridynamics can reduce the computational complexity to $O(N \log_2 N)$ and memory allocation to $O(N)$. The FCBM can be implemented for these PD models in the future to make 3D simulations affordable.